University
of Southampton

Static and Dynamic Phases of Vortices in the High Temperature Superconductor $YBa_2Cu_3O_{7-\delta}$

by

Andreas Peter Rassau

A Thesis Submitted for the degree of
Doctor of Philosophy

June 2000

UNIVERSITY OF SOUTHAMPTON

ABSTRACT

FACULTY OF SCIENCE

DEPARTMENT OF PHYSICS

Doctor of Philosophy

Static and Dynamic Phases in the Vortex State of the High Temperature Superconductor $YBa_2Cu_3O_{7-\delta}$

By Andreas Peter Rassau

Transport measurements have been used to probe static and dynamic vortex states within clean single crystalline samples of the high temperature superconductor $YBa_2Cu_3O_{7-\delta}$. A bespoke software tool has been designed to execute complex series of experimental instructions, facilitating the systematic investigation of a range of different history effects within the vortex system. A new approach has been developed for controlling the interaction of vortices with the underlying pinning potential, by means of the driving current modulation form and magnitude.

A wide range of evidence from both transport and ac-susceptibility techniques is presented in support of the existence of a finite width transition region (TR) in the vicinity of the melting line, over which vortex liquid and solid phases coexist. Dynamic behaviour in this TR has been explained in terms of the percolation of vortex liquid between vortex solid domains. Furthermore, within the TR we have observed current induced switching effects from low to high resistivity states and attributed this behaviour to a redistribution of vortex solid domains. A novel 'history dependence' technique has been developed for probing relaxation processes across the phase diagram. We have demonstrated that the relaxation properties of the system change abruptly across the TR but that there is no relaxation over experimental time-scales at any point within this region. This is contrary to expectations for a model of glassy relaxation but entirely consistent with the notion of a region of coexistent vortex liquid and solid phases.

We have found that the dynamics of this vortex solid are crucially dependent upon the modulation form of the driving current. In particular, we have demonstrated that the driven vortex system has the tendency to stabilise in two particular dynamic phases, one ordered the other relatively disordered, dependent on the nature of the applied drive. Transient responses observed on switching between drive modulation-forms were interpreted in terms of changeovers between these phases. In response to oscillatory drives that were asymmetric either with respect to their amplitude or to the positive and negative part of their period, we observed a highly unusual dynamic state. This state manifested itself in terms of large-amplitude oscillations of the voltage amplitude which were independent of the drive modulation-frequency but highly dependent on the asymmetry of the drive. This anomalous response has been explained in terms of distinct regions of ordered and disordered dynamic phases coexisting within the sample, their relative proportions changing periodically with time. From such observations we have demonstrated that the ordered dynamic state is inherently stable, in that it is easier to coherently drive an ordered-phase domain out of the sample than it is to break it apart.

The real voyage of discovery is not in seeking new landscapes but in having new eyes.

Marcel Proust

CONTENTS

CHAPTER 1. INTRODUCTION 1

CHAPTER 5. THEORIES OF VORTEX DYNAMICS 91

CHAPTER 6. VORTEX LIQUID TO SOLID TRANSITION REGION 124

ACKNOWLEDGMENTS

A work of this nature cannot be created in isolation and the list of people to whom I am genuinely indebted is long and distinguished. I have seen it as a great privilege to work alongside some of the finest scientists in our field. I only hope that I will continue to carry the incisiveness and curiosity that I have learned from them, on into my new life.

Firstly I would like to thank Peter de Groot, my supervisor, for providing me with the chance to chance to probe some of natures' more elusive secrets. Thank you Peter for providing me with the opportunity and the resources to conduct this study.

Special thanks are due to Sergey Gordeev, for the innumerable ways in which he has helped me over the course of my Ph.D. studies. Thank you Sergey, for teaching me the value of true understanding; for your apparently boundless patience whilst I was learning; for always taking the time to listen to my ideas. Not least I wish to thank you for the considerable assistance that you have provided in the preparation of this document.

Another person to whom I am considerably indebted is Mike Sawicki. Thank you Mike for providing me with moral support through those long evenings; for helping to see the way through to the best technical solutions. You have truly inspired me by with your ingenuity and tenacity.

Others that I would like to thank for helping to the develop the ideas presented within this thesis include Sasha Zhukov, Hans Fangohr, Mohand Oussena, Tim Pickrell, Viv Lyons, Stelios Kokkaliaris, Konstantantinos Deligiannis and Louis Jansen. In particular, thanks are due to Hans, for proof reading my theory chapters and providing me with many valuable suggestions.

An experimental Ph.D. cannot be conducted without considerable technical support. In this area thanks are due to Nick Hinchcliffe, Dave Beckett. I would also due to Gordon Macmillan for sharing with me his considerable experience of cryogenic systems and Colin and Tom for providing me with the helium to conduct these experiments.

Finally I would like to thank Engineering and Physical Sciences Research Council (UK) for providing me with the funding to conduct this research. Gratitude is also due to the European mobility of Researchers programme, for funding my trips to the Grenoble High Magnetic Field Laboratory.

For Methodius and all the other students from
Ndanda Sekondari that helped me to see the true
value of education.

CHAPTER 1. INTRODUCTION

1.1 Historical Context

Discovered by the Dutch physicist Kamerlingh Onnes in 1911 [1], superconductivity has proved to be one of the most important physical phenomena of the 20th century. Basic **Type-I Superconductivity** manifests itself as the simultaneous development at a critical temperature T_c, of zero resistivity and perfect diamagnetism, the diamagnetism being supported by screening currents flowing in the surface of the sample (the Meissner-Ochsenfeld effect [2]). Further to this, there is a distinct **Type-II** class of superconducting behaviour, whereby above a temperature dependent field $H_{c1}(T)$ magnetic flux penetrates the bulk of superconductor in the form of localised quantised lines, also known as **vortices**.

Building upon a long history of development, to which London & London [3, 4] and Pippard [5] made major contributions, in 1950 Ginzburg and Landau (**GL**) published the first complete phenomenological theory of the type-I superconducting state [6]. This theory introduced many important concepts, most notably the idea that the superconducting state could be described in terms of a macroscopic effective wave function. Just a few years later, a physical explanation for this wave function arrived in the form of the Bardeen Cooper and Schrieffer (BCS) microscopic model [7]. In this theory superconductivity was explained in terms of a phonon-mediated pairing-interaction between electrons forming a so-called Cooper-pair condensate. At approximately the same time, following on from the GL theory, Abrikosov proposed the existence of the type-II superconducting state [8] and almost immediately a wealth of evidence emerged in support the Abrikosov concept. Over subsequent years a sound understanding of both type-I and II superconductivity has developed.

At the same time as such major developments were being made towards understanding the physics of superconductors, considerable difficulties had been experienced in developing economically viable applications. Throughout the 1960s and 1970s a number of demonstrators were constructed but while progress was made in terms of the engineering, cost-effective applications remained elusive [9]. This was largely due to the very low critical temperatures of the elemental and alloy superconductors known at the time (T_c ~10 K). By the start of the 1980s interest in the engineering applications had all but disappeared. Moreover, by this stage it seemed that the physics of the superconducting state had been more or less fully elucidated. It appeared, therefore, that the phenomenon of superconductivity would be relegated to the status of a topic which has been understood and explained and yet was without widespread practical application. Then, in 1987, something quite remarkable happened.

Up until the late 1980s the record for the highest critical temperature in a superconductor was 23 K in Nb_3Ge [10]. Over the 70 preceding years, progress towards increasing T_c had been painstakingly slow. In March 1987, Georg Bednorz and Alexander Müller of the IBM research laboratory in Zürich published a paper with the unassuming title "*Possible high T_c superconductivity in the Ba-La-Cu-O system*" [11]. In this paper they presented evidence for superconductivity at a temperature of 30 K which, on the face of it, this did not seem to be particularly remarkable. Moreover, this was not the first time someone had claimed to observe "high temperature" superconductivity. In this context many scientists dismissed the findings as an improbable claim of no real interest.

However, there was one important factor that attracted attention to the Bednorz-Müller compound. Contrary to all previous observations the new superconducting compound was an oxide. The observation of superconductivity at relatively high temperatures within an oxide system pointed to the existence of a new class of superconducting compounds, potentially with higher critical temperatures than had previously been observed. Inspired by this logic, a number of groups around the world quickly sought to reproduce and build upon the Bednorz-Müller results. A dramatic race ensued, and in the autumn of 1988 several papers were published virtually simultaneously, reporting superconductivity in the compound $YBa_2Cu_3O_{7-\delta}$ with T_c ~ 90K [12].

The discovery of so-called "high-temperature" superconductors (**HTS**), with critical temperatures above the temperature of liquid nitrogen, stimulated a massive amount of interest in the field. Undoubtedly in many cases the original motivations were economic, as researchers sought to make a contribution to what they saw to be a burgeoning new technological area. However, as interest in this new class of compounds developed, it became increasingly apparent that there were many exciting and perplexing features in terms of the physics of this new class of compounds. Indeed, it is a remarkable fact, that in spite of over 10 years of intensive investigation, the physics of high temperature superconductors remains far from fully elucidated. There is still no consensus as to the nature of the superconducting pairing mechanism in HTS [13]. Moreover, new physics continues to be discovered in relation to the vortex-state of HTS.

It was in this context, that the work of this thesis was conducted. Contained within this document are contributions to the understanding of the equilibrium and dynamic properties of the vortex state in high temperature superconductors. In this chapter, an overview is provided of some of the key concepts required to understand the physics of vortices in general and in high temperature superconductors in particular. In Section 1.2, a brief introduction is provided to the various important length-scales within the type-I and II superconducting states. In Sections 1.3 and 1.4 the properties common to type-II superconducting materials are considered. In section 1.5, properties specific to high temperatures superconductors are discussed. Finally in section 1.6, an overview is provided of the content of the remainder of this thesis.

1.2 Important Length-Scales in the Superconducting State

A convenient phenomenological framework for analysing superconducting systems was provided by the Ginzburg-Landau (**GL**) model [6]. Although only really applicable in the vicinity of T_c, a number of concepts which arise out of the this model have proved generally useful for characterising superconducting systems. An essential assumption of GL-theory is that the superconducting system can be described in terms of an effective macroscopic wave-function ψ. It turns out that in conventional superconductors ψ, is related to the local density of superconducting Cooper paired electrons $n_s = \psi(\mathbf{r})^2$. The important length-scales which arise out of the GL model are:

(i) **Coherence length,** ξ: length scale for variations in the superconducting wave-function

(ii) **Penetration depth,** λ: length scale over which magnetic field penetrates into the bulk of a superconductor

(iii) **Ginzburg-Landau parameter, $\kappa = \lambda(T)/\xi(T)$**

Whereas λ and ξ vary with T, κ is approximately constant making it useful in characterising superconducting materials. This is especially true, in terms of establishing the distinction between type-I and type-II superconducting behaviour.

The GL-parameter is important since it controls the surface energy of the boundary between normal and superconducting regions, the crossover from positive to negative surface energies occurring for $\kappa = 1/\sqrt{2}$ [14]. For pure elemental superconductors $\lambda(T) << \xi(T)$ thus $\kappa << 1$. This leads to a positive surface energy for all fields and temperatures, consistent with the idea of a bulk-screened superconductor. The effect of alloying a superconducting material is to substantially reduce the coherence length ξ. At the same time λ increases due to non-local effects, thus the net result is a strong reduction in Ginzburg-Landau parameter κ. Thus in alloyed or compound materials, for the majority of fields and temperatures in the superconducting region $\kappa > 1/\sqrt{2}$. This implies a negative Normal-Superconducting surface energy and it follows that in this case it is energetically favourable to maximise the area of *N-S* boundaries. Under such conditions the system undergoes a transition into the very different Type-II superconducting state.

1.3 Type-II Superconductivity: The Vortex State

While it was clear from Ginzburg Landau theory, that in certain superconducting materials, there should be a crossover into a regime with negative *N-S* surface energy, it was Abrikosov who first elucidated the nature of this regime [8]. Abrikosov reasoned that in order to maximise the *N-S* surface area, the normal region should penetrate into the bulk of the superconducting material, dividing up on the finest possible scale. In fact, this subdivision is limited by flux quantisation, the penetrating field being divided up into units of one flux quantum ($\phi_0 = h/2e$). Thus, a situation is attained whereby flux lines penetrate the superconductor, locally driving the system normal whilst the bulk of the system remains superconducting. These quantised lines of flux came to be known as vortex–lines or vortices, since they are screened from the bulk of the superconductor by vortices in the electron superfluid. In a pure material at zero temperature the vortices should be straight parallel lines arranged into a triangular or **Abrikosov lattice** also known as a **flux-line-lattice (FLL).**[*] Thus, in certain types of superconducting compound, known collectively as type-II superconductors, above a **lower critical field H_{c1}(T)** it becomes energetically favourable for flux lines to penetrate into bulk of the superconductor. Above this critical field the state of the system is known variously as the Type II, Schubnikov phase or vortex state. This state extends up as far as an **upper critical field H_{c2}(T)**, at which the system becomes normal.

The structure of an individual vortex line is best visualised by considering the variation in the superconducting order parameter and local magnetic flux density in its vicinity (see Fig. 1.1, overleaf). Due to the circulating screening current, the magnetic induction falls off as $\exp(-r/\lambda)/\sqrt{r}$ on moving away from the centre of the vortex. Thus the Ginzburg–Landau penetration depth (λ) provides an approximate dimension for the region over which flux

---

[*] It should be noted that the term flux-line-lattice is applied somewhat more generally than Abrikosov lattice, since it is used to describe configurations in which vortices are distorted away from their ideal lattice positions.

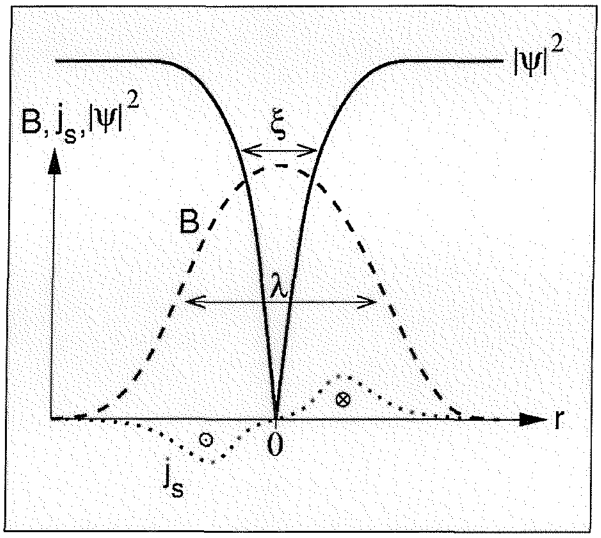

Fig. 1.1 *Schematic representation of an isolated vortex, showing the variation in the superconducting order parameter* $|\psi|^2$ *and local magnetic induction B. Also indicated is the variation in the superconducting electron current density* (j_s) *around the vortex core.*

penetrates. In terms of the screening action of the condensate electrons themselves, the circulation velocity diverges on approaching the centre of the vortex. This drives the local electron density, and hence the superconducting order parameter to zero at the axis of the vortex. Moving out from the centre of the vortex, the condensate wavefunction reaches its asymptotic value over a range defined by the superconducting coherence length ξ. The tube of diameter ξ around the vortex axis is commonly described as the **vortex core**.

1.4 Forces Acting on Vortices within Type-II Superconductors

Due to basic electrodynamic and superconducting state properties, a wide range of different forces act on vortices within the type-II superconducting state. Indeed, competition between such forces leads to a rich complexity of behaviour in the static and dynamic phases of the vortex system. In the following sections we will review some of the main interactions influencing the distribution and motion of vortices within type-II superconductors.

1.4.1 Intervortex Interactions

In all real systems both impurities and thermal interactions influence vortex distributions. However, for simplicity we will initially consider an ideal pure system at zero temperature. In this case the vortex separation and distribution are controlled by the so-called inter-vortex interactions. In fact, there are two such interactions, each of which is important in different regions of the phase diagram:

(i) **Long range interaction** of circulating screening currents (repulsive for parallel and attractive for anti-parallel flux lines). Extends out as far as the currents themselves, i.e. over an approximate range λ.

(ii) **Short range attractive interaction** due to the fact that the order parameter drops off at vortex core (it is energetically favourable for two such cores to overlap).

For the purpose of simulations these interactions are often approximated to a two body potential dU between flux line elements dl_1 and dl_2 separated by a distance r_{12} [15]:

$$dU = dl_1 . dl_2 e^{-r_{12}/\lambda'} - |dl_1| . |dl_2| e^{-r_{12}/\xi'} . \qquad (1.1)$$

The first and second terms in this expression reflect the long and short-range interactions respectively. Here λ' and ξ' represent the effective field-dependent penetration depth and coherence length respectively ($\lambda' = \lambda / \sqrt{1 - B/B_{c2}}$ and $\xi' = \xi / \sqrt{1 - B/B_{c2}}$). In fact, except in the immediate vicinity of H_{c2}, the long range repulsive interaction dominates.

It follows, that the long-range intervortex interaction should have consequences in terms of defining the rigidity of the vortex system. Any displacement of vortices away from their equilibrium positions results in a redistribution of screening currents and hence in a net force on the vortices. The force per unit length on any particular vortex line is given by: $\underline{f} = \phi_0 \underline{J}_s \times \underline{n}$, where $\underline{J}_s$ is the superimposed supercurrent density due to all the other vortices within the sample, ϕ_0 represents one flux quantum and $\underline{n}$ is a unit vector along the vortex line.

This rigidity of the system is commonly expressed in terms a set of elastic moduli, reflecting the response to different kinds of distortion. These moduli are: the shear modulus C_{66}; tilt modulus C_{44}; and compression modulus C_{11} respectively

1.4.2 Transport Current Lorentz Forces & Flux Flow Dissipation

Just as the screening current redistribution that arises as a result of vortex system distortions exerts forces on individual vortices, a similar effect can be achieved by imposing an external transport current. The difference is that, in this case, all vortices within the system are subjected to a current flowing in a common direction.[†] In this case the net Lorentz force on the system can be written as: $\underline{F}_L = \underline{J} \times \underline{B}$. Here $\underline{J}$ is current density due to the externally imposed transport current. The change in flux linkage that arises as a result generates a dissipative emf $\underline{E} = \underline{v}_\phi \times \underline{B}$, where $\underline{v}_\phi$ is the flux-line-lattice velocity. It follows that in the absence of pinning, a transport current will always lead to dissipation. In the simple geometry $\underline{J} \perp \underline{B}$ the **flux flow resistivity** is approximately given by [14]:

$$\rho_{ff} = \frac{\phi_0 B}{\eta}, \tag{1.2}$$

where η represents the viscous drag retarding the vortex motion. From a fundamental point of view, it is now believed that the dissipation arising from flux–line motion can be attributed to two distinct mechanisms providing approximately equal contributions:

(i) **Dipolar eddy currents** surrounding each moving vortex and passing through the normal region at the vortex core [16].

(ii) **Retarded recovery of the order parameter** at places where the vortex core has just passed [17].

1.4.3 Vortex Pinning Interactions

Pinning is the name given to any mechanism that restricts the free motion of vortices, thereby preventing or inhibiting dissipative flux motion. In the case where there is no net motion of the vortex system, in spite of the application of a transport current, then the system is described as being **pinned**. If a sufficiently large transport current, known as a **depinning current**, is applied then the system will free itself from this pinning and dissipation will develop as a result.[‡]

In general, pinning occurs where a vortex's self energy is dependent on position. This positional energy dependence can arise due to material inhomogeneities or else as a result of structural features inherent to the superconducting compound. Some of the main sources of pinning with HTS compounds are summarised in the following table.

(i) **Pinning by point defects**. Some time ago Tinkham predicted [18] that oxygen vacancies in HTS compounds should provide a doping dependent source of weak pinning. Recently it was demonstrated that in pure detwinned $YBa_2Cu_3O_{7-\delta}$ single crystals, oxygen vacancies are indeed the dominant source of pinning [19].

(ii) **Pinning by extended defects** (e.g. ion tracks or twin-plane boundaries): The essential pinning mechanism is the same as for point defects but since the defects are extended, the overall pinning force may be considerably larger. The pinning effect of extended defects varies considerably with the orientation of the applied magnetic field relative to the defect. For example, in Ref. 20 Fleschler *et al.* present detailed transport studies on the angular dependence of twin boundary pinning.

(iii) **Intrinsic pinning**: This type of pinning is unique to layered HTS, whereby the superconducting order parameter falls to a minimum between CuO_2 layers. Thus, when

---

[†] Here we make the simplifying assumption that the applied transport current is uniformly distributed across the sample cross-section. In practical transport measurements it is a major experimental consideration to ensure that this is indeed the case (see Chapter 3).

[‡] The depinning current should not be confused with critical current density (J_c) at which the kinetic energy of the Cooper pairs becomes equal to the superconducting condensation energy.

the magnetic field is oriented parallel to the superconducting layers this can lead to a variety of lock-in and commensurability effects (see for example Ref. 21).

The dominant source of pinning in a particular measurement will depend on the specific sample, as well as the magnetic field orientation. If a number of different types of pinning act in combination, it can often prove difficult to separate their relative contributions.

Fundamentally speaking, vortex-core pinning arises due to two distinct mechanisms [22, 23, 24], namely: pinning by local variations in the superconducting order parameter (δT_c pinning); and pinning by variations in the charge carrier mean free path (δl pinning). Critical current studies by Griessen *et al.* on $YBa_2Cu_3O_{7-\delta}$ films have provided evidence that δl pinning may be the dominant pinning mechanism at temperatures below 80K and in moderate fields (< 2 T) [25].

Thus far we have considered pinning in terms of the forces acting between pinning sites and individual vortices. From an observational point of view, it often more important to understand how such individual pinning forces act in combination to pin the vortex system as a whole. This necessitates the statistical summation over individual pinning interactions, in order to obtain an expression for the overall pinning force. At the limit of strong intervortex interactions and weak randomly distributed point disorder, it is expected that the pinning interaction should average to zero. In practise, however in real systems there is always a finite pinning force. This occurs due to the distortion of the vortex system away from the ideal lattice configuration, since partial correlation between the vortex and pin distributions gives rise to a finite overall pinning interaction. Indeed at the limit of very weak intervortex interactions and strong pins, it is expected that vortices should correlate directly with pinning sites. In this case, the overall pinning force can be expressed as direct summation of the individual pin-interactions:

$$j_c B = n_p f_p \,. \qquad (1.3)$$

Here n_p represent the pinning site density, and f_p the r.m.s. force for a single pin on a given flux line. It has been recognised for some time, however, that this type of strong pinning behaviour is not relevant in most physical situations [26].

In most cases the effective overall pinning force arises out of a competition between intervortex and pinning interactions. The problem of carrying out a statistical summation over pin sites in such situations was first solved by Larkin and Ovchinnikov (LO) [27, 28]. The most important idea to arise out of the LO theory, is that while pins do distort the FLL, short-range order persists over a correlated volume given by:

$$V_c = \frac{4C_{44}^2 C_{66}^4 \xi^2}{n_p^3 f_p^6} . \qquad (1.4)$$

Here f_p represents the r.m.s. force for a single pin on a given flux line; n_p reflects the density of pins; and C_{66}, C_{44} represent the shear and tilt moduli respectively. From Eqn. 1.4 it is apparent that the correlation volume decreases with increasing pin density and increases strongly with increasing intervortex interaction.

From the LO model we obtain the idea that within each of these correlation volumes, f_p acts randomly. Thus overall, the system effectively comprises a collection of elastic correlated domains, the volume of which will be determined by the competition between pinning and intervortex interactions. This leads quite naturally to the idea of **collective pinning**, as originally proposed by Pippard [29]. Here the essential idea is that rather than regarding pinning as an interaction between individual vortices and individual pins, we should think about it as a coupling of correlated volumes within the vortex system with the disorder potential across those volumes. That is to say, over a large range of parameter space the characteristic correlation length-scales are longer than the intervortex spacing, hence we should regard vortices as being collectively rather the individually pinned.

1.4.4 Thermal Interaction

Thermal interactions affect the vortex system in many different ways, from the temperature dependence of the intrinsic parameters to the thermal Langevin shaking force (for a more detailed discussion see Chapter 4). Indeed, by virtue of their high critical temperatures thermal effects are particularly important in HTS (see Section 1.5.1). From the point of view of visualisation is useful to think of the thermal interactions as a random shaking force upon the vortices. Mathematically, we can relate the mean-square amplitude of the shaking motion $\langle u^2 \rangle$ to the temperature via the expression: $\langle u^2 \rangle \propto T$, where the constant of proportionality is determined by the elastic moduli of the FLL. Thus, if the shaking is sufficiently violent, then the vortex system should break apart. Above the point where this occurs, vortices will no longer bear any fixed relation to their nearest neighbours. By analogy with conventional systems, this transition has been denoted as the **melting transitions from a vortex solid to a vortex liquid state.** Melting lines have been deduced for these transitions using conventional Lindemann criteria. In terms of the thermal (E_{th}) and intervortex (E_{vv}) interaction energies thermodynamic melting can be characterised as the point where: $E_{\mathrm{th}} \sim E_{\mathrm{vv}}$. Above the melting transition vortex system responses are characterised by linearity and ohmic behaviour. In contrast, below the melting transition, a competition between intervortex and pinning and thermal interactions leads to a variety of different glassy regimes.

1.5 Properties Specific to High Temperature Superconductors

High temperature superconductors are a very special type-II superconductor, in that they manifest a range of vortex-state properties unobserved or only barely observable in conventional superconducting materials. The reason for this can be traced back to the unusual intrinsic parameters for HTS compounds, in particular their extremely short coherence lengths and high critical temperatures. In the following sections we will consider the three main areas in which HTS materials differ from their low temperature counterparts.

1.5.1 Importance of Thermal fluctuations

The fundamental parameter determining the strength of thermal fluctuations within the vortex state is the Ginzburg number [22]:

$$Gi = \left[\frac{T_c}{H_c^2(0)\varepsilon\xi^3(0)\sqrt{2}}\right]^2. \qquad (1.5)$$

Here ε represents the sample anisotropy. Due in particular to their relatively short coherence lengths and high critical temperatures, HTS have much larger Ginzburg numbers than conventional low temperature superconductors. This has the following important consequences.

(i) Increased width of the thermal fluctuation regime near to H_{c2}.

(ii) Increased area of the depinned region on the H-T phase diagram

(iii) Increased area of the melted region on the phase diagram.

Thus in HTS compounds, strong competition between the various energy scales leads to a rich phenomenology of behaviour. This is in contrast to low temperature superconductors, for which the melted and depinned regions are confined to a very narrow and virtually unobservable region in the immediate vicinity of H_{c2}.

1.5.2 Influence of Anisotropy

One obvious difference between HTS and conventional type-II superconductors arises due to the physical structure of the compounds themselves. Whereas conventional low temperature superconductors such as Nb are isotropic, HTS materials have an inherently layered structure consisting of CuO_2 planes separated by varying blocks of heavy elements (see Chapter 2). For HTS materials, anisotropies vary from what we might call moderate values in compounds such as $YBa_2Cu_3O_{7-\delta}$ ($\varepsilon \sim 10$) to the more extreme values seen in compounds such as $Bi_2Sr_2CaCu_2O_8$ ($\varepsilon \sim 100$). Anisotropy has a number of important consequences for the properties of the vortex system, as summarised below.

(i) **Angular dependence of intrinsic properties**. Values such as ξ and λ depend on orientation relative to the layers within the HTS structure. For a sample with moderate anisotropy, the angular dependences of these parameters can be determined using the anisotropic forms for GL equations [22]. The parameter dependences have a number of effects, including distortions in the shape of the vortex core and variations in transport properties, dependent on the angle of orientation of the applied field to the CuO_2 planes.

(ii) **Intrinsic pinning**. As already mentioned in Section 1.4.3, vortices parallel to the layers of HTS materials tend to become locked between CuO_2 planes. This arises due to a modulation of the order parameter between successive superconducting planes [21].

(iii) **Dimensionality crossover**. In extremely anisotropic HTS materials a state can arise whereby adjacent superconducting layers are coupled only via a relatively weak Josephson interaction [30]. In such systems a decoupling transition is observed from a 3D vortex line state into a 2D state comprising stacks of weakly coupled vortex pancakes. In $Bi_2Sr_2CaCu_2O_8$ it has been demonstrated, that the loss of long range correlation along the c-axis (the decoupling transition) occurs simultaneously to the thermodynamic melting transition [31]. This implies simultaneous sharp drops in both C_{66} and C_{44}.

1.5.3 Importance of Surface Barriers

In addition to the effect of bulk pinning, there are a range of surface barriers which can potentially impede the motion of vortices into a superconducting sample. Brandt identifies seven distinct type of barrier [32], the most important of which are the **Bean-Livingstone surface barrier** which arises due to the spatial variation in the supercurrent density near to the sample surface [33] and the **Geometric Barrier** which is dependent on sample shape (See for example Ref. 34).

The Bean-Livingstone surface barrier is commonly described in terms of penetration field field H_p ($>H_{c1}$) at which vortices are able to overcome the repulsive Lorentz force due to the surface supercurrents. For a perfect surface it is possible to show that [35]:

$$H_p \approx H_c \approx \kappa / \ln \kappa \tag{1.6}$$

where H_c is the thermodynamic critical field and κ is the Ginzburg Landau parameter. In HTS κ is exceptionally large (~100) and from this follows that so too must be the penetration field. In practise, this penetration field will be significantly suppressed due to sample surface impurities, and thus lie somewhere between H_{c1} and H_c [36]. However, due to their high values of κ, the HTS materials, are expected to have significantly greater Bean-Livingstone surface barriers than conventional superconductors.

In the case of the geometric barrier, the main controlling factor is the sample shape. This barrier arises due the competition between the elongation energy of a vortex entering the sample and the Lorentz force. This type of barrier can be very important in HTS single crystalline samples, as a result of their thin platelet geometry.[§] Indeed in the case of highly anisotropic superconductors such barriers can be the controlling factor in the vortex dynamics. For example, in recent hall probe measurements by Fuchs *et al.* [37] on $Bi_2Sr_2CaCu_2O_8$ single crystals, it was demonstrated that under certain conditions strong geometric barriers can cause most of the current to flow around the edges of a sample, rather than through the bulk. Whilst many studies have demonstrated the importance of geometric surface barriers in the case of $Bi_2Sr_2CaCu_2O_8$ single crystals (see Ref. 38 and references contained therein), in $YBa_2Cu_3O_{7-\delta}$ surface barriers are not thought to have such a large influence. This is due to the fact that edge and barrier effects are most pronounced at low

---

[§] Due their anisotropic layered structure the natural growth process for HTS materials tends to favour the formation crystals with a thin platelet geometry.

fields, in the vicinity of H_{c1} [32]. Whereas in the case of $Bi_2Sr_2CaCu_2O_8$ the main transitions within the system are in close proximity to the lower critical field line, for $YBa_2Cu_3O_{7-\delta}$ such transitions occur at significantly higher fields. It follows that surface barriers are much less pronounced in this case. Furthermore, magnetisation measurements have shown that the most important effects of surface barriers on vortex state properties are confined to the region of the phase diagram below the irreversibility line [36, 39, 40]. In transport measurements, sensitivity limitations ensure that observations tend to be constrained to the region *above* the irreversibility line (see Chapter 3). In follows, therefore, that in the case of transport measurements on $YBa_2Cu_3O_{7-\delta}$, the subject of this thesis, the effect of surface barriers can reasonably be ignored.

1.6 Outline Of Thesis

Broadly speaking, this dissertation can be divided into two sections. In Chapters 2 through to 5 we consider the experimental and theoretical background to work, placing it in the context of other findings in this area and explaining the main difficulties experienced in obtaining our results. The experimental results themselves are to be found in Chapters 6, 7 and 8. As far as possible I have attempted to indicate the interconnections between the results in these three chapters. In outline, the structure of the thesis is as follows.

In Chapter 2 we consider the structural features of $YBa_2Cu_3O_{7-\delta}$ and how these are reflected in its physical properties. This chapter also includes a description of the techniques used for attaching electrical contacts to samples. In Chapter 3 we consider issues specific to the transport technique. Particular emphasis is placed on temperature measurement and control since a high degree of temperature control accuracy was a prerequisite for performing many of the experiments described in this thesis. Chapter 3 also includes a description of the experimental setups used in acquiring our results.

In Chapters 4 and 5 we provide a theoretical context for the experimental results. Whereas Chapter 4 reviews the current understanding of the equilibrium phase diagram, Chapter 5 attempts to review the still controversial area of vortex dynamics. In both cases I have chosen to constrain the discussion to theories specific to moderately anisotropic superconductors with weak random point disorder.

Chapter 6 is the first of the experimental results chapters, and in this chapter we will consider a range of evidence, from both transport and ac-susceptibility techniques, supporting the idea of a well-defined transition region in the vicinity of the melting line. An interpretation of the behaviour of the vortex system across this transition region, is presented in terms of a model of coexistent vortex liquid and solid phases.

Chapter 7 builds on the results presented in Chapter 6 by focussing on the variation of vortex pinning interactions across the region of the melting transition. In this chapter we introduce a novel technique for probing relaxation and history dependence within the vortex system. We show that the history dependence observations provide strong support for the coexistent phase model of the melting transition region.

In Chapter 8 we present detailed investigations on the drive modulation dependence of the voltage response for the driven vortex solid state. We provide an interpretation for this drive dependent behaviour in terms of dynamic phases with varying degrees of relative disorder arising in response to different types of drive.

In Chapter 9, we review the main conclusions arising from his thesis. A brief discussion is also provided that could potentially be conducted in the future in order to build upon this work.

Finally at the end of this thesis there are three appendices. Appendix A contains a summary of the characteristics of the samples used within this thesis. In Appendix B, the characteristics of the various different temperature sensors used within our studies are summarised. Appendix C contains excerpts from the manual of the GENDAT, the software used in acquiring many of the results presented within this thesis. This software was developed by the author of this thesis, in order to meet the requirement for executing complex series of experimental steps.

References

[1] H. Kamerlingh Onnes, Leiden Comm. **120b, 122b, 124c** (1911).
[2] W. Meissner and R. Ochsenfeld, Naturwissenschaften **21** (1933) 787.
[3] F. and H. London, Proc Roy. Soc. (London) **A149** (1935) 71.
[4] F. London, Superfluids I (Wiley, New York) 1950.
[5] A. B. Pippard, Proc. Roy. Soc (London) **A216** (1953) 547.
[6] V. L. Ginzburg and L .D. Landau, Zh. Exsperim. I Teor. Fiz. **20** (1950) 1064.
[7] J. Bardeen, L. N. Cooper and J. R. Schrieffer, Phys. Rev. **108** (1957) 1175.
[8] A .A. Abrikosov, Zh Eksp. Teor. Fiz. **32** (1957) 1442; Sov. Phys. JETP **5** (1957) 1174;
[9] Notes from Cambridge Winter School in Superconductivity (1996).
[10] J. R. Gavaler, Appl. Phys. Lett. **23** (1973) 480.
[11] J. G. Bednorz and K. A. Müller , Z. Phys. **B64** (1986) 189.
[12] M. K. Wu R. Ashburn, C. J. Tong, P. H. Hong, R. L. Meng, L. Gao, Z. J. Huang, Y. Q. Wang and C. W. Chu, Phys. Rev. Lett. **58** (1987) 908; S. Hikami, T. Hirai and S. Kagoshima, Jpn J. Appl. Phys. **26**, L314 (1987); Z. X. Zhao *et al.*, Kexue Tongbao **33** (1987) 661.
[13] For a discussion of some of the most recent ideas see A. A. Abrikosov *et al.*, Cond-mat 9912394 and references contained therein.
[14] M. Tinkham, Introduction to Superconductivity Second Edition (McGraw-Hill, 1996)
[15] L. F. Cohen and H. J. Jensen, Rep. Prog. Mod. Phys. B **60** (1997) 1581.
[16] Bardeen and Stephen, Phys. Rev. A **140** (1965) 1197.
[17] Tinkham, Phys. Rev. Lett. **13** (1964) 804.
[18] M. Tinkham, Helv. Phys. Acta **61** (1988) 443.
[19] R. M. Langan, S. N. Gordeev, P. A. J. de Groot, A. G. M. Jansen, R. Gagnon and L. Taillefer, Phys. Rev. B **58** (1998) 14548.
[20] S. Fleschler, W. K. Kwok, U. Welp, V. M. Vinokur, M. Smith, J. Downey and G. W. Crabtree, Phys. Rev. B **47** (1993) 14448.
[21] M. Oussena, P. A. J. de Groot, R. Gagnon and L. Taillefer, Phys. Rev. Lett. **72** (1994) 3606.
[22] G. Blatter, M. V. Feigel'man, V. B. Geshkenbein, A. I. Larkin and V. M. Vinokur, Rev. Mod. Phys. **66** (1994) 1125.
[23] C. J. van der Beek and P. H. Kes, Phys. Rev. B **43** (1991) 13032.
[24] E. V. Thuneberg *et al.*, Phys. Rev. Lett. **48** (1982) 1853.
[25] R. Griessen, W. Hai-hu, A. J. J. van Dalen, B. Dam, J. Rector, H. G. Schnack, S. Libbrecht, E. Osquiguil, and Y. Bruynseraede, Phys. Rev. Lett. **72** (1994) 1910.
[26] H. R. Kerchner, J. Low Temp Phys. **50** (1983) 335.
[27] A. I. Larkin, Zh. Eskp. Teor. Fiz. **58** (1970) 1466
[28] A. I. Larkin and Yu. V. Ovchinnikov, J. Low Temp. Phys. **34** (1979) 409.
[29] A. B. Pippard, Phil Mag. **19** (1969) 220.
[30] W.E. Lawrence and S. Doniach, Proc. 12th Int. Conf. Low Temp Phys. LT12 1971, Ed. E. Kanda (Kyoto, Academic Press of Japan) p 361.
[31] R. A. Doyle, IRC (Cambridge) Research Review (1998) p142.
[32] E. H. Brandt, Rep. Prog. Mod. Phys. **58** (1995) 1465.
[33] C. P. Bean and J. D. Livingstone, Phys. Rev. Lett. **12** (1964) 14.
[34] E. Zeldov, A. I. Larkin, V. B. Geshkenbein, D. Majer, M. Konczykowski, V. Vinokur and H. Shtrikman, Phys. Rev. Lett. **73** (1994) 1428.

---

[35] P. G. de Genes (1966) *Superconductivity of Metals & Alloys* (New York: Benjamin)
[36] M. Konczykowski, L. Burlachov, Y. Yeshurun and F. Holtzberg, Phys. Rev. B **43** (1991) 13707.
[37] D. T. Fuchs, E. Zeldov, M. Rappaport, T. Tamegai, S. Ooi and H. Shtrikman.
[38] R. A. Doyle, S. F. W. R. Rycroft, T. B. Doyle, E. Zeldov, T. Tamegai and S. Ooi, Phys. Rev. B **58** (1998) 135.
[39] N. Chukimoto, M. Konczykovski , N. Motohira, and A. P. Malozemoff, Phys. Rev. Lett. **69** (1992) 1260
[40] E. Zeldov, D. Majer, M. Konczykowski, A. I. Larkin, V. M. Vinokur, V. B. Geshkenbein, N. Chukimoto and H. Shtrikman, Europhys. Lett. **30** (1995) 367.

CHAPTER 2. STRUCTURE, GROWTH AND PREPARATION OF $YBA_2CU_3O_{7-\delta}$ SINGLE CRYSTALS

2.1 $YBa_2Cu_3O_{7-\delta}$ as a Member of the HTS Class

The high temperature superconductors (HTS) comprise a class of compounds clearly distinct from their low-temperature superconducting cousins. Indeed, they differ so radically in basic structure from the conventional elemental, intermetallic and simple-alloy superconductors that initially it came as a surprise that they should superconduct at all. It took a great deal of insight on the part of pioneers in the field, Bednorz and Müller of the IBM Research Laboratory in Zürich [1], to realise that it is precisely ***because*** of their unusual structure that not only would they superconduct but that they would do so at much higher temperatures than had previously been observed.

The HTS compounds (notably $La_{2-x}Sr_xCuO_4$, $YBa_2Cu_3O_{7-\delta}$, $Bi_2Sr_2CaCu_2O_8$, and $HgBa_2Ca_2Cu_3O_8$) share many structural features in common, and this is reflected in their physical properties. All of the compounds in the class have a layered structure comprising modified perovskite units (stoichiometry ABO_3), separated by variable thickness and spacing rock-salt layers (stoichiometry AO). From the point of view of their physical properties, these systems can simplistically be considered as consisting of superconducting CuO_2 layers or **sheets** separated by variable thickness insulating metallic-oxide **blocks**. Since their discovery, it has become clear that the superconducting properties of the HTS materials arise due to a complicated interplay between the sheets and the blocks.

One idea has been that the blocks exert a kind of "chemical pressure" confining charge on the sheets. Following the discovery by Bednorz and Müller of superconductivity in a La-Ba-Cu-O system ($T_c \sim 35$ K) [1], several groups had the idea that an improvement in T_c might be achieved by increasing the chemical pressure on substituting Y for La. Indeed, it was as a result of this guesswork, that the $YBa_2Cu_3O_{7-\delta}$ system ($T_c \sim 90$ K) was discovered [2]. Subsequently, evidence has amassed, revealing the importance of externally imposed pressure in determining the critical temperatures of HTS materials [see for example Ref 3]. Indeed, the current record, $T_c = 147$ K, is held the mercury based compound $HgBa_2Ca_2Cu_3O_{8+\delta}$ under a pressure of 150 kBar [4]. In addition to such pressure effects, it has become apparent that both normal and superconducting properties of the cuprates are dependent on coupling between the sheets and chain-like structures running through the blocks (see for example Ref 5).

As a consequence of their layered structure, the cuprate materials exhibit a pronounced anisotropy perpendicular and parallel to the CuO_2 planes (following crystallographic conventions denoted the *c*-axis and *ab*-plane respectively). In terms of their superconducting properties, this anisotropy can be characterised by the ratio of their charge carrier effective masses : $\gamma \equiv (m_c/m_{ab})^{1/2}$ Anisotropies vary considerably between the different HTS materials, ranging from $\gamma \sim 100$ in $Bi_2Sr_2CaCu_2O_8$ [6] to the value of $\gamma \sim 8$ for optimally doped $YBa_2Cu_3O_{7-\delta}$ [7]. These effective mass anisotropies are reflected in other intrinsic parameters such as the coherence length and as such have an effect on the properties of the vortex state. For example, the difference in anisotropy between $YBa_2Cu_3O_{7-\delta}$ and $Bi_2Sr_2CaCu_2O_8$ means that whereas the *c*-axis oriented vortex system in $YBa_2Cu_3O_{7-\delta}$ is essentially 3D in character, for the same field orientation vortices in $Bi_2Sr_2CaCu_2O_8$ exhibit a crossover from 2D to 3D behaviour [8].

The studies presented in this thesis focus on one particular member of the HTS class, the moderately anisotropic compound $YBa_2Cu_3O_{7-\delta}$. In this chapter, we describe the structure and preparation methods of the single crystalline samples used in our studies. Sections 2.2 and 2.3 discuss the structural properties of $YBa_2Cu_3O_{7-\delta}$. In section 2.4 we review issues related to the growth and preparation of high quality $YBa_2Cu_3O_{7-\delta}$ single crystals. Section 2.5 describes the techniques used for attaching electrical contacts to $YBa_2Cu_3O_{7-\delta}$ single crystals.

2.2 Structure of $YBa_2Cu_3O_{7-\delta}$

$YBa_2Cu_3O_{7-\delta}$ (often abbreviated to YBCO) is a nonstoichiometric compound whose properties vary markedly with its oxygen deficiency δ. In all cases, the compound is based upon a tripled perovskite structure, but as δ is varied from 0 to 1 the structure changes from orthorhombic to tetratragonal. The two limiting cases (fully oxygenated and fully deoxygenated) are depicted in Fig 2.1.

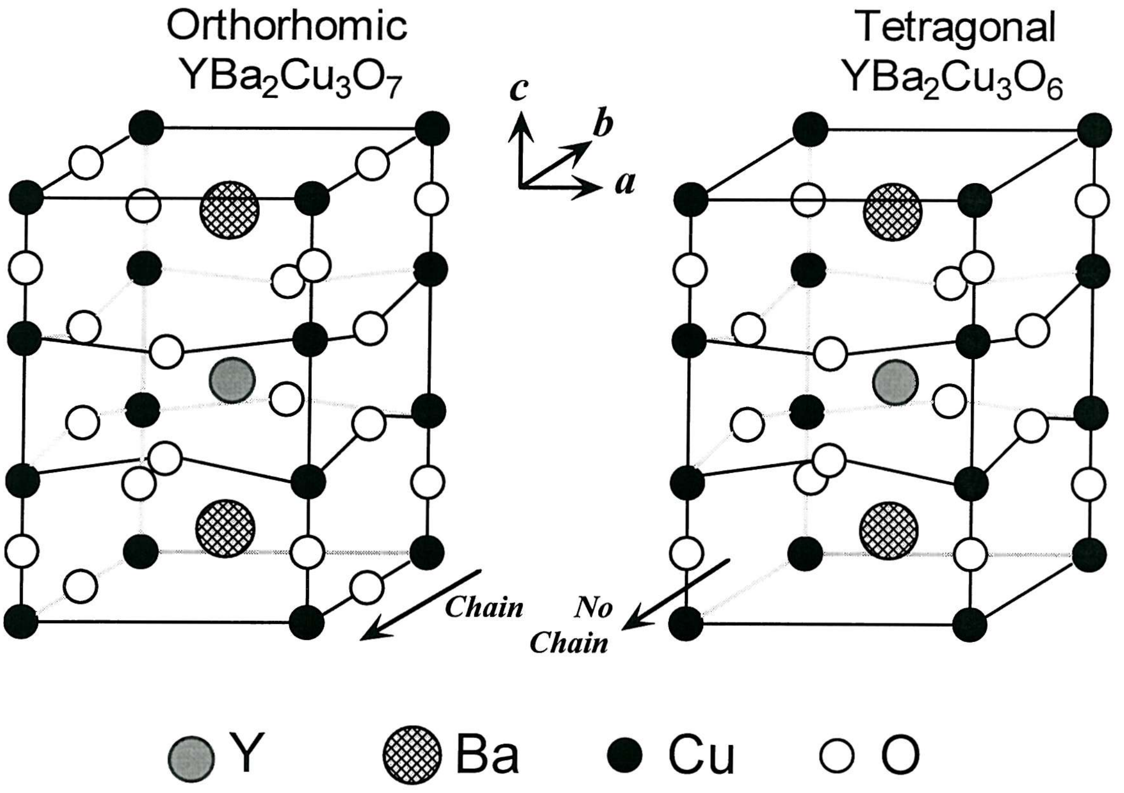

Fig. 2.1 *Unit cell structures of orthorhombic and tetragonal $YBa_2Cu_3O_{7-\delta}$*

In fact, the system only displays superconducting behavior in the orthorhombic phase. The structural transition between phases occurs at an oxygen deficiency of $\delta = 0.65$ [9]. Indeed, it was for this reason that all of the samples used in our studies had values for the oxygen deficiency $\delta < 0.6$. The lattice parameters vary with oxygenation, but at the orthorhombic limit they have the values $a = 0.381$ nm, $b = 0.388$ nm and $c = 1.165$ nm.

Referring to the previous discussion of common features in the HTS materials, the two main structural features to note from Fig. 2.1 are:

(i) **The CuO_2 sheets** in the *ab*-plane. In the orthorhombic phase these are the site of the superconductivity. Note, the puckering of the sheets is due to the strong attraction from the Y^{3+} ions as a result of their small ionic radius.

(ii) **The CuO chains**, present along the *b*-axis direction in the orthorhombic but not in the tetragonal case. Changes in oxygenation only affect the oxygen atoms in these chains.

The marked dependence of the properties of the system on oxygenation is also reflected in the effective mass anisotropy. As demonstrated by Chien *et al.* [10], between $\delta = 0.60$ and $\delta = 0.07$, the anisotropy varies between $\gamma=105\pm7$ and 8.7 ± 2. One of the main effects of oxygenation at this limit is the attainment of ordering and connectivity within the chains. Thus, although they are not in themselves inherently superconducting, it seems that the CuO chains play an important role in determining the superconducting properties of overall system. One idea is that they act as a charge reservoir, providing Cooper pair vacancies for the superconducting planes [11]. Other studies have indicated that such chains might in themselves become superconducting, by virtue of proximity effects [12]. Indeed it is certainly not correct to regard the chains and the planes as separate entities, since the detailed properties of the $YBa_2Cu_3O_{7-\delta}$ system are now widely believed to originate from coupling between the planes and the chains (see for example Refs. 5 and 13).

Even within the orthorhombic phase, the properties of the superconducting system vary markedly with oxygenation. The effect of oxygenation upon the intrinsic parameters of the system is most obviously reflected in the marked variation of the critical temperature (T_c)

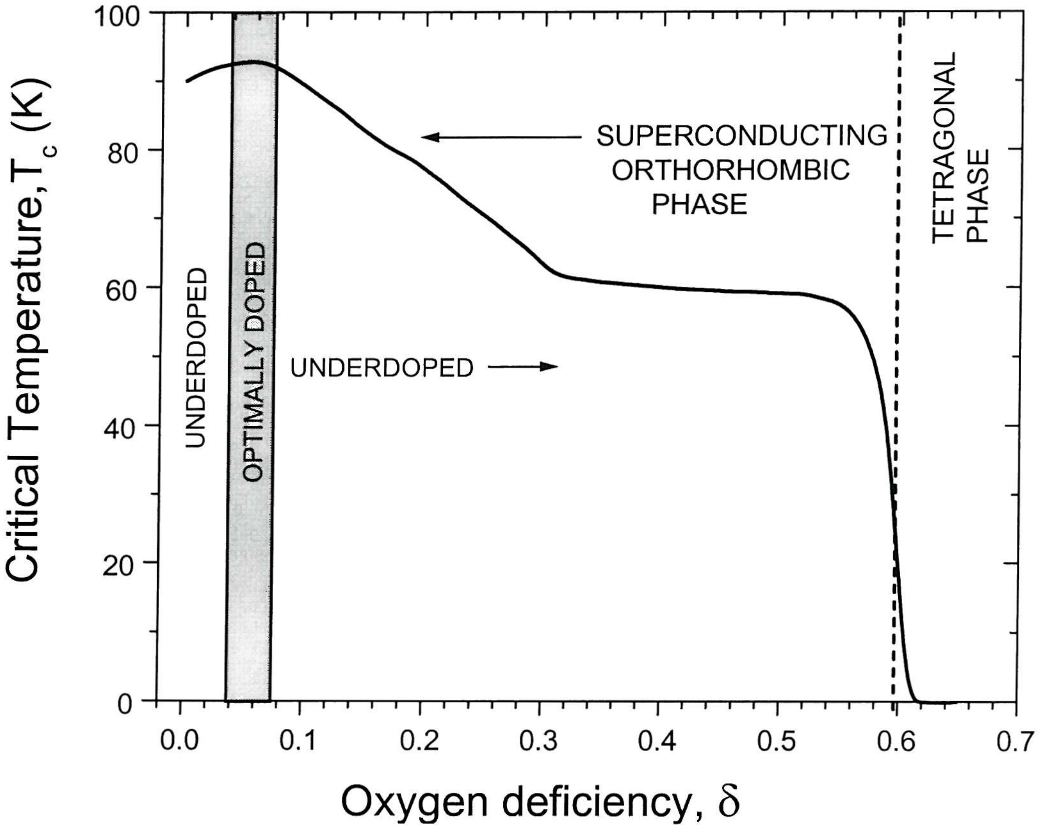

Fig. 2.2 *Schematic representation of the variation of critical temperature $YBa_2Cu_3O_{7-\delta}$. single crystals, as function of oxygen deficiency δ.*

with δ. Fig. 2.2 is a schematic representation, depicting the approximate form of the T_c versus oxygen deficiency dependence, based upon the results of several different studies [9, 14, 15]. The main features are:

(i) The peak in T_c close to $\delta = 0.07$.

(ii) The plateau in T_c for δ in the approximate range 0.3-0.5, which has been associated with a plateau in the effective valence of the Cu atoms within the planes [15].

(iii) The sharp drop-off in T_c close to $\delta = 0.6$ marking the crossover from the orthorhomic superconducting phase into a tetragonal anti-ferromagnetic phase.

Samples with δ values in the region of the peak in T_c are normally described as being **optimally doped**. Correspondingly, samples with doping levels above and below this peak are described as **overdoped** and **underdoped** respectively. The majority of studies on $YBa_2Cu_3O_{7-\delta}$ single crystals, including those presented in this thesis, have been carried out on optimally doped samples. As such, the behaviour of the system at the overdoped and underdoped limits is much less well understood. Indeed, recent studies carried out by our group have indicated that at the underdoped limit the system may manifest highly unusual behaviour, possibly in part a reflection of the low carrier concentrations [16].

In the region of optimal doping, oxygenation also plays an important role in determining the pinning properties of the vortex system. In relatively pure single crystals oxygen vacancies often act as the main pinning site for vortices. Hence, within the optimally doped regime the main effect of changing the oxygenation is a change in the density of such pinning sites [17]. In the underdoped regime (δ>0.08) variations in oxygenation also have an effect upon pinning properties but at this limit the dominant contribution is due to variations in intrinsic parameters such as the coherence length ξ and the penetration depth λ [18].

2.3 Twin Boundary Pinning

A further important structural feature of $YBa_2Cu_3O_{7-\delta}$ is related to the tetragonal to orthorhombic transition, which takes place during growth. As a consequence of the slight mismatch between the in-plane lattice parameters for the orthorhombic phase (a = 0.381 nm, b = 0.388 nm), on undergoing this transition crystallites develop with two different orientations. This leads to a number of distinct domains within the sample the boundaries between which are known as twin planes. These twin boundaries act as pinning sites for vortices. Indeed, due to the their extended 2D nature, twin planes can often be the dominant source of pinning in optimally doped $YBa_2Cu_3O_{7-\delta}$ single crystals. As such, twin boundary (TB) pinning can have a pronounced effect on the dynamics of vortices, often masking more subtle physical effects due to point disorder. For this reason it is often desirable to remove the effect of TB-pinning.

As shown in Fig. 2.3 the presence of twin planes can be revealed under polarised light microscopy. From this figure it can be seen that the planes occur in two possible orthogonal orientations. Samples with twin planes in just one orientation are described as being **simply twinned**. Others, such as the sample depicted in Fig. 2.3, contain both possible twin plane orientations and are thus described as having **complex twinning**.

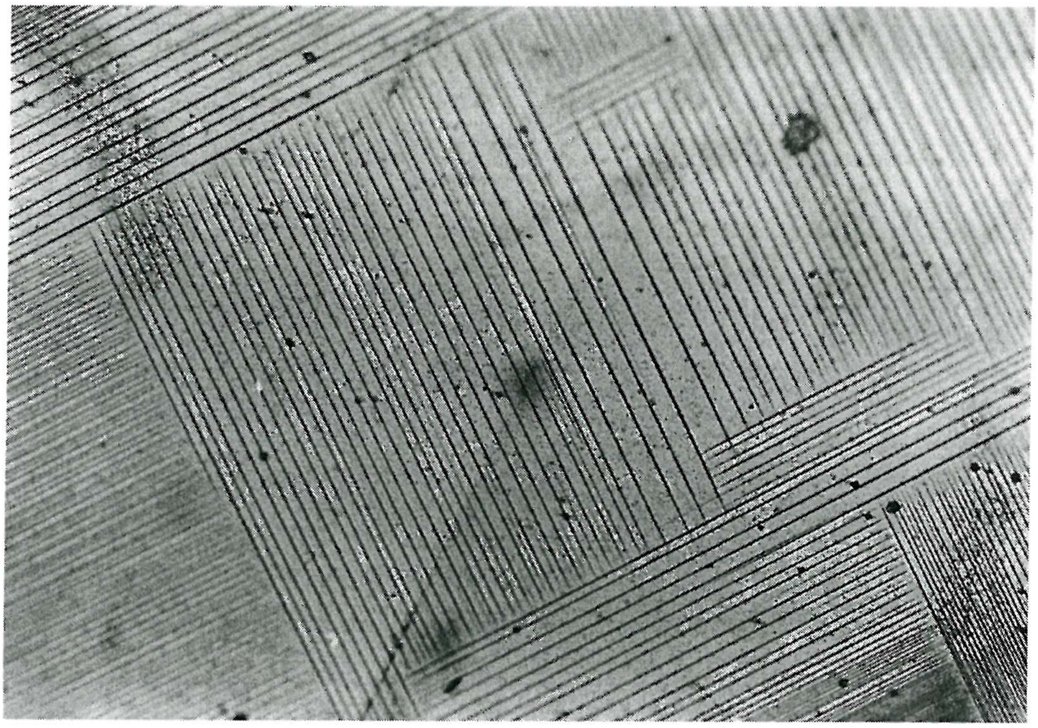

Fig. 2.3 *Photograph of twin planes revealed under polarised light microscopy in a densely twinned $YBa_2Cu_3O_{7-\delta}$ single crystal. Note that the planes occur in two orthogonal orientations corresponding to the crystallographic (1 1 0) and (1 -1 0) directions respectively.*

There are two ways to eliminate twin boundary pinning, in order to reveal more subtle underlying physical effects. In the first place, we can attempt to remove the twin planes altogether, by application of a uniaxial pressure at high temperatures [19, 20]. The problem with this approach, is that there is a high probability of shattering the sample, especially if there are any irregularities in its shape. For this reason, truly detwinned sample are rare. An alternative method for getting around this problem takes advantage of the 2D nature of TB pinning. It has been demonstrated that if the angle of inclination between the applied field and the twin planes exceeds a certain angle (≈15°), then the effect of the TB-pinning [21] can be removed. Hence, TB-pinning can be avoided, simply by tilting the sample relative to the applied field.

2.4 Sample Preparation

The single crystalline samples used in our studies were produced by Robert Gagnon and Louis Taillefer of McGill University, Canada. Samples were grown using a self-flux method in yttria stabilised crucibles, thereby minimising the inclusion of impurities and the growth of secondary phases [22]. Oxygen diffusivity studies on $YBa_2Cu_3O_{7-\delta}$ single crystals have demonstrated a clear reproducible dependence of a sample's ultimate oxygenation, on annealing temperature [23, 24]. As such, we were able to vary the oxygen deficiency of our samples by annealing them at a carefully controlled temperature and pressure (see Fig. 2.4). Such annealing was normally carried out over several days in order to ensure that the oxygenation as uniform as possible. It should be noted, however, that even after annealing for such a length of time, it is unlikely that the oxygen distribution will be entirely uniform. This is due to the complexities of the diffusion dynamics [23] and in particular the effect that twin planes can have on the ultimate oxygen distribution [25].

As standard, the samples used in our studies were oxygenated for 6 days in flowing O_2 at 500°C and then quenched in air at room temperature. According to Ref. 23 this should produce optimally doped samples, with oxygen deficiencies close to 0.07. Indeed, this has been confirmed by measurements the critical temperature, which yielded values close to the peak value T_c^{max}= 93.6K. Where different oxygenations were required, this was achieved by reannealing at a temperature determined by the calibration data of Ref. 24 (see Fig. 2.4). Samples were annealed for at least seven days in flowing O_2, using quartz furnace tubes. Such tubes are thought to introduce significantly less impurities than glazed or unglazed ceramic equivalents, especially when annealing at high temperatures [26].

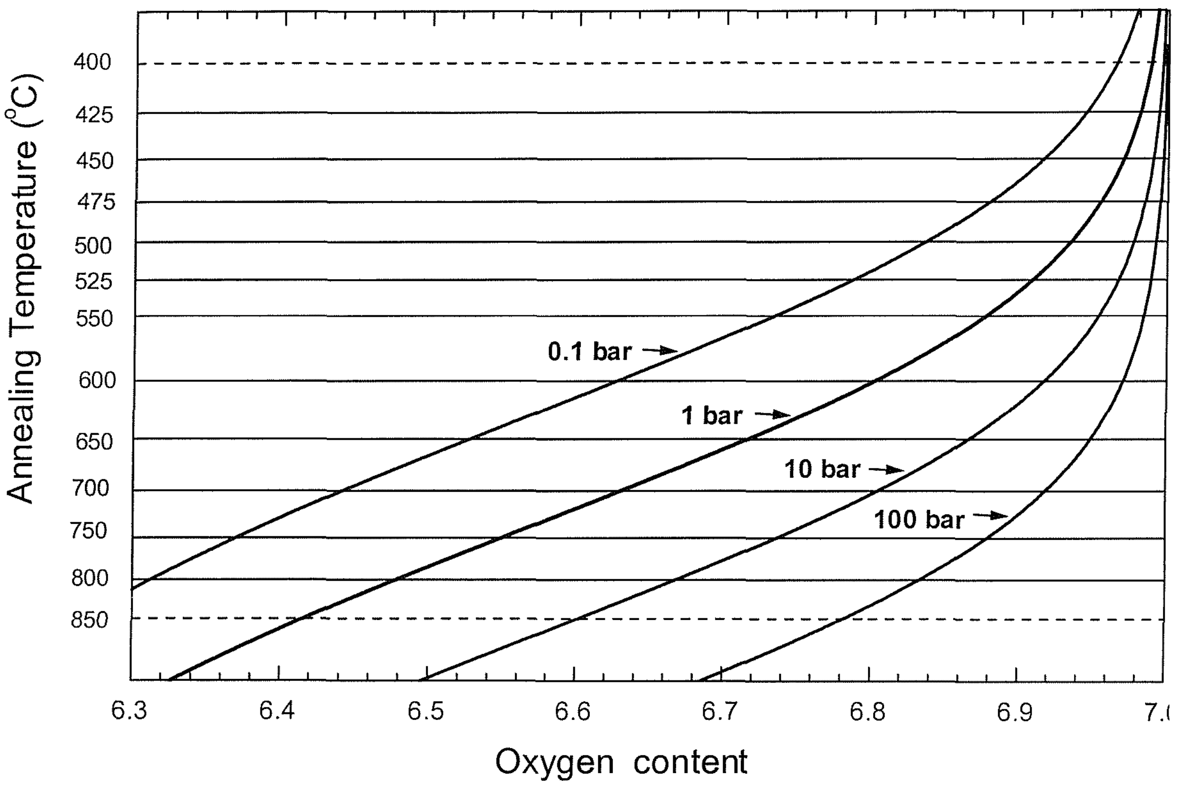

Fig. 2.4 *Calibration curve of ultimate oxygen deficiency as a function of the annealing temperature, plotted from the data of Ref. 27.*

Where detwinned samples were required for our studies, this was achieved by applying a pressure ~50MPa at a temperature of 550°C for 30 minutes. The original oxygenation was then restored by reannealing at 500°C in flowing oxygen for one day. An initial check for the presence of twin planes can be made using polarised light microscopy. This revealed that detwinning was not always completely successful and in some cases a few twin planes remained, concentrated around irregularities on the edges of the sample. Such partially detwinned samples will henceforth describes as being **sparsely twinned**. The absence of visible twin-planes under polarised light microscopy does not of course guarantee their absence on the sub-micrometer level. However, since twin-boundary pinning always leads to a pronounced dip in the angular dependence of the transport resistivity [28], this allowed us to definitively test for their presence or absence.

2.5 Electrical Contacts to $YBa_2Cu_3O_{7-\delta}$ Single Crystals

2.5.1 General Problems of Attaching Contacts to $YBa_2Cu_3O_{7-\delta}$ Single Crystals

In order to carry out transport measurements on $YBa_2Cu_3O_{7-\delta}$ single crystals it is first necessary to manufacture rugged, ohmic, low resistance electrical contacts. Contact resistances are important for a number of reasons, but in particular because they control the maximum current which can be passed without Joule heating (see also Chapter 3, Section 3.3.2.1). In fact, various properties of $YBa_2Cu_3O_{7-\delta}$, contrive to make this task extremely difficult. The three main factors affecting contact manufacture can be summarised as follows:

(i) As a reflection of their anisotropy, $YBa_2Cu_3O_{7-\delta}$ single crystals tend to grow in a thin platelet geometry. Furthermore, the high purity crystals used in our samples were all fairly small (typical dimensions 1mm x 0.5mm x 50 μm). Thus, from a purely practical point of view, it is very challenging to attach the contacts.

(ii) The complicated chemistry of HTS materials means that their surfaces tend to degrade over time, especially on reacting with atmospheric water [29]. Contacts attached to such a degraded surface will tend to have a very high electrical resistance. To try to prevent such problems arising, samples are usually stored in an anhydrous atmosphere. Some improvement may also be affected by abrading, etching, or cleaving the sample surface prior to attaching contacts.

(iii) There is no ideal material for use in contact manufacture. In order to preserve the samples' oxygen stoichiometry, it is vitally important that the contact material does not readily oxidise and thereby draw oxygen out of the HTS compound thus changing its stoichiometry. This means that the Noble metals such as gold and silver are the only really suitable contact materials. However, this lack of reactivity also means that such metals do not form strong chemical bonds at the sample's surface. This can lead to contacts which are weak both physically and in terms of electrical connection.

From these practical factors, it follows that there are two main areas of difficulty, when attempting to manufacture contacts to $YBa_2Cu_3O_{7-\delta}$ single crystals. Firstly, it is vitally important to ensure that the sample surface is sufficiently "clean" before attaching contacts. If the surface is degraded then the quality of the electrical contact is almost irrelevant since the contact resistances will be high in any case. Having obtained a sufficiently clean surface the next stage is to ensure an adequate connection. As mentioned above, the noble metals are only weakly reactive and specifically, it has been demonstrated that they have very low solubility in $YBa_2Cu_3O_{7-\delta}$ [30]. Indeed, high resolution transmission microscopy studies have revealed that in some cases the interface between an $YBa_2Cu_3O_{7-\delta}$ sample and noble metals contacts may be atomically sharp [31]. Certainly, it is still not precisely clear how the ultimate properties of contacts relate to the interfacial microstructure. From practical experience, however, we have found that the quality and robustness of electrical contacts can be improved by using a noble metal epoxy.

2.5.2 Method of Contact Manufacture

In all cases for the samples used in our transport studies contacts were attached in a standard four point configuration (see also Section 3.2.1), with current contacts along the edges of the sample so as to ensure uniform current flow along the *ab*-plane. Voltage pads were placed between the current contacts, taking care to ensure that there was no connection between them. A typical example of such a contact configuration is shown in Figure 2.6 (overleaf).

In terms of the practicalities of contact manufacture, the following standard method was employed. Crystals to which contacts were to be attached, were fixed in place on a sapphire mount by placing small drops of silver paint under the edges of the sample to which the current contacts were to be eventually attached. The purpose of the silver paint was merely to fix the sample in place and not to form an electrical contact. Care was taken to ensure that paint did not run under the sample creating an alternative path for current flow. Having

Fig. 2.5 *Typical four point contact-configuration, attached to a partially detwinned* $YBa_2Cu_3O_{7-\delta}$ *single crystal as photographed under polarised light microscopy. Notice the region of residual twin-planes in the bottom right-hand corner of the sample.*

allowed the silver paint to dry, electrical contacts were then painted onto the sample using a particular silver epoxy (Dupont 6838). The contacts were then annealed in flowing oxygen (1 Atm) at a temperature chosen to maintain the sample's original oxygenation (see Fig. 2.4). Both our own experience and studies by other groups [30, 32, 33] have indicated that, in the absence of such annealing, contacts tend to have very high resitivities. Following annealing, samples were quenched in air at room temperature before attaching fine gold wires (diameter 25 μm) to the contact pads, again using silver epoxy. The final stage was to cure these connections at a temperature of 150^{o}C in flowing oxygen. This temperature is high enough to provide the contacts with rigidity, whilst at the same time being sufficiently low for oxygen out-diffusion from the sample to be negligible. Contacts produced in this way typically had resistances ~1Ω.

References

[1] J. G. Bednorz and K. A. Müller, Z. Phys. B **64**, (1986) 189.
[2] M. K. Wu R. Ashburn, C. J. Tong, P. H. Hong, R. L. Meng, L. Gao, Z. J. Huang, Y. Q. Wang and C. W. Chu, Phys. Rev. Lett. **58** (1987) 908; S. Hikami, T. Hirai and S. Kagoshima, Jpn J. Appl. Phys. **26**, L314 (1987); Z. X. Zhao *et al.*, Kexue Tongbao **33** (1987) 661.
[3] R .J. Winjngaarden, J. J. Scholtz, E. N. Eenige and R. Griessen, in *Frontiers of High Pressure Research* (eds H. D. Hochheimer and R. D. Etters) 339 (Plenum, New York, 1991)
[4] C .W. Chu, L. Gao, F. Chen, Z . J. Huang, R. L. Meng and Y. Y. Xue, Nature **365** (1993) 323.
[5] R. Gagnon, P. Song, B. Ellman and L. Taillefer, Phys. Rev. Lett. **78** (1997) 1976.
[6] D.E. Farrell, S. Bonham, J. Foster, Y.C. Chang, P.Z. Jiang, K.G. Vandervoort, D.L. Lam, and V.G. Kogan, Phys. Rev. Lett. **63**, 782 (1990); J.C. Martinez, S.H. Brongersama, A. Koshelev, B. Ivlev, P.H. Kes, R.P. Griessen, D.G. de Groot, Z. Tarnavski and A. A. Menovsky, Phys. Rev. Lett. **69**, 2276 (1992).
[7] D. E. Farrell, J.P. Rice, D. M. Ginsberg, and J. Z. Lin, Phys. Rev. Lett. **64**, 1573 (1990).
[8] R. A. Doyle, IRC (Cambridge) Research Review (1998) p142
[9] J. D. Jorgensen, B. W. Veal, A. P. Paulikas, L. J. Nowicki, G. W. Crabtree, H. Claus and W. K. Kwok, Phys. Rev. B **41** (1990) 1863.
[10] T. R. Chien *et al.*, Physica C **229** (1994) 273.
[11] P. P. Edwards and C. N. R. Rao, Chemistry in Britain, **30**, (1994) 727.
[12] J. L. Tallon, C. Bernard, U. Binninger, A. Hofer, G. V. M. Williams, A. J. Ansaldo, J. L. Budnick and C. Niedermayer, Phys. Rev. Lett. **74** (1995) 1008.
[13] R. Combescot and X. Leyronas, Phys. Rev. Lett. **75** (1995) 3732.
[14] V. Breit, P. Schweiss, R. Hauff, H. Wühl, H. Claus, H. Rietschel, A.Erb and G. Müller-Vogt, Phys. Rev. B **52** (1995) R15 727.
[15] R. J. Cava, A. W. Hewat, B. Batlogg, M. Marezio, K. B. Rabe, J. J. Krajewski, W. Peck and L. W. Rupp Jr, Physica C **165** (1990) 419.
[16] A. P. Rassau, S. N. Gordeev, P. A. J. de Groot, R. Gagnon and L. Taillefer, Physica B (in press)
[17] R. M. Langan, S. N. Gordeev, P. A. J. de Groot and A. G. M. Jansen, R. Gagnon and L. Taillefer, Phys. Rev. B **58** (1998) 14548-14555.
[18] J. G. Ossandan, J. R. Thompson, D.K. Christen, B. C. Sales, L. H. Kerchner, J. O Thomson, Y. R. Sun, K. Y. Lay and J. E. Tkaczyk, Phys. Rev. B **45** (1994) 12534.
[19] H. Schmid, E. Burkhardt, B. N. Sun and J. P. Rivera, Physica C **157** (1989) 555.
[20] U. Welp, M. Grimsditch, H. You, W. K. Kwok, M. M. Fang and G. W. Crabtree, Physica C **161**, 1 (1989).
[21] W. K. Kwok, U. Welp, G. W. Crabtree, K. G. Vandervoort, R. Hulscher and J. Z. Liu, Phys. Rev. Lett. **64** (1990) 966
[22] R. Gagnon, M. Oussena and M. Aubin, J. Cryst Growth **121** (1992) 559; R. Gagnon, C. Lupien and L. Taillefer, Phys. Rev. B **50** (1994) 3458.
[23] J. R. LaGraff and D. A. Payne, Physica C **212**, 478
[24] P. Schleger, W. N. Hardy and B. X. Yang, Physica C **176** (1991) 261.
[25] Y. Yan, W. Y. Liang, T. Walther and W. M. Stobbs, Phys. Rev. B **54** (1996) 16,234.
[26] R. Gagnon, Private Communication.
[27] D. J. L. Hong and D.M. Smyth. J.Am.Ceram.Soc., **74** (7) 1751-1752 (1991)
[28] S. Fleschler, W. K. Kwok, U. Welp, V. M. Vinokur, M. K. Smith, J. Downey and G. W. Crabtree, Phys. Rev. B **47** (1993) 14,448.
[29] W. R. Flavell and R. G. Egdell, Chemistry in Britain **30** (1994) 735
[30] R. Bohenkamp-Weiss and R. Scmid-Fetzer, Physica C **220** (1994) 396.
[31] Z. H. Gong *et al.* , Appl. Physics Lett. **63** (1993) 836.
[32] T. A. Friedmann, M. W. Rabin, J. Giapintzakis, J. P. Rice, D. M. Ginsberg, Phys. Rev. B **42** (1990) 6217.
[33] J. W. Ekin, T. M. Larson and N. F. Begren, Appl. Phys. Lett. **52** (1988) 1819.

CHAPTER 3. DETAILS OF THE MAGNETO-TRANSPORT TECHNIQUE

3.1 Introduction to the Transport Technique

As explained in the introductory chapter, when a sufficiently large current flows through the vortex state of a type-II superconductor then the resultant motion of vortex lines generates a dissipative emf. In the case of the magneto-transport technique, this emf is measured in the most direct way possible, by attaching current and voltage contacts to the sample and measuring the voltage arising in response to an applied current. Both the amplitude and the noise levels of this response can provide useful clues about the nature of the transport-current-induced vortex motion.

In this chapter we will consider the experimental and instrumentational factors affecting transport measurements on the vortex state. In section 3.2, the role of the transport technique is considered in the context of other types of experimental technique. Section 3.3 addresses some of the major instrumentational factors affecting low-level transport measurements. In section 3.4, issues relating to temperature measurement and control are addressed. Finally, in Section 3.5, descriptions are provided of the specific experimental setups used to acquire the data presented in this thesis. The methods used for attaching electrical contacts to the single crystalline samples are considered elsewhere in Chapter 2.

3.2 Role of the Transport Measurements in the Context of Other Techniques

A wide variety of different experimental techniques can be used to explore the static and dynamic properties of vortices in type-II superconductors. These methods can be loosely categorised as follows:

(i) **Transport measurements**

(ii) **Local and Bulk Magnetization measurements**: including dc-magnetization, ac-susceptibility, local hall probe measurements, torque magnetometry and mechanical oscillator experiments

(iii) **Calorimetric measurements**: include specific heat and entropy measurements

(iv) **Structural studies**: including neutron diffraction and scanning hall-probe microscopy

Each of these techniques has its own particular area of usefulness and they are to some extent complementary. Transport and ac-susceptibility measurements can be useful for identifying and characterising phase transitions within the vortex system. However, to unequivocally determine whether a transition is first or second order, very sensitive thermodynamic measurements are required.[*] Structural measurements provide uniquely unambiguous information about vortex distributions, but are for the most part limited to the observation of static vortex configurations at relatively low fields. The precise details of all of these various different methods will not be considered here. There is, however, some value in making a direct comparison between the transport and magnetization techniques.

---

[*] By definition, it is the calorimetric and DC magnetisation techniques which provide us with thermodynamic information.

3.2.1 Comparison of Transport and Magnetization Techniques

To understand the relationship between transport and magnetization measurements, it is necessary to consider the responses that they generate, as well as the practical limits on measuring such responses. In transport measurements an *E*-field is induced by an externally applied current of density *J*, typically in a constant applied field *H*. In contrast, in a "sweep-creep" magnetization measurement the applied field is swept, inducing a current density *J* proportional to the irreversible magnetization. From basic electromagnetic theory, it is implicit that this magnetic screening current must arise in *direct* response to an *E*-field. Indeed, Zhukov has demonstrated that for an annular ring-like sample of outer radius *r*, at the sample periphery, this *E*-field takes a value $E_p \approx \mu_0 r\dot{H}_{app}/2$ [1]. This notion of an E-field within a "sweep-creep" magnetization measurement allows us contemplate direct comparison of the two techniques. However, as pointed out by Caplin *et al.* [2] and summarised below in the following table, practical constraints are such that the transport and magnetization techniques access entirely different regions of the *E-J-H* parameter space.

	Practical Limit on *J*	**Practical Limit on *E***
Transport measurement	**Maximum** applied current density due to Joule heating effects, dependent on sample contact resistance (see Section 3.3.2.1). $J_{max} \sim 10^3$ Am^{-1}	**Minimum** measurable voltage determined by noise levels in the measurement circuitry and the sensitivity of measurement devices (see section 3.3.2). *Conventional measurement electronics* $E_{min} \sim 10^{-6}$ Vm^{-1} [3] *SQUID voltmeter* $E_{min} \sim 10^{-9}$ Vm^{-1} [4]
"Sweep-Creep" Magnetization measurement	**Minimum** measurable current density as determined by the noise floor in terms of the measurement of the magnetic moment. For a typical vibrating sample magnetometer [5]. $J_{min} \sim 10^6$ Am^{-1}	**Maximum** field sweep rate and hence maximum applied *E*-field. $E_{max} \sim 10^{-5}$ Vm^{-1}

In general, transport techniques are limited to measuring responses in the weakly pinned regime, above and in the immediate vicinity of the transition into the true superconducting state. In the strongly pinned state, sufficiently far below this transition, the maximum transport currents that can be applied are insufficient to produce a voltage response measurable by the transport technique. In contrast, it is in precisely this strongly pinned region that magnetization measurements are most useful. To our knowledge, there is just one instance in the literature where a simultaneous measurement was made of magnetization and resistivity responses [6]. In this paper by Fendrich *et al.*, magnetization was measured by means of a SQUID sensor, with static position in relation to the sample. As pointed out by the authors, however, this particular technique can only really be used to identify relative changes in the magnetization, since SQUID sensors are subject to a low-frequency drift in their voltage base-line.

3.2.2 Applications of the Transport Technique

In addition to the clues provided about underlying thermodynamic interactions, transport measurements are useful for revealing behaviour unique to the dynamic system. Simply by varying the driving current modulation form and magnitude it is possible to access a wide range of different dynamic regimes. In summary, therefore, the main benefits of using a magneto-transport techniques are as follows:

(i) *Relative straightforwardness of interpretation: provided that samples are contacted appropriately, current should flow in well controlled manner through the sample.*[†]

(ii) Helps to explain the complex competing interactions in the region of the vortex liquid to solid melting transition.

(iii) Provides unique information about the phenomenology of the dynamic vortex system.

[†] This makes the assumption that single crystalline samples are being used: for polycrystalline samples transport behaviour is governed by a more complex mixture of inter- and intra-granular properties.

3.3 Low Level Voltage Measurement Considerations

One of the major limitations of the transport technique is its inability to measure a response deep in the superconducting state. Whilst, by definition, it is not possible to measure a voltage in the true superconducting state, clearly it is desirable to measure as far as possible down the transition to the zero resistivity. In order to achieve this, it is necessary to minimise noise contributions in the measurement circuit and eliminate any spurious offsets. In the following sections we will examine the main sources of noise and errors in low level transport measurements, providing details of how they can be minimised or eliminated.

3.3.1 Lead Resistance Offset

One of the most obvious and easily eliminated sources of error in low-level transport measurements, is that associated with the voltage drop across the contacts and measurement leads. Clearly it is desirable to measure only the voltage or resistance contribution originating from the sample itself. For this reason transport measurements are typically carried out using a four-point contact configuration. As schematically represented in Fig 3.2, the four point configuration avoids measuring the lead resistance by using one pairs of contacts to pass a current and a separate pair to measure the voltage (see also Fig. 2.5 of Chapter 2).

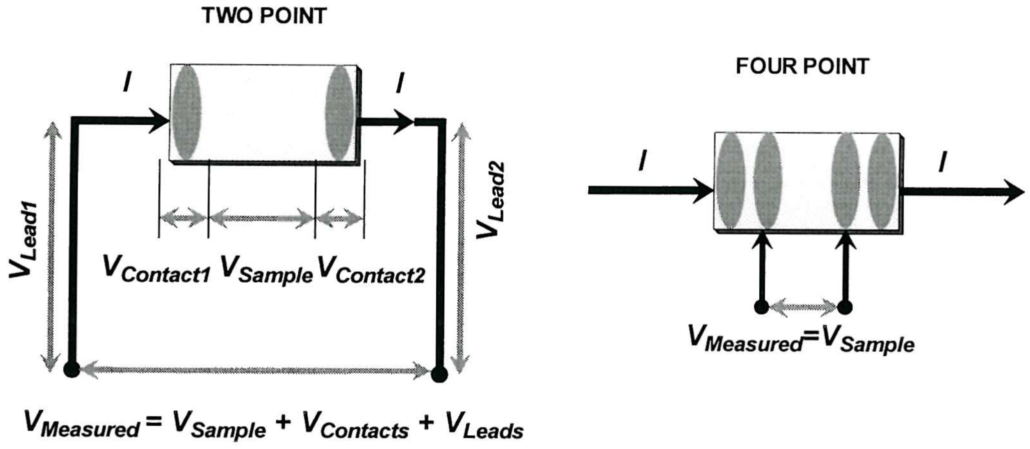

Fig. 3.1: *Comparison of two and four point configurations for transport measurements.*

3.3.2 Intrinsic Noise

It is well known that the sensitivity of any voltage measurement is limited by noise generated in the resistive components of the measurement circuit. There are two main components to this noise, namely $1/f$ noise and Johnson noise. The former noise source, as its name suggests, is strongly frequency dependent and arises due to fluctuations of the measurement circuit resistance. There is no general expression for $1/f$ noise, since it dependent on the precise details of measurement circuit construction. However, this component of the noise can be effectively avoided by carrying out a.c. lock-in measurements at higher frequencies (see Section 3.3.2.3). In fact, it is for this reason that transport measurements are not usually carried out using a.c. driving currents with frequencies lower than about 10 Hz.

Whilst $1/f$ noise can be limited by operating at higher frequencies, Johnson noise is truly intrinsic to all current carrying measurement systems. This type of noise arises due to thermal fluctuations in the electron density within the resistive components of the measurement circuit. The r.m.s. Johnson noise voltage developed in a resistor at temperature T is given by:

$$E_{rms} = \sqrt{4kTR\Delta f}\ , \tag{3.1}$$

where k is the Boltzmann constant, and Δf is the noise bandwidth in Hz [3]. Equation (3.1) reflects the three main ways in which Johnson noise can be limited.

(i) **Operating at lower temperature**: This works to our advantage, since measurements on superconductors are in any case carried out at cryogenic temperatures.

(ii) **Reducing circuit resistance**: Resistive noise components arise due to sample contacts, the measurement leads and the measurement devices themselves (see section 3.3.2.1).

(iii) **Reducing noise bandwidth**: Johnson noise is white noise, with a uniform power distribution across the frequency spectrum. As such, effective reductions of noise power can be achieved by using signal processing techniques to reduce the noise bandwidth (see sections 3.3.2.2 and 3.3.2.3).

3.3.2.1 Limiting Measurement Circuit and Contact Resistance

As mentioned above, one of the simplest ways of limiting intrinsic noise is to reduce the resistance of the measurement circuit. The two main areas to be addressed are the lead resistance (typically $R_{\mathrm{lead}} \sim 10\ \Omega$) and the sample contact resistances (for high quality contacts $R_{\mathrm{con}} \sim 1\ \Omega$). In practice, it is very difficult to reduce the lead resistance below a certain level due to conflicting requirements of system design.[‡] For this reason, it is particularly important to limit the resistance of the sample contacts. A further important reason to limit sample-contact resistance is Joule heating. In the cryogenic regime, even relatively small currents could result in a local heating effect, if contact resistances are insufficiently low. This can lead to temperature gradients across a sample, which in turn lead to highly unpredictable vortex-state behaviour. Thus, the onset of joule heating defines the limiting current for a particular sample.

3.3.2.2 Simple Signal Processing Techniques for reducing noise bandwidth

Since Johnson noise is uniformly distributed across a wide range of frequencies, an effective reduction in the resistive noise contribution can be achieved by reducing the noise bandwidth [see Eqn. (3.1)]. On the simplest level, a reduction in noise bandwidth can be achieved by averaging adjacent time-series data points. This can be carried during the acquisition process, or else on subsequent analysis of the measured data. Up to a point, this technique can be very useful and in fact a large proportion of the data presented in this thesis were either 5 or 10 point adjacent averaged. However, simple adjacent point averaging suffers from an important limitations, in that it obscures the variation in time of the signal. This limits the amount of data point averaging that can be applied without distorting the form of the measured dependences. Indeed, when attempting to measure particularly sharp features such as peaks in the measurement response, adjacent point averaging is not usually applied.

[‡] From the point of view of noise limitation, it is better to use wires with larger cross-sectional areas so as minimise their resistance. However, in cryogenic systems very small diameter wires are used so as to limit heat transfer and hence the boil-off rate.

3.3.2.3 Lock-in Detection Measurements

In addition to the simple methods described above for achieving effective reductions of noise, the noise bandwidth can be actively limited through the action of measurement devices or specially introduced filtering components. One of the most effective ways of separating a signal from the noise background is to use an a.c. lock-in detection technique. The basic arrangement for a lock-in transport measurement is illustrated in Fig. 3.2.

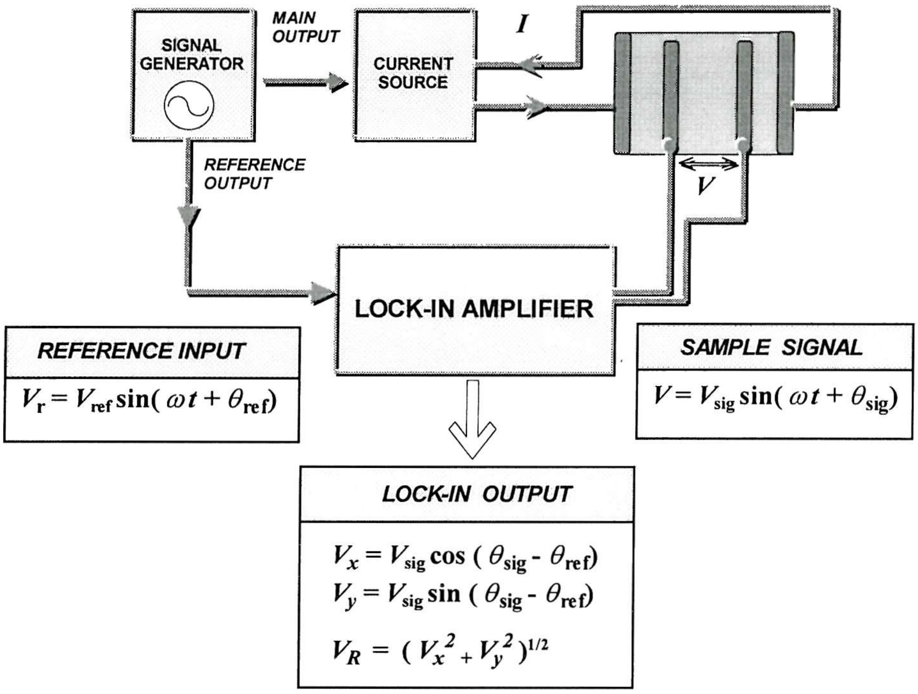

Fig. 3.2 *Standard lock-in detection scheme for the measurement of alternating voltages. Here a sinusoidal current has been applied to a sample in the linear response regime. In this case the reference signal and the response signal have exactly the same angular frequency ω. The lock-in amplifier separates the signal into in-phase (V_x) and out-of-phase (V_y) components.*

Essentially a lock-in amplifier (LIA) is just a very high Q ($f/\Delta f$) filter. Q-factors for LIAs can be as high as 10^6 as compared to 10^2 for a very good band-pass filter [7]. Further to this, lock-in detection is useful for eliminating any low-frequency drift in measurement base-line, such as that arising from thermal EMFs (see Section 3.3.3.3).

3.3.3 External Noise Sources : Synchronous and Asynchronous

It is important to distinguish between noise sources which are intrinsic to the process of current flow (Johnson and $1/f$ noise) from those which are generated by external interference. Whereas the intrinsic noise sources, as discussed above, introduce noise over a range of frequencies, external sources typically introduce a noise component at a particular frequency or narrow range of frequencies. Examples of external noise sources are rotary pump motors and switch-mode power-supplies.

Usually, noise sources are asynchronous, i.e. they couple to the system at frequencies unrelated to that of the measurements signal. This type of external noise can be effectively removed by using frequency filtering techniques such as the lock-in amplification (see preceding section). It is clear, however, that care should be taken not to carry out a.c. measurements at a frequency coincident with a known environmental noise frequency, such as the mains frequency.[§] Some types of external noise are directly related to the measured signal and as such are synchronous to it. These types of noise are much more problematic, since they add directly to the measured signal and cannot be removed by frequency filtering techniques. Earth loop currents are one very common source of synchronous noise (see Section 3.3.3.2).

External noise arises due to the way in which a measurement system couples to its environment and as such can be effectively screened-out by appropriate system design. In the following sections, the main sources of external noise affecting low level-voltage measurements will be discussed. We will also consider the specific design-steps taken to minimise the effects of external noise on our transport rigs.

[§] Many lock-in amplifiers include notch filters for 50Hz noise.

3.3.3.1 Inductive Coupling

Generally speaking, inductive coupling arises due to changes in the magnetic flux threading a measurement-circuit. This can arise as a result of a time-varying magnetic fields or else due to the motion of the measurement-circuit cables within a static field. Even in the earth's magnetic field (~ 0.1 mT), noise voltages of the order of nV can be generated in response to moving cables. Clearly this has a major impact on measurements of the vortex state of HTS, since the applied magnetic fields in this case are typically ~ 1 T. When operating at such high fields, the stray-field from the magnetic-coils has the potential to generate large inductive voltages, particularly when the field is being swept. Since the inductive emf is proportional to the area of the pick-up loop, the main way in which it can be limited is reducing the area of the measurement circuit. Twisted pair cabling was used throughout our measurement systems and further to this, steps were taken to minimise the overall cable lengths. Where possible, cables were well-fastened, to prevent them from moving within the magnetic field. In the case of the magnets used at the Grenoble High Magnetic Field Laboratory (see Section 3.5.2), special bridges had been constructed to hold the cables static in the magnetic field.

3.3.3.2 Resistive Coupling

Resistive coupling arises when currents flow through ground connections. Such currents are a particular problem when they originate in the measurement circuit itself and thus are synchronous with the measured signal. In an experiment on a superconductor, it becomes apparent that ground loops are present when a large voltage signal persists deep into the superconducting state. The effect arises due to different devices on the measurement circuit being connected to points on the ground bus with slightly different potentials. Where possible, in our measurement systems, we have used floating earth devices to avoid ground loop connections. Other devices without a floating earth option had their chassis grounds wired to a common earthing point.

3.3.3.3 Thermal EMFs

Thermal EMFs arise due to thermal gradients across connections between conductors in the measurement circuit (the effect is largest for connections between dissimilar metals). Any connector in the measurement circuit should be considered a potential source of thermal EMFs. From a physical design point of view, thermal EMFs can be limited by using clean crimped on copper-to-copper connectors. Efforts should also be made to keep ambient temperatures constant by avoiding direct sun-light and preventing air-flows across the instrumentation. Such precautions can be very important when making DC measurements. However, by far the simplest method to remove the effect of thermal EMFs is to use a current reversal method. From a diagnostic point of view, thermal EMFs can be identified by simply switching the current connections to the measurement circuit. Although the signal voltage changes direction on current reversal, thermal EMFs are independent of the current direction. Thus the signal voltage (V_{SIG}) that we actually wish to measure can be readily separated from the thermal EMF (V_{EMF}) simply by measuring the two voltages V_+ and V_-:

$$\left.\begin{array}{l} V_+ = V_{EMF} + V_{SIG} \\ V_- = V_{EMF} - V_{SIG} \end{array}\right\} \Rightarrow V_{SIG} = \frac{V_+ - V_-}{2} \tag{3.2}$$

In an a.c. measurement, thermal EMFs manifest themselves as a drifting offset to the alternating signal. Provided that measurements are not conducted at very low frequencies, frequency selection techniques such as lock-in detection are very effective at removing this type of spurious contribution. The majority of the results described within this thesis were obtained using a.c. lock-in techniques hence in such cases the effect of thermal EMFs can be reasonably disregarded. In the few cases where d.c. measurements were made contact switching techniques were employed to estimate the magnitude of the thermal EMF. This offset voltage was then subtracted from the measured data.

3.4 Temperature Measurement & Control

Well-designed temperature measurement and control systems are a prerequisite to performing meaningful transport measurements on the vortex state. Without sufficient accuracy or reproducibility, it is impossible to repeat measurements and obtain the same results. Furthermore, if we are to measure the response of the system at as particular temperature then it is important that this temperature should be stable, otherwise it becomes difficult to separate the underlying physics from effects arising due to thermal drifts. Temperature control issues are of particular importance when investigating complex history dependences (see Chapter 7). If we are to understand the differences which arise due to subtle changes in measurement history, then it is clear that this history should be extremely well controlled.

In the following sections, the importance of each of the main aspects of temperature measurement and control will be considered. The practical steps taken to ensure that that optimal temperature performance was achieved in our experiments will also be described.

3.4.1 Temperature measurement accuracy

Before attempting to control the thermal environment of a sample it is first necessary to have an accurate means of determining temperature. Here we ought to distinguish between absolute and relative accuracy. Absolute accuracy is the degree of agreement between a particular reading of temperature and a primary standard, as related to an absolute gas thermometer scale [8]. Formally, relative accuracy is defined as the accuracy of a measuring instrument relative to a secondary standard. However, here we will consider relative accuracy in a broader sense as the ability of a temperature measurement system to have a well-defined and reproducible response. This response should reflect the thermal state of the system in isolation, prior to the measurement being made. Whilst it is clearly desirable to measure temperature to a high absolute accuracy, it is far more important that we always measure the same temperature when the system is under the same thermal conditions.

3.4.1.1 Choice of sensor

Clearly the choice of sensors is one of the most important decisions to be made in designing a reliable temperature measurement and control system. The main factors to take into account are as follows.

(i) **Temperature range of maximum sensitivity**: sensors should be chosen to have a good sensitivity over the temperature range of interest. For transport measurements on HTS this typically encompasses the range 60-100K.

(ii) **Magneto-resistance (MR)**: it is crucial that the sensor should not have a strong response to magnetic field. This can be particularly important when operating at very high fields above 10 T.

(iii) **Packaging**: the sensor size and shape may determine both the ease with which it can be fitted into the measurement system and also how easy it is to obtain a good thermal contact between the sensor and its environment.

(iv) **Compatibility with measurement devices**: not all sensors can be readily measured. It is relatively easy to measure the response of resistance and diode thermometers. In contrast, capacitative and thermocouple sensors require specially designed measurement devices.

For reasons of varying requirements we have used a variety of different temperature sensors in our experiments. See Appendix B for a summary of the important characteristics of the different types of sensors used in our studies.

At this stage a distinction should be drawn between sensors used for sample temperature measurement or primary-control, and those used to control the cryostat environment temperature. The requirements for these two types of function differ, since in the former case much higher sensitivity and reproducibility are required. For environment-temperature control-sensors, it is sufficient to know how fast the temperature of the system is changing and hence to modify the control-loop output accordingly.

For reasons of their low magneto-resistance and high sensitivities over the relevant temperature range, Cernox sensors (Lakeshore 1050 and 1080) were used for most of our measurements of sample temperature. In the case where a secondary environment temperature control loop was employed, as for our 16 T magnet setup (see Section 3.5.1), a carbon glass sensor provided sufficient reproducibility and sensitivity. For the SQUID pV-meter arrangement (see Section 3.5.3), where magnetic fields were limited to 5T a GaAlAs sensor (LakeShore TG-120) was used. In the special case where very high magnetic fields were applied, in our measurements at the Grenoble High Magnetic Field Laboratory, a specialised capacitative bridge set-up was used for temperature control.

3.4.1.2 Important Sources of Error in temperature measurements

Temperature sensor resistances are usually measured using a four point technique analogous to that employed in transport measurements (see Section 3.3.1). Temperature sensor data are also affected by drifting offsets due to thermal EMFs (see Section 3.3.3.3). To obtain reliable temperature measurements, these offsets should be removed using current reversal techniques. In the SQUID pV-meter (see Section 3.5.3), the control electronics measured the temperature by averaging responses obtained in forward and reverse bias directions. A similar procedure is employed by the Lakeshore 340 temperature controller [9], as used in conjunction with our 16T transport rig (see Section 3.5.1).

Another problem affecting temperature measurement is that of inductive pick-up in the cables connecting the temperature sensor to the measurement device (see also Section 3.3.3.1). This is a particular problem in the case of sensors used for precise control of the sample temperature, since inductive coupling, especially at high fields, can lead to instability of the sample temperature. As with all low-level measurements, the standard precaution is to minimise the area of the induction loop, and for this reason twisted pair cabling was used in all of our experimental arrangements when making connections to temperature sensors.

A final important factor affecting temperature measurements is that of Joule heating in the sensor. Manufacturers provide data on the maximum excitation voltage that can be applied to a given sensor without significantly raising its temperature. Since such parameters are dependent on the environment temperature, special care should be taken when operating at low temperatures. Normally there is a balance to be drawn between the higher measurement accuracies obtained by using higher currents or voltages and the potential for Joule heating effects. This is best understood by considering an illustrative example.

At 77 K a typical Cernox temperature sensor has a resistance ~ 200 Ω. On its 999 kΩ measurement range, a Keithley 196 multimeter produces a current ~ 50 μA. If a Keithley 196 set to its 999kΩ scale were used to perform a four point resistance measurement on a typical Cernox sensor at 77 K, then an excitation voltage of 10mV would be developed. Since the Keithley 196 has a 5 digit display, this would be displayed in the format 000.10 V. The temptation, therefore, would be to increase the measurement sensitivity by adjusting the Keithley to a lower measurement scale. However, Lakeshore recommend that (for temperatures above 1K) excitation voltages across their Cernox series sensors do not exceed ~5mV [10]. Thus, even on the 999kΩ scale at 77K there could be significant Joule heating effects. This problem would become much worse as sensor resistance increased at lower temperatures. Also, the adjustment of the Keithley to a lower measurement scale would further exacerbate the problem since increases of accuracy on going to a lower scale are achieved by using a higher measurement current (~150μA in the case of the 99kΩ scale). The advanced read-out electronics of the Lakeshore 340 temperature controller allowed us to avoid such problems by automatically adjusting sensor-excitations dependant on the temperature range. In other cases, where this particular device was not available, Joule heating effects were avoided by using measurement devices with a larger number of digits of accuracy. This obviates the need to perform measurements on the lower resistance ranges, where measurement currents are correspondingly higher.

3.4.2 Sample Temperature Control

Being able to accurately measure temperature is only half the problem, since if we are to be able perform meaningful transport measurements then we must be able to actively control the sample temperature. This implies that we should be able to both:

(i) Stabilize on a particular point and maintain this temperature constant to a very high accuracy. This is required to measure $V(I)$ and $R(B)$ dependences.

(ii) Sweep the temperature across a particular range at a constant rate. This is required to measure $R(T)$ dependences.

On a simplistic level, it might seem that all that is required to achieve this is some sort of heater with a means to modify its output according to the reading of an accurate temperature sensor. In practice, the situation is far from simple, since factors such as thermal masses and response times need to be taken into account. As such, there are a number of key experimental considerations for achieving reliable temperature control in cryogenic systems.

3.4.2.1 Physical Design Techniques for Temperature Control

The first thing to ensure, in any temperature control setup, is that the temperature at the thermometer is as close as possible to the actual sample temperature. It is no use having an accurate temperature sensor if the reading that it provides does not reflect the temperature that we actually want to measure. In order to minimise thermal gradients, both the sample and the sensor, together with their contact leads, should be well thermally anchored to the sample mounting. Normally this mounting is made from highly conductive metals such brass or ultra-pure copper.[**] If thermal contact is poor, then the temperature at the sample may show a non-linear dependence on the sensor temperature.

[**] It is essential that the sample-mount assembly has a very low density of magnetic impurities otherwise this could significantly distort the magnetic field profile experienced by the sample.

Another vital physical design consideration in that of passive temperature stabilisation. Whilst we can compensate for a certain amount of variation in the sample-environment temperature by means of an actively controlled heater output (see below), clearly it is desirable to minimise external temperature fluctuations before we even get to the stage of active control. In a typical cryostat arrangement this is achieved by means of a combination of:

(i) Vacuum shielding

(ii) Radiation shielding

(iii) Cryogenic liquid jackets (often an inner liquid helium jacket is contained within an outer liquid nitrogen jacket).

These practical measures help to minimise temperature fluctuations arising due to conduction or radiation. Further to this, steps are usually taken to prevent heat flows due to convection. Within our experimental arrangements this was achieved by incorporating baffles onto the sample insert, which split up the sample space into cells insufficiently large to support convection. In a gas flow cryostat there is further potential for temperature instability arising due turbulent flow of the gas across the sample. This can be prevented by enclosing the sample in a casing which prevents it from coming into direct thermal contact with the coolant gas.

A further important issue for consideration, is that of thermal response times. Suppose, for the purposes of understanding, we consider a copper block at temperature of 100 K, in contact via a thermal link to a helium bath at a temperature of 4.2 K. If the copper block has a thermal capacity C JK^{-1} and the link to the block presents a thermal resistance R KW^{-1}, then product $\tau = CR$ is the thermal time-constant for cooling-down the system [11]. Suppose we have 1 mole of copper, then at 100 K its heat capacity $C = 16$ JK^{-1} [12]. To achieve a time constant $\tau = 300$ s we would require a thermal link resistance of $R \approx 20$ K/W. Since thermal resistance is related to thermal power via the expression $P = \Delta T / R$, where $\Delta T \approx 100$ K is the temperature differential between the copper block and the heat sink, this implies a rate of heat flow down the thermal link of 5 W. This heat flow will boil off 7*l* of liquid helium in 1 hour [13], which is far too high for all practical purposes. There are a number of different ways to work around this problem.

(i) Reduce the mass to be cooled by reengineering the sample mount to have a more light-weight construction. This can be achieved by using materials with a lower heat capacity such as tufnol, or alternatively by using thinner parts.

(ii) Accept much longer time-constants. This will increase the cool-down time at the beginning of experiments and reduce the maximum rate at which the temperature can be swept.

(iii) Increase the temperature of the heat sink. Often this is achieved by cooling the sample with He gas in a continuous flow cryostat. In such an arrangement we can control the cooling power by means of a needle valve. To warm-up the system quickly, the needle valve can be closed completely. Typically, optimal responsiveness for temperature control is achieved with the needle valve just slightly open.

Just as the system can be cooled by means of a heat sink, it can also be heated by means of some sort of heating coil. The thermal time-constants of the system imply that there will always be some delay between applying an output to heater and the desired increase in temperature being experienced at the sample. To heat the system at a similar rate to that at which it naturally cools, the applied heater-power should be twice that required to maintain the system at a steady temperature.

From the discussion outlined above, it should be apparent that thermal response times are a key consideration in designing a sample mounting for insertion within a cryostat. From the point of view of reducing response times, it might seem that we would want to make the insert as light-weight as possible. However, there is a compromise to reached, since any reduction in the thermal response time is achieved at the expense of stability to environmental temperature fluctuations. As such, inserts can be designed with a bias towards either responsiveness of stability, depending on the type of measurements that are to be performed. In transport experiments, we frequently need to measure resistivity as a function of temperature, hence sample inserts are typically of a relatively light-weight thermally-responsive construction.

Irrespective of sample mount design, some thermal lag always persists between the sample temperature and that measured at the temperature sensor. This lag is dependent on the temperature sweep rate. For a typical sweep at rate ~ 0.2 K/min it is normal to expect an offset ~ 20 mK due to the thermal lags. If it is desired to measure a $\rho(T)$ dependence entirely without thermal lags, then it is necessary to reduce the sweep rate to such an extent that the lag becomes negligible. To estimate the offset for a particular setup, resistivity curves can be measured on warming and cooling at the same constant rate across the region of the superconducting transition. The offset is then deduced from the shift between these two curves. For all of the results presented within this thesis, the offsets due to thermal lags have been subtracted.

3.4.2.2 Feedback Systems for Active Temperature Control.

In the previous section we suggested that the sample temperature could be controlled by means of a heater, the output of which is varied according to the reading obtained from the sample temperature sensor. On the simplest level, we could attempt to achieve this by means of an ON-OFF system, whereby the heater is switched on when $T < T_{\text{target}}$ and switched off when $T > T_{\text{target}}$. It is evident that in this case, however, that the system would always overshoot the target temperature and further to this, that it would never stabilize on this target. Instead the temperature would oscillate up and down past the target-level as the heater switched repeatedly on and off.

The next level of sophistication would be to vary the output to the heater proportional to the temperature difference between the sample temperature and the target temperature. This type of **proportional control** will, however, always lead to an offset between the temperature fixed upon and the actual target temperature. At the target temperature itself the error correction [error (e) = Target Temperature – Feedback Reading] falls to zero and it follows that for a purely proportional feedback this would result in zero output to the heater coil. Clearly the temperature cannot be maintained constant if the heater output is zero. As such, there should always be some minimum offset, at which the output from the heater is a well-defined fraction of full-scale power. This offset can be reduced by increasing the gain of the feedback system, however there is a limit in how far this can be applied, since if the gain is too high then this will again lead to oscillations about the target temperature.[††] Identifying suitable values for the proportional control parameter is normally a matter of trial and error.

In order to remove the temperature offset error, it is necessary to incorporate a further type of feedback into the system whereby an adjustment is made to the heater signal which is proportional to the integral over time of the out-of-balance signal. Where the error is zero, this integral contribution maintains the heater-output constant. Finally, there a third type of control known as derivative (or rate) control, which applies a correction to the heater output proportional to the rate at which the target temperature is being approached. Analogous to a viscous damping term, this type of control minimises the temperature overshoot on approaching the target temperature. This can be useful in fast changing systems but is often turned off in steady state control since it tends to react too strongly to small changes in the environment temperature.

All electronic temperature control units, such as the Oxford Instruments ITC4 or the Lakeshore 340 incorporate proportional (P), integral (I) and differential (D) feedback parameters. Precise definitions of the parameters vary from instrument to instrument, but in the case of the Lakeshore 340 the PID equation can be written as [9]:

$$Heater\ Output = P\left[e + I\int e(t)dt + D\frac{de(t)}{dt}\right] \tag{3.3}$$

[††] A very high gain proportional feedback arrangement can be considered effectively equivalent to a simple ON-OFF system

Regardless of the precise controller used, PID parameters must be carefully tuned to suit the characteristics of a particular measurement system. Normally different PID parameters are appropriate over different temperature ranges. Further to this there is the additional complication that the best choice of parameters will depend on the type of measurement to be made. For example, when measuring temperature sweeps the optimal parameter choices are different to those when measuring responses at fixed temperature. For more details on how to select appropriate PID parameters for particular measurement on a particular measurement system see Ref 9.

3.4.2.3 Procedural Steps for Reducing Temperature Overshoots

In Chapter 7 we describe experiments in which we explore in detail the response of the vortex system to thermal cycling in the vicinity of the vortex solid to liquid melting transition. To perform this type of experiment we needed to be able to sweep to a target temperature-point with an absolute minimum of overshoot past this point. In the previous section we saw that temperature overshoots can be minimised by the introduction of a carefully chosen differential feedback parameter. In many cases this is sufficient for all practical purposes. However, to carry out a detailed investigation of history dependences in the immediate vicinity of the vortex liquid to solid melting transition, then even a small overshoot (> 10 mK) may prove crucial. The virtual elimination of such overshoots was a key step towards performing meaningful temperature-history measurements. Both reproducible and unreproducible overshoots can compromise results, respectively by generating spurious trends, or entirely masking the history-dependent systematics.

We have developed a set of procedures for reducing temperature overshoots on approaching a target temperature. Due to differences in the thermal response of the system on warming and cooling, the procedure adopted for ramping-up to a given temperature differed slightly from that on ramping-down. In addition, the number of intermediate steps required to minimise the temperature overshoot, depended on the magnitude of the difference between

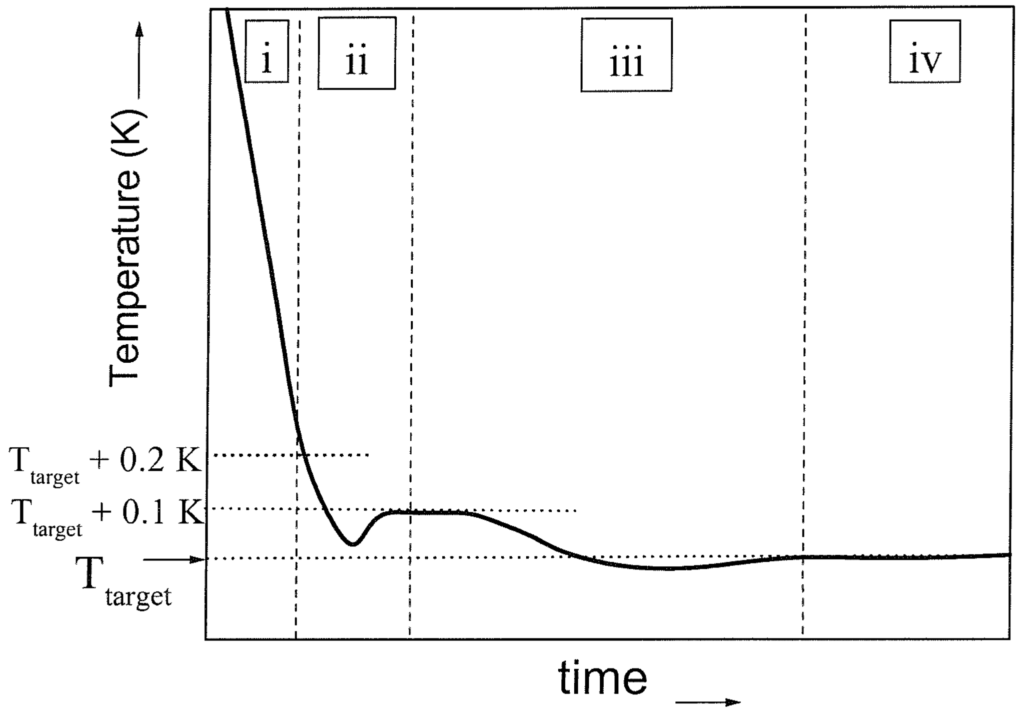

Fig. 3.3 *Schematic representation of the main stages used to fix on a particular target temperature,* T_{target}*. (i) Sweep to* T_{target} *+ 0.2 K at a controlled constant sweep rate. (ii) Stabilise on* T_{target} *+ 0.1 K (iii) Stabilise on* T_{target} *(iv) Wait to ensure stability.*

the start temperature and the target temperature. The principle features of the procedures adopted are be summarised in the schematic representation of Fig. 3.3. The constant rate sweep [stage (i)] is used to reduce the length of time taken to reach the target temperature. On reaching the end of this sweep at T_{target} + 0.2 K there is a significant overshoot past this end point. However, by then stabilising the system on T_{target} + 0.1 K [stage (ii)] we ensure that the temperature does not fall below T_{target}. By stabilising on T_{target} + 0.1 K before finally dropping to T_{target} [stage (iii)], we significantly reduce the height of the temperature-step down to the final target temperature. Thus, as schematically illustrated in the figure, while there may still some temperature overshoot past T_{target} it should now be minimal. Following this type of procedure we managed to limit temperature overshoots to less than 5 mK.

3.5 Details of Specific Experimental Arrangements Used

3.5.1 Oxford Instruments 16 T Transport Rig

The Oxford Instruments (OI) cryomagnet is a high field superconducting magnet system that can provide a field of 14 T at $T = 4.2$ K and 16 T at $T = 2.2$ K.[‡‡] The cryogenic system is contained within a vacuum insulated liquid helium cryostat with an additional liquid nitrogen jacket. Enclosed within this cryostat is a standard gas-flow variable temperature insert (VTI) into which the sample rod is inserted.

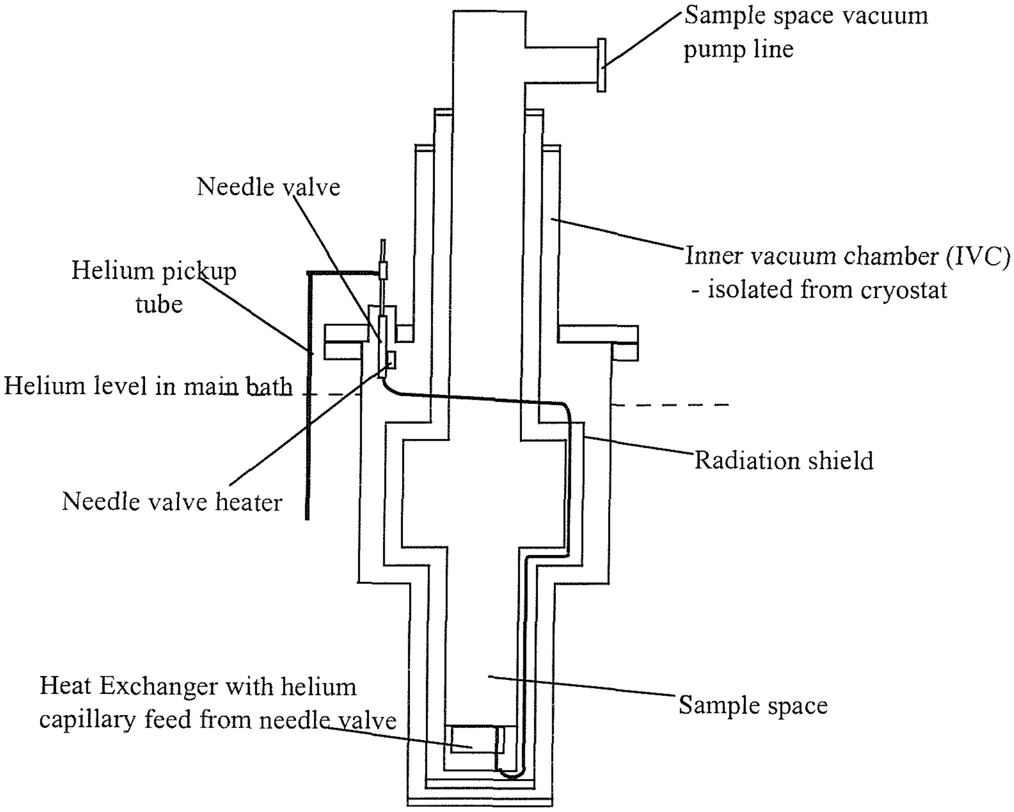

Fig. 3.4 *Oxford instruments variable temperature insert. The sample rod is inserted into the sample space (sample space diameter 20 mm).*

[‡‡] Field homogeneity at coil centre : 1% over 10 mm.

The rate of gas flow across the sample is controlled by means of a needle valve, which in most cases was left just slightly open in order to provide maximum responsiveness to heater output variations.

The sample insert itself was of a standard design, with rotating sample platform fixed in such a way as to maintain the sample centrally within the field coil. We optimised the system for maximum responsiveness and reproducibility in terms of temperature control, by incorporating the following key features:

(i) Dual stage temperature control : Sample-space temperature is regulated within a standard flowing gas variable temperature insert (VTI) [14]. This is effected by means of a temperature-sensor/heater combination attached to a needle valve controlling the flow of gas into the sample space. The temperature in the immediate vicinity of the sample is regulated by means of a temperature-sensor/heater pair attached to the high thermal conductivity brass sample-platform. In order to obtain the best possible estimate of sample temperature, the temperature sensor was placed in a groove ***directly*** underneath the sample and well thermally-anchored to both the sample and the underlying platform using thermally conductive glue. To minimise thermal gradients the heater was thermally anchored to the sample platform as close as possible to sample.

(ii) Fully optimised dual channel temperature control unit: The heater outputs to the temperature control loops were controlled by means of a dual channel Lakeshore 340 temperature controller. This was fully optimised in terms of its Proportional (P), Integral and Differential (D) feedback parameters. Different parameters were applied to each of the two loops and for each loop across different temperature ranges (the Lakeshore 340 has the facility to store ranging information).

(iii) Closed cap around sample platform: Minimises temperature fluctuations due to turbulent gas flow within the VTI (see Section 3.4.2.1).

A schematic layout of the full experimental arrangement is shown overleaf in Fig. 3.5.

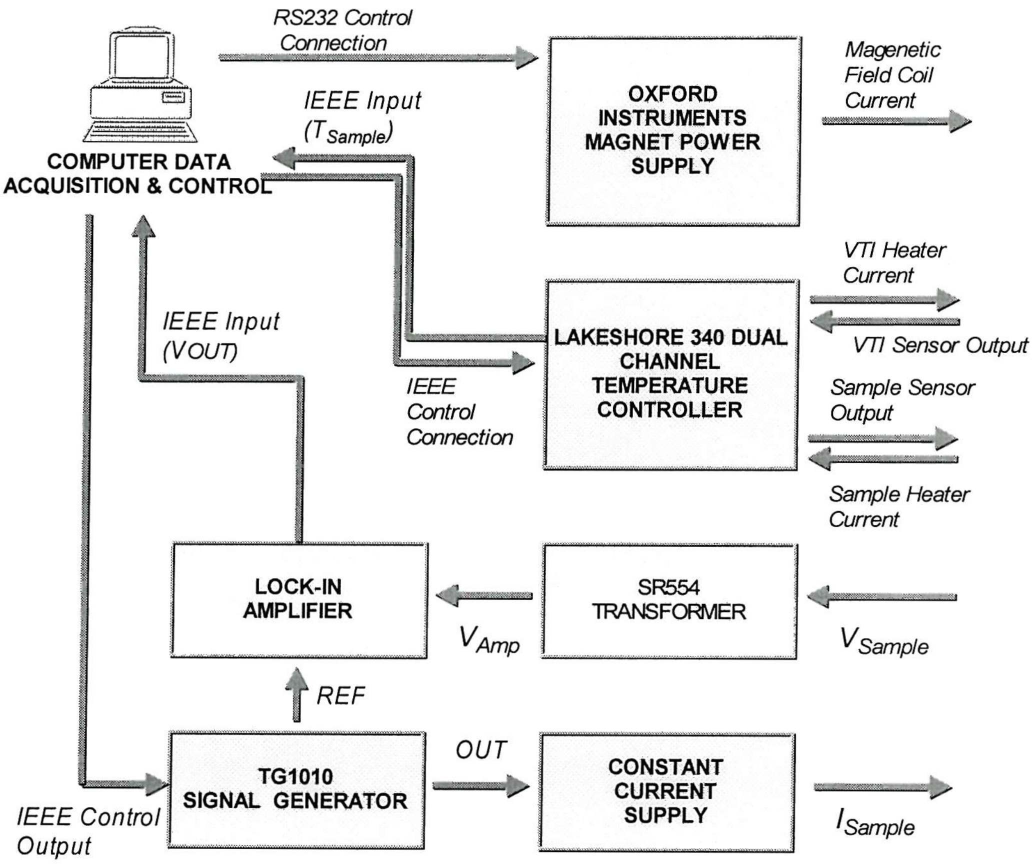

Fig. 3.5 *Schematic Representation of equipment used in conjunction with the Oxford Instruments 16T magnet VTI.*

The setup is basically a standard lock-in detection arrangement, with an additional transformer (gain ~100) to amplify the voltage signal from the sample. The arrangement was controlled by means of purpose written control-software, as developed by the author of this thesis. This software allowed for the execution of a complex series of experimental steps, by means of a purpose written scripting language (see Appendix C).

3.5.2 Grenoble High-Field Transport Arrangement

A few of the results presented in this thesis were obtained at the Grenoble High Magnetic Field Facility (GHMFL)[15]. At GHMFL various magnets are available providing fields of up to 30 T [16]. The magnets that we obtained access to at Grenoble (providing fields of up

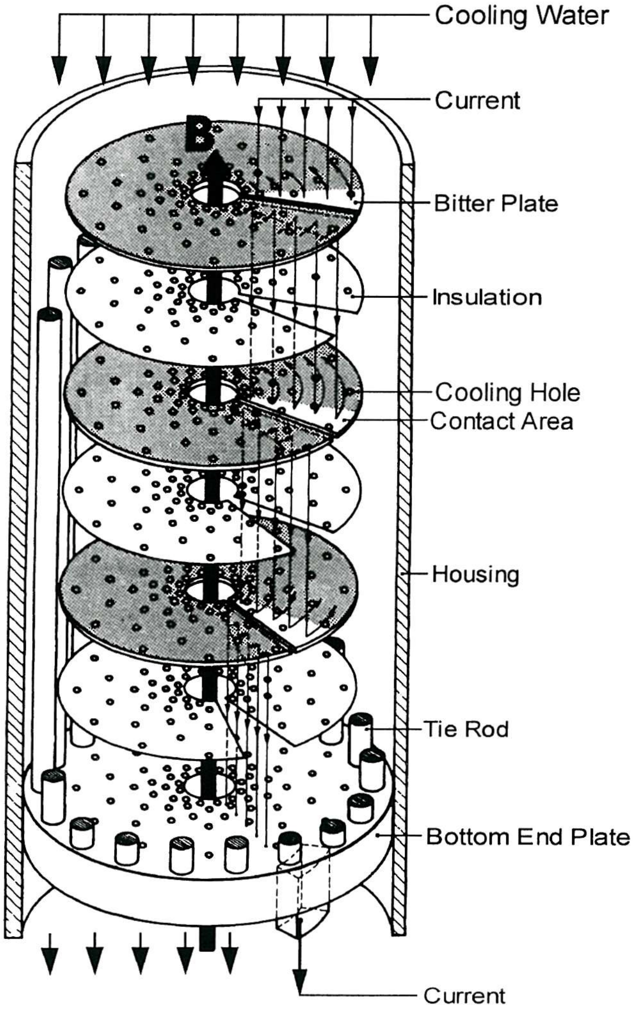

Fig. 3.6 *Bitter magnet construction as implemented at the Grenoble High Magnetic field laboratory [16].*

to 23 T in a bore of 50 mm) were all based upon a resistive Bitter coil design, as illustrated in Fig. 3.7. The Bitter coil comprises a stack of circular copper plates insulated from each other except along a radial slit in the insulation. Current is then passed from plate to plate within this coil in a spiral-like fashion. In order to dissipate the heat produced in this arrangement cooling water is passed through at a variable rate, dependent on the applied current. Notice that, as shown in Fig. 3.4, the holes through which the cooling water is passed are concentrated towards the centre of the plates, where the current density is expected to be at its highest. The power supply used to drive such coils is quoted to have a stability of 10 parts per million over a period of 10 minutes. Due to the very high fields applied, extra precautions had to be taken to fix cables so that they did not move within the field and thereby induce noise voltages at the output (see Section 3.3.3.1).

The device arrangement for the transport measurements was exactly the same as that described in relation to the Oxford Instrument 12T magnet setup (see Fig. 3.6). Basic temperature control was, however, on a simpler level with single temperature-control-loop, controlled by means of an Oxford Instruments ITC4 temperature controller. This device does not allow for the PID parameters to be dynamically varied across different temperature ranges. Hence the temperature control was not nearly so well-refined as for the systems used at the University of Southampton. A further factor which needed to be taken into consideration, was the magnetoresistance of Cernox temperature sensor used in conjunction within the GHMFL arrangement (see Appendix B). Had this been the sole means for controlling the sample temperature, then it would not have been possible to maintain the temperature constant whilst sweeping the magnetic field up to highest levels. In order to combat this problem an additional control loop was employed when measuring field sweeps, which utilised a single channel Lakeshore temperature-controller, connected to a capacitative temperature sensor. This type of sensor has the clear advantage of having virtually zero magnetoresistance (see Appendix B). While this control-loop was not particularly well calibrated in terms of accuracy or reproducibility, it did allow for the temperature to be maintained at a constant level while sweeping the magnetic field.

3.5.3 Purpose Built 5T SQUID Picovoltmeter

As has already been discussed (see Section 3.3), intrinsic noise places a fundamental limit on the sensitivity of conventional measurement systems. For example, if we desire to measure a voltage with output impedance ~ 1 Ω, room temperature voltage measurements are intrinsically limited to a sensitivity ~ 1 nV [3]. However, when carrying out studies on superconductors at low temperatures, it desirable to resolve voltages at much lower levels. In order to meet this metrological requirement, voltmeters have been developed based around Superconducting Quantum Interference Devices (SQUIDs) [4]. Following these advances, the University of Southampton Condensed Matter Physics Group in collaboration with the Moscow Institute of Radioengineering and Electronics developed a SQUID-voltmeter arrangement,[§§] capable of measuring voltages ~10-100 pV.[***]

In terms of its construction, a dc-SQUID consists of a pair of Josephson junctions wired in parallel, such that together they form a superconducting loop broken by two weak links. The particular SQUID sensor used in our apparatus was manufactured at the Institute of Radio-Engineering and Electronic in Moscow and comprised a pair of Nb-Al_xO_y-Nb resistively shunted tunnel junctions [17]. From a metrological point of view, such a SQUID sensor can be simply regarded as a sensitive flux to voltage transducer. It follows that an important figure of merit for SQUID sensors is the spectral density of the flux-noise,[†††] $S_\phi(f)$ at 4.2 K. Equivalently, this can be expressed as an energy sensitivity $\varepsilon(f) = S_\phi(f)/2L$, where L is the SQUID ring inductance. This energy sensitivity can be quoted for the SQUID ring alone [ε(f)] or else for the SQUID coupled with its associated measurement circuitry [ε_c(f)]. The energy sensitivities quoted for the SQUID sensor used in our picovoltmeter arrangement

---

[§§] The SQUID pv-meter was built by A.Volkozub, formerly of our group, working in collaboration with the Institute of Radioengineering and Electronics, Moscow.

[***] Dependent on contact resistance : the sensitivity is higher for lower contact resistances.

[†††] Here we refer to white noise : this is distinct from the $1/f$ noise which arises for frequencies below about 1 Hz.

were: $\varepsilon(f) = 5 \times 10^{-32}$ J/Hz and $\varepsilon_c(f) = 5 \times 10^{-31}$ J/Hz [17]. These values are comparable to those quoted for other SQUID sensors in the literature [18]. Since the V-ϕ dependence of a SQUID sensor is highly non-linear, to simplify readout it is normal to linearise the output by means of feedback circuitry. In such an arrangement the SQUID operates as a null detector, changes in the external magnetic field being compensated by the feedback response. Hence, the SQUID-detection system is maintained at a so called working point on the transfer characteristic. In the case of the pV-meter arrangement used in our studies this was carried out by a current nulling method, the basic form of the feedback circuitry being illustrated below in Fig. 3.4.

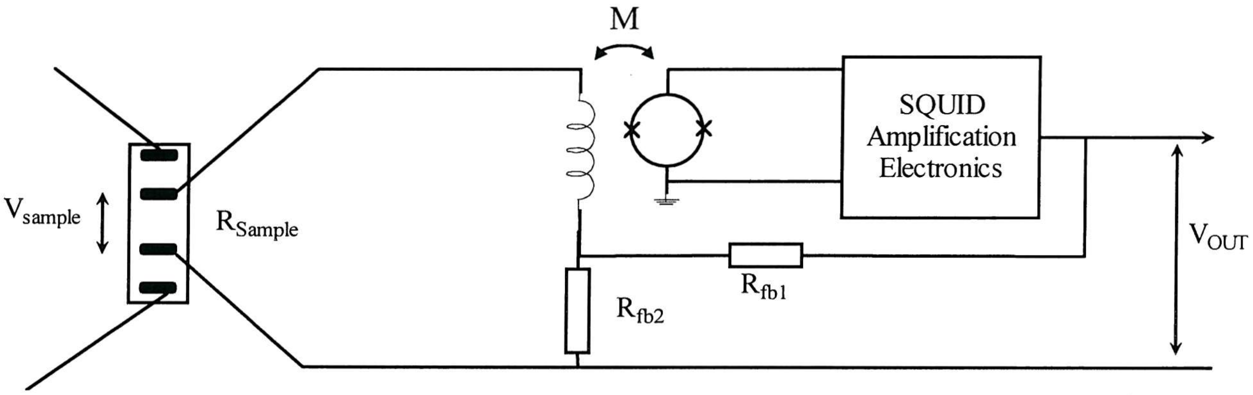

Fig. 3.7 *Simplified representation of the current-nulling feedback arrangement used in the SQUID pV-meter.*

Using this SQUID feedback circuitry it was possible, under optimal conditions,[‡‡‡] to measure the sample voltage to an accuracy of between 20 and 50 pV. However, the impedance of the input circuit was such that this was to some extent limited by the sample resistance. The higher the sample resistance, the lower was the accuracy that was attainable. This provided an additional justification for minimising contact resistances. A further important limitation to the arrangement is that its output saturates for sample voltage signals

---

[‡‡‡] Without, for example, excessive source of external noise

~1 μV. The setup does, however, benefit from a wide frequency bandwidth ~3 kHz. This proved important, in that it allowed for the distortion free measurement of signals with a variety of different modulation-forms and frequencies.

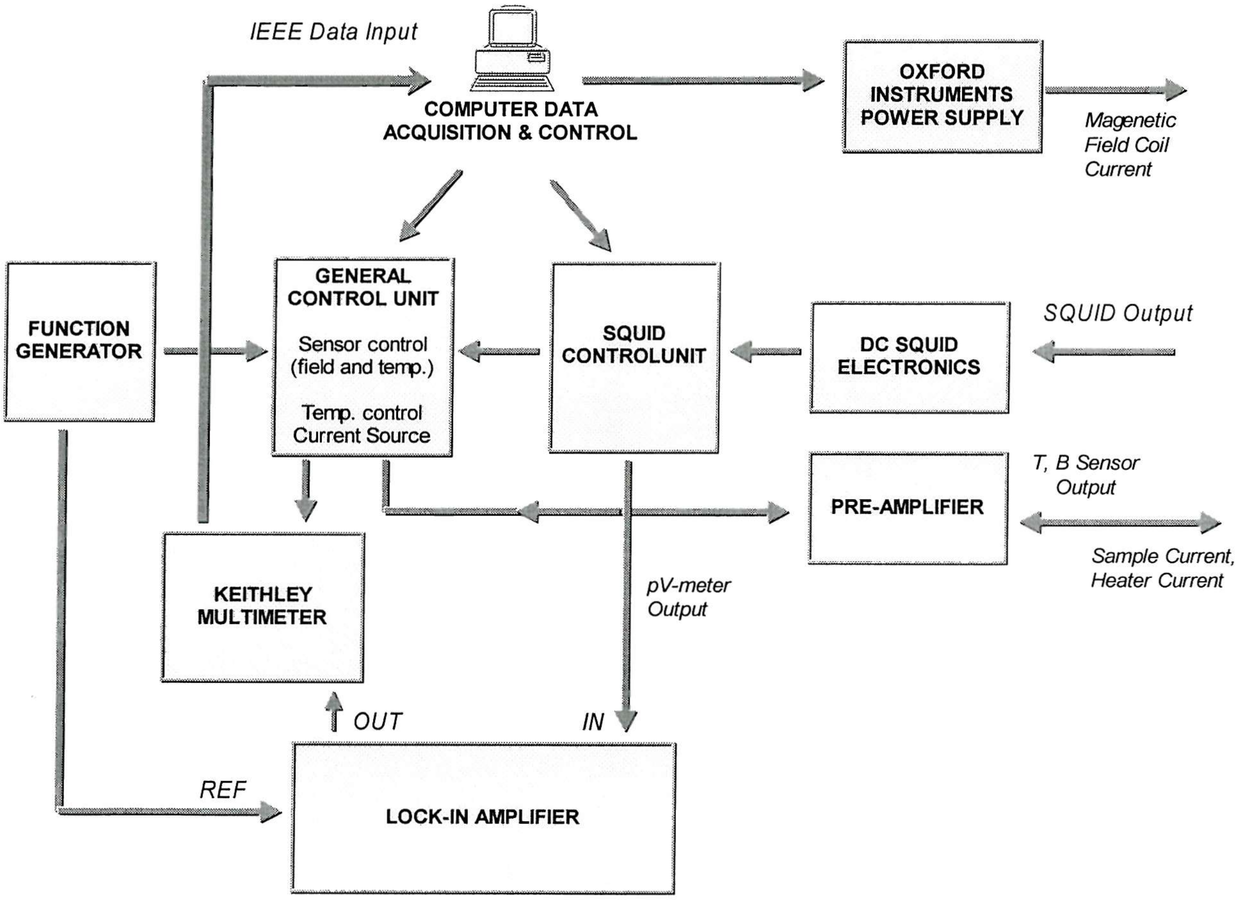

Fig. 3.8 *Basic circuit layout for the the SQUID pv-meter arrangement.*

The overall device configuration of the picovoltmeter is depicted above in Fig. 3.8. The cryogenic system used in conjunction with this arrangement comprised a simple liquid helium cryostat without a gas flow VTI or outer liquid nitrogen insulation jacket. Temperature control responsiveness and reproducibility were improved by enclosing the sample within a closed cap and manufacturing the components of the sample insert to be as lightweight as possible (see Section 3.4.2.1).

References

[1] A. Zhukov, Solid. State. Commun. 82 (1992) 983-5.
[2] A. D. Caplin, L. F. Cohen, G. K. Perkins and A. A. Zhukov, Supercond. Sci. Technol. 7 (1994) 412-422.
[3] Low Level Measurements (4th Edition), Keithley Instruments Inc.
[4] V. Polushkin, D. Drung and H. Koch, Rev. Sci. Instrum. 65 (1994) 3005-3011.
[5] Oxford Instruments, Manual for 12 T Vibrating Sample Magnetometer.
[6] J. A. Fendrich et al , Phys. Rev. Lett. 77 (1996) 2073-2076
[7] Stanford Research System, SR830 Lock-in amplifier, Instruction Manual.
[8] B. W. Magnum, "A new temperature scale, The International Temperature Scale of 1990 is adopted", NIST (Maryland).
[9] LakeShore Model 340 Temperature Controller, User's manual.
[10] Temperature Measurement and Control, Lakeshore Cryotronics Ltd. (1997).
[11] C. M. Muirhead, Notes from Course on Techniques in Low Temperature Physics
[12] G. W. C. Kaye and T. H. Labye, *Tables of Physical and Chemical Constants and Some Mathematical Functions* (Longman, London, 1978).
[13] S. W. van Scrirer, Helium Cryogenics (Plenum, 1986).
[14] Oxford Instruments, User manual for VTI.
[15] Access obtained under the Training and Mobility of Researchers Programme of the European Community.
[16] Grenoble High Magnetic Field Laboratory, *Access to the High Magnetic Field Installation* (1999).
[17] Institute for Radioengineering and Electronics (Moscow), documentation for planar technology dc-SQUID devices.
[18] J. Clarke, SQUID Sensors: Fundamentals, Fabrication and Applications

CHAPTER 4. EQUILIBRIUM PHASE DIAGRAM

4.1 Introduction

Shortly after the discovery of high temperature superconductors (**HTS**), it became apparent that the phase diagrams of these materials were significantly more complicated than those of their low temperature counterparts. This complexity of behaviour can be attributed to the dual effect of anisotropy and the increased role of thermal fluctuations due to the elevated critical temperatures [1, 2]. This leads to strong competition between the intervortex, thermal and pinning interactions over a large region of the parameter space. Increasingly, over recent years, a consensus has been reached as to the structure of the equilibrium vortex phase diagram [3, 4]. Some differences have been identified between the phase diagrams for moderately anisotropic compounds such as $YBa_2Cu_3O_{7-\delta}$ as compared to the more strongly anisotropic compounds such as $Bi_2Sr_2CaCu_2O_8$. Since all of the experiments in this thesis were conducted on samples of $YBa_2Cu_3O_{7-\delta}$, in this chapter we will focus on features specific to the essentially 3D limit. For an excellent summary of the importance of 2D behaviour and decoupling effects in highly anisotropic compounds such as $Bi_2Sr_2CaCu_2O_8$ see Ref. 5.

In spite of the differences between the various HTS compounds, a "universality" has begun to emerge in terms of the essential structure of the vortex phase-diagram. In the following sections we review the present understanding of the "generic" vortex phase diagram for high temperature superconductors. In Section 4.2 we begin by considering the simplest case of a system at the clean limit, i.e. in the absence of significant pinning disorder. In Section 4.3 we then progress to an consideration of the more complicated (and realistic) case of a system in the presence of point disorder. Finally in Section 4.4 we present an overview of the structure of the equilibrium phase diagram as it is presently understood.

4.2 Vortex Phase Diagram at the Clean Limit

Since disorder significantly complicates the vortex phase diagram, for the purposes of understanding we start by considering the simplified case of a clean system. From a practical point of view, this limit would only apply to systems without extended defects and with only a very low (effectively zero) density of point defects. In the conventional picture of a clean superconductor the phase diagram comprises a Meissner phase region up to a lower critical field line H_{c1}, within which there is perfect bulk diamagnetic screening (see Fig. 4.1). Between H_{c1} and the upper critical field H_{c2} magnetic flux penetrates into the bulk of the superconductor in the form of quantised flux lines. In this conventional picture, throughout the region between H_{c1} and H_{c2}, vortices are arranged in a hexagonal close packed Abrikosov lattice phase. Furthermore it is predicted [6] that the transition from the superconducting phase into the normal state at H_{c2} should be continuous. Physically this reflects the point at

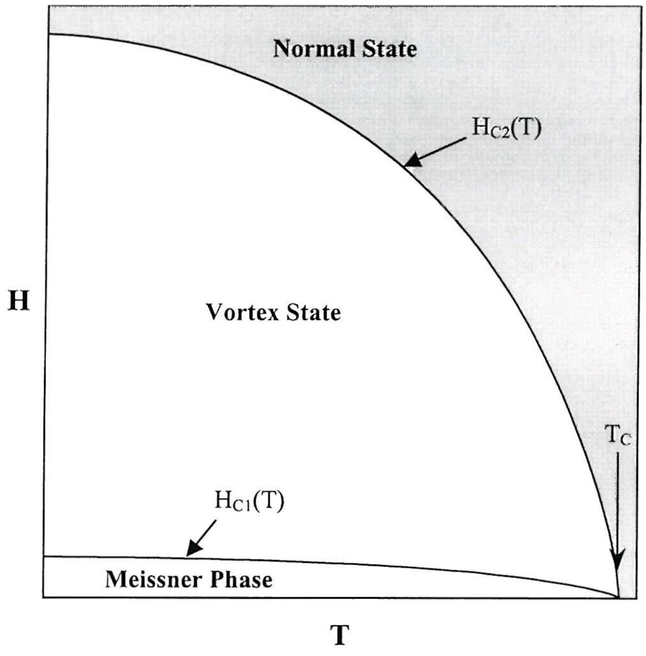

Fig. 4.1 *Traditional picture of the vortex phase diagram for a clean isotropic superconductor.*

which vortex cores start to overlap. Intuitively, however, in addition to the phase lines shown in Fig. 4.1, we would also expect to cross a line within the vortex phase region between H_{c1} and H_{c2}, above which thermal fluctuations are sufficiently large to break up the ideal Abrikosov lattice i.e. a type of **melting transition**. Indeed, this turns out to be the case, although in conventional superconductors the melting transition line lies so close the upper critical field line as to be virtually indistinguishable from it [7].

It was Nelson [8] who first predicted that, due to the increased importance of thermal fluctuations, the vortex melting transition should be observable distinct from the upper critical field line in high temperature superconductors. Indeed, Houghton, Pelcovits and Sudbø (**HPS**). [9] subsequently demonstrated that the vortex lattice is in fact much softer than is predicted by a purely local model. As such, in HTS the melting transition is predicted to lie substantially below the upper critical field line. In both Refs. 4 and 5 the shape of the melting line was deduced from within the framework of a conventional semi-quantitative Lindemann analysis. The central assumption of this analysis is that the Abrikosov lattice become unstable to thermal fluctuations, when the mean square amplitude of these thermal fluctuations exceeds a certain critical fraction (c_L) of the lattice spacing. That is to say :

$$\left\langle u(T_m)^2 \right\rangle = c_L{}^2 a_0{}^2 . \tag{4.1}$$

Here, the triangular brackets are taken to denote a thermal average and a_0 represents the vortex spacing within the ideal Abrikosov lattice. For vortex lattice melting in HTS the Lindemann criterion c_L is normally chosen to be between 0.1 and 0.2 and is any case only weakly dependent on the specific material [1]. In a Lindemann analysis, the essential problem is, therefore, to calculate the dependence of $\left\langle u^2 \right\rangle$ on the temperature. Nelson performed this calculation by considering a single vortex within a cage potential due its nearest neighbours, expressing the shear modulus in terms of the curvature of the harmonic confining potential [8]. In this way he arrived at the following expression:

$$\left\langle u^2 \right\rangle = \frac{k_B T}{\sqrt{c_{44} c_{66}}} . \tag{4.2}$$

As usual, c_{44} and c_{66} represent the shear and tilt moduli respectively and k_B is the Boltzmann constant. In their more rigorous analysis, taking into account the full *k*-vector dependences of the elastic moduli, HPS used the form [9]:

$$\left\langle u^2 \right\rangle = k_B T \int_0^{\infty} \frac{\mathrm{d}k_z}{2\pi} \int_0^{\Lambda^2} \frac{\mathrm{d}k_\perp}{2\pi} \left[\frac{1}{c_{66}(k) k_\perp^2 + c_{44}(k) k_z^2} + \frac{1}{[c_L(k) + c_{66}(k)] k_\perp^2 + c_{44}(k) k_z^2} \right] . \tag{4.3}$$

Here the integration is performed over a Brillouin zone in *k*-space of radius Λ. Note that in the case of both equations 4.2 and 4.3 the mean square displacement is proportional to the temperature. The differences arise in terms of the constant of proportionality, reflecting the different ways in which the elastic moduli are calculated. The final result of the HPS calculation is an implicit equation relating the reduced melting field $b_m(t) = B_m(T) / H_{c2}(T)$ to the reduced temperature $t = T / T_c$:

$$\frac{\sqrt{b_m(t)}}{1 - b_m(t)} \frac{t}{\sqrt{1-t}} \left[\frac{4\sqrt{2} - 4}{\sqrt{1 - b_m(T)}} + 1 \right] = \frac{2\pi c_L^2}{\sqrt{Gi}} \equiv \mathrm{K} . \tag{4.4}$$

Here *Gi* represents the Ginzburg number, a measure of the importance of thermal fluctuations (see section 1.5.1 of the Introductory Chapter). It should be noted that Eqn. 4.4 applies only in the case of an isotropic material or in the special case of an anisotropic material with *H* // *c*. A full solution of Eqn. 4.4, substituting in typical parameter values for a specific HTS compound, yields a prediction for the shape of the melting transition line. The form of the curve derived from such analysis is illustrated schematically in Fig. 4.2, overleaf. Here, the parameter values used in constructing the figure correspond to typical values for $YBa_2Cu_3O_{7-\delta}$, namely: $H_{c1}(0)$ =730 G, $H_{c2}(0)$ =230 T, ξ = 16 Å, λ_L = 1400 Å and effective mass anisotropy $\varepsilon = \sqrt{m_{ab} / m_c}$ =1/5.

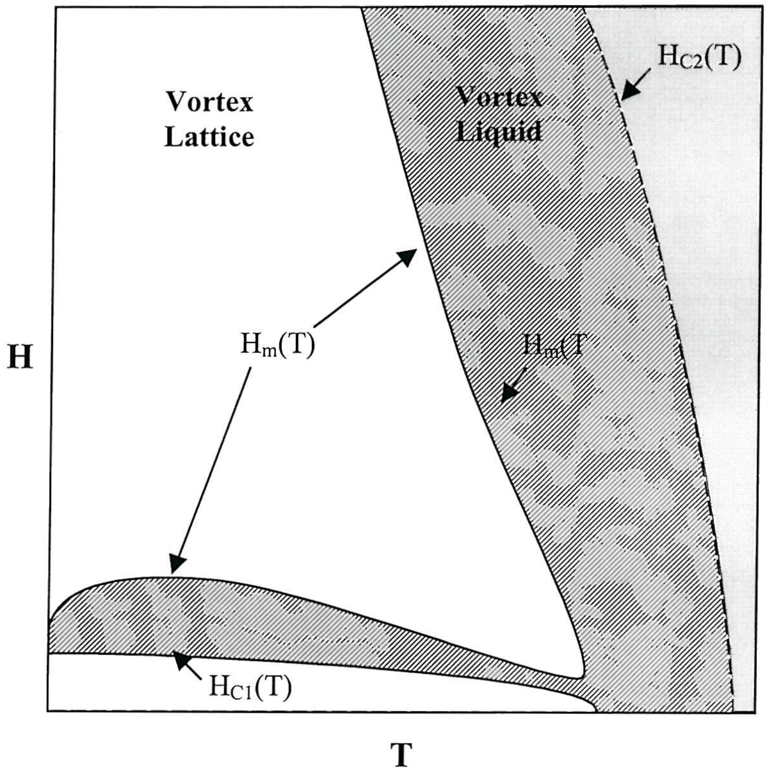

Fig.4.2 *Schematic representation of the phenomenological phase diagram for a clean HTS with the typical parameter values of* $YBa_2Cu_3O_{7-\delta}$. *Note in particular the extensive region of the phase diagram over which the FLL is in the liquid phase. Melting can occur either by increasing thermal fluctuations on increasing temperature or else by reducing magnetic field. [Based on Fig. 2 of Ref. 11]*

The re-entrant melting behaviour in the lower region of the phase diagram can be accounted for in terms of an exponentially vanishing shear modulus at low fields. Recently, evidence of such re-entrant behaviour was provided by Ravikumar *et al.* in the case of the LTS, $NbSe_2$ [10]. In HTS such as $YBa_2Cu_3O_{7-\delta}$ it is still an open question whether or not it will be possible to observe a reentrant melting transition.

Commonly, an approximate form of Eqn. 4.4 is used in order to model experimental result in the temperature region close to T_c. In this region the melting line falls well below the upper critical field (see Fig. 4.2) and we can therefore assume $b_m(t) << 1$. At this limit Eqn. 4.4 can be approximated to :

$$B_m(T) \approx \beta_m \frac{c_L^4}{Gi} H_{c2}(0) \left[1 - \frac{T}{T_c} \right]^\alpha , \tag{4.5}$$

where the power law index $\alpha = 2$ and the numerical factor $\beta_m \approx 5.6$ [11]. In the case of $YBa_2Cu_3O_{7-\delta}$ this simple power law relation is expected to be valid in the regime extending down to a few kelvin below T_c [11]. Further away from T_c , Eqn. 4.4 predicts that the melting line should move closer to the H_{c2} line. From a phenomenological point of view, this amounts to an effective reduction in the power law index α of equation 4.5. Following this motivation, a number of attempts have been made to fit experimental data obtained from $YBa_2Cu_3O_{7-\delta}$ samples to melting lines with more general power law form: $B_m(T) \propto (1 - T/T_c)^\alpha$. In this way a wide range of values for the power law exponent have been obtained, extending over the approximate range $1 < \alpha < 2$ [12]. In fact, this merely serves to illustrate that the attribution of a general power law dependence to the melting line should be regarded as convenient method for describing the data rather than an fundamental physical concept [1].

All of the result described thus far were derived within the framework of a phenomenological Lindemann analysis. At this point it is important to clarify the limitations of this technique. In the first place, the Lindemann analysis cannot tell us anything about the order of the melting transition. It should be mentioned, however, that there is now a range of evidence from calorimetric [13] and magnetisation [14] studies to indicate that in pure single crystals the melting transition is first order. Equally, Lindemann calculations such as those discussed in the preceding section, cannot reveal the nature of the fluctuations which actually lead to melting, e.g. dislocations or disinclinations. Within the conventional Kosterlitz-Thouless theory, melting is supposed to be mediated by unbinding of dislocation pairs [15]. On attempting to apply a similar approach to melting of the 2D vortex system, Ma and Chui obtained evidence of a mechanism for FLL melting involving the proliferation of edge dislocations [16]. They showed that the negative energy contribution of dislocations increases with increasing temperature such that the overall energy of the dislocation vanishes at the melting temperature. More recently Feinberg [17] proposed a phenomenological model for melting of FLL melting based on screening of the elastic shear modulus by mobile or partially pinned dislocations.

Note that thus far we have considered a system free from pinning disorder: the extension of melting theory to systems with disorder will be considered below in Section 4.4.2. Even in the clean limit, to determine the form and order of the melting transition with absolute rigour it would be necessary to find a method of calculating from first principle the point at which the homogeneous shear modulus falls to zero.* Such a calculation has not yet successfully been performed for any 3D system [18].

4.3 Vortex Phases in the Presence of Point Disorder

In the preceding section we considered structure of the phase diagram for an ideal clean material with typical parameters such as those of $YBa_2Cu_3O_{7-\delta}$. From this we arrived at the essential concept of vortex lattice melting. By using an analysis based upon a standard Lindemann criterion, we were able to predict the approximate form of the melting transition line. Questions now arise as to how the vortex solid phase and the melting transition are affected by the sort of pinning disorder present in all real samples. Given that the experiments presented in this thesis were performed on detwinned samples or twinned samples with the field tilted at such an angle as to remove the effect of twin boundary pinning, we will limit the discussion here to the case of point disorder. For samples with significant pinning due to extended defects it is expected that additional phases will arise (see, for example, Ref. 19).

In the preceding discussion of the vortex solid phase we assumed an ideal Abrikosov lattice throughout the vortex solid phase. Even from a purely intuitive point of view it is clear

---

* The short wave-length shear modulus remains non-zero, even in the liquid phase.

that there should some distortion from the ideal configuration in the presence of disorder. Indeed, if the vortex solid did remain an ideal Abrikosov lattice phase, then even in the presence of pinning disorder, we would expect it to remain effectively unpinned: Without any correlation between the vortex and pin distributions the net overall pinning force would average to zero. As a consequence, we would expect the vortex system to be more strongly pinned in the vortex liquid phase than in the vortex solid phase, contrary to experimental observations (see for example Ref 20).

Instead of a straightforward melting line, early observations on HTS indicated the presence of a so called **irreversibility line** [21]. Below this line the system exhibited strongly non-linear *V(I)* curves together with history dependences and irreversibility in the magnetic properties. Moreover, from initial indications it seemed that the transition into the liquid phase at the irreversibility line was second order [22]. This seemed to hint towards the existence of some sort of glassy solid phase in which there are many low-lying metastable states. In the following sections we will review the various theories which have been used to describe the so-called "glassy" vortex solid phases arising in the presence of disorder.

4.3.1 Theory of Collective Pinning: the Larkin-Ovchinnikov Model

Up until the advent of high temperature superconductors it was assumed that there was a unique disordered state of the vortex system in the presence of pinning disorder. As mentioned briefly in Section 1.4.3 of the introduction, within this picture it was thought that the effect of varying disorder was to vary the correlation volumes within this disordered state. It is now believed that this so-called **Larkin-Ovchinnikov (LO)** picture of pinning is only valid as a limiting case of the more complete theory of the vortex state [41]. However, in order to better understand current theories of the disordered vortex state it is useful to review some of the concepts arising out of the LO theory.

The LO model was the first attempt to consider the effect of pinning on a system in the presence of weak random point disorder[†] [23]. LO proposed that the vortex system comprises correlated volumes (V_c) within which the system is short range ordered. The criterion used to define the linear dimension associated with such domains (R_c) was that the relative shifts of the of the FLL across a domain should be less than the action force radius r_f of the pinning sites i.e.:

$$\left\langle [u(R_c)-u(0)]^2 \right\rangle = r_f^2 . \tag{4.6}$$

Regions whose relative shifts exceed r_f can be regarded as responding independently to pinning centres. Thus, when a transport current is applied to system of **Larkin domains**, each domain is expected to displace independently, as a correlated unit. These domains may therefore be considered as large **collective pinned** regions of the vortex solid.

A full elastic theory derivation for the typical dimensions of a Larkin domain is provided within Ref. 24. This derivation is, however, reasonably complicated and an order of magnitude estimate of the various length-scales can be obtained from simple energy considerations [23]. Consider a system with a density of pinning centres $\boldsymbol{n}$ and a typical force $\boldsymbol{f}$ due to individual pinning centre. Given that pinning centres are randomly distributed then the pinning per unit volume force acting within a Larkin domain is given by :

$$f_p = f(nV_c)^{1/2}V_c^{-1} = f(n/V_c)^{1/2} . \tag{4.7}$$

We have already seen that within a domain the relative vortex displacement is of the order of the pinning force action radius r_f. There are many different cases where $r_f \approx \xi_0$, namely [23]: close to H_{c2}; in the case of small defects; and in the case of defects with sharp edges.

Assuming that we are referring to one of these regimes then we can write the free-energy of the Larkin domain as [23]:

[†] By weak disorder we mean the case where each individual pinning centre causes only a weak deformation of the FLL.

$$\delta F = \frac{1}{2}C_{66}\left(\frac{\xi_0}{R_c}\right)^2 + \frac{1}{2}C_{44}\left(\frac{\xi_0}{L_c}\right)^2 - \xi_0 f\left(\frac{n}{V_c}\right)^{1/2} \qquad (4.8),$$

where ξ_0 / R_c and ξ_0 / L_c represent the fractional distortions parallel and perpendicular to the *ab*-plane respectively. On minimisation with respect to R_c and L_c the following expressions for the correlation length scales can be obtained:

$$R_c = \frac{2^{1/2} C_{44}^{1/2} C_{66}^{3/2} \xi_0^2}{nf^2};\; L_c = \frac{2\, C_{44} C_{66} \xi_0^2}{nf^2};\; V_c = L_c R_c^2 = \frac{4C_{44}^2 C_{66}^4 \xi_0^4}{n^3 f^6}. \qquad (4.9)$$

The key point to note here is that the volume of the correlated regions increases with the elastic rigidity of the system, as reflected by the shear and tilt moduli C_{66} and C_{44} respectively. However, the correlation volume decreases strongly (f^{-6}) with the pinning strength.

Using the expression for the correlation volume given by Eqn. 4.9 we are now in a position to obtain an expression for the critical current density. Equating the applied-current Lorentz force to the pinning force, we can write :

$$j_c B = f\left(\frac{n}{V_c}\right)^{1/2} = \frac{n^2 f^4}{2C_{44} C_{66}{}^2 \xi_0^2}. \qquad (4.10)$$

Thus, remarkably, merely by considering the length-scales of the static problem we are able arrive at estimate for a crucial parameter in the dynamic situation, namely the critical current j_c. It should be noted that in spite of the elegance of the LO model, it has a major restriction, in that it is only truly valid at zero temperature.

4.3.2 Theories of Vortex Creep

In general we use the term **creep** to describe a type of motion of the vortex system whereby there is a significant interaction due to pinning. Within the framework of the LO model this would apply at length-scales greater than R_c. It is only recently that a full understanding has emerged of what happens within the so-called flux-creep regimes.

However, an initial attempt to understand this in the context of HTS, was provided within the framework **collective creep model** of Feigel'man *et al.* [25]. The collective creep model was based an earlier theory of Anderson and Kim [26] which had successfully been used for many years to describe the form of current-voltage dependences in the case of conventional superconductors. Here we will briefly consider the Anderson-Kim theory before progressing to the more advanced model of collective creep.

Anderson and Kim considered dynamics in the creep regime in terms of thermally activated hopping of flux bundles between adjacent pinning wells [26] and this theory has subsequently been developed by other authors [28, 29]. Taking into account the motion of bundles in both the forward and reverse directions with respect to the drive, Dew-Hughes was able to write an expression for the net hopping rate as [28]:

$$R_{net} = 2\Omega_0 \exp\left(-\frac{U_0}{k_B T}\right)\sinh\left(\frac{\Delta W}{k_B T}\right). \tag{4.11}$$

Here Ω_0 represent the attempt frequency (typically ~ 10^8 Hz [1]) and U_0 represents the depth of the potential well in zero current. The parameter ΔW represent the effective tilt of potential well due to applied current, and is given by the expression : $\Delta W = JB\delta_x V$ where V is the volume of the unpinned flux-bundle and δ_x represents the distance by which the bundle moves as it jump across the barrier. Using Eqn. 4.11 it is possible to deduce an expression for the E-field arising as a result of the net flux motion:

$$E = R_{net}B\delta_x = 2B\delta_x\Omega_0 \exp\left(\frac{-U_0}{k_B T}\right)\sinh\left(\frac{\Delta W}{k_B T}\right). \tag{4.12}$$

In two limiting cases this can be reexpressed as:

$$\Delta W >> k_B T: \; E = 2B\delta_x\Omega_0 \exp\left(\frac{-U_0}{k_B T}\left(\frac{J_c - J}{J_c}\right)\right), \tag{4.13}$$

$$\Delta W << k_B T: \; E = 2B\delta_x \Omega_0 \left(\frac{JU}{J_c k_B T} \right) \exp\left(\frac{-U_0}{k_B T} \right). \tag{4.14}$$

Equation 4.13 reflects the limit of high current densities or low temperatures conventionally described as the **flux creep regime**. In the vicinity of J_c this leads to a resistivity dependence of the form $\rho \propto \exp(J / J_c)$. A variety of experiments have indicated that this is the relevant regime in the case of low temperature superconductors [27].

In contrast, Eqn. 4.14 reflects the limit of low-current densities or high temperatures, often called the **thermally assisted flux flow (TAFF)** regime. In low temperature superconductors it had always been considered that operating temperatures were sufficiently low for any TAFF resistivity to be negligible. In the context of HTS, however, it appeared that TAFF might be very important, following the observation of thermal depinning over a large temperature interval below T_c [28, 29]. This so-called **giant flux creep** has been associated with reversible behaviour above an **irreversibility line** in the *H(T)* plane [30].

Following these studies, Griessen *et al.* considered in detail the implications of the Anderson-Kim model at the $\Delta W << k_B T$ limit [31]. The main conclusions of this analysis were that the elevated critical temperatures of the HTS imply that $k_B T$ should be comparable to U_0 over a significant proportion of the parameter space. Hence, according to the TAFF model there could be significant thermally activated motion even for very small driving forces ($J << J_c$):

$$\rho_{TAFF} = 2\rho_c \frac{U_0}{k_B T} \exp\left(-\frac{U_0}{k_B T} \right). \tag{4.15}$$

The important point to note here is that Eqn. 4.15 implies non-zero resistivity at all finite temperatures. It was in response to this apparent paradox that the collective creep theory of Feigel'man *et al.* was developed [25]. The **collective creep model** is an elastic theory which considers the activated motion of correlated vortex bundles across potential barriers. The size of these activated flux bundles was assumed to increase with decreasing applied current, again conceptually consistent with the Larkin-Ovchinnikov model. Within the framework of this model rather than energy barriers being fixed, they scaled with the same exponent as the flux bundle size. Based upon such arguments it is possible to arrive at a current density dependent expression for the activation barrier height:

$$U(J) = U_0\left(\frac{J_c}{J}\right)^{\alpha} - U_0 . \tag{4.16}$$

Where α is a scaling exponent. It has been demonstrated theoretically that the scaling exponent increases with decreasing current density (and therefore increasing bundle size) from a limiting value of $\alpha = 1/7$ for single vortex lines to a maximum value $\alpha \sim 7/9$ for vortex bundles [25, 32, 33]. Significantly the collective creep model of Feigel'man *et al.* [25] predicts that $U(J) \to \infty$ as $J \to 0$. It follows that within the vortex solid phase diverging energy barriers should lead to true vanishing linear resistivity even at finite temperatures.

4.3.3 Vortex Glass Theory

In parallel to the work of Feigel'man *et al.*, efforts were being made at the same time to understand the effect of disorder in HTS within the framework of a glassy-model. The concept of a glassiness was well known from spin-glass systems, in which a range of different interactions arise within a dilute solution of magnetic impurities. Due to the structure of such materials spins are constrained to lie on a regular translationally invariant lattice. The glassiness arises due to the positional disorder of the magnetic impurities. This leads to a corresponding random distributions in the coupling terms between adjacent spins. Spin-glasses are characterised a wide range of characteristic behaviour, including relaxation dynamics, irreversibility and metastability [34].

In the **vortex glass** theory, developed by Fisher, Fisher and Huse (**FFH**) [35, 36], it was postulated that the introduction of quenched disorder into the vortex system could give rise to a glassy state in some ways analogous to that observed in spin-glasses. It is a basic assumption of this model that both translational and topological order are completely destroyed by the introduction of pinning disorder. This is sharp contrast to the approach taken within the collective-creep model, in which disorder was considered as acting on line objects within a classical elastic system. Although the two models are based upon fundamentally different assumptions, their main conclusion is the same: both predict a vortex solid phase characterised by diverging energy barriers $U(j)$ at small current densities j.

The essential idea of the vortex glass model was that melting should be regarded as a continuous phase transition between a glassy solid phase and an entangled liquid phase. Within the framework of a critical scaling analysis FFH were able to demonstrate the divergence of correlation length-scale (ξ_g) and relaxation time-scales (τ_g) on approaching the glass transition temperature T_g.

$$\begin{aligned} &(i)\ \xi_g \propto \left|T - T_g\right|^{-\nu} \\ &(ii)\ \tau_g \propto \left|T - T_g\right|^{-z\nu} \end{aligned} \tag{4.17}$$

Here ν and z represent critical scaling exponents. The glassy solid phase was expected to manifest highly nonlinear current voltage dependences, and it was proposed that within the vortex glass the mechanism of dissipation should be via the nucleation of vortex loops. Within the framework of such a model of dissipation it is possible to arrive at an expression for the energy barriers to flux motion:

$$E(j) \propto \exp\left[\left(\frac{-U_c}{k_B T}\right)\left(\frac{j_c}{j}\right)^{\mu}\right] \tag{4.18}$$

Here μ is a scaling exponent, which FFH predicted be less than one for $T < T_g$. Also arising out of the vortex-glass model is a scaling relation for the resistivity within the vortex liquid phase:

$$\rho_l \propto \left|T - T_g\right|^{\nu(z-1)} \tag{4.19}$$

Here $\rho_l = \lim_{j\to 0} \rho(j)$ represents the linear resistivity measured on approaching the glass transition from above. A number of attempts have been made to fit experimental resistivity data to the vortex glass model [22, 37]. In general, in the earlier studies performed on samples with relatively high densities of point defects [22, 37], it was found that there was a reasonable correspondence between the scaling relation and the experimental data across the full experimental range.

However, problems arose when attempts were made to apply this theory to samples with much lower defect densities [38]. In such cases, it is generally found that whereas the resistivity scaled well with Eqn 4.19 at high fields and lower temperatures, in the low field region, scaling broke down. A wealth of evidence has subsequently emerged from thermodynamic measurements to indicate that in this low-field region, the transition is in fact first order [13,14]. These observations seem to hint towards the existence of a distinct and considerably more ordered solid phase at low fields. Thus for samples with relatively low pin-densities, whereas at high fields we can successfully describe the system in terms of "vortex glass" model this description cannot be extended down to low-fields. Indeed, a range of transport measurements on $YBa_2Cu_3O_{7-\delta}$ have indicated that there is a well-defined crossover at a **multicritical point** between a regime at low fields and high temperatures where the melting transition is first order, to a entirely different regime at high fields and low temperatures where the transition is continuous [39]. This crossover into a qualitatively different regime at low fields and high temperatures seems to imply that an entirely different theory is required.

4.3.4 Bragg Glass

A number of recent theoretical investigations have attempted to elucidate the nature of the low-field solid phase [3, 4, 40, 41, 42, 43, 44]. In particular, Giamarchi and Le Doussal (GLeD), have made a number of predictions within the framework of an elastic model entirely free from topological defects [3, 40, 41]. This approach is in contrast to both the vortex-glass [35] and collective creep [25] models, which both allow for some degree of topological disorder. The collective creep theory predicts a power law growth of displacement leading to topological defects over a length scale R_a, whereas the vortex glass theory assumes disorder always favours the presence of dislocations.

GLeD started by questioning the assumption that even weak disorder always leads to the generation of topological defects. They cited in support of this elastic medium hypothesis both the observation of a first order melting transition (as discussed above) and the evidence of large dislocation free regions in decoration experiments at low fields [45]. In a subsequent paper GLeD went on to demonstrate, on the basis of energy arguments, the existence of dislocation free phase at weak disorder [41]. In particular GLeD demonstrated that the wandering exponent ζ of flux lines falls to zero over large length-scales. This is crucial for the existence of a topologically ordered phase, otherwise dislocations would appear spontaneously at arbitrarily small disorder, as was predicted in Refs. 46 and 47. This result, that dislocations are not favoured in the case of weak disorder, has subsequently been corroborated via the refined energy and scaling arguments of D. S. Fisher [43]. Additional support has been provided by both numerical simulations [48] and analytical calculations [44] in a layered geometry.

The essential prediction of the GLeD model was that while disorder produces algebraic growth of displacements over short length scales, periodicity has a strong effect over longer length-scales. This suggests the existence of a vortex solid phase with perfect topological order and nearly perfect translational order i.e. a **quasi-long-range ordered phase**. Since this phase is nearly a perfect lattice it is expected that it should melt via a first order phase transition. However, given that there is some degree of "glassiness" in terms of translational ordering, unlike a perfect Abrikosov lattice, this phase would be expected to interact with the underlying pinning potential. These predictions correspond very closely to the observations for the low-field solid phase. Given that such a phase is expected to manifest Bragg peaks in its diffraction spectrum, GLeD have described it as a **Bragg-glass phase.**

The GLeD findings were based upon model of the vortex system comprising stacks of 2D triangular vortex lattices. The starting point for their calculation is an expression for the total energy of the system:

$$H = \frac{1}{2}\int d^2\boldsymbol{r}dz[(C_{11} - C_{66})(\partial_\alpha u_\alpha)^2 + C_{66}(\partial_\alpha u_\beta)^2 + C_{44}(\partial_z u_\alpha)^2] + \int d^2\boldsymbol{r}dz\, V(\boldsymbol{r},z)\rho(\boldsymbol{r},z), \qquad (4.20)$$

where the former term represents the elastic energy contribution whereas the latter reflects the coupling between the disorder potential $V(\boldsymbol{r},z)$ and the vortex density distribution $\rho(\boldsymbol{r},z)$. Here $\boldsymbol{r}$ represents in the in-plane position whereas z is the coordinate perpendicular to the superconducting planes. In principle this equation could be solved using the full wave-vector dependent expressions of the elastic moduli. However, as we shall see below, in terms of understanding the stability of the elastic phase it is only really necessary to consider nearest neighbour interactions. Certainly order of magnitude estimates of the scales involved can be obtained by using simple constant elastic moduli [3].

In order to describe the structure of the phase diagram, the essential problem is to solve the elastic energy description of Eqn. 4.20 to obtain expressions for the translational and displacement correlation function, $\tilde{B}(r) = \overline{\langle [u(0,0) - u(r,0)]^2 \rangle}$. To study their model GLeD mainly used the Gaussian variational method as originally developed to study elastic manifolds in random media [49]. The validity of this approach was demonstrated using independent renormalization group calculations [41]. One of the most surprising results of the GLeD analysis was the fact that $C_k(\boldsymbol{r})$ decays as a power law at large distances. This suggests the existence of a highly unusual quasi-long-range-ordered state which has the peculiar property of being a glass with many metastable states, whilst at the same time manifesting Bragg-peaks very much like an ideal lattice. Note that this so-called Bragg glass is a much more special case than the ***hexatic phase*** often referred to in the literature (see for example Ref. 45) which merely reflects the absence of topological defects.

To determine the region of stability of the topologically perfect Bragg phase GLeD assumed that the elasticity would be destroyed when the displacement of nearest neighbour vortices became of the order of the lattice spacing. Therefore using a modified Lindemann criterion the stability of the Bragg phase can be determined according to :

$$\tilde{B}(r=a)=\overline{\left\langle [u(0,0)-u(a,0)]^2 \right\rangle}=c_L^2a^2\,. \tag{4.21}$$

Here the implicit assumption is made that the Lindemann constant c_L is independent of the field. Eqn. 4.21 reflects the combined displacement due to both disorder and thermal fluctuations and these two contributions can be conveniently separated :

$$\tilde{B}(r=a)\approx 2\left\langle u^2 \right\rangle_T + B_{dis}(r=a) \tag{4.22}$$

It follows from Eqns. 4.21 and 4.22 that the crossover into the Bragg-glass phase should be pushed downwards by increasing point disorder. Furthermore Eqn. 4.22 demonstrates that there are two ways in which the topological ordering of the Bragg glass phase can be destroyed. On increasing temperature thermal fluctuations increase such that a point is reached where the translational order is broken. In this case a melting transition occurs which is analagous to the vortex-lattice to vortex-liquid transition of the pure system (see Section 4.2). Alternatively, on increasing the magnetic field, disorder induced displacements increase (this argument will be re-examined in Section 4.4.1). As such, a point will be reached where the system becomes sufficiently disordered that, even at short length scales, ordering will be lost.

Thus, these observation predict the existence of two transition lines, a vortex solid-to-liquid melting and a vortex solid-to-solid entanglement line, delimiting the region of phase space over which the Bragg-glass phase is expected to be stable. The full implications in terms of the phase diagram will be considered in the following sections.

4.4 Equilibrium Phases Diagram in the Presence of Weak Random Point Disorder

Increasingly, over recent years, a consensus has emerged from theoretical studies as to the structure of the vortex phase diagram in the presence of weak random point disorder [40-44]. As outlined in the discussion of the preceding sections it now seems that there are two distinct phases of the vortex solid namely: a quasi-long-range ordered Bragg glass phase at low-fields (see Section 4.3.4) and a topologically disordered glassy phase at high fields (Section 4.3.3). A variety of experimental support for this basic idea has been provided by neutron diffraction studies [50], magnetisation experiments [51, 52] on $Bi_2Sr_2CaCu_2O_8$, as well as more recently from magnetisation studies on $YBa_2Cu_3O_{7-\delta}$ [53, 54]. Additional support for the notion of two distinct phases of the vortex solid has been provided by numerical studies [48]. From these various theoretical, experimental and numerical findings an understanding of the structure of the phase-diagram has emerged, as schematically illustrated in Fig. 4.3 .

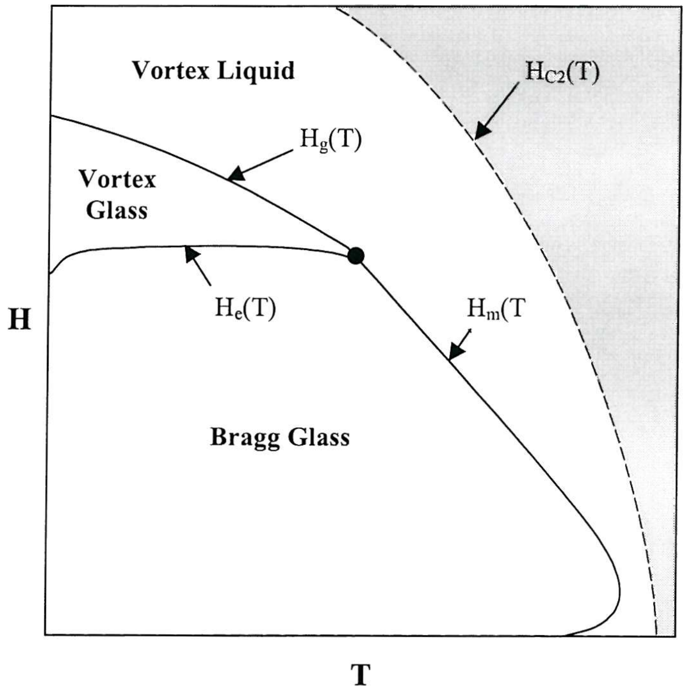

Fig. 4.3 *Schematic representation of the theoretically predicted vortex phase diagram in the presence of weak random point disorder. Indicated in this diagram are the distinct phases expected, together with the transition lines between them.*

From this diagram three phase-transition lines can be identified, namely :

(i) The lattice melting line, $H_m(T)$, between the quasi-long-rang-ordered Bragg-glass phase and the vortex liquid;

(ii) The glass melting line, $H_g(T)$ between the topologically disordered "vortex-glass" phase and the vortex liquid;

(iii) The vortex-solid entanglement line $H_e(T)$ between the Bragg-glass and vortex glass phases.

A number of theoretical studies have attempted to elucidate the position of the transition lines, on the basis of Lindemann criteria, generalised to the case of systems with disorder [3, 44, 55]. A further important question relates to the order of the phase transitions. Although this cannot be confirmed within the framework of the Lindemann models, it is now believed that whereas the lattice melting transition [$H_m(T)$] is first order, the vortex glass transition [$H_g(T)$] is second order [41, 55]. Indeed, there is a wide range of experimental data to support this supposition [12-14, 20]. The situation is less clear in the case of the entanglement transition. From purely qualitative arguments it has been proposed that this transition may be second order [3, 4]. However, recent magnetisation measurement by Kokkaliaris *et al.* provided evidence of history dependences in the vicinity of the entanglement transition of $YBa_2Cu_3O_{7-\delta}$, of a type typically observed in the vicinity of first order phase transitions [54]. Furthermore, magnetisation measurements on $Bi_2Sr_2CaCu_2O_8$ [52] provided indications that the entanglement transition is in fact very sharp: a feature normally only associated with first order transitions.

Many basic methods and results of the various Lindemann criterion models are essentially the same [3-44]. However, here we will consider in more detail the model of Nelson and Vinokur [55]. We have chosen this particular for two reasons. Firstly it is the only model thus far to consider the effect on the phase diagram of the anisotropy intrinsic to the layered HTS materials. Secondly it provides a useful framework for visualising the essential physics of the various transitions within the phase diagram. Nelson and Vinokur modelled vortex-interactions in terms of a mean-field-like model in which any given vortex-line is constrained within a "cage-potential" with respect to its nearest neighbours. Lindemann criteria were described in terms of the characteristic energies of the various transitions. Vortex lattice melting was supposed to occur when $T = E_{el}$: that is to say when the energy of thermal fluctuations becomes equal to the elastic energy barriers maintaining vortices in their equilibrium positions. Following similar arguments, vortex glass melting should occur when the characteristic pinning energy matches the energy of thermal fluctuations, i.e. $T = E_{pin}$. At low temperatures the influence of quenched disorder increases with increasing field. Thus at this limit we expect a transition from the quasi long-range ordered Bragg-glass phase into a highly entangled and topologically disordered vortex solid where $E_{pin} = E_{el}$. In the following sections, we will consider each of the three main transitions in turn within the framework of a generalised Lindemann analysis.

4.4.1 Solid Entanglement Transition

Against a background of random point disorder at low temperatures vortices follow an optimal path determined by a balance between elastic and pinning energies. The mean-square transverse displacement of points along such line, separated by a lateral distance L, provides a useful characteristic measure of ***roughness*** for the vortex lines [55]:

$$u(L) = \overline{\left\langle \left[\boldsymbol{u}(L) - \boldsymbol{u}(0) \right]^2 \right\rangle} \approx \xi (L / L_c)^{\zeta} . \tag{4.23}$$

The latter approximate equality in this expression refers to the limit of large L. Here the roughness exponent $\zeta = 3/5$; L_c is the Larkin correlation length along the direction of the vortex lines (representing the typical length of a coherently pinned vortex segment); and ξ is the coherence length.

Considering a vortex line within a cage-potential of transverse size a_0 it is possible to arrive at an expression for the characteristic elastic energy of the vortex [55]:

$$E_{el} = \varepsilon\varepsilon_0 u^2 / a_0, \tag{4.24}$$

where ε is the anisotropy parameter and $\varepsilon_0 = \phi_0^2/(4\pi\lambda_L^2)$. We identify the entanglement transition as the point at which the typical vortex displacement becomes of the order of the lattice parameter. Hence the value of the elastic energy at the entanglement transition can be established according to the Lindemann criterion $u^2 = c_L^2 a_0^2$ as:

$$E_{el} = \varepsilon\varepsilon_0 c_L^2 a_0 \tag{4.25}$$

Minimisation of the full elastic energy expression with respect to L provides us with a measure of the characteristic size of the longitudinal fluctuations[55]:

$$L_0 = \sqrt{\varepsilon^2 \varepsilon_0 u^2 / a_0} \approx 2\varepsilon a_0 \tag{4.26}$$

That is to say for $L >> L_0$ local distortions of the vortex line become independent. In this sense L_0 can be regarded as a longitudinal dimension of the confining cage potential.

Ertas and Nelson [56] predicted that in the case of moderately anisotropic HTS such as $YBa_2Cu_3O_{7-\delta}$, the transverse correlation length should lie within the range $d < L_c < L_0$ (where d is the interlayer spacing). In this case the characteristic pinning energy can be expressed as:

$$E_{pin} = T_{dp}(L_0 / L_c)^{2\zeta-1} \approx T_{dp}(2\varepsilon a_0 / L_c)^{2\zeta-1}, \tag{4.27}$$

where T_{dp} is the depinning temperature for a single vortex line.

On comparing expression 4.25 and 4.27 it can be seen that whereas the elastic energy varies with the magnetic flux density as $E_{el} \propto a_0 \propto B^{-1/2}$ the pinning energy varies as $E_{pin} \propto a_0^{2\zeta-1} \propto B^{-(2\zeta-1)/2}$. Since ζ=3/5 this implies that the pinning energy decays much less rapidly with magnetic fields, as $B^{-1/10}$. Thus this implies that at low fields elastic forces dominate, providing support for the notion of a quasi long-range ordered Bragg-glass phase at this limit. In contrast, at high fields, the pinning energy dominates, hence the system is found to be in a highly disordered state. Simply by comparing elastic and pinning energy equations

4.25 and 4.27 it is now possible to derive an expression for the solid entanglement transition field :

$$B_e(T) = B_0\left(\frac{T_0}{T_{dp}}\right)^{\frac{2\zeta}{1-\zeta}} \quad \text{where } s < L_c < L_0 . \tag{4.28}$$

Here $B_0 = c_L^2\phi_0/\xi^2$ and $T_0 = c_L\varepsilon\varepsilon_0\xi/2$. Given that at low temperatures $E_{\text{pin}}(T)$ is approximately constant, this results in a flat $B_e(T)$ dependence in the low temperature regime. With increasing temperature, however, E_{pin} is expected to decrease therefore an upturn is expected in the transition line at intermediate temperatures. This prediction is consistent with the form observed for the entanglement transition line, deduced from magnetisation experiments on both $YBa_2Cu_3O_{7-\delta}$ [53] and $Bi_2Sr_2CaCu_2O_8$ [52]. A further important prediction arising out of equation 4.33 is that $B_e \propto \varepsilon^2$ and should therefore strongly decrease with crystal anisotropy. This has been confirmed by observations on $Bi_2Sr_2CaCu_2O_8$ crystals with a range of anisotropies [52, 57].

4.4.2 Lattice and Glass Melting Transitions

It is a relatively straightforward matter to describe the melting transition at high temperatures and low-fields. Within this regime disorder-induced displacements are negligible on the level of the nearest neighbours, hence thermal fluctuations dominate. At this limit, using a standard Lindemann criterion, it is relatively easy matter to recover a field-dependence analogous to the conventional melting line for a pure system by setting $E_{\text{el}} = T$ [55]:

$$B_m(T) \approx \frac{\phi_0\varepsilon^2\varepsilon_0^2}{T^2} \tag{4.29}$$

If we assume that the effect of disorder-induced and thermally-induced fluctuations can be summed directly, then at any given field, the lattice melting transition in the presence of disorder should occur at a lower temperature than in the clean limit. It follows that the effect of increased pinning disorder should be to push the melting line down to slightly lower temperatures [3, 4]. This is in agreement with transport studies on untwinned $YBa_2Cu_3O_{7-\delta}$ single crystals which have observed systematic slight suppression of the first order melting line following both electron-irradiation [58] and reduction in oxygen doping [59].

In addition to the effect of varying the inherent disorder, following the arguments outlined in the preceding section it is expected that the effective disorder should increase with increasing magnetic field. Hence, just as there a transition line between a quasi long-range ordered Bragg glass and a disordered glass, there should be a corresponding point along the melting transition line at which the melting transition changes its fundamental character. This seems to correspond closely to the so called multicritical point T_{cp} observed in transport measurements [39], at which the melting transition crosses over from being first to being second order. From qualitative arguments T_{cp} should correspond to the point at which the $H_{\mathrm{m}}(T)$, $H_{\mathrm{e}}(T)$ and $H_{\mathrm{g}}(T)$ lines meet [4]. At present, however, a rigorous description of the transition lines in the vicinity of T_{cp} is not available. Further to this, from the experimental point of view there is a problem in determining the crossover point between the Bragg-glass and lattice-melting transitions. Whereas the melting transition is typically deduced from transport measurements, the Bragg-glass line is normally obtained from magnetisation measurements. Due to experimental limitations, there is typically no overlap in the windows of accessibility of the two techniques in the vicinity of the Bragg glass transition (see Section 3.21). Thus, studies which have attempted to compare transport and magnetisation measurements in the vicinity of the critical point were not able to link the entanglement transition line directly to the meeting point of the two melting transition lines [52, 53].

References

[1] G. Blatter, M.V. Feigel'man, V.B. Geshkenbein, A.J. Larkin and V.M. Vinokur, Rev. Mod. Phys, **66** (1994) 1125.
[2] E. H. Brandt, Rep. Prog. Mod. Phys. **58** (1995) 1465-1594.
[3] T. Giamarchi and P. Le Doussal, Phys. Rev. B **55** (1997) 6577
[4] V. M. Vinokur, B. Khaykovich, E. Zeldov, M. Konczykowski, R. A. Doyle and P. H. Kes, Physica C **295** (1998) 209.
[5] R. A. Doyle, IRC (Cambridge) Research Review (1998) p 142.
[6] A. A. Abrikosov, Zh. Eksperim. I Teor. Fiz. **32**, 1442 (1957); Sov. Phys. JETP **5** 1174 (1957).
[7] E. Brezin, D. R. Nelson and A. Thiaville, Phys. Rev. B **31** (1985) 7124.
[8] D. R. Nelson, Phys. Rev. Lett. **60** (1988) 1973; D. R. Nelson, J. Stat Phys. **57** (1989) 511.
[9] A. Houghton, R.A. Pelcovits and A. Sudbo, Phys. Rev. B., **40** (1989) 6763.
[10] G. Ravikumar *et al.*, Physica C **276C** (1997) 9.
[11] G. Blatter, B. I. Ivlev, Phys. Rev. B **50** (1994) 10272.
[12] D. E. Farrel, J. P. Rice and D. M. Ginsberg, Phys. Rev. Lett. **67** (1991) 1165; L. Krusin-Elbaum, L. L. Civale, F. Holtzberg, A. P. Malozemoff and C. Field, Phys. Rev. Lett. **67** (1991) 3156; A. Schilling, H. R. Ott and T. Wolf, Phys. Rev. B **46** (1992) 14253; H. Safar, P. L. Gammel, D. A. Huse, D. J. Bishop, W. C. Lee and D. M. Ginsberg, Phys. Rev. Lett. **70** (1993) 3800; W.K. Kwok, S. Fleshler, U. Welp, V.M. Vinokur, J. Downey, and G.W. Crabtree, Phys. Rev. Lett., **69** (1992) 3370; W.K. Kwok, J. Fendrich, U. Welp, S. Fleshler, J. Downey, and G.W. Crabtree, Phys. Rev. Lett., **72**, (1994) 1088.
[13] A. Schilling, R. A. Fisher, N. E. Phillips, U. Welp, D. Dasgupta, W. K. Kwok and G. W. Crabtree, Nature (London) **382** (1996) 791; M. Roulin, A. Junod, K. Q. Wang, E. Junod and J. Miller J. Low Temp. Phys. **105** (1995) 1099.
[14] T. Nishizaki, Y. Onodera, N. Kobayashi, H. Asaoka and H. Takei Phys. Rev. B **53** (1996) 82; R. Liang, D. A. Bonn and W. N. Hardy, Phys. Rev. Lett. **76** (1996) 835; U. Welp, J. A. Fendrich, W. K. Kwok, G. W. Crabtree and B. W. Veal, *ibid.* **76** (1996) 4809.
[15] J. M. Kosterlitz and D. J. Thouless, J. Phys. C **6** (1973) 1181.
[16] H. Ma and S. T. Chui, Phys. Rev. Lett. **67** (1991) 505.
[17] D. Feinberg 1998 Condmat preprint (Condmat 9805080 v2).
[18] L. F. Cohen and H. J. Jensen, Rep. Prog. Phys. **60** (1997) 1581.
[19] L. N. Bulaevskii, M. P. Maley and V. M. Vinokur, Phys. Rev. B **57** (1998) R5626.
[20] H. Safar, P. L. Gammel, D. A. Huse, D. J. Bishop, W. C. Lee, J. Giapintzakis and D. M. Ginsberg, Phys. Rev. Lett. **69**, 824 (1992); **70**, 3800 (1993); W.K. Kwok, S. Flesher, U. Welp, V.M. Vinokur, J. Downey, G.W. Crabtree and M.M. Miller, Phys. Rev. Lett. **69**, 3370 (1992); W.K. Kwok, J. Fendrich, U. Welp, S.Fleshler, J. Downey and G.W. Crabtree, Phys. Rev. Lett. **72**, 1088 (1994); **72**, 1092 (1994); M. Charalambous, J. Chassy, P. Lejay and V. Vinokur, Phys. Rev. Lett. **71**, 436 (1993); W. Jiang, N-C. Yeh, D. S. Reed, U. Kriplani and F. Holtzberg, Phys. Rev. Lett. **74**, 1438 (1995).
[21] A. P. Malozemoff, T. K. Worthington, Y. Yeshurun, F. Holtzberg and P. H. Kes, Phys. Rev. B **38** (1988) 7203.
[22] R. H. Koch, V. Foglietti, W. J. Gallagher, G. Koren, A. Gupta and M. P. A. Fisher, Phys. Rev. Lett. **63** (1989) 1511.
[23] A. I. Larkin, Yu. U. Ovchinnikov, J. Low Temp. Phys.**34** (1979) 409.
[24] A. I. Larkin, Zh. Eksp. Teor. Fiz. **58** (1970) 1466.

---

[25] M. Feigel'man, V. Geshkenbein, A. Larkin and V. Vinokur, Phys. Rev. Lett. **63** (1989) 2303; M. Feigel'man and V .Vinokur, Phys. Rev. B **41** (1990) 8986; M. V. Feigel'man, V .B. Geshkenbein, A. I. Larkin and V. M. Vinokur, Physica C **167**(1990) 177; V. Vinokur, P. H. Kes and A. E. Koshelev, Physica C **168** (1990)29.
[26] P. W. Anderson, Phys. Rev. Lett. **9** (1962) 309; P. W. Anderson and Y. B. Kim, Rev. Mod. Phys. **36** (1964) 39.
[27] M. R. Beasley, R. Labusch and W. W. Webb, Phys. Rev. **181** (1969) 682; C. Rossel, E. Sandvold, M. Sergent, R. Chevrel and M. Potel, Physica C **165** (1990) 233; P. Berghuis and P. H. Kes, Physica B **165-166** (1990) 1169; M. Suenage, A. K. Gosh, Y. Xu and D. O. Welsh, Phys. Rev. Lett. **66**(1991) 1777.
[28] D. Dew-Hughes, Cryogenics **28** (1988) 674
[29] Y. Yeshurun and A. P. Malozemoff, Phys. Rev. Lett. **60** (1988) 2202; P. H. Kes, J. Aarts, J. van den Berg, C. J. van der Beek and J. A. Mydosh, Supercond. Sci. and Technol. **1** (1989) 242.
[30] J. Yazyi, A. Arribere, C Duran, F de la Cruz, D. B. Mitzi and A. Kapultnik, Physica C **184**(1991) 254; A. Schilling, H. R. Ott and T. Wolf, Phys. Rev. B **46** (1992) 14253; A Schilling, R. Jin, J. D. Guo, and H. R. Ott, Phys. Rev. Lett. **71** (1993) 1899.J. Deak, M. McElfresh, J. R. Clem, Zh. Hao, M. Konzczykowski, R. Muenchausen, S. Foltyn and R. Dye, Phys. Rev. B **49** (1994) 6270.
[31] R. P. Griessen, Physica C, **172** (1991) 441.
[32] T. Natterman, Phys. Rev. Lett. **20** (1989) 2454.
[33] K. H. Fischer and T. Natterman, Phys. Rev. B **43**(1991) 10,372.
[34] J. A. Mydosh, Spin Glasses: An Experimental Introduction (Taylor and Francis, London, 1993)
[35] M. P. A. Fisher, Phys. Rev. Lett. **62** (1989) 1415.
[36] D. S. Fisher, M. P. A. Fisher and D. A. Huse, Phys. Rev. B **43**(1991) 130.
[37] P. L. Gammel, L. F. Schneemeyer, J. V. Waszczakand and D. J. Bishop, Phys. Rev. Lett. **61** (1988) 1666
[38] W. K. Kwok, J. Fendrich, S. Fleschler, U. Welp, J. Downey and G.W. Crabtree, Phys. Rev. Lett. **72** (1994) 1092-1095; J. A. Fendrich, W. K. Kwok, J. Giapintzakis, C. J. van der Beek, V. M. Vinokur, S. Fleschler, U. Welp, H. K. Viswanathan and G. W. Crabtree, Phys. Rev. Lett. **74** (1995) 1210-1213.
[39] See for example, H. Safar, P. L. Gammel, D. A. Huse, D. J. Bishop, W. C. Lee and D. M. Ginsberg, Phys. Rev. Lett. **70** (1993) 3800.
[40] T. Giamarchi and P. Le Doussal, Phys. Rev. Lett **72** (1994) 1530.
[41] T. Giamarchi and P. Le Doussal, Phys. Rev. B **52** (1995) 1242.
[42] Y. Y. Goldschmidt, Phys. Rev. B **56** (1997) 2800.
[43] D .S. Fisher, Phys. Rev. Lett. **78** (1997) 1964.
[44] J. Kierfeld, T. Natterman, and T. Hwa, Phys. Rev. B **55** (1997) 626.
[45] D. Grier, C. A. Murray, C. A. Bolle, P. L. Gammel, D. J. Bishop, D. B. Mitzi and A.Kapiltulnik, Phys. Rev. Lett. **66** (1991) 2270.
[46] E. Chudnovsky, Phys. Rev. Lett. **65** (1990) 3060.
[47] J. P. Bouchard, M. Mezard and J. Yedidia, Phys. Rev. Lett. **67** (1991) 3840; Phys. Rev. B **46** (1992) 14,686.
[48] M. J. P. Gingras, and D. A. Huse, Phys. Rev. B **53** (1996) 15,193; S. Ryu, A. Kapitulnik and S. Doniach, Phys. Rev. Lett. **77** (1996) 2300.
[49] M. Mezard and G. Parisi, J. Phys. I (France) **4** (1991) 809.

---

[50] R. Cubitt, E. M. Forgan, G. Yang, S. L. Paul, H. A. Moon, M. Yethiraj, P. H. Kes, T. W. Li, A. A. Menovsky, Z. Tarnawski and K. Mortensen, Nature **365** (1993) 407
[51] N. Chukimoto, M. Konczykowski, N. Motohira, K. Kishio and K. Kitazawa, Physica C **185-189** (1991) 2201; N. Chukimoto, M. Konczykowski, N. Motohira and A. P. Malozemoff, Phys. Rev. Lett. **69** (1992) 1260; B. Khaykovich, M. Konczykowski, E. Zeldov, R. A. Doyle, D. Majer, P. H. Kes and T. W. Li, Phys. Rev. B **56** (1997) R517.
[52] B. Khaykovich, E. Zeldov, D. Majer, T. W. Li, P. H. Kes and M. Konczykowski, Phys. Rev. Lett. **76** (1996) 2555.
[53] K. Deligiannis, P. A. J. de Groot, M. Oussena, S. Pinfold, R. Langan, R. Gagnon and L. Taillefer, Phys. Rev. Lett. **79** (1997) 2121
[54] S. Kokkaliaris, P. A. J. de Groot, S.N. Gordeev, A. A. Zhukov, R. Gagnon and L. Taillefer, Phys. Rev. Lett. **82** (1999) 5116-5119.
[55] D. R. Nelson and V. Vinokur, Phys. Rev. B **48** (1993) 13060; A. I. Larkin and V. M. Vinokur, Phys. Rev. Lett. **75** (1995) 4666.
[56] D. Ertas and D. R. Nelson, Physica C **272** (1996) 79.
[57] T. Hanguri, T. Tsuboi, A Maeda, T. Nishizaki, N. Kobayashi, Y. Kotaka, J, Shinoyama and K. Kishio, Physica C **256**(1995) 111.
[58]J. A. Fendrich, W. K. Kwok, J. Giapintzakis, C. J. van der Beek, V. M. Vinokur, S. Fleshler, U. Welp, H. K. Viswanathan, and G. W. Crabtree, Phys. Rev. Lett. **74** (1995) 1210.
[59] R. M. Langan, S. N. Gordeev, P. A. J. de Groot, A. G. M. Jansen, R. Gagnon and L. Taillefer, Phys. Rev. B **58** (1998) 14548.

CHAPTER 5. THEORIES OF VORTEX DYNAMICS

5.1 Introduction

In the preceding Chapter we saw how the static or equilibrium properties of the vortex system vary across the different regions of the *H(T)* phase diagram. The key question to now ask, is how this can be related to the results of transport experiments in which the dynamic response of the system is probed by applying an external Lorentz force? In fact, it is crucial to recognise that the dynamic response of the vortex system cannot simply be regarded as an extension of the equilibrium regime [23]. Indeed, there are a number of effects such as drive-induced anisotropy and non-linearities due to interaction of the driven system with disorder which have no direct analogue in the equilibrium regime. It is important to realise, that for any given thermodynamic phase of the system there are a number of different dynamic phases. The elucidation of the detailed nature of these phases and their relation to the underlying thermodynamic and pinning conditions is a highly complex problem. Indeed, whereas increasing consensus is now being reached on the equilibrium phase-diagram, there are still very many open questions in relation to the detailed nature of driven vortex phases.

Vortex dynamic responses are fundamentally different in the vortex liquid and solid states. Since the work of this thesis is predominantly concerned with dynamic responses within the vortex solid regime (see Section 5.3), in this chapter we will mainly focus on this area. However, in section 5.2 we will briefly overview some of the important physics of the dynamic vortex liquid state.

5.2 Vortex Liquid Dynamics

Above the melting transition the dynamics of the vortex system are characterised by linearity and reversibility. In transport measurements, this manifests itself in terms of reproducible ohmic responses. It follows that the influence of pinning on the vortex liquid state must be relatively weak. Indeed, it was supposed until relatively recently that the vortex liquid phase was, in all cases, effectively unpinned. Recent studies, however, have provided evidence of pinning induced viscosity in the vortex liquid state. In the following sections we will consider the physics of both pinned and unpinned vortex liquid states.

5.2.1 Unpinned Liquid

Dynamic responses within the vortex liquid regime are characterised by linearity and reversibility, reflecting the mobility of vortices in the liquid state. In the complete absence of pinning such vortex liquid dynamics can be described within the framework of the Bardeen-Stephen flux flow behaviour as [1]:

$$\frac{\rho(T)}{\rho_n(T)} = \frac{B}{B_{c2}}, \tag{5.1}$$

where ρ is the measured resistivity and ρ_n represents the linear extrapolation of the normal state resistivity down to the measurement temperature. The response in this case should therefore be characterised not only by ohmicity, but also by scaling with the magnetic field B. Indeed, Tinkham argued from the point of view of qualitative arguments that in the presence of weak point-disorder this relation should remain valid [2]. The essential point made by Tinkham was that at elevated temperatures, flux-lines should have no shear rigidity at long-wavelengths, hence following such simplistic arguments no interaction with the pinning should be expected. As we will now see, however, the real situation is substantially more complicated.

Early transport measurements by Worthington *et al.* provided the first evidence of pinning within the vortex liquid regime of $YBa_2Cu_3O_{7-\delta}$ [3]. Moreover, Worthington *et al.* demonstrated that this pinning influence appeared to increase with decreasing temperature on approaching the melting transition from above. Following this early indication, a succession of studies found resistivities substantially lower than the flux flow values even at temperatures close to T_c (see for example Ref. 4). More recent studies, however, have indicated that it is possible to observe pure flux flow behaviour in relatively clean $YBa_2Cu_3O_{7-\delta}$ single crystals [5, 6].

In their recent analysis of the time-dependent Ginzburg-Landau equation Ivlev and Kopnin obtained a more rigorous expression for the resistivity in the regime $B \,\square\, B_{c2}$ [7]:

$$\rho_{ff}(T) = \frac{\rho_n(T)B}{\eta B_{c2}(T)} \tag{5.2}$$

where $\eta = 1.45$ and $\rho_n(T)$ is a linear extrapolation of the normal state resistivity from the high temperature regime. This equation is essentially the same as Eqn. 5.1 as obtained from qualitative considerations by Bardeen and Stephen [8]. The difference is that the Ivlev Kopnin calculation provides a value for the numerical factor η. Using a type of $\rho(T,B)$ scaling analysis based upon Eqn. 5.2, Langan *et al.* were able to determine the limits of the flux flow regime [5]. In this way they showed that the resistivity dependences exhibit flux flow scaling for the majority of the temperature range above the T_m. Only in the immediate vicinity of T_m was deviation from pure-flux-flow observed. More recently this scaling analysis was extended by Gordeev *et al.* [9] to quantify the development of the pinning contribution at the onset of the freezing transition.

5.2.2 Pinned Liquid

The dynamics of the vortex liquid in the presence of significant pinning disorder are crucially dependent on the relative values of three time scales, namely: pinning time τ_{pin}; thermal time τ_{th} and plastic time τ_{pl} [1, 10]. The first of these parameters, τ_{pin}, represents the typical time taken for a vortex-line to move a distance equal to the effective range of the pinning potential. The second parameter is the characteristic time-scale of thermal-phonon-like fluctuations. The final time-scale τ_{pl} is the characteristic plastic-smoothening time over which spatial inhomogeneity is preserved in the liquid. In a regime where $\tau_{pl} << \tau_{pin}$ the averaging over thermal fluctuations leads to a completely homogeneous structure. This is the case in conventional liquids such as water and is attributable to low-viscosity. In the case of the vortex liquid state of HTS, however, it can be shown that [1]:

$$\frac{\tau_{pin}}{\tau_{th}} \propto \frac{j_0}{j_c} \tag{5.3}$$

where j_0 and j_c are the densities of the depairing and depinning critical currents respectively. However, it is not obvious what value is taken by the plastic smoothening time τ_{pl} in the case of vortex liquid dynamics. Certainly that there is a possibility of significant viscosity arising due to the entanglement of the 2D vortex lines, as originally proposed by Nelson and Seung [11]. Such a **viscous liquid regime** would be expected to be characterised by relaxation times such that $\tau_{pl} > \tau_{pin}$. Indeed the recent scaling analysis of the transport resistivity data by Gordeev *et al.* provided strong evidence for a viscous vortex liquid regime in the case of $YBa_2Cu_3O_{7-\delta}$ [9].

Theory predicts that a viscous vortex liquid should be pinned effectively by random disorder, this pinning arising due to the large characteristic smoothening time of the plastically deformed structure [10]. The liquid nature of a highly viscous system is only expected to manifest itself over time-scales greater than τ_{pl}. Over shorter time-scales it behaves effectively like a solid. At the limit τ_{pl} □ τ_{pin} the system is expected to be highly inhomogeneous and should, therefore, be very effectively pinned. On increasing temperature above the melting transition τ_{pl} is expected to drop rapidly following the relation [1, 10]:

$$\tau_{pl} \propto \tau_{th} \exp(U_{pl} / T) \, , \tag{5.4}$$

where the plastic energy barrier U_{pl} is very large in comparison to T. At a temperature T_{k} where $\tau_{\mathrm{pl}} = \tau_{\mathrm{pin}}$ a crossover from a pinned to an unpinned state is expected to occur. This crossover can also be described as a transition from viscous to a conventional liquid. Below T_{k} the vortex motion should be controlled by the large energy barriers associated with short-wavelength plastic deformations of the vortex system. Indeed, Geshkenbein *et al.* were able to estimate the associated energy barrier as $U_{pl} \sim \varepsilon\varepsilon_0 a_0$, where ε is the anisotropy and ε_0 represents the vortex-line tension [12]. The height of such activation barriers is expected to decrease with increasing temperature following the form $U_{pl} = U_0\left(1 - T/T_c\right)$ and therefore becomes zero at T_{c}.

Blatter *et al.* have considered the effect of disorder on the dynamic properties of a viscous liquid, within the framework of a perturbative analysis [1]. This analysis lead to an expression for the resistivity of the form:

$$\rho_{liq} = \left(1/\rho_{ff} + 1/\rho_{pl}\right)^{-1}. \tag{5.5}$$

Here ρ_{ff} is the conventional flux-flow resistivity and $\rho_{pl} = \exp\left[-U_0\left(1 - T/T_c\right)/T\right]$ is the component of the resistivity arising due to activation across plastic barriers. Recent transport studies on $YBa_2Cu_3O_{7-\delta}$ have revealed an excellent fit to Eqn. 5.5 over a broad resistivity window above T_{m} [5, 9].

The plastic energy at the melting temperature can be used to distinguish between various different models of vortex viscosity. This energy can be expressed in the form $U_{pl}(T_m) = cT_m$, where the value of the constant c is determined by the detailed mechanism of vortex liquid plasticity. If plasticity within the vortex system were due to entanglement, then it follows that activation energy barriers should be determined by the vortex cutting and reconnection energies. Carraro and Fisher have calculated vortex cutting energies for a system consisting of a twisted vortex pair [13]. Their calculations yielded a value for $U_{pl} = 0.8\,\varepsilon\varepsilon_0 a_0$, for $B \approx 5$T. On substituting in a value $T_m = 0.098\,\varepsilon\varepsilon_0 a_0$, obtained from the numerical simulations of Ref. 14, then the result for a twisted-pair can be re-expressed as: $c_{pair} = U_{pl}(T_m)/T_m \approx 8$. A similar calculation by Schönberger *et al.* considered the case of a twisted triplet configuration [15], and from the outputs of their analysis it is possible to deduce a value for the activation constant $c_{triplet} \approx 18$. These values can be compared with values in the approximate range $10.8 < c < 12.8$ derived from our transport resistivity data [9]. Since the values deduced from the numerical simulations represent upper-limit estimates, it seems experimental data are in potential agreement with the twisted triplet model of vortex cutting but not the twisted pair model. Thus the implication is that the twisted-pair is unstable and that the basic entangled configuration within the vortex liquid is more likely to be a twisted-triplet.

5.3 Dynamics of the Vortex Solid

The dynamic response of the vortex solid regime is considerably richer than that of the liquid. Transport studies of the vortex solid regime have revealed a wide range of non-ohmic behaviour, history dependence and criticality contingent not only on the underlying thermodynamic conditions but also on the modulation form and magnitude of the driving force (see also Chapter 8). Indeed, vortex solid dynamics provides just one example of the complicated generic problem, namely that of an interacting system driven against a background of random disorder. This problem is of relevance to a diverse range of physical systems, from charge density waves in disordered conductors [16] to fluids in porous media [17]. In fact, by virtue of the tuneability of the intervortex interaction via changes in the magnetic field, the FLL provides an excellent test environment for answering general questions about the physics of such systems.

In very general terms, the complexity of the vortex solid dynamics, especially in the immediate vicinity of the melting-line, can be attributed to a strong competition between the various characteristic energy scales of the vortex system. A vast range of experimental, numerical and theoretical studies have attempted to elucidate the detailed nature of the various dynamic regimes of the vortex solid. For simplicity, we will restrict our discussion to the case of random point disorder. A number of different studies have attempted to ascertain the influence of extended defects on the dynamics of the driven system, such as randomly distributed columnar defects [18], twin boundaries [19] or periodic pinning centres [20, 21]. These studies will not be considered here, since pinning by point defects represented the most important source of pinning for the samples investigated within this thesis.*

5.3.1 Basic Dynamic Regimes : Plasticity, Elasticity and Criticality

Although the precise structural details of the various dynamic phases remains controversial, it is now becoming increasingly accepted that there are three broad regimes in the dynamics. As illustrated in Fig 5.1 (overleaf) these can be classified as

(i) **Creep regime**: At low driving forces, far below the zero temperature threshold of the system, there is a regime within which the response arises solely due to thermal activation effects. This regime has been described within the collective creep theory of Feigel'man [22].

(ii) **Critical regime**: Generally speaking, in the vicinity of the depinning transition the system response exhibits non-linear behaviour and criticality reflecting strong competition between the pinning and driving forces.

(iii) **Large velocity regime**: At high driving forces, impurities appear as weak barriers that deflect portions of the vortex lines without impeding the overall drift. As such, at this limit the driven vortex system displays a much higher degree of ordering than it does in the vicinity of the depinning transition.

In the following sections we will focus on regimes (ii) and (iii). The Creep regime is discussed elsewhere in Section 4.3.2. Indeed the approach taken in the case of the creep

---

* Although some of the crystals contained twin-planes, the effect of twin boundary pinning was avoided by tilting samples at an angle in excess of the locking angle (see Section … of Chapter 2)

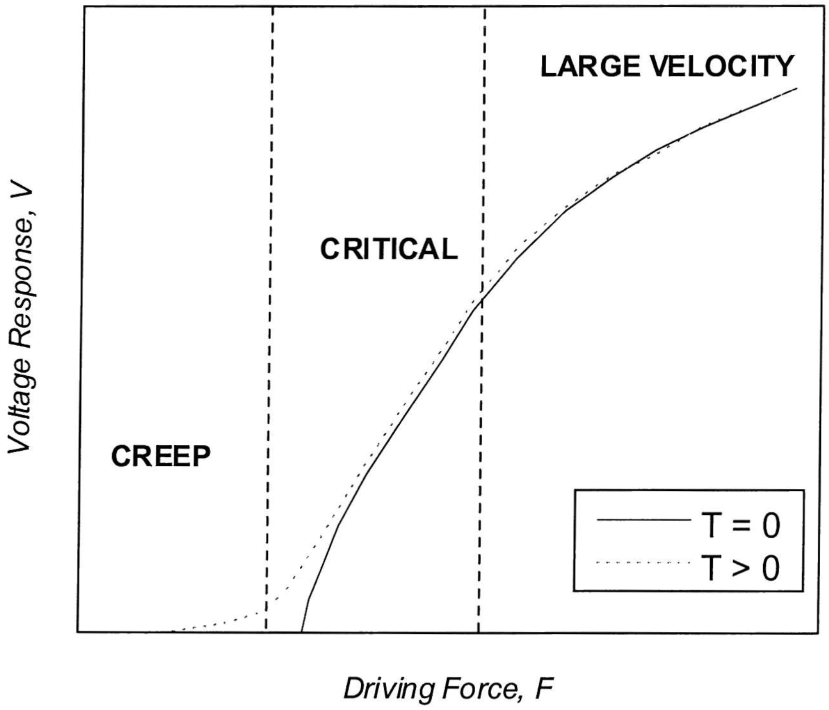

Fig. 5.1 *Generalised driving forve (F) versus voltage response (V) characteristics for the driven vortex system both at zero temperature and in finite temperature. Notice that the system is expected to depin much more abruptly in the zero temperature case (based on Fig. 4 of Ref. 23)*

regime differs fundamentally from that applied in the other two cases: since whereas creep can be regarded as an extension on the static limit the responses in regimes (ii) and (iii) are ***inherently dynamical*** in nature.

Commonly regimes (i) and (ii) are referred to in the literature as the plastic and elastic dynamic regimes respectively. In the context of vortex dynamics an **elastic dynamic regime** is one in which vortices do not change their lattice position within the moving frame. Hence in a purely elastic regime, a given vortex within the system will always retain the same nearest neighbours. From an experimental point of view, this type of coherent motion is expected to give rise to reversible linear responses with low noise levels. In a **plastic dynamic regime**, in contrast, vortices are expected to move through the system with a range of different velocities. This leads to a highly incoherent mode of motion characterised by the presence of mobile dislocations. There are expected to be a variety of signatures of a plastic dynamic regime, ranging from non-linearity and irreversibility, to metastability and history dependence,

In fact these "broad-brush" categorisations should be applied with caution, since in reality the distinction between the various regimes is seldom so sharp. As we will see in Section 5.3.2.2, even in the so-called "high-driving-force elastic-regime" **local plasticity** may remain.[†] Equally, it remains an open question whether as to depinning should always occur via a plastic mechanism such as the opening of channels, or whether in a relatively clean system can depin coherently into an elastic dynamic regime. As a further word of caution, it should be noted that the term "elastic regime" is used somewhat loosely in the literature, to indicate a regime overall elastic in terms of its dynamic response, but may displaying some degree of local plasticity. For consistency we will adhere to the same convention of nomenclature. It should, however, be borne in mind that a regime described as elastic may not be entirely elastic in nature.

In terms of modelling the dynamic vortex response, it is clear that the elastic dynamic regime is by far the simplest case. Indeed, as we will see in the following sections, considerable progress has been towards developing a theoretical understanding of the nature of the elastic dynamic regime at the high driving force limit. In contrast, the dynamics of the vortex system in the critical regime are far less well understood. Such is the complexity of the competing interactions immediately above the depinning threshold, that thus far this situation has only proved tractable to modelling via numerical methods. In Section 5.3.3 we will review some of the main findings arising out of these simulations.

[†] Local plasticity is expected to have a far more subtle effect than the bulk proliferation of dislocations which occurs in a true plastic regime.

5.3.2 Dynamics at the Elastic Limit

At the elastic limit it is assumed that the driven system is entirely free from dislocations. Although in some cases this regime may persist down to the depinning threshold, the general approach is to start from the high velocity expansion. As in the case of the equilibrium phase diagram, strictly speaking such an approach can only really be used as a self consistency test of the limits of the "true elastic" flow regime. Nonetheless, the simplified dislocation free case has proved a very useful starting point for understanding the more general physics of the system at the elastic limit as utilised in a number of recent studies [24, 25, 23].

5.3.2.1 Shaking Effect of Disorder & Dynamic Reordering at the High Driving Force Limit

In a pioneering study, Koshelev and Vinokur (KV) [26] investigated the dynamics of a 2D model vortex system with analytical and numerical techniques. Prior to the KV investigation, studies of vortex dynamics had considered the effect of pinning in terms of statistically calculated overall average [22, 27, 28]. Koshelev and Vinokur (KV) had the insight to recognise that on driving an interacting system against a background of quenched disorder, a fluctuating pinning force component arises, which has implications for the nature of the overall dynamics. KV noted that in the lowest-order perturbation expansion over disorder, these fluctuations resemble a thermal Langevin force. They therefore argued it should be possible to characterise the statistical properties of the pinning force F_p in terms of an ***effective shaking temperature*** T_sh. If we assume that this shaking temperature superimposes directly onto the real temperature then we can write an expression for the effective temperature $T_{eff}(F_{ext}) = T + T_{sh}(F_{ext})$. Given that the effective temperature decreases with increasing driving force then at the limit of large driving forces, $T_{eff} \to T$. Within the driven vortex solid regime ($T < T_\mathrm{m}$) this implies that a threshold force (F_t) will be reached such that $T_{eff}(F_t) = T_m$.

According to these arguments, for forces $F_{ext} < F_\mathrm{t}$ we would expect the driven system to be effectively in a vortex-liquid state. As such, the dynamics of the system at this limit are expected to be disordered and incoherent. On increasing the driving force to above F_t then we would the expect some sort of ***dynamic crystallisation*** transition to occur, into a more coherent dynamic regime. In fact KV were able to demonstrate that the threshold (F_t) for this crossover increases with increasing temperature and diverges on approaching T_m, according to the form:

$$F_t(T) \propto \frac{n_v}{(T_m - T)}, \tag{5.6}$$

where $n_v = B/\Phi_0$ represents the vortex density. This is in contrast to the critical depinning force F_c which is predicted to decrease with increasing temperature, on account of the increased importance of thermal fluctuations. This seems to imply that, for sufficiently weak disorder, F_c should merge with F_t at some finite temperature.

Above the dynamic crystallisation transition KV found that the Thermal Langevin approximation was no longer applicable and that instead the motion was better described within the framework of an elastic medium approximation. At this limit, it was found that effective pinning could be described in terms of a different fictive temperature, with substantially lower values than shaking temperature T_{sh} that applied below T_m. Furthermore, KV demonstrated that the driving force dependences of the respective fictive temperatures did not converge on a common value in the vicinity of F_t. In combination these findings seemed to imply that at transition at F_t should be a first order.

KV went on to perform molecular dynamics simulations of vortices by solving the Langevin equations of motion for the vortices at different values for F_{ext} and T. In these simulations they used a triangulation procedure to calculate the number of vortices with triangulation numbers greater than or lesser than six, thereby characterising the degree of irregularity within the moving system. Starting from high velocities where the system was assumed to be homogeneous they calculated the dependence of the defect concentration and the average velocity on the applied external force at different temperatures. In this way they obtained a dynamic phase diagram of the form depicted in Fig. 5.2, overleaf.

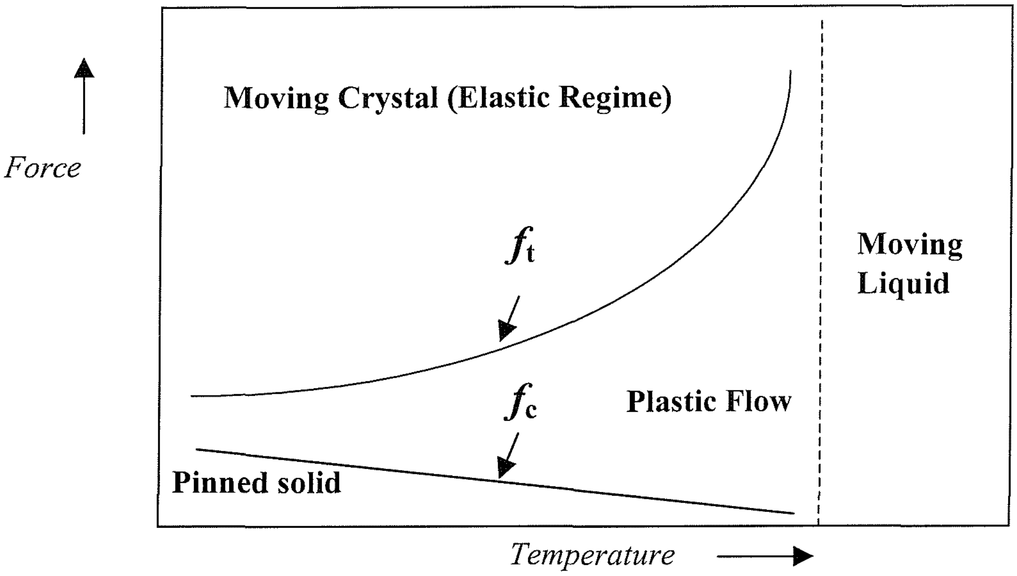

Fig. 5.2 *Applied force versus temperature dynamic phase diagram predicted by Koshelev and Vinokur in Ref. 26 on the basis of numerical simulations.*

Within this figure the threshold force f_t (lower case notation used to distinguish from the analytical result) represents a transition at which the concentration of defects was observed to increase sharply and then saturate. In addition, at low temperatures this sharp transition into a disordered state was found to be accompanied by an increase in the dynamic frictional force. In the vicinity this reordering transition, hysteresis was observed in both the dynamic friction and the density of defects. This supports the analytical prediction that the dynamic reordering transition should be first order.

One of the first papers to follow on from the dynamic melting idea of Koshelev and Vinokur, was that of Moon *et al.* [29]. Based on overdamped molecular dynamics simulations at zero temperature, Moon *et al.* developed a dynamic phase diagram very similar in basic structure to that of Koshelev and Vinokur. Moon *et al.* chose to approach the problem by measuring the structure factors $S(\mathbf{k})$ for particular dynamic regimes. In this way they found a sharp transition on increasing driving force between a dynamic phase in which $S(\mathbf{k})$ was characterised by a structureless ring to one in which sharp six-fold Bragg-peaks developed. This provided a clear evidence of a transition from a topologically disordered plastic dynamic-phase into a phase with a high degree of ordering. In the case of weak disorder, Moon *et al.* found no evidence of an intervening plastic flow regime between the pinned and coherently moving dynamic phases. They interpreted this, in the context of then recent findings of Giamarchi and Le Doussal on the static system [30], as a transition directly from a pinned Bragg-glass into an ordered dynamic phase.

A key prediction of this model of Moon *et al.* was that, even in the case of relatively strong disorder, at the high driving force limit there should exist a dynamic state of the system characterised by a very high degree of ordering as manifested by the appearance of Bragg peaks in its structure factor. This is, of course, a prediction which can be tested in diffraction experiments and one which was confirmed to be relevant in real physical systems by the neutron diffraction studies of Yaron *et al.* on the vortex state of the layered LTS $NbSe_2$ [31]. In transport experiments, the high driving force ordered dynamic phase has been associated with the convergence of the differential resistivity on an asymptotic value [32].

5.3.2.2 Detailed Nature of the High Driving Force Dynamic Phase

It is evident from the combined theoretical and experimental evidence presented thus far, that the dynamic-phase of the system at the high driving force limit should display a considerable degree of ordering. However, the precise nature of this ordering is not clear from these observations. From the analysis of the Burger's vectors Moon *et al.* [29], arrived at a picture of the system at the high driving force limit in terms of a series of elastic domains separated by phase slip lines. This **moving glass** picture of the vortex solid rests on the argument that certain components of the disorder do not average out but rather present a static perturbation to the otherwise coherent motion. In this case vortices are expected to move along static elastic channels separated by lines of dislocations. This moving glass picture also implies the existence of a finite transverse critical current.

A similar picture of the dynamic phases and phase transitions was obtained in the Langevin dynamics simulations of Ryu *et al.* [33] (again on a 2D system). In this case, a dramatic enhancement was observed in the hexatic order parameter at the high driving force limit. Within this dynamic regime, however, translational ordering was observed to be disrupted by a co-moving pattern of neutral disinclination pairs. As such, Ryu *et al.* dubbed this state a **moving hexatic vortex glass**.

Whilst numerical simulations provide a useful framework for visualisation, a full understanding of the high driving force limit dynamic phases should of course arise out of a 3D analytical theory. A major development in the theory of the dynamic vortex solid was made by Giamarchi and Le Doussal (GLeD) in their 1996 paper [34]. GLeD reconsidered the shaking effect of disorder, as originally investigated by Koshelev and Vinokur (KV) [14]. However, unlike KV, GLeD also incorporated the effect of vortex periodicity into their model system. Indeed, it was following this consideration of the effects of periodicity that GLeD made their original prediction of the Bragg-glass phase within the static regime [30]. The main finding of GLeD was that some modes of disorder are not affected by the motion, even at the limit of large velocity. As such they made a prediction than rather that being a perfect lattice, as was suggested by KV calculation, the high driving force phase was some sort of moving glass. This is an agreement with the predictions of the 2D pancake vortex simulations of Moon *et al.* and Ryu *et al.*, as discussed above.

In the investigation of Ref. 34, GLeD focussed on the simplest case of the dynamics, namely that of the fully topologically ordered system at the high driving force limit. GLeD recognised that, in the case where the system is driven along one of its internal directions then, in common with any general moving lattice structure, this should lead to a static non-linear pinning force in the transverse direction. This transverse force component F^{stat} persists even in a fast moving system. By considering the density modes of a system moving along the x-direction it is possible to obtain an equation of motion in terms of the transverse displacement. In the laboratory frame this can be expressed in the following form [34]

$$\eta\partial_t u_y + \eta v \partial_x u_y = c\nabla^2 u_y + F^{stat}[r, u_y(r,t)] + \zeta(r,t), \qquad (5.7)$$

Here η is the coefficient of friction, $\zeta(r,t)$ represents force component due to the thermal noise and c is an isotropic elastic constant (this simplified model does not consider the effect of anisotropy). A key point arising from the result expressed in Eqn. 5.8, is that transverse displacements of the system are to a large extent independent of the structure of the system along the direction of motion. This results in pinning of the transverse displacements into preferred static configurations within the laboratory frame. It follows that the dynamics of the system can be described in terms of rough time-independent channels, along which vortices follow each other in lines[‡]. The structure of the channel configuration is determined by static disorder. This indicates that contrary to the "shaking temperature" concept of Koshelev and Vinokur, the transverse shaking effect on vortices a is, in fact, highly correlated in space and time.

There is of course the possibility of coupling between particles in different channels (Eqn. 5.7 does not assume anything about such coupling). In fact there are two potential scenarios: The first possibility is for there to be full elastic coupling between particles in different channels. This would lead to a fully topologically ordered moving structure, in spite of the roughness of the channels. Such a structure is reminiscent of a static Bragg glass phase, hence GLeD dubbed this potential dynamic phase a **moving Bragg glass**. The alternative scenario is that of decoupling of channels by means of dislocations occurring beyond a certain length-scale R_d. The phase arising in this case has been dubbed the **moving transverse glass**. Note the marked similarity between the moving glass phase observed in the simulations of Moon *et al.* [29] and the moving transverse glass phase. It was not, however, possible from the original GLeD paper to decide which of these two regimes was the relevant or whether they could both occur at different points in the parameter space. These issues were considered in more detail in a subsequent paper by GLeD [23], the results of which will be reviewed in Section 5.4.

Although not mentioned explicitly above, a key point to note is that the GLeD model was based upon the assumption that that the dominant effect on the dynamics arises due to the

---

[‡] Note that this "elastic" channel regime, is distinct from the types of channelling predicted to occur within the plastic dynamic phase (see Section 5.3.3, below).

static (time-independent) component of the displacement field, F_{stat}. This implies that the effect of the time varying component F_{dyn} can be considered to be negligible. In a recent comment by Balents, Marchetti and Radzihovsky [35] (BMR), this basic assumption was called into question. BMR argued that the longitudinal ***dynamic*** force F_x^{dyn} does not in fact average to zero in a coarse grained model. Instead they suggested that this dynamic force component should give rise to effective random static drag force, $f_d(\boldsymbol{r})$, which can be physically understood in terms of spatial variations in the impurity density. These arguments lead to a modified elastic description of the dynamics, as expressed in terms of the following equation of motion (c.f. Equation 5.7) [35]:

$$\eta\partial_t u_\alpha + \eta \boldsymbol{v}.\nabla u_\alpha = c_{11}\partial_\alpha \nabla \boldsymbol{u} + c_{66}\partial_\alpha \nabla^2 u_\alpha + \delta_{\alpha y} F_y^{stat}(u_y) + \delta_{\alpha x} f_d(\boldsymbol{r}) \qquad (5.8)$$

Here thermal fluctuations have been neglected. The solution of this equation of motion yielded an expression for the longitudinal displacement correlator,

$$\tilde{B}_x(\boldsymbol{r}) = <[u_x(\boldsymbol{r}) - u_x(0)]^2> \sim (\Delta_d / c_{66}^2) r^{4-d}, \qquad (5.9)$$

which indicates that in $d < 4$ there should be algebraic growth in displacements along the longitudinal direction. It follows that even within the framework of the elastic description, translational correlations along the x-direction are very short range. BMR therefore argued that the at the high driving force limit, the system arranges into a **moving smectic phase** with vortices moving via a stack of liquid-like channels. In their response to the Balents-Marchetti-Radzihovsky comment [36], Giamarchi and Le Doussal agreed that there was indeed expected to be a u-independent random force $f_d(\boldsymbol{r})$ acting along the direction of motion, but disagreed on its significance. They pointed out the simplified perturbation theory employed by BMR could not be used as proof of the relevance of this force. Instead they pointed to their own renormalisation group calculations, as discussed in some detail in Ref. 23 We will consider some of the finding of Ref. 23 in Section 5.4, below. However, for the time being, it suffices to comment that on the basis of their modified calculations GLeD found, somewhat surprisingly, that $f_d(\boldsymbol{r})$ does not affect the transverse correlator $\tilde{B}_y(\boldsymbol{r})$.

Following on from the work of GLeD, a paper by Spencer and Jensen (SJ) raised further questions about the nature of the high driving force dynamic regime [37]. The findings of Spencer and Jensen were based upon a finite temperature 2D molecular-dynamics simulation of pancake vortices, similar in concept to studies carried out by authors such as Koshelev and Vinokur [26] and Moon *et al.* [29]. However, in contrast to the predictions of previous simulations, SJ found that in the case of their model system, there was no topological ordering at any driving force. The main difference between the SJ method and that used in previous simulations, was that whereas in previous cases the starting point was a perfectly ordered lattice at driving force, SJ initialised their system by relaxing it into a pinning potential. Experimentally speaking, this corresponds to field cooling the system in the absence of an applied current. Following such an initialisation procedure, a vortex distribution was generated with a high degree of topological disorder (~50% miscoordination). On ramping up the applied driving force they found a strong peak in the defect density close to the threshold depinning value and thereafter a tendency towards an asymptotic finite value at high driving forces. In the asymptotic regime both the differential resistivity and defect density were found to be independent of the driving force, which implied an elastic dynamic phase. Hence this suggests a **co-moving dynamic regime** in which defects are frozen in within the coherently moving system. This serves to illustrate the fact that a system may behave elastically but still have a substantial degree of topological disorder. Following these results, SJ argued that the observation of topological order in previous simulations [26, 38] was merely an artefact of their original conditions. The final conclusion from the Spencer Jensen paper, was that the high driving force dynamic phase exhibits long-range orientational order but no topological ordering.

5.3.3 Plasticity and Criticality in the Vicinity of the Depinning Threshold

In the preceding section we saw that the high driving force phase of the driven vortex system is expected to display a some degree of ordering, although the precise nature of this ordering remains controversial. In the vicinity of the depinning transition, due to strong competition between drive and disorder, the situation is expected to be considerably more complicated. On the simplest possible level, the depinning transition can be regarded as the point at which the energy associated with the applied transport current becomes comparable to the characteristic pinning energy E_{pin}. In a real system there is of course an additional component of the response due to thermal activation, this being most important at low temperatures well below the melting transition. In the following section, however, we will be focusing on the dynamic critical behaviour and plasticity at the depinning threshold itself.

5.3.3.1 Notion of Elastic Depinning

The notion of collective pinning of the vortex system and thus, it follows, collective depinning was first examined within the framework of the Larkin-Ovchinnikov (LO) theory [27] (as considered in more detail in Section 4.3.1). Within, the LO approach, the depinning transition was identified as the point at which the applied driving force per unit volume became equal to the pinning force per unit volume of an elastically correlated domain of characteristic volume V_c. The volume of these so called Larkin domains varied to reflect the degree of disorder of the pinned system, hence within the framework of the LO theory a more disordered system would simply manifest a higher degree of fragmentation and hence a higher depinning threshold. This is, of course, a highly simplified representation. Following on from this early work, a number of studies to described the transition in terms of threshold critical phenomena [39, 40, 41]. This development was made by analogy with similar effects occurring in other physical system such as charge density waves [42] or interfaces in porous media [43]. Within the framework of this type of analysis, the depinning response is characterised in terms of divergent length scales and long relaxation times associated with reordering.

An important drawback of the particular threshold critical approach used in Refs 39-41 is that it was based upon a mean-field elasticity theory. Such theories predict that in all cases the system will depin as a single coherently moving elastic medium. No allowance is made for the possibility of depinning being accompanied by the formation of topological defects.

As we will see below, there is now a wide range of evidence from both experimental and numerical studies to indicate that, in most cases, when the FLL depins it breaks apart and flows plastically. This does not preclude the possibility of coherent depinning in a relatively clean system. However, it is evident that any theory that does not allow for the presence of topological defects, cannot be used to provide a general description of the threshold depinning phenomena.

5.3.3.2 Dynamic Criticality and Depinning

Increasingly over recent years it has become apparent that in order to understand the depinning of the vortex system, we must think in terms of dynamic critical phenomena. Insights into this area have come from studies on other physical systems such as charge density waves [44] and interfaces driven through random media [45]. For such systems, when the driving force is weak the system is trapped in a metastable state and therefore stationary. If a force in excess of a threshold critical value is then applied then the system begins to move. At this point, many elastically coupled degrees of freedom collectively depin. It follows that in such cases, depinning is a collective critical phenomenon, and therefore can be characterised by universal scaling laws.

Recently the methods applied to CDW and interface systems were extended to full 3D limit, in order to describe the dynamics of FLL depinning [46]. Considering a vortex line driven with a force slightly in excess of the depinning threshold, the motion is predicted to be highly nonuniform comprising of rapid jumps as portions of the line depin from pinning centres, superimposed onto gradual steady advance. These jumps are reminiscent of avalanches in other slowly driven systems. Further to this, the length-scale of avalanche sizes diverges on approaching the threshold as: $\xi \sim (F - F_c)^{-\nu}$. Beyond ξ different regions of the FLL depin more or less independently. Hence it seems that on approaching F_c by monotonically increasing the drive force F we force the system into progressively higher energy metastable states. The actual depinning threshold itself corresponds to the point at which the last metastable state disappears.

In the case of CDWs and interfaces a so-called no-passing rule applies such that where one part of the system is moving it must all be moving [47]. It is crucial to recognise that due to dimensionality considerations, this rule does not apply in the case of FLL depinning. As such, near to the depinning threshold it is theoretically possible to have coexistent stationary and moving flux-lines or else lines moving with different net velocities i.e. a plastic dynamic phase. The precise distribution of vortices within this plastic dynamic phase is expected to be dependent on the form of the underlying disorder potential. It seems therefore from considerations of threshold criticality that it is theoretically possible for depinning to occur into a plastic dynamic phase.

5.3.3.3 Experimental Evidence of Plasticity in the Depinning Response

A wide variety of experimental observations have provided evidence of inhomogeneous plastic responses at the vicinity of the depinning transition. Whilst the plasticity of the dynamics at this limit are now more or less accepted, the precise nature of this plasticity is still very much an open question. Early indications of the highly non-linear dynamics came from the observation of non-monotonic critical-current dependences as a function of temperature (the peak effect) in conventional superconductors [48]; layered low temperature superconductors such as NbSe2 [32, 49, 50, 51]; as well as in $YBa_2Cu_3O_{7-\delta}$, [52, 53]. Subsequent differential resistivity studies on $NbSe_2$ have revealed so-called "fingerprint phenomena" in the vicinity of the depinning threshold [49, 54]. Specifically, it was observed that depinning of the FLL proceeded via a series of reproducible steps in the $V(I)$ curves. It was suggested that this behaviour arises due to **fracturing** of the system at the onset of depinning, into well-defined chunks characterised by a length scale L_v. It was supposed that each of these chunks depinned at different times and that following depinning that the time-averaged velocity of the vortices was correlated across any given chunk.

Further insights into the nature of vortex system plasticity were provided by experiments on the flux flow resistivity. One very clear result was that flux-flow noise levels were much higher in the "plastic regime" than in the high driving force ordered dynamic regime [55, 56, 57]. In fact, more detailed analysis of the results of these flux-flow-noise experiments indicated the existence of a wide range of different plastic dynamic regimes. Safar *et al.* [56], for example, interpreted their results in terms of the motion of independent vortex bundles, in which case Poisson statistics are anticipated, with a single time constant for vortices moving across the width of the sample [58]. In contrast, noise measurements by D'Anna *et al.* [57] were interpreted in terms of the opening and closing of channels of "easy" vortex flow, yielding Lorentzian noise spectra. More recently, measurements by Merithew *et al.* [59] on $NbSe_2$ provided evidence that neither flux bundles nor opening and closing channels could account for the non-Gaussian noise spectra in their observations. Instead they provided a description of the dynamics in terms of a network of persistent channels, the pattern of which was supposed to be determined by the background of disorder.

One thing to note with respect to all of these observations is that the plastic response is inherently sample dependent. This is due to the intimate relation between plasticity and disorder. Furthermore, as we shall be examining in some detail in Chapter 8, responses depend not only on the magnitude but also on the precise modulation form of the applied drive. In this context, it is perhaps not surprising that entirely different descriptions of the plastic dynamic regime should be arrived at from different experiments. With this in mind it seems all the more important to obtain a single consistent theory to explain vortex dynamics within the plastic regime.

5.3.3.4 Numerical Simulations of Dynamic Responses in the Vicinity of Depinning

In fact, the results of simulations are almost as confusing as the experimental results in terms of their diversity. Some of the earliest studies in this area were 2D molecular dynamics simulation, performed by Jensen and co-workers [60]. Jensen *et al.* demonstrated that that on driving the FLL against a background of quenched disorder, that in general the system depins plastically rather than in a single coherent chunk. Specifically, they found that in the vicinity of the depinning transition, the dynamic mode assumed by the system depended crucially on the strength of individual pins. For weak pinning, they found that the system deformed

UNIVERSITY OF SOUTHAMPTON LIBRARY

elastically and reversibly. However, the size of this "weak pinning" region was found to shrink to zero for a system of macroscopic dimensions. For intermediate disorder it was found that the system could be reasonably well described within the framework of a Larkin Ovchinnikov model, reflecting the motion of correlated flux bundles (see Section 5.3.3.1 above). This would correspond to a system with elastic instabilities but not plastic deformations. In fact, Jensen *et al.* predicted that plasticity should only occur at the limit of strong disorder. At this limit they found that individual vortices become trapped and as a consequence, highly defective plastic flow developed, as vortices moved along channels between pinned regions. Furthermore, the precise nature of this so-called **channeling regime** was found to be crucially dependent on the density of pinning sites. At high pin densities a sharp distinction was observed between vortices in moving and non-moving regions, leading to bottlenecks in the channels, the overall motion of the system being controlled by strings of vortices hopping through such bottlenecks. For lower pin densities, the channels became much broader and less distinct, with a distribution of velocities such that the velocity was highest at the centre of the channels.

In a more recent simulation Faleski *et al.* [61] focussed on establishing a connection between the various different types of flow and the form of the macroscopic responses. As in the case of the studies by Jensen and co-workers, the studies of Faleski *et al.* were based on 2D molecular dynamics simulations at $T = 0$. From these simulations Faleski *et al.* identified three different types of dynamics near to threshold, dependent on the level of disorder.

(i) **Weak disorder** : FLL contained very few dislocations and moved via correlated patches of vortices making jumps at different times. In this so called **crinkle mode** defects are concentrated around the edges of the correlated regions.

(ii) **Intermediate disorder** : Crossover to a spatially inhomogeneous regime of flux flow in which vortices flow along channels around pinned islands. In this **dynamic channelling regime** the topology of channels is not fixed, hence channels continuously open and close over the course of time. This could be analogous to the regime observed in the experiments of D'Anna *et al.* [57].

(iii) **Strong Disorder** : Individual channels become longer lived and at the limit of very strong disorder a **filamentary dynamic structure** develops, analogous to that proposed by Merithew *et al.* in order to account for their noise observations [59].

These various different regimes, as predicted by the numerical simulations of Faleski *et al.*, were characterised by qualitatively different spatial distributions of vortex velocities. In the crinkle mode [regime (i)], the distribution of vortex velocities near to threshold had a single maximum which shifted to higher velocities with increasing driving force. In the plastic modes [regimes (ii) and (iii)], the distribution of velocities had a clear bimodal structure reflecting the coexistence of pinned and flowing vortices.

More recently still, Spencer and Jensen performed 2D molecular dynamics simulations at finite temperature [37]. Their key finding was that pinning strength required to induce plastic flow vanishes logarithmically as the thermodynamic limit is approached. As a consequence, they deduced that, in the vicinity of the depinning threshold, the system is *always* in a plastic flow regime. Crucially, they argued that any distinction between strong and weak pinning should disappear at the thermodynamic limit. Indeed, it was an extension of these arguments that led to their suggestion that dislocations remain frozen-in, even at the limit of very high driving forces. This lead to the notion of a defective but nonetheless elastic regime (see Section 5.3.2.2, above). In terms of a description of the dynamic regime in the vicinity of the depinning threshold, Spencer and Jensen identified two different plastic regimes dependent on the value of the driving force F_{dr} in relation to the critical depinning force F_{c} (at which a finite voltage response develops) as well as two other critical threshold forces of the driven system.

(i) $\underline{F_{\mathrm{c}} < F_{\mathrm{dr}} < F_{1}}$: At this limit the time averaged velocity distribution was observed to manifest a double peak structure with a strong peak at $<v> = 0$. This indicated that some regions of the vortex lattice must have remained permanently trapped (pinned islands) while others vortices flowed around them. In this respect the prediction is similar to that made by Faleski *et al.* [61] in the intermediate disorder regime i.e a frozen-in filamentary channeling regime. Equally this description can be compared to the description applied to the experimental results of Merithew *et al.* [59].

(ii) $F_{dr} > F_1$: The critical force F_1 marks the point at which the peak in the velocity distribution at $<v> = 0$ disappears hence by this point all of the vortices have become depinned. Within this regime the velocity distribution still has finite width. This is not inconsistent with the description of a time varying channeling regime, as previously proposed by Faleski *et al.* [61] and D'Anna *et al.* [57]. However, it is not possible to determine from the velocity distribution alone whether at any point in time some regions of the vortex system are pinned. An alternative description could be that all vortices move at all times, but with a range of different velocities.

It seems, therefore, on the basis of evidence from numerical studies that there is the possibility of a wide range of different plastic dynamic regimes in the vicinity of the depinning threshold.

5.3.4 Local Plasticity and Dislocations Dynamics

5.3.4.1 Sources of Local Plasticity in Pin Free Systems

From the results presented thus far we might make the assumption that vortex system plasticity arises only as a consequence of bulk-pinning disorder. In fact, further studies, have provided some evidence of plasticity in pure pin-free systems. Aranson and Vinokur (**AV**), for example, considered a thin defect free 2D strip and investigated the nucleation of vortices at the surface both analytically and numerically [62]. Naively we might assume that in this pure-system case the dynamics would always be elastic and coherent. In fact, even in this case, AV found evidence to suggest the existence of driving force dependent dynamic regimes, which they related to changes in the wavelength of perturbations.

For currents just above the depinning threshold, instabilities were observed to have a long wavelength character, typically much larger than the bulk vortex spacing. This resulted in a local disordering of the hexagonal lattice as it nucleated across the sample surface. As a consequence, the lattice flowed plastically via the motion of large coherent chunks of vortex lattice, separated by "cracks" or channels. Hence this leads to the a kind of plastic flow across the sample surface which AV dubbed **ice-floe-like plastic regime**. Note that this type of plastic dynamics, in which large sections of the vortex lattice slide with respect to each other, is entirely distinct from the various channelling regimes observed to arise in response to bulk pinning disorder (see preceding section).

At higher currents, in excess of a threshold ~15-30 % of I_c, the spacing of nucleation sites became equal to the lattice spacing. As a consequence, the system underwent a transition into a regime within which the lattice moved coherently. Thus, it seems that the phenomenon of dynamic reordering is not merely a feature of systems containing bulk pinning disorder. A further point to note, although this is not something which AV themselves discussed, relates to the relative ordering of vortices within the bulk system, as opposed to those nucleating across the sample surface. On re-examining the vortex-distribution images arising out of the AV simulation it seems that whilst the nucleation of vortices across surfaces may be plastic in nature. The vortex system seems to become gradually more ordered as it is driven into the sample interior. Thus, it appears that there was some sort of dynamic healing of surface generated dislocations as the vortex system was driven across the bulk of the sample. Since the AV simulation considered only a very thin sample, it may be that this effect is even more pronounced in bulk samples. Thus in a pure system, the plasticity envisaged by Aranson and Vinokur could be confined to a thin layer on the surface of the sample. It is quite possible that this plasticity would then fail to manifest itself in experimental observations.

An additional distinct mechanism for plasticity in a clean superconductor, was proposed by Braun *et al.* [63] following their time-dependent-Ginzburg-Landau calculations. Braun *et al.* argued that the self-field of current flowing through the bulk of a superconductor should induce a gradient of the magnetic induction and therefore of the vortex density. They proposed that a series of aligned dislocations would form in order to accommodate the resulting strains in the structure. Thus overall the system should contain **fault lines**, separating regions of approximately uniform structure, the close-pack direction alternating across the fault lines. Clearly the number of fault lines required to support a particular dynamic structure will depend upon the gradient in the field induction and hence upon the applied current magnitude. Crucially, the fault-lines were observed to remain more or less stationary as the lattice moved. As a consequence, from an experimental point of view the dynamics response of this regime could well be virtually indistinguishable from the ideal coherently moving case.

5.3.4.2 Studies of Dislocation Dynamics

Thus far we have considered studies focussing on the dynamics of vortices, deriving the distribution and density of dislocations as an output of the simulations. An alternative and in some senses complementary approach is to consider a system with a fixed density of dislocations and then to study the interaction between these dislocations and the pinning centres. In this case the vortex system can be considered as a kind of elastic medium through which the dislocations propagate. Probably the first attempt to model the interaction of a dislocation field with pinning centres was made by Khalil [64]. At high temperatures, Khalil identified two key components in the equation of motion of dislocations, namely :

(i) Interaction between the stress field of the pinning centres and the dislocation strain field.

(ii) Viscous drag between dislocations and vortex lattice phonons

Khalil's analyis suggested that the interaction of point defects with the dislocation field, generates clouds of vortex lattice defects, extending to a distance R_L of the order on the interaction range. Within each of these clouds the forces acting on the FLL are uniform. Hence, it follows that the velocity of the FLL lattice should be correlated across these clouds. It seems, therefore, that the clouds predicted by the Khalil analysis, could correspond to the chunks proposed in Refs 50 and 51 in order to explain the observation of fingerprint depinning phenomena (see Section 5.3.3.3).

More detailed studies on the dynamics of dislocations in a 2D vortex lattice have subsequently been carried out by Scheidl, Aranson and Vinokur [65, 66]. Scheidl and Vinokur (**SV**) [65] considered the dynamics of dislocations in the presence of both thermal fluctuations and pinning disorder, under the influence of an external homogeneous drive. They pointed out that due to its homogeneity the drive itself cannot exert shear stresses on dislocations. Thus, the motion of dislocations relative to the FLL can only arise as a consequence of inhomogeneity induced shear-strains. In the absence of pinning disorder, lattice strains only arise due to thermal fluctuations, hence dislocations undergo **diffuse undirected motion**. In the presence of pinning disorder, however, shear strains develop in direct opposition to the applied drive. This leads to a **directed motion** of dislocations relative to the vortex lattice.

Key to the SV approach was their demonstration that the dislocation dynamics is dominated by the elastic response of the vortex system over intermediate length-scales. If, in the elastic limit, we suppose vortices to move along static correlated channels[§], then this favours dislocations with Burgers vectors parallel to the velocity. There is least resistance to dislocation motion along the **glide direction** parallel to the Burgers vector, whereby motion occurs due to the slips of individual vortices. Motion perpendicular to the to the velocity (climb) can only occur in combination with the creation of vacancies or interstitials. SV demonstrated that the **drift or glide velocity** of dislocations relative to the vortex lattice $V_d \propto v^{-4}$, where v is the vortex system velocity.

The KV findings imply that there is ***always local plasticity in the driven vortex system*** due to directed dislocation glide. In fact, KV found that dislocations glide in bound pairs moving in direction respectively parallel and antiparallel to v. Thus it is possible to have dislocation glide (plasticity) while still retaining the overall topological order of the system. This is clearly distinct from the large-scale plasticity due to multiple creation of defects occurring for

---

[§] Analogous to the dynamic Bragg glass regime proposed by Giamarchi and LeDoussal [23] (see Section 5.3.2.2, above) driving forces below the dynamic reordering transition. Indeed, the SV result is are only strictly valid in the topologically ordered high driving force regime. The dynamics of dislocations in the various plastic channelling regimes are expected to be considerably more complicated.

A final prediction arising out of the SV study is that, within the elastic phase at very high driving velocities, the system undergoes a transition at a critical velocity v_C into a **comoving regime**. Within this regime dislocations move with the same velocity as vortices. Whether or not this regime manifests itself should depend on the relative strength of pinning and specifically on the size of v_C relative to the dynamic reordering velocity v_R (see Section 5.3.2).

(i) **Strong Pinning Case**: $v_C < v_R$ and hence v_C is meaningless since the lattice is not ordered at any velocity up to v_C. In this case on increasing driving force the vortex system is expected to undergo a single stage transition into an elastic co-moving phase at v_R.

(ii) **Weak Pinning Case**: $v_C > v_R$ thus a two stage ordering of the system should occur on increasing driving force. On exceeding v_R the system should transform into a topologically ordered regime in which there is still some element of plasticity due to the glide of coupled dislocation pairs. On further increasing the driving force above v_C the system will undergo a transition into a regime within which dislocations are frozen relative to the moving-frame of the vortex system.

It seems from this discussion that the SV comoving regime could well correspond to the regime of frozen in dislocations observed by Spencer and Jensen at high driving forces (see Section 5.3.2.2).

In a subsequent paper Aranson, Koshelev and Vinokur (AKV) considered in more detail the mechanisms of dislocation interaction and proliferation [66]. As mentioned in Section 4.2, even in the static case the fundamental mechanism of dislocation unbinding in relation to lattice melting has only been fully elucidated in 2D (within the Kosterlitz Thouless theory[67]). In the nonequilibrium situation it is not possible to apply energy balance considerations, hence the problem becomes even more complicated. AKV approached the problem from the point of view that dislocation unbinding is controlled by interaction over long length-scales. In this case it is possible to approximate the vortex lattice dynamics using a coarse grained description.

AKV based their analysis on a dynamic model previously applied to 2D interfaces [68], which crucially lead to the introduction of a so-called ***Kardar-Parisi-Zhang*** (**KPZ**) nonlinear term in the equation of motion. This type of nonlinearity is intrinsic to the dynamic system and arises due to the nature of the disorder. AKV predicted that due to the KPZ term in the equation of motion an exponential screening interaction should arise between dislocations. As such, even an arbitrarily weak thermal noise or random force results in dislocation unbinding. This results in the destruction of topological order. In this situation the Kosterlitz-Thouless unbinding temperature for dislocations drops to zero, hence the main prediction of the AKV model is that topological order is always destroyed over large length-scales.

5.4 Overview of the Dynamic Phase Diagram for the Vortex Solid Regime

In the preceding sections, we summarised a range of observations and predictions on the dynamics of the driven vortex system. In the recent paper by Le Doussal and Giamarchi (LeDG) [23], an attempt was made to correlate all the various findings into a unified picture of the phase diagram. Although the detailed structure of this phase diagram has yet to be fully verified or agreed in the literature, we will reproduce the main findings here. In Fig. 5.3 (overleaf) we illustrate the effect of disorder strength on the phases of the driven system at zero temperature. Here the main uncertainty is in relation to the shaded region at centre of

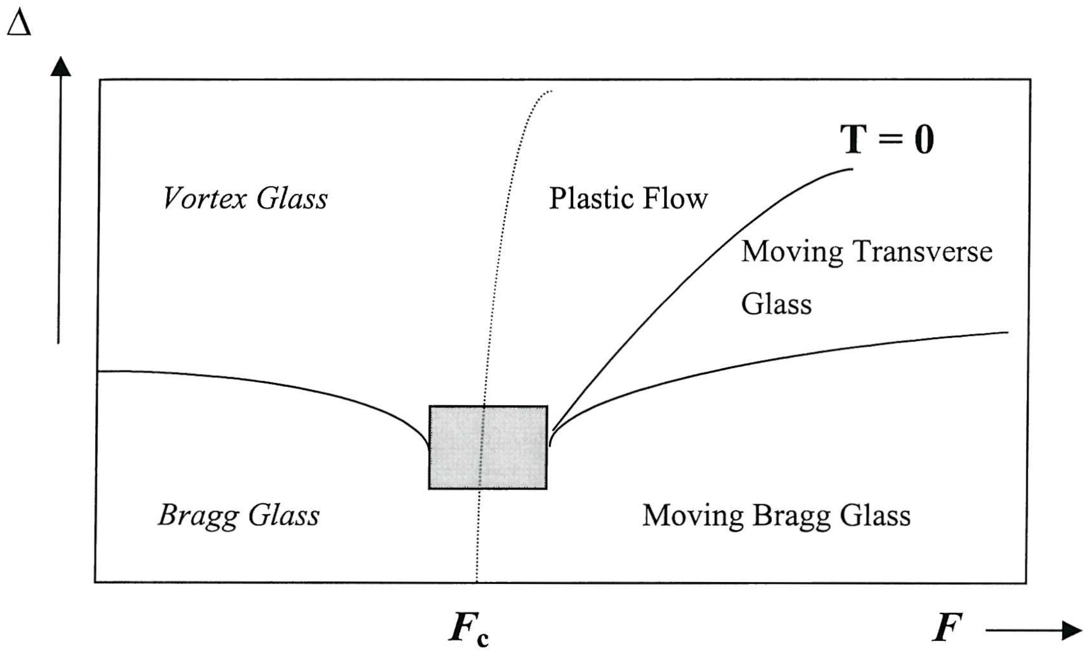

Fig. 5.3 *Schematic phase diagram for a 3D model of the vortex system at zero temperature, illustrating the effect of disorder strength, Δ (based on Fig. 17 of Ref. 23)*

this diagram. Clearly apparent from this diagram is a crossover from coherent depinning at low disorder (Bragg-glass to moving-Bragg-glass) to incoherent depinning for stronger disorder (vortex-glass to plastic-flow). Further to this, at high drives the system is seen to undergo a transition into an at least partially ordered state. If the effect of a third parameter temperature is now included, then a representation can produced of the various phase boundaries within a three dimensional parameter space. The basic form of this dynamic phase diagram is illustrated in Fig. 5.4 (overleaf).

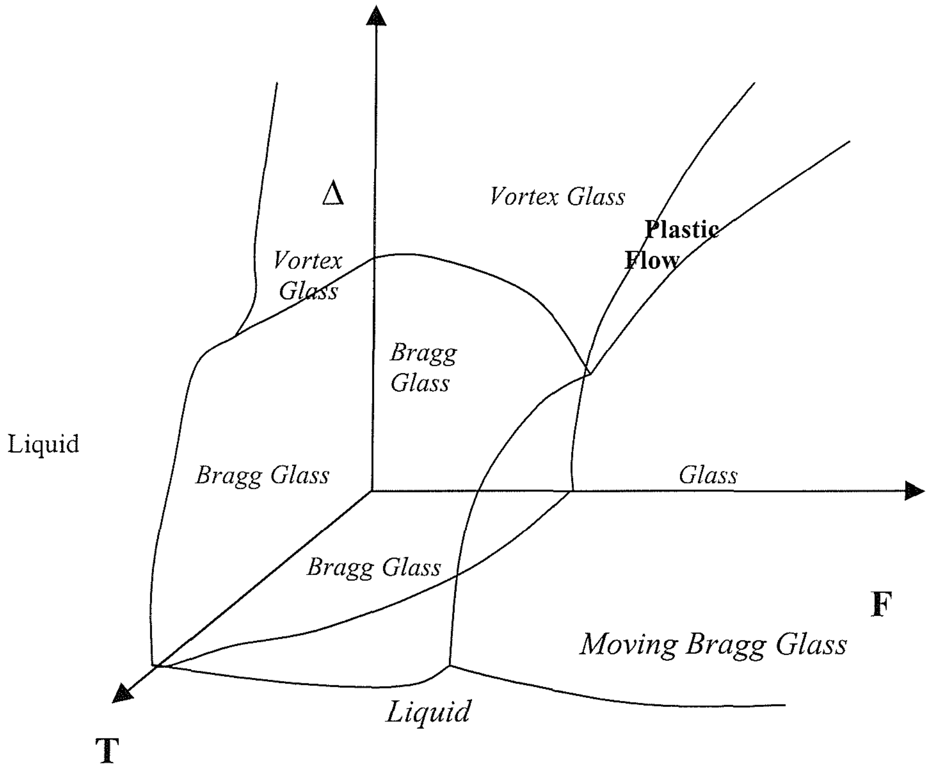

Fig. 5.4 *Schematic phase diagram, illustrating the effect of temperature (T), driving force (F), and disorder(Δ) on the dynamic phase of the driven vortex system (based of Fig. 16 of Ref 23)*

This concludes the discussion of the dynamic of phases of the driven vortex system. However, we will return to many of the issues discussed in this chapter as we come to present our experimental results.

References

[1] G. Blatter, M.V. Feigel'man, V.B. Geshkenbein, A.J. Larkin and V.M. Vinokur, Rev. Mod. Phys, **66** (1994) 1125.
[2] M. Tinkham, Phys. Rev. Lett. **61** (1988) 1658.
[3] T. K. Worthington, F. H. Holtzberg and C. A. Field, Cryogenics **30** (1990) 417.
[4] H. A. Blackstead, Supercond. Sci. Technol. **6** (1993) 579.
[5] R. M. Langan, S. N. Gordeev, P. A. J. de Groot, A. G. M. Jansen, R. Gagnon and L. Tailleffer, Phys. Rev. B **58** (1998) 14,584; Physica C **313** (1999) 294.
[6] J. A. Fendrich *et al.* , Phys. Rev. Lett. **74** (1995) 1210
[7] B. I. Ivlev and N. B. Kopnin, Phys. Rev. B **42** (1990) 10 052; Europhys. Lett. **15** (1992) 3370.
[8] J. Bardeen and and M. J. Stephen, Phys. Rev. **140** (1965) A197.
[9] S. N. Gordeev, A.P. Rassau, R. M. Langan, P. A. J. de Groot, V. B. Geshkenbein, R. Gagnon and L. Taillefer, Phys. Rev. B **60** (1999) 10477-10483.
[10] V. M. Vinokur, M. V. Feigel'man, V. B. Geshkenbein, A. I. Larkin and V. M. Vinokur, Phys. Rev. Lett. **65** (1990) 259.
[11] D. R. Nelson, Phys. Rev. Lett. **60** (1988) 1973; D. R. Nelson and H. S. Seung, Phys. Rev. B **39** (1989) 1953.
[12] V. B. Geshkenbein, A. I. Larkin, M. Feigel'man and V. M. Vinokur, Physica C **162-164**(1989) 239.
[13] C. Carraro and D. S. Fisher, Phys. Rev. B **51** (1995) 534.
[14] A. E. Koshelev and H. Nordborg, Phys. Rev. B **59** (1999) 4358.
[15] A. Schönberger, V. Geshkenbein and G. Blatter, Phys. Rev. Lett. **80** (1995) 1380.
[16] G. Grüner, Rev. Mod. Phys. **60** (1988) 1129.
[17] M. A. Rubio, C. A. Edwards, A. Dougherty and J. P. Gollub, Phys. Rev. Lett. **63** (1989) 1685.
[18] C. J. Olson, C. Reichardt and F. Nori, Phys. Rev. Lett. **81** (1998) 3757.
[19] J. Groth, C. Reichardt, C. J. Olson, S. Field and F. Nori 77 (1996) 3625.
[20] P. Zisweiler, V. Geshkenbein and G. Blatter, Phys. Rev. B **56** (1997) 416.
[21] C. Reichardt and F. Nori, Phys. Rev. Lett. **82** (1999) 414.
[22] M. Feigel'man, V. Geshkenbein, A. Larkin and V. Vinokur, Phys. Rev. Lett. **63** (1989) 2303; M. Feigel'man and V. Vinokur, Phys. Rev. B **41** (1990) 8986; M. V. Feigel'man, V .B. Geshkenbein, A. I. Larkin and V. M. Vinokur, Physica C **167**(1990) 177; V. Vinokur, P. H. Kes and A. E. Koshelev, Physica C **168** (1990)29.
[23] P. Le Doussal and T. Giamarchi, Phys. Rev. B **57**(1998) 11,356.
[24] S. Scheidl and V. M. Vinokur, Phys. Rev. E **57** (1998) 2574.
[25] L. Balents and M. P. A. Fisher, Phys. Rev. Lett. **75** (1995) 4270.
[26] A. E. Koshelev and V. M. Vinokur, Phys. Rev. Lett. **3580** (1994) 3580.
[27] A. I. Larkin, Yu. U. Ovchinnikov, J. Low Temp. Phys.**34** (1979) 409.
[28] A. Schmid and W. Hauger, J. Low Temp. Phys. **11** (1973) 667.
[29] K. Moon, R. T. Scalettar and G. Zimáni , Phys. Rev. Lett. **77**(1996) 2778.
[30] T. Giamarchi and P. Le Doussal, Phys. Rev. Lett **72** (1994) 1530.
[31] U. Yaron *et al.*, Nature **376** (1995) 753-755.
[32] S. Bhattacharya and M. J. Higgins, Phys. Rev. Lett. **70** (1993) 2617
[33] S. Ryu, M. Hellerqvist, S. Doniach, A Kapitulnik and D. Stroud, Phys. Rev. Lett. **77** (1996) 5114.
[34] T. Giamarchi and P. Le Doussal, Phys. Rev. Lett. **76** (1996) 3408.

[35] L. Balents, M. C. Marchetti and L. Radzihovsky, Phys. Rev. Lett. **78** (1997) 751.

[36] T. Giamarchi and P. Le Doussal, Phys. Rev. Lett. **78** (1997) 752.

[37] S. Spencer and H. J. Jensen, Phys. Rev. B **55** (1997) 8473.

[38] A. -C. Shi and A. J. Berlinsky, Phys. Rev. Lett. **67** (1991) 1926.

[39] D. S. Fisher, M. P. A. Fisher and D. A. Huse, Phys. Rev. B **43**(1991) 130.

[40] D. S. Fisher, Phys. Rev. B **31** (1985) 1396.

[41] D. R. Nelson and V. M. Vinokur, Phys. Rev. Lett. **68**, 2398 (1992).

[42] H. Fukayama and P. A. Lee, Phys. Rev. B **17** (1978) 535; P.A. Lee and T. M. Rice, Phys. Rev. B **19** (1979) 3970.

[43] R. Bruinsma and G. Aeppli, Phys. Rev. Lett. **52** (1984) 1547; J. Koplik and H. Levine, Phys. Rev. B **32** (1985) 280.

[44] H. Fukayama and P. A. Lee, Phys. Rev. B **17** (1978) 535; P. A. Lee and T. M. Rice, Phys. Rev. B **19** (1979) 3970.

[45] O. Narrayan and D. S. Fisher, Phys. Rev. B **48** (1993) 7030.

[46] M. Kardar, Cond-mat/9704172 (21 Apr 97).

[47] A. A. Middleton and D. S. Fisher, Phys. Rev. Lett. **66** (1991) 92; Phys. Rev. B **47** (1993) 3530.

[48] R. Wördenweber, P. H. Kes, C. C. Tsuei, Phys. Rev. B **33** (1986) 3172

[49] W. Henderson , E. Y. Andrei, M. J. Higgins and S. Bhattacharya, Phys. Rev. Lett. 77(1996) 2077.

[50] M. J. Higgins and S. Bhattacharya, Physica C **257** (1996) 232.

[51] S. Bhattacharya and M. J. Higgins, Phys. Rev. B **49** (1994) 10,004.

[52] X. S. Ling and J. I Budnick, in *Magnetic Susceptibility of Superconductors and other Spin Systems*, edited by R. A. Hein *et al.* (Plenum Press: New York) 1991, p377.

[53] W. K. Kwok, J. A. Fendrich, C. J. van der Beek and G. W. Crabtree, Phys. Rev. Lett. **73** (1994) 2614.

[54] S. Bhattacharya and M. J Higgins, Phys. Rev. B , **52** (1995) 64.

[55] A.C. Marley, M. J. Higgins and S. Bhattacharya, Phys. Rev. Lett. **74** (1995) 3029.

[56] H. Safar, P. L. Gammel, D. A. Huse, G. B. Alers, D. J. Bishop, Phys. Rev. B **52** (1995) 6211.

[57] G. D' Anna, P. L. Gammel, H. Safar, G. B. Alers, D. J. Bishop, J. Giapintzakis and D. M. Ginsberg, Phys. Rev. Lett. **75** (1995) 3521.

[58] J. R. Clem, Phys. Rep. **75** (1981) 1.

[59] R. D. Merithew, M. W. Rabinand M. B. Weissman, M. J. Higgins, and S. Bhattacharya, Phys. Rev. Lett. **77** (1996) 3197.

[60] H. J. Jensen, A .Brass and A .J. Berlinsky, Phys. Rev. Lett. **60** (1988) 1676; A. Brass, H. J. Jensen and A. J. Berlinsky, Phys. Rev. B **39** (1989) 102; H. J. Jensen *et al.*, J. Low Temp. Phys. **74** (1989) 293.

[61] M. C. Faleski, M. C. Marchetti and A. A. Middleton, Phys. Rev. B **54** (1996) 12,427.

[62] I. Aranson and V. M. Vinokur, Phys. Rev. Lett. **77** (1996) 3208.

[63] D .W. Braun, G. W. Crabtree, H. G. Kaper, A. E. Koshelev, G. K. Leaf, D. M. Levine, V. M. Vinokur, Phys. Rev. Lett. **76** (1996) 831.

[64] A. E. Khalil, Phys. Rev. B **54** (1996) 12,437.

[65] S. Scheidl and V. M. Vinokur, Phys. Rev. B **56** (1997) R8522.

[66] I. Aranson, S. Scheidl and V. M. Vinokur, Phys. Rev. B **58** (1998) 14,541.

[67] J. M. Kosterlitz and D. J. Thouless, J. Phys. C **6** (1973) 1181.

[68] M. Kardar, G. Parisi and Y. –C. Zhang, Phys. Rev. Lett. **56** (1986) 889.

CHAPTER 6. VORTEX LIQUID TO SOLID TRANSITION REGION

6.1 Introduction

As was discussed in more detail in Chapter 1, due to their high transition temperatures and large anisotropies, thermal fluctuations play an extremely important role in the phase diagram of high temperature superconductors [1, 2]. One consequence of this, is that unlike conventional superconductors, the thermodynamic melting transition falls substantially below the upper critical field. Over recent years, this melting transition has been extensively characterised both from the experimental [3] and theoretical [2] points of view. In spite of this, many questions remain to resolved with regard to the behaviour of the vortex system in the vicinity of this transition.

In this chapter we will be considering various features of the dynamic behaviour of the vortex system across the region of the vortex solid to liquid melting transition. In addition to presenting new observations, we will attempt to re-examine well known features of the melting transition incorporating them into our overall understanding. In outline, the chapter will be organised as follows. In section 6.2 experimental details specific to the studies presented in this chapter are described. By way of an introduction, section 6.3 provides a description of the various ways in which the melting transition manifests itself in transport measurements. Sections 6.4 and 6.5 contain the main experimental results, describing respectively the hysteretic behaviour and finite width associated with the melting transition. In section 6.6 the various different results are interpreted in the context of a coexistent phase model. Finally, in section 6.7 the main findings of this chapter are summarised.

6.2 Specific Practical Details

Presented in the chapter, are a combination transport and ac susceptibility[*] data obtained on a range of different twinned and detwinned samples (for specific details of the samples used, see Appendix A). During transport measurements, the twinned samples were inclined at an angle of 15° to the applied field, in order to avoid the effect of twin boundary pinning (see Section 2.3). In the case of the detwinned samples, the field was applied parallel to the crystalline *c*-axis.

Unless otherwise indicated, transport measurements were carried out using the SQUID picovoltmeter arrangement as described in Section 3.5.3. For the majority of the transport measurements, the driving currents ($J \parallel ab$) had a double polarity square wave modulation form with a frequency 68 Hz. For the measurements described in Section 6.4 a single polarity square wave current (again with a frequency of 68 Hz) was used. With the exception of the data presented in Fig. 5.6, all resistivity versus temperature curves were measured on cooling, at a constant rate of 0.2 K/min.

The ac susceptibility measurements were performed using a high field ac-susceptometry rig as described in detail elsewhere [4]. A primary coil was used to superimpose an AC magnetic field ($f = 2.978$ kHz) onto the DC field background and the response was measured using a pair of secondary pick-up coils wound in serial opposition, coaxial to the primary coil. All of the ac-susceptibility results presented in this chapter were measured in a DC field of 2.2 T.

---

[*] Measurements were performed by D. Bracanovic, formerly a member the University of Southampton Condensed Matter Physics Group.

6.3 Transport Signature of the Melting Transition

Early transport measurements by Worthington *et al.* on $YBa_2Cu_3O_{7-\delta}$ provided some of the first evidence of a temperature induced transition occurring in the vortex system, well below the upper critical field line [5]. The kinks observed in the tails of the low current (ohmic) resistivity dependences by Worthington *et al.* were not nearly as sharp as would be expected in the case of a first order phase transition. As such, these data seemed consistent with the idea of a continuous vortex glass transition, at a temperature T_g with diverging correlation-lengths and characteristic relaxation times as proposed by Fisher, Fisher and Huse [6]. More recent studies have demonstrated very sharp drops in the tail of the resistivity dependences when sufficiently pure single crystalline samples are used [7, 8, 9, 10, 11]. Indeed, the observation of such a sharp drop, together with associated hysteresis, was taken as the first compelling evidence in support of a first order vortex melting transition. As discussed above, unambiguous evidence came later, in the form of thermodynamic studies on the same and similar samples. Transport studies remain, however, a powerful tool for probing the detailed nature of processes occurring across the melting transition.

From controlled studies of twin boundary [10, 11, 12] pinning and pinning by point disorder [13], it has become apparent that the first order melting transition is suppressed in the presence of significant pinning. In the highest purity single crystalline samples, a sharp melting transition is observable. However, for the majority of less pure samples a broader, more continuous glass-like transition is observed. In Fig. 6.1 low-current resistivity transitions are contrasted for two $YBa_2Cu_3O_{7-\delta}$ samples with very different pinning properties. The data in Frame (a) were obtained on a sparsely twinned $YBa_2Cu_3O_{7-\delta}$ single crystal (Sample A) grown with particular regard to sample purity. In contrast the curves in Frame (b) reflect the resistive behaviour of a melt-grown sample (Sample E), with a significantly higher level of pinning disorder.

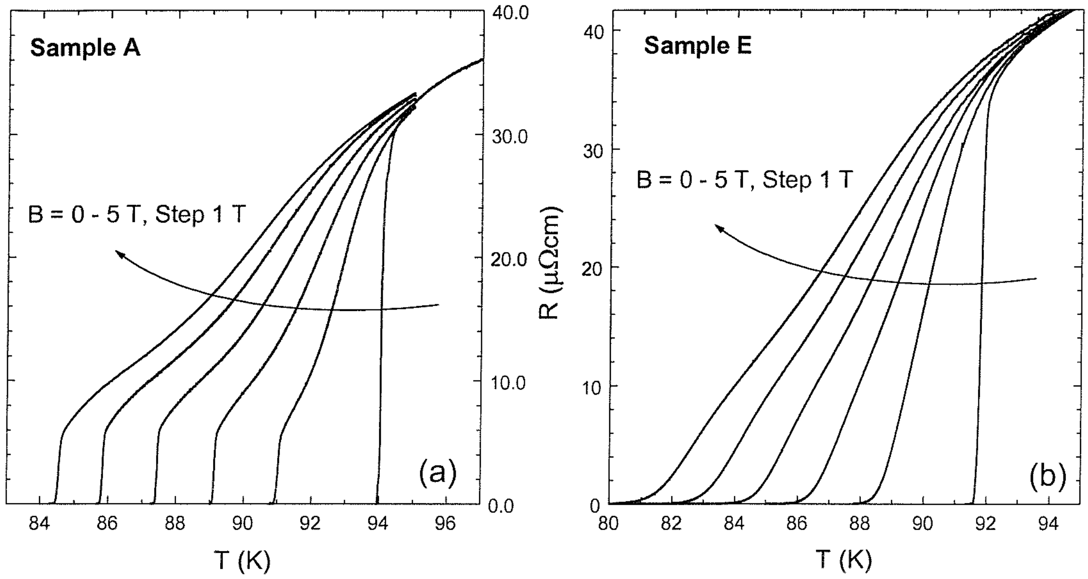

Fig. 6.1 *Low current (I = 0.1mA) resistivity dependences of two different samples, for fields in the range 1-5 T.* ***Frame (a)*** *:sparsely twinned single crystal (Sample A).* ***Frame (b)*** *: melt-grown sample (Sample E). Both samples were tilted at an angle of 15° to eliminate the effect of twin boundary pinning.*

For both samples, the low current ohmic resistivity transition broadens with increasing magnetic field. However, the nature of the ultimate transition to zero resistivity differs markedly in these two cases. For the single-crystalline sample [frame (a)] the sharp drops in tails of the resistivity dependences reflect an abrupt transition from a mobile vortex liquid to a static vortex solid state. No such sharp feature is apparent in the tails of the dependences for the melt-grown sample, instead there is only a slight change of slope at low temperatures, perhaps reflecting the onset on a continuous vortex-glass transition. In fact, samples exhibiting behaviour similar to that depicted in frame (b) are considerably more common than those which display a sharp drop in the resistivity at a vortex freezing transition. This more continuous transition towards zero resistivity is indicative of a relatively high degree of pinning disorder within a sample. Indeed, high quality twinned samples can be made to exhibit resistivity dependences analogous to those shown in both frames (a) and (b) simply by changing the inclination of the applied field with respect to the twin planes and hence the degree of effective of pinning within the sample [14]. This having been said, for the studies conducted within this thesis it was of paramount importance that pinning disorder was carefully controlled. As such, the results presented within the remainder of this thesis correspond to the case exemplified by the curves in Frame (a).

In addition to being sensitive to pinning disorder, the first order melting transition is also suppressed by sufficiently high magnetic fields [15, 16]. Indeed higher magnetic fields can in some senses be regarded as equivalent to increases of effective disorder [17]. Different criteria can be used to define the so-called **multi-critical point**, at which the transition crosses over from being first order to being second order. Unfortunately, the value obtained for the multicritical field B_{mc} is to some extent criterion dependent. From a purely qualitative point of view, however, the crossover point is normally apparent from examination of the $\rho(T)$ dependences for a range of different fields (see, for example, curves of Fig. 6.2).

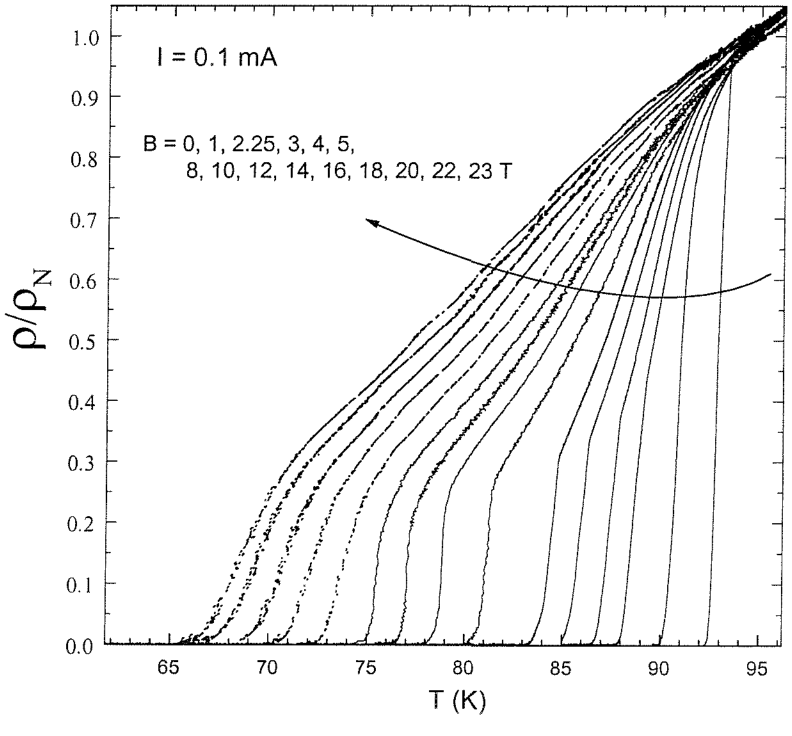

Fig. 6.2 *Broadening with increasing field of the low current ohmic resistivity transition for Sample D, as measured at the Grenoble High Magnetic Field Laboratory. For fields above 14 T the first order melting transition is clearly suppressed.*

In Fig. 6.3, we have used a simple 0.1 ρ_N criterion to elucidate the field dependence of the transition temperature for the curves shown in Fig. 6.2. The transition line shows a clear kink at a field of 14 T, which we denote as the multi-critical field B_{mc}.

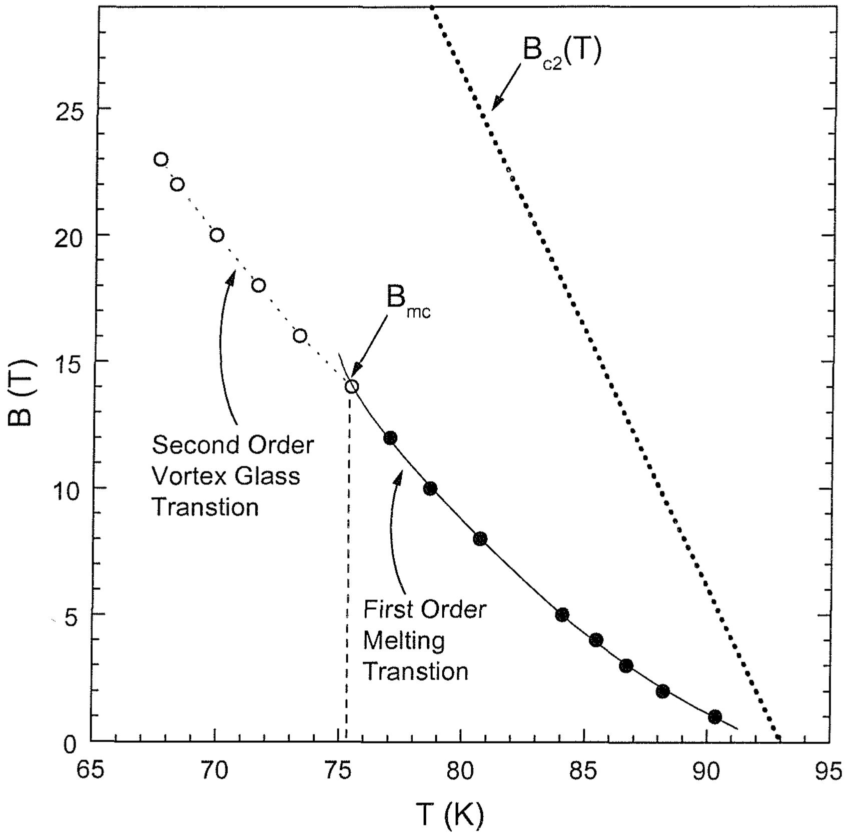

Fig. 6.3 *Field-temperature phase diagram, for an overdoped $YBa_2Cu_3O_{7-\delta}$ single crystal (sample D). Data-points (circles) extracted using from the curves of Fig 5.2 using a simple 0.1 ρ_N resistivity criterion. The crossover from a first order to a second order transition is apparent as a change in slope at the multicritical field B_{mc}. Also shown for reference is the upper critical field line [$B_{c2}(T)$] deduced from $\rho(T)$ data [13].*

The multi-critical field B_{mc} is strongly dependent on pinning strength and can be pushed to lower fields via the controlled introduction of pinning sites such as oxygen vacancies [13]. In the remainder of this chapter we will be focussing on the region of the phase diagram below the multicritical point where the vortex freezing transition is first order.

6.4 Hysteresis and Switching Effects Associated with the First Order Vortex Freezing/Melting Transition

6.4.1 Resistivity Hysteresis

As we have seen, in resistivity measurements the first order melting transition manifests itself as a sharp drop in the ohmic resistivity at the transition line B_m(T). Is has been known for some time that this transition is hysteretic [7, 9, 11], however there has been considerable controversy concerning the precise nature of this hysteresis [18, 19, 20, 21]. In Fig. 6.4, we show the typical form of the resistivity hysteresis in the vicinity of the melting temperature T_m Curves were measured at the extremely low rate of ±10mK/min, in order to distinguish the intrinsic hysteresis from the dynamic shifts between sample and sensor temperatures, always

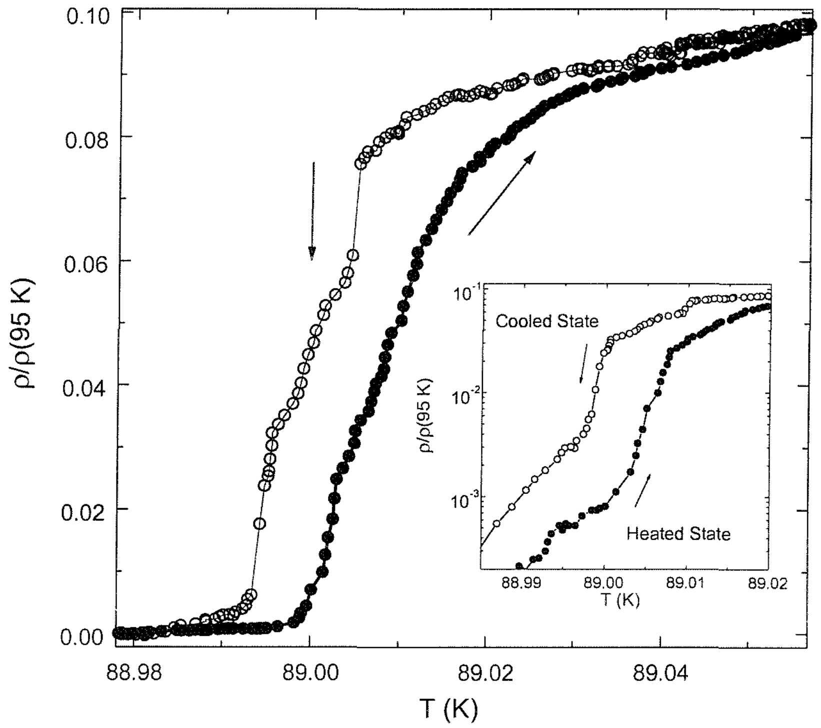

Fig. 6.4 *Temperature dependence of the normalised resistivity at B=2T showing the hysteresis around T_m (Sample B).*

present when sweeping at higher rates (see Section 3.4.2). Notice, as is typically observed [18-20], the hysteresis is asymmetric: Whereas the curve obtained on warming is relatively smooth, the cooling curve is broader and contains a number of step-like features. For current-densities less than a threshold value $J_t = 0.6$ A/cm^2, the shape of the $\rho(T)$ curves and the width of the hysteresis were independent of the current density. As would be expected for a thermodynamic transition, very similar hysteretic behaviour has also been observed in the $\rho(B)$ dependences (see for example Ref. 20).

6.4.2 *E-J* Hysteresis and Current Induced Switching Effects.

It seems reasonably evident that the $\rho(T)$ hysteresis described above should also manifest itself within $E(J)$ dependences. Indeed, we recently presented the first observations of $E(J)$ hysteresis, at temperature and fields in the vicinity of the vortex melting transition [21]. Associated with this hysteresis were current induced switching effects, reflecting externally driven changes in the structure of the system. From the detailed analysis of such switching effects, we have been able to obtain valuable clues about the structural changes occurring in the vicinity of the vortex liquid to solid melting transition.

We have found that *E-J* curves, measured at the same temperature in the vicinity of T_m, differ markedly dependent on whether they are obtained after cooling down from well above T_m, or following warming up from the vortex solid state below T_m. We denote these two states of the system the **cooled-state** and **warmed-state** respectively. In Fig. 6.5 a set of isothermal *E-J* curves is shown for $B = 2$ T. The isothermal cooled-state curves (lines) were obtained on sweeping from 0 to 10 A/cm^2. At high temperature, above T_m, these curves have an ohmic form, reflecting the dynamics of a vortex liquid. In the vicinity of melting transition the curves take on a characteristic S-shaped form.

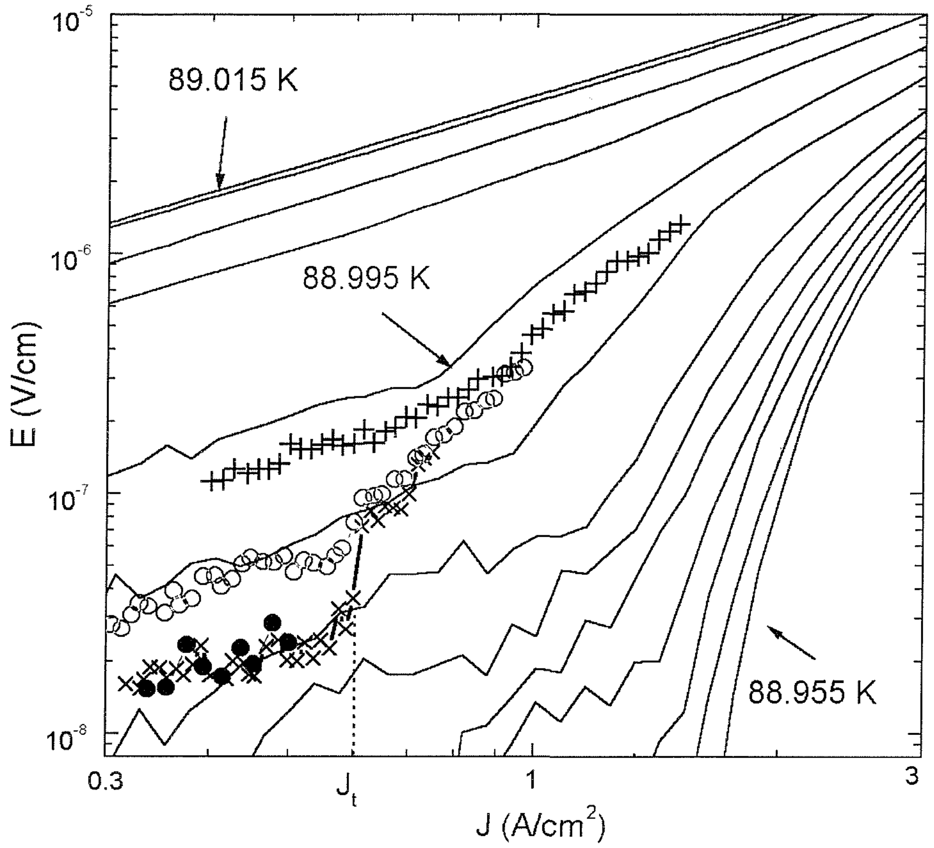

Fig. 6.5 *E-J curves in the vicinity of T_m for $B = 2$ T.* ***Lines***: *E-J curves obtained on cooling to temperatures in the range 88.955-89.01 K (step 5mK).* ***Symbols***: *E-J curves obtained, in succession, after warming to a temperature of 88.995K. For each of these warmed state curves the current was swept from zero up to a progressively higher maximum: J_{max}: [●] 0.5 A/cm^2; [x] 0.75 A/cm^2; [○] 1.0 A/cm^2 and [+] 1.5 A/cm^2 (Sample B).*

The S-shaped form of the cooled-state curves in the transition region can be divided into three clear sections:

(i) Ohmic response at low currents

(ii) Non-ohmic response at intermediate currents

(iii) Ohmic response at high currents

We will return to consider the nature of the dynamics in these three different regimes in Section 6.6.3.3.

Also shown in Fig. 6.5 are warmed-state curves (symbols) for one particular temperature (88.995K. The data-sets represented by different symbols were measured sequentially, on ramping to successively higher currents. As can be seen, for the initial run (closed circles), the warmed-state response was shifted relative to the *E-J* cooled-state curve for the same temperature.

On comparison with Fig. 6.4, it can be seen that width of the *ρ(T)* hysteresis ~ 8 mK, corresponds closely to this effective temperature shift between the heated and cooled-state curves. In fact, we have found that provided that the current density did not exceed a specific threshold value $J_t \approx 0.6$ A/cm^2, the heated-state curve was reproducible. This is illustrated by the initial section of the data-set represented by diagonal crosses. On exceeding the threshold value J_t, however, the resistivity jumped discontinuously to a much higher level (diagonal crosses, second part). Following this **current induced switching** effect[†], subsequent *E-J* dependences no longer retraced the same curve (open circles and vertical crosses). Instead, the low current ohmic section of the curves was shifted upwards. For currents in excess of the threshold value J_t, the higher the maximum probing current density, the larger was the low current ohmic resistivity on subsequent runs. Saturation occurred when currents in excess of approximately $2J_t$ were applied. Thereafter, the response once again retraced the same reproducible dependence, irrespective of the maximum current reached. The saturation *E-J* curve corresponded very closely to the "cooled state" curve for the same temperature, a small vertical shift being within the temperature reproducibility limits of the system (~ 2 mK over 1K cycles for the SQUID picovoltmeter arrangement).

In Fig. 6.6 (overleaf), we show that a similar switching effect can be observed in relation to the *ρ(B)* hysteresis i.e. after sweeping *B* at constant *T*. The solid lines are *E(J)* curves for cooled- states, obtained in the same way as for the data of Fig. 6.5. The data represented by

---

[†] Such effects could, in principle, be induced by Joule heating effects in the sample contacts. However, if this were the case, the consequent increase in temperature would lead to pronounced upward curvature of *all* the *E(J)* curves (the Joule heating effect increases with increasing current).

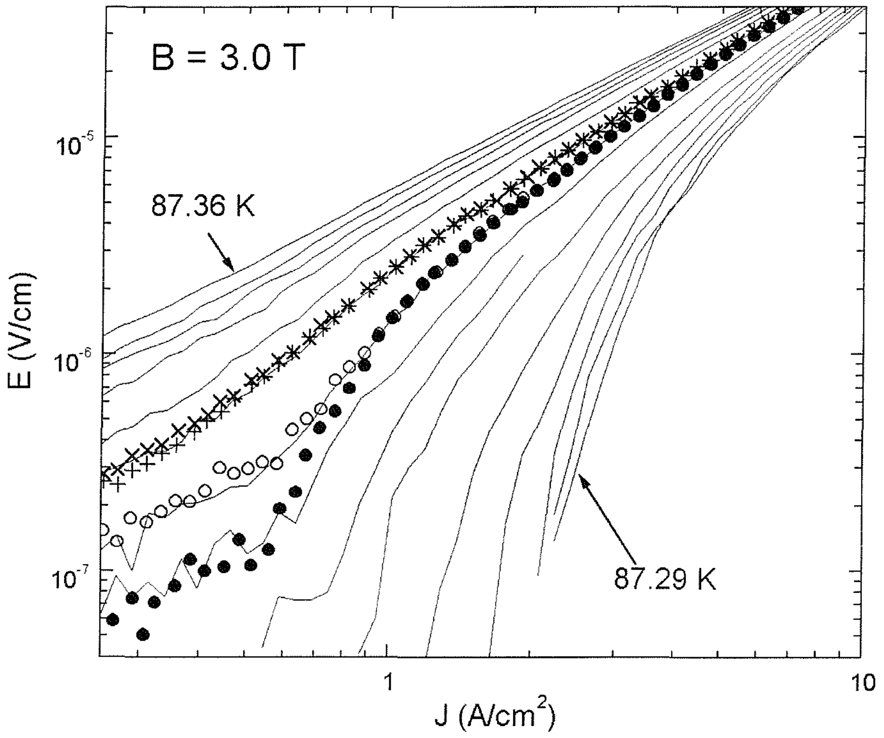

Fig. 6.6 *Isothermal E(J) curves, demonstrating hysteretic switching effects in relation to the ρ(B) hysteresis.* ***Lines***: *cooled state curves prepared as for Fig. 6.5, but for B=3T and temperatures in the range 87.29-87.36 K, step 5 mK.* ***Circles***: *correspond to a state equivalent to the "heated-state", obtained after dropping the field from 3 T to 2.5 T and then ramping back to 3 T, all at constant temperature T=87.330 K. Two successive ramps from 0 to 10 A/cm^2 were obtained in the order, opened circles then closed circles.* ***Crosses***: *correspond to a state equivalent to a "cooled-state", obtained after ramping the field from 3 T to 3.5 T and then dropping back to 3 T, all at constant temperature T=87.335 K. Two successive ramps from 0 to 10 A/cm^2 were obtained in the order, vertical then diagonal crosses (Sample B).*

symbols were obtained following field-cycling at constant temperature. The circles represent a state obtained (at $T = 87.33$ K) after dropping from 3.0 T down to 2.5 T and then ramping back up to 3 T. In view of the essential similarity of the hysteresis observed in the *ρ(B)* and *ρ(T)* dependences, it seems likely that the state obtained in this way should be in a certain sense equivalent to a state obtained on warming. Indeed, the two successive *E(J)* curves (open circles then closed circles) measured following this procedure, show remarkable similarity to the data represented by the diagonal and vertical crosses in Fig. 6.5.

Just as a state equivalent to the heated-state can be obtained on field ramping, one equivalent to the cooled-state can be obtained on dropping to the measurement field. The data represented by crosses in Fig. 6.6 represent a state obtained after increasing B up to 3.5 T and dropping back to 3 T (with constant $T = 87.335$ K). The stability of this state is demonstrated by the similarity of the *E(J)* curves for two successive current sweeps (vertical and diagonal crosses) and also their similarity to the cooled state *E(J)* dependence at the same temperature.

It is clear that there are considerable similarities between the *E(J)* data obtained on temperature and field cycling. In both cases the data provide strong evidence of current induced switching occurring between two distinct states of the vortex system. Further to this, we have found that the threshold density J_t, at which current begins to affect the heated or field-ramped state almost coincides with J_{cr} at which the *E(J)* curve (for the same temperature) deviates from ohmic behaviour. This implies that both effects are consequences of the same dynamic process.

6.4.3 Discussion of Hysteresis in Transport Dependences

Hysteresis of the resistivity dependences has been taken as direct evidence of the first order nature of the melting transition [7, 9, 11] and specifically, attributed to a combination of superheating and supercooling effects [7]. Subsequently, Jiang *et al.* proposed an alternative non-thermodynamic interpretation of the hysteresis [19]. Their idea was, that on cooling, the vortex system remains mobile until the work done by the current exceeds the shear elastic energy. In contrast, Jiang *et al.* pointed out that on warming the system, the vortex velocities are lower and hence less work should be done by the transport current in this case. They argued that this should result in a current induced resistivity hysteresis, independent of the underling thermodynamic processes.

In fact, as we will now outline below, our results provide clear evidence that the resistivity hysteresis cannot be due to the mechanism proposed by Jiang *et al.* The measurements presented in Sections 6.4.1 and 6.4.2 were performed using a single polarity square-wave current, thus for half of each modulation period the current flowing through the sample was zero. During these half-periods, the work done by the current must also have been equal to zero. According to the interpretation of Jiang *et al.*, for temperatures at which the shear modulus was finite, the vortex system should then have frozen. This should occur in the same way irrespective of whether temperature was increasing or decreasing. Thus, in this case of a single polarity driving current, the mechanism proposed by Jiang *et al.* cannot explain the difference between the curves obtained on warming and cooling. Since the mechanism of Jiang *et al.* cannot account for the resistivity hysteresis in this specific case, it follows that it is not the correct interpretation of the more general hysteretic behaviour.

Further compelling evidence for the thermodynamic origins of the resistivity hysteresis at T_m, was provided by Crabtree *et al.* from their observation of sub-loops within a main $\rho(B)$ hysteresis loop [20]. These data were particularly striking, since the partial loops had a shape similar to that of the main loop: partial transformation of the system close to a first order transition should follow the same thermodynamic pattern as when the system changes as a whole. An additional clue as to the nature of the resistivity hysteresis was provided by the work of Charalambous *et al.* [18], in which they demonstrated that changes in probing current only had an effect on the $\rho(T)$ curves obtained on heating and not those obtained on cooling. They thereby concluded that the vortex system can be superheated but not supercooled.

From within the context of our own data, it becomes clear that there are actually ***two distinct states*** of the system at any given temperature in the transition region, as reflected in both $E(J)$ and $\rho(T)$ dependences. These two states, whose resistivities can differ by more than an order of magnitude at some points in the transition region, are accessed via different thermomagnetic histories:

(i) **Low resistivity (LR) state**: reached on warming or field ramping

(ii) **High resistivity (HR) state**: reached by cooling or field-dropping.

Furthermore as our data have a demonstrated, a sufficiently large transport current can be used to drive the system from the low to the high resistivity state. As schematically represented in Fig. 6.7 this current induced switching effect corresponds to switching from the lower to the upper branch of the resistivity hysteresis loop.

Our observation of switching from the LR to the HR state strongly suggests that these states reflect ***different structural configurations*** of the vortex system. This is as opposed to a purely thermodynamic model of the hysteresis, in which the two branches of the hysteresis curve reflect different degrees of relaxation with a uniformly unstructured system. If the resistivity hysteresis were due to time dependent homogeneous changes, then it should not be possible to switch between states. The essential idea is that on switching between states, the

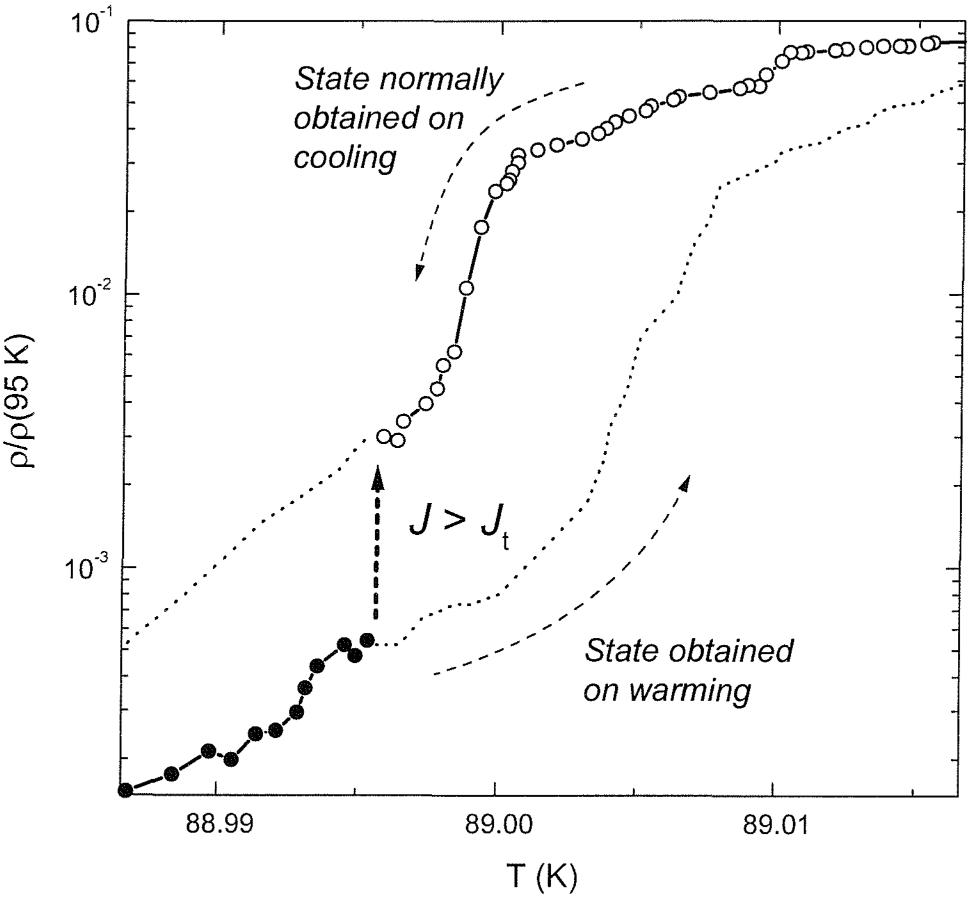

Fig. 6.7 *Schematic representation, indicating how an applied current density twice as large as the threshold value J_t effectively switches the system from the branch of the hysteresis obtained on warming to a state normally obtained on cooling.*

vortex system undergoes a structural rearrangement. As should be expected for such a current-driven rearrangement, the switching process only occurs in one direction. It is possible to switch from the LR to HR state but not vice-versa, and having driven the system into the HR state it again becomes more stable.

Further support for this idea of a current driven structural rearrangement is provided by the close correspondence between the threshold switching current J_t and the crossover from ohmic to non-ohmic behaviour on the HR state $E(J)$ curve at the same temperature. This close correspondence strongly suggests a common dynamic rearrangement process, resulting in a substantial change in the driven system. In Section 6.6, we further examine the details of this transition, in the context of a more general interpretation of the transition region properties of the vortex system.

6.5 Vortex Solid to Liquid Melting Transition Region

6.5.1 Non-ohmic Broadening of the Resistive Melting Transition

According to theory [22], the collapse of the shear modulus C_{66} at the first order melting transition should lead to a transition which is very sharp with respect to both temperature and magnetic field. Indeed, this seems to correspond closely to the sharpness with which the resistivity falls-off on freezing at the low current limit. However, on applying higher currents, the melting transition is seen to broaden strongly, this broadening often being associated with the appearance of a pronounced minimum in the resistivity versus temperature dependence.

Shown in Fig 6.8 (overleaf) are $\rho(T)$ curves in the region of the melting transition for a sparsely twinned single crystal (Sample A). As is typical, for low currents, below about 1 mA, the $\rho(T)$ curves drop off very sharply with decreasing temperature. For this reason, the melting temperature T_m is conventionally defined relative to these low-current ohmic responses, using a minimum resistivity criterion.

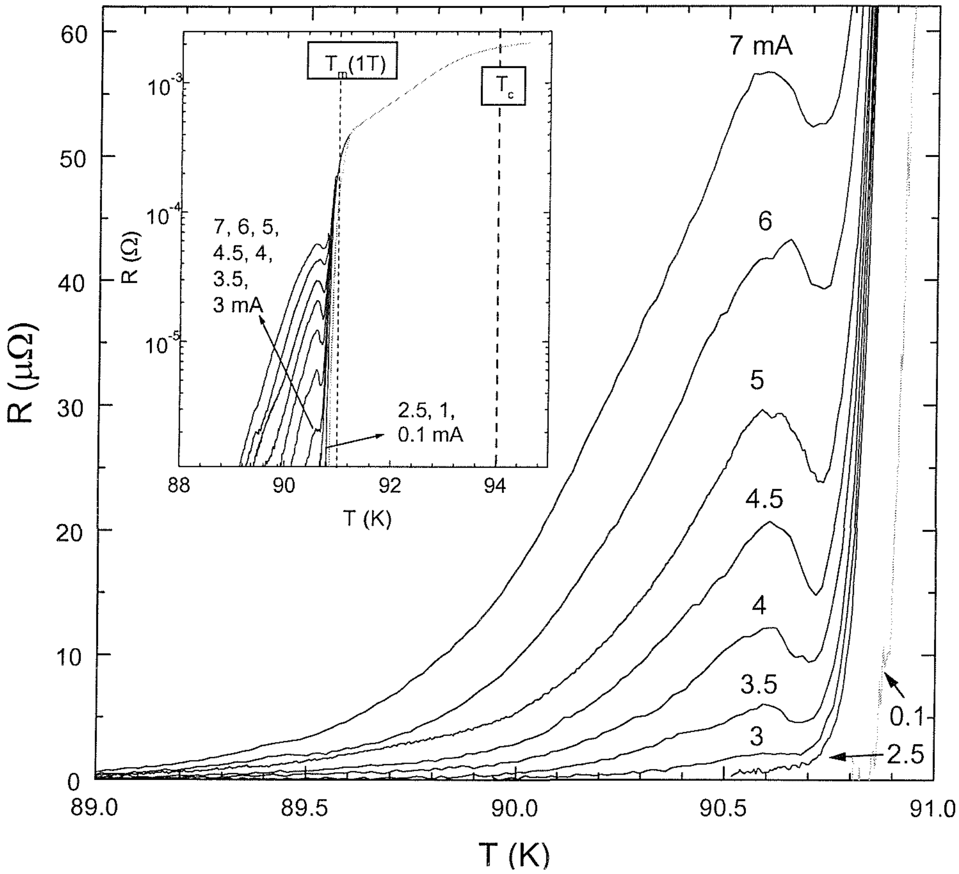

Fig. 6.8 *Strong non-ohmic broadening of the resistivity versus temperature curves below the vortex liquid to solid melting transition (Sample A). Curves are shown for a range of different currents in a field B=1T.* ***Inset*** *shows the same curves plotted on a logarithmic scale.*

Strong non-ohmic broadening starts to occur for currents above 1 mA, this being indicative of much more complicated dynamic behaviour. Pronounced minima appear in the resistivity just below the melting transition for applied currents $I \geq 3$ mA. These anomalous minima in the resistivity are a manifestation of a phenomenon known as the peak effect (PE)[‡]. Well known from conventional superconductors [23], the effect has traditionally been attributed to some sort of pre-melting softening of the vortex system [24, 25] for which a variety of different mechanisms have been proposed [26, 27, 28].

[‡] The name arises from the fact that the resistivity minimum marks a *peak* in the strength of pinning.

As illustrated by the data of Fig 6.8, we have found that the PE occurs at approximately the same temperature, independent of the applied current. From a purely qualitative point of view, it seems not unreasonable, therefore, to describe the peak effect as a precursor to the main melting transition. As such, we have chosen to describe the region between the peak effect temperature T_p and the melting temperature T_m as a **transition region (TR).** In fact, as we will see in the following sections, the fixed-width region of non-ohmic broadening between T_p and T_m is merely the most obvious indication of a well-defined TR.

6.5.2 Signature of the Transition Region in AC-susceptibility Measurements

Perhaps the clearest indication of a TR in the vicinity of the melting transition has been provided by a comparison of ac-susceptibility and transport measurements [21, 29, 30]. This is illustrated in Fig. 6.9 (overleaf), which compares the resistivity $\rho(T)$ and the real part of the a.c. susceptibility $\chi'(T)$ in the vicinity of the melting line (at $B = 2$ T) for a detwinned single crystal (Sample C). From this it can be seen that the vortex liquid-to-solid transition manifests itself as a simultaneous change in both $\rho(T)$ and $\chi'(T)$ dependences.

However, whereas the ohmic resistivity drops off sharply at T_m, $\chi'(T)$ falls off more gradually across a well-defined linear region. The temperature width of the linear region (in this case $\Delta T_{tr} = 0.35$ K) was independent of the applied a.c. field and therefore on the magnitude of the induced currents. These results show striking similarities to the work of Fendrich *et al.* [31], in which a comparative study of transport and magnetic properties revealed a simultaneous onset of the resistivity and magnetisation transitions at T_m. Moreover, they found that the reversible d.c. magnetisation showed a sharp linear increase over a temperature interval ~ 0.2 K, in striking correspondence to our own observations.

Fendrich *et al.* have associated the temperature-interval, across which the magnetisation increases linearly, with a region in phase-space over which vortex liquid and solid phases coexist [31]. Specifically, they suggested that the linear increase in the magnetisation with increasing temperature, was due to the increasing the fraction of the system in the liquid

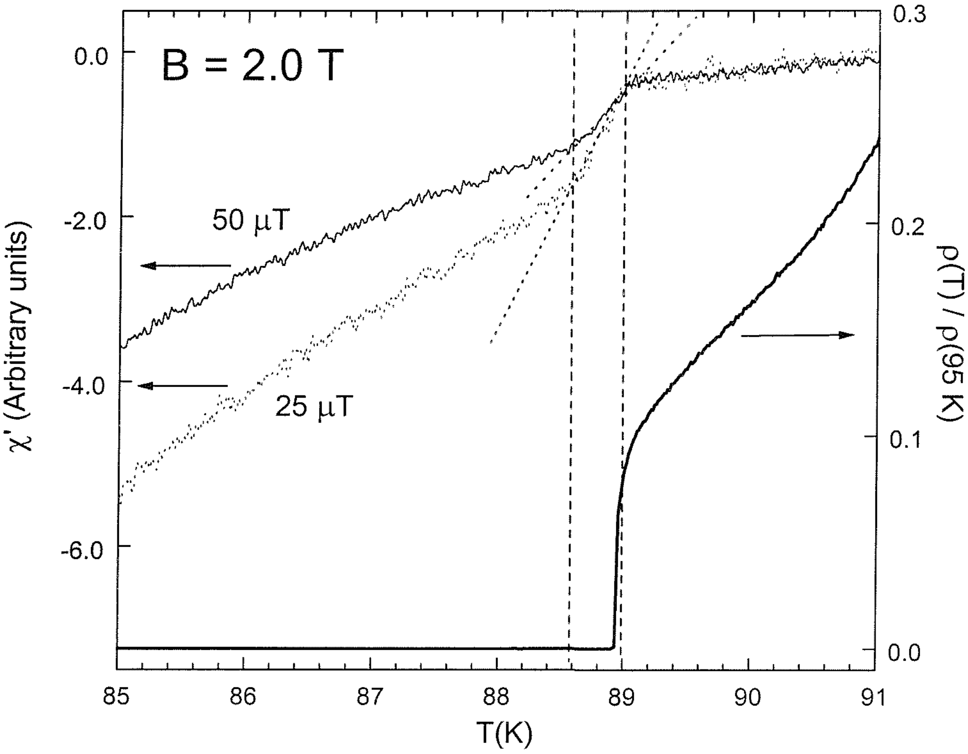

Fig. 6.9 *Signature of the melting transition in ac-susceptibility measurements. Also shown for comparison is the low current ohmic resistivity transition (Sample C).*

phase. Unlike the magnetisation measurements of Fendrich *et al.*, our own a.c. susceptibility data cannot be interpreted as a direct probe of the thermodynamic properties of the vortex system. In the case of a.c. measurements the reversible and irreversible contributions to the response cannot be readily separated. There is no guarantee that the measured responses reflect the reversible properties of the system. This being said, there is a remarkable correspondence, both in shape and position, between the linear region observed in our $\chi'(T)$ dependences and that observed by Fendrich *et al.* in magnetisation measurements. It seems, therefore, that the transition region that we identified as existing close to T_m, from both transport and a.c.-susceptibility data, could be due to the **coexistence of vortex liquid and solid phases**. This interpretation will be considered in more detail in section 6.6, where it will be seen that a coexistent phase model can explain many features of the non-equilibrium behaviour across the transition region.

6.5.3 Analogy Between ac-Susceptibility Transition Region and that Observed in Transport Measurements

In the preceding sections we presented evidence from both a.c.-susceptibility and non-ohmic transport data, of a clear transition region close to the melting line. From the data presented thus far, however, it is difficult to tell whether these transition regions are directly comparable. In this section, we describe an alternative method for presenting the resistive responses, which allows for a more direct comparison for these two types of response. Shown in Fig. 6.10 are a typical set of voltage-current isothermals for a sparsely twinned single crystal (sample A) across the region of the vortex liquid to solid transition. In this particular case, three sets of curves have been measured. The first set of curves in the sequence (fine lines) runs from 90.0 K to 89.2 K separated by a temperature interval of 0.1 K. These curves

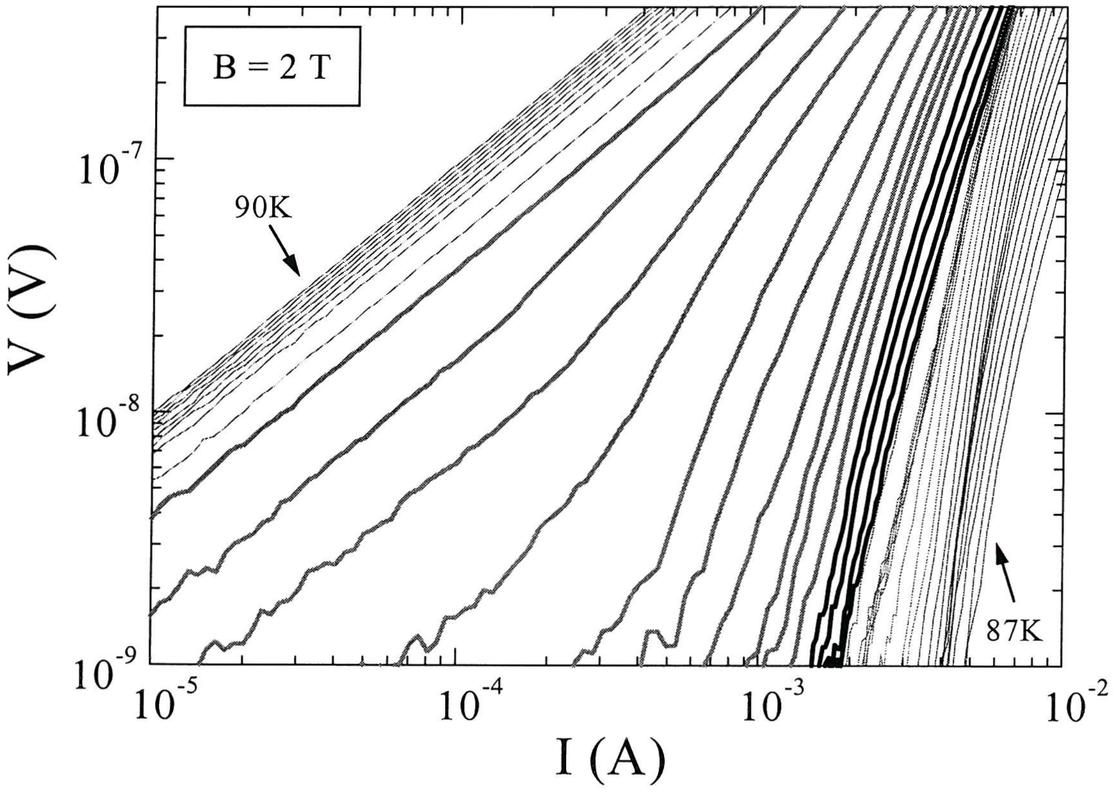

Fig. 6.10 *Isothermal voltage versus current dependences measured in the region of the melting transition at a field of B = 2 T (Sample A). Thin lines are separated by a temperature interval of 100 mK, whereas thick lines have a separation of 20 mK.*

can be seen to be ohmic, reflecting the dynamics of a vortex liquid state. The bold lines in Fig. 6.10 encompass the temperature region between 89.18 K and 88.92 K (step 20 mK), over which the form *V(I)* curves evolves rapidly: this is the region, of interest in the present discussion. The final set of curves (fine lines), for temperatures in the range 88.9 K to 87.0 K (step of 0.1K), illustrates the highly nonohmic responses typical of the vortex solid state.

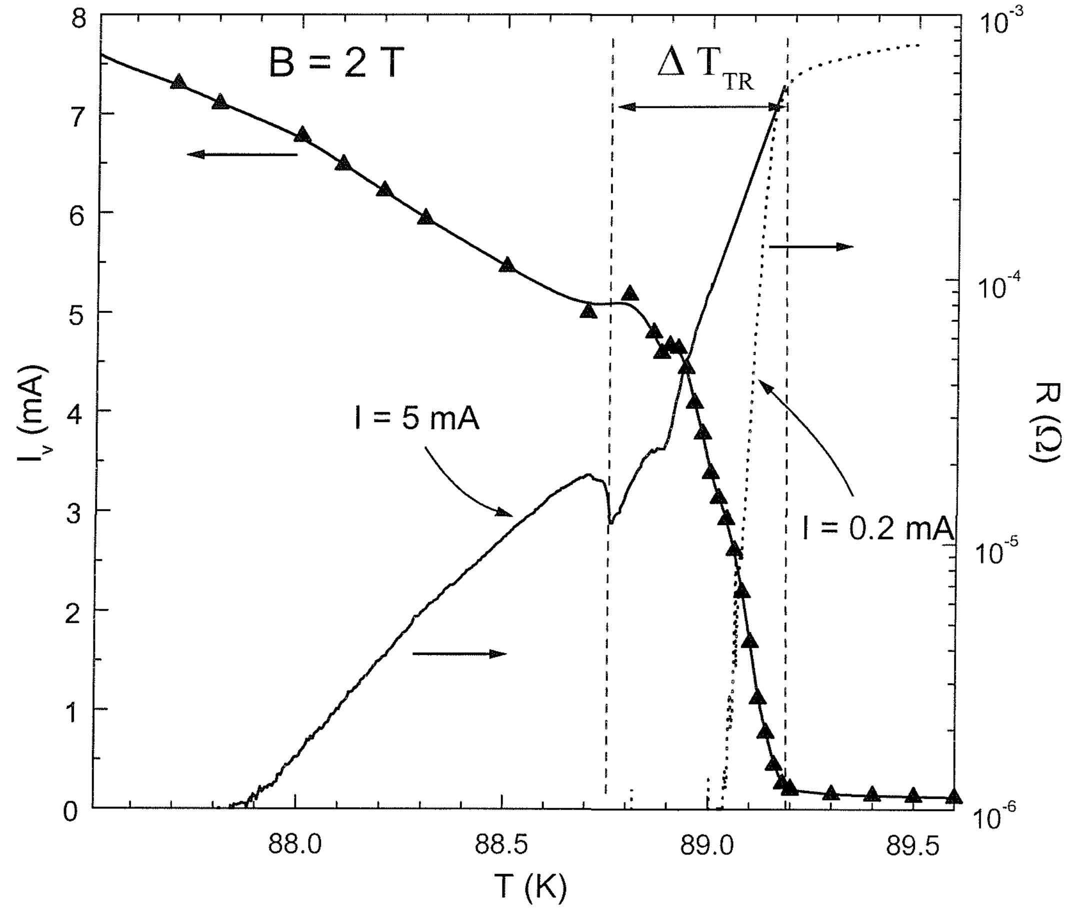

Fig. 6.11 ***Triangles*** *: Temperature dependence of the threshold current deduced from the curves in Fig. 6.10 using a 100 nV criterion (B = 2 T).* ***Continuous Line****: non-ohmic resistivity versus temperature dependence (I=5 mA).* ***Dotted Line****: low-current (I=0.2 mA) ohmic resistivity drop on freezing (Sample A).*

We have found that a clearly defined transition region becomes apparent, when the threshold currents for a particular voltage criterion are extracted from curves such as those shown in Fig. 6.10. In Fig. 6.11 the dependence on temperature of the threshold current (I_v), determined from the curves of Fig. 6.10 using a 100 nV criterion, is compared to the non-ohmic *R(T)* dependence over the same temperature region. As is expected, the threshold current drops substantially on undergoing the transition into the vortex solid state. Note that the threshold current drops off over a relatively well-defined region (of width ΔT_{tr}), between T_p and T_m.

In Fig. 6.12 threshold current versus temperature dependences are compared for three different voltage criteria, from which it can be seen that the width of the transition region, as defined relative to these curves, is independent of the criterion used. From this particular presentation of the transport data striking similarities with the a.c.-suceptibility responses becomes evident. Shown in Fig. 6.13 are the temperature dependences of the out-of-phase(dissipative) component of the a.c.-susceptibility for the same sample. The curves

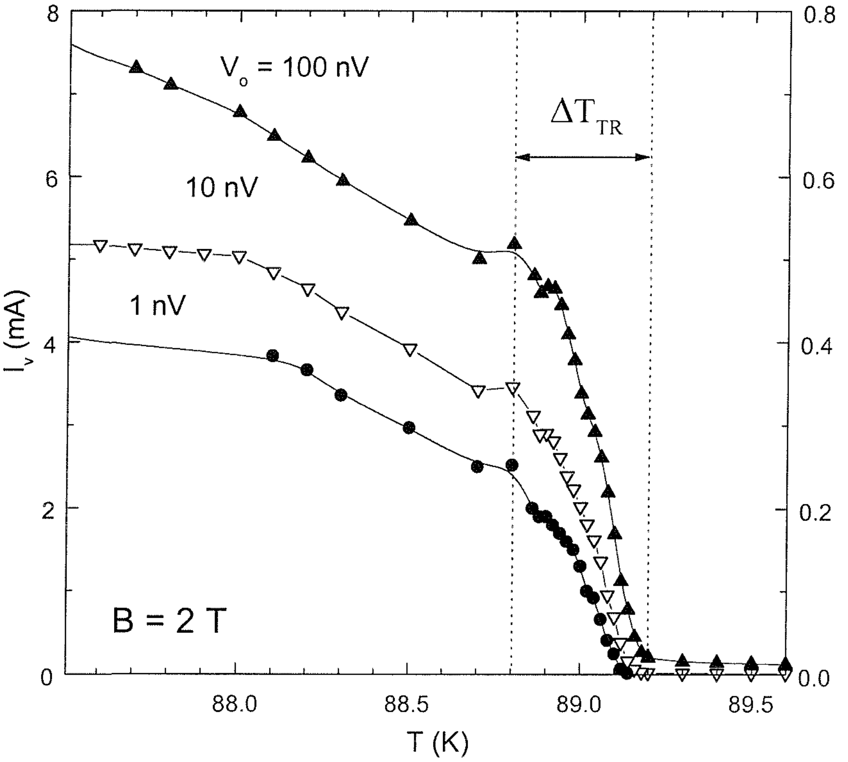

Fig. 6.12 *Threshold current versus temperature curves deduced from the data of Fig. 6.10 using three different voltage criteria: up-triangles, 100 nV; down-triangles, 10 nV and circles, 1 nV (Sample A).*

obtained for three different a.c.-fields show a striking similarity in form to the threshold current versus temperature dependences obtained for three different voltage criteria.

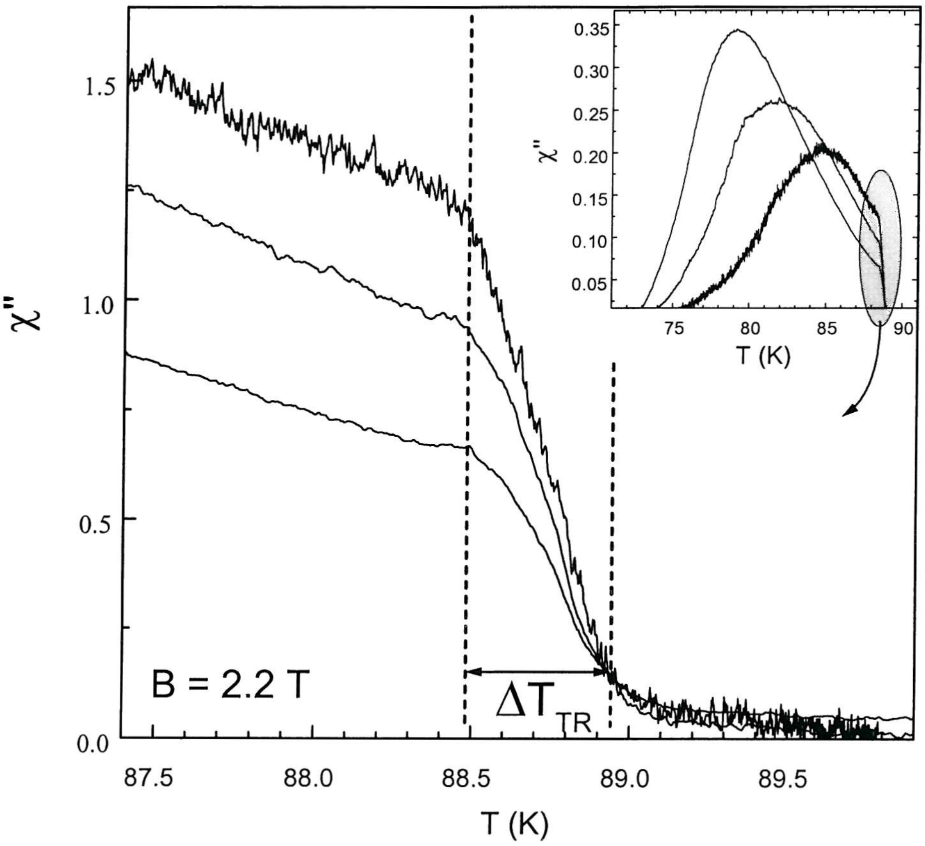

Fig. 6.13 *Temperature dependence of the out-of-phase component of the ac-suceptibility of Sample A, in the vicinity of the melting transition, for three different applied ac-fields. Compare with the threshold current versus temperature dependences of Fig. 6.12.* ***Inset*** *positions the curves of the main frame in relation to the variations in the response over a wider temperature range.*

The analogy between the applied a.c.-field and the voltage criteria can be readily understood from basic electromagnetic considerations. In a time varying B-field an instantaneous E-Field is induced that is proportional to the rate of change of the B-field. Higher a.c.-field amplitudes imply a higher peak rate of change of the magnetic field. Thus, an increase in the applied a.c.-field is equivalent to an increase in the E-field within the sample. This close correspondence between the transport and ac-susceptibility data provides further support for the idea of well defined transition region between the vortex liquid and solid phases

6.5.4 Sample Dependence of the Transition Region Temperature Width

We have found that the temperature width of the transition region, for a particular applied field, is sample dependent. This is illustrated by the data in Fig. 6.14, in which we compare threshold current versus temperature dependences for two different samples in a field $B = 2$ T. In both cases the data were deduced from isothermal current voltage curves using a 100 nV criterion. As we have already seen, the width of the transition region deduced in this way is criterion independent, hence it is only necessary to show the data for one particular criterion. From Fig. 6.14 it is clear that the width of the transition region for sample A is

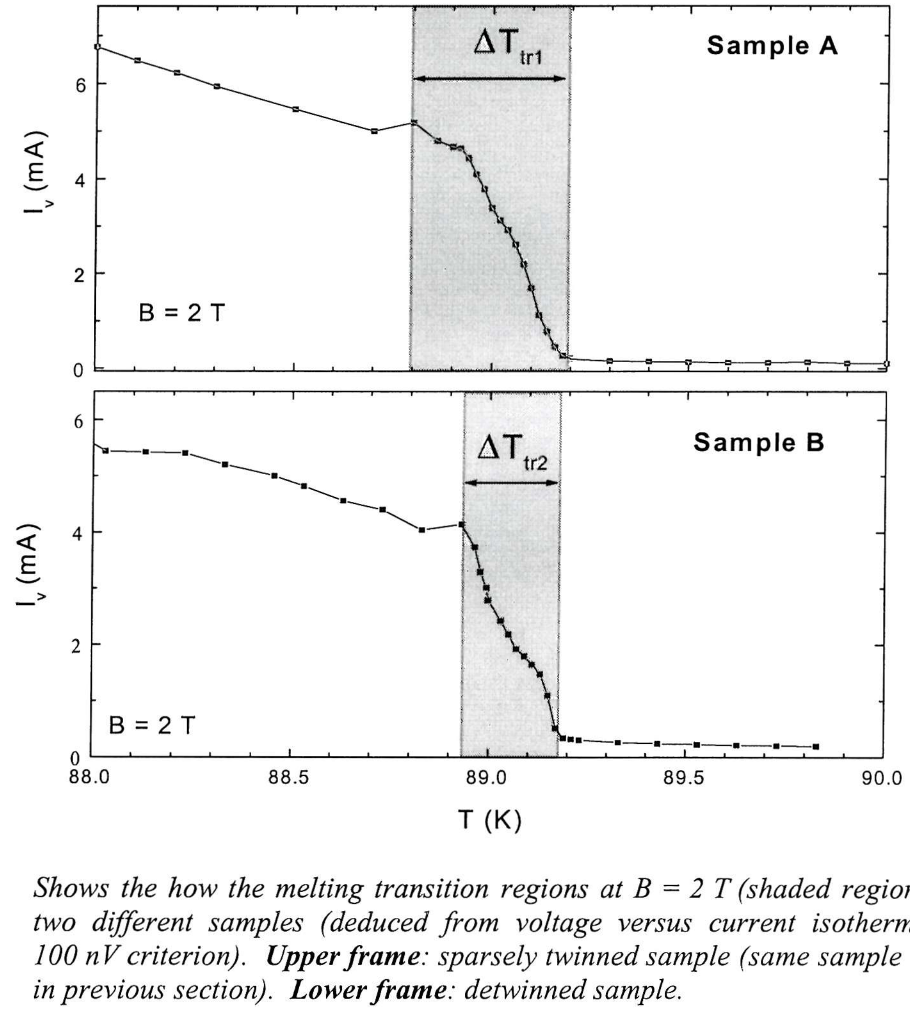

Fig. 6.14 *Shows the how the melting transition regions at $B = 2$ T (shaded regions) differ for two different samples (deduced from voltage versus current isothermals using a 100 nV criterion).* ***Upper frame***: *sparsely twinned sample (same sample as described in previous section).* ***Lower frame***: *detwinned sample.*

substantially greater than that for sample B ($\Delta T_{\mathrm{tr1}} > \Delta T_{\mathrm{tr2}}$). From studies on a variety of different single crystalline sample we found that the transition width, as deduced from threshold current versus temperature dependences, varied over the approximate range 100 mK to 450 mK. Our studies are not yet sufficiently comprehensive to deduce a relationship between the transition width and sample specific parameters such as oxygen deficiency

6.5.5 Transition Region from Isofield *V(I)* Curves

Just as there is a well defined transition region with respect to temperature in fixed field, a similar region can be identified from the magnetic field dependences at fixed temperature. As illustrated in Fig. 6.15, this is most clearly seen from threshold current versus field dependences obtained from isofield *V(I)* dependences at fixed temperature. The isofield

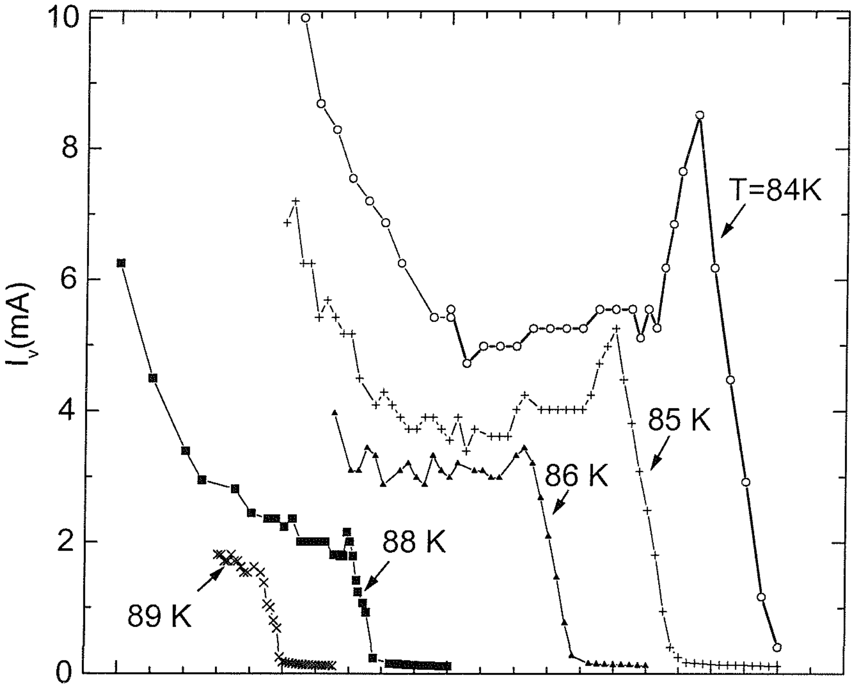

Fig. 6.15 *Threshold current versus field dependences, deduced from isofield V(I) dependences using a 100 nV criterion (Sample A).*

dependences from which these curves deduced, were analogous in form to the isothermal dependences shown in Fig. 6.10. The only difference is that instead of measuring a series of *V(I)* curves for different temperatures in constant applied field, *V(I)* curves were measured for a range of different fields at constant temperature. As for the $I_V(T)$ curves of Figs. 6.11 and 6.12, distinct transition regions are clearly observable in these $I_V(B)$ dependences for all of temperatures shown Here, the onsets of the transition region are marked by peaks in the threshold current, these peaks being especially pronounced at low temperatures. Using these peaks to define the lower limit (in field) of the transition region, and a standard resistive criterion to define the melting temperature, a phase diagram can be constructed. Such a phase diagram is shown in Fig. 6.16.

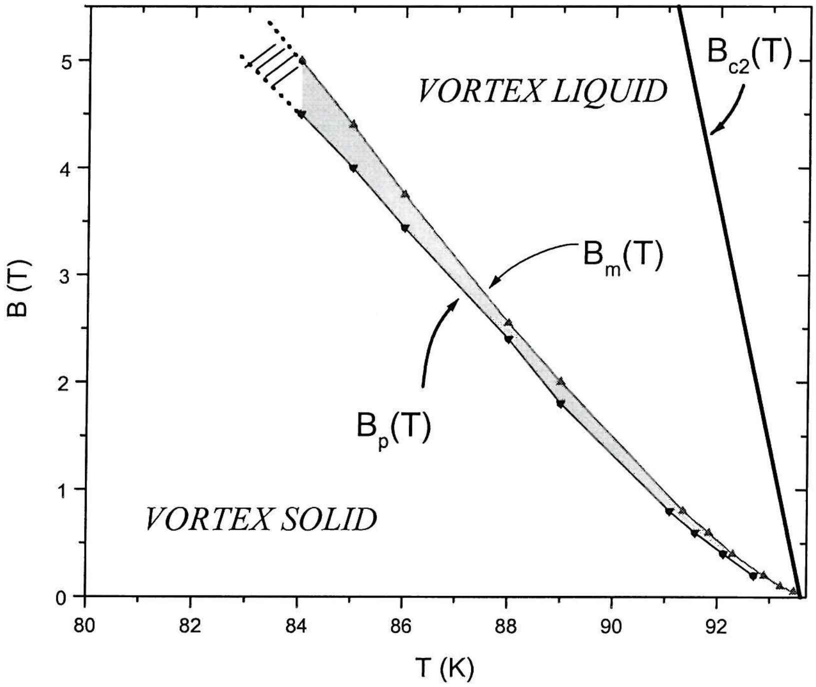

Fig. 6.16 *Phase diagram for sample A in the region of the vortex liquid to solid melting transition below the multicritical point (B_{mc} = 6.5 T). **Up triangles**: melting line defines the upper limit of the transition region. **Down triangles**: threshold current peak, defines the lower limit of the transition region. **Shaded area**: region where it is supposed that vortex liquid and solid phases coexist. Also shown for reference is the upper critical field line $B_{c2}(T)$ deduced from resistivity measurements.*

6.6 Interpretation

6.6.1 Origins of the Transition region

From the preceding sections we have seen that there is a great deal of evidence to support the idea of a well-defined region separating the vortex liquid and solid phases. There are two possible mechanism which could potentially contribute to broadening of the melting transition across this well-defined region:

(i) **Broadening could arise due to glassy relaxation across the TR.** From theory it is well known that, a vortex melting transition can retain its sharp first order character in the presence of weak disorder [32]. More recently Geshkenbein predicted that such weak disorder should lead to glassy relaxational dynamics, controlled by the energy barriers between metastable states [33]. It is clear that glassy relational effects would produce some broadening of the melting transition. However, it is difficult to see how these effects alone could lead to a well-defined criterion independent transition region.

(ii) **Broadening could be due to the coexistence of vortex liquid and solid phases within the TR.** Slight variations of the local melting temperature within the sample could lead to a situation whereby, at temperatures in the vicinity of the melting transition, vortex liquid and solid phases coexist. Such variations in the local melting temperature would delimit a melting transition region with a well-defined and sample dependent width.

From the data presented in this chapter, it is not possible to determine which of these mechanisms is dominant. However, we can say ***all*** of features of the dynamic behaviour across the transition region are consistent with a coexistent phase model. The same cannot be said of the glassy relaxation model. In the following sections we will describe how a wide variety of dynamical behaviour across the transition region, can be explained in terms of a model of coexistent vortex liquid and solid phases. Further strong proof for the validity of the coexistent phase model is provided by the data of Chapter 7.

6.6.2 Coexistent Phase Model

In order for liquid and solid and phases to coexist it is a requirement that there should be a positional dependence within the sample of the effective local melting temperature. In the conventional solid to liquid transition of elemental metals such as gold, it is believed that melting is surface-initiated [34, 35]. This equates to a suppression of the effective local melting temperature at the sample surface. It is not clear, however, in how far we can draw parallels between conventional melting and the melting of the vortex system. One thing that we can be fairly confident of, however, is that there should be some variation in the local melting temperature as a result of slight sample inhomogeneity. Due to complexities of the oxygen diffusion process [36], even the most carefully oxygenated $YBa_2Cu_3O_{7-\delta}$ single crystals are not expected to have completely homogeneous oxygen distribution. Twin planes, in particular, are known to have a pronounced effect on the oxygen diffusion dynamics [37]. Local variations of the oxygenation would be expected to result in weak fluctuations of the melting temperature.

Irrespective of the precise origins or form of the melting temperature variations, the concept of a profile in the local melting temperature can be used to explain much of the observed behaviour across the region of the melting transition. Fig 6.17 provides a schematic representation one particular melting temperature profile. Note, the precise form chosen is

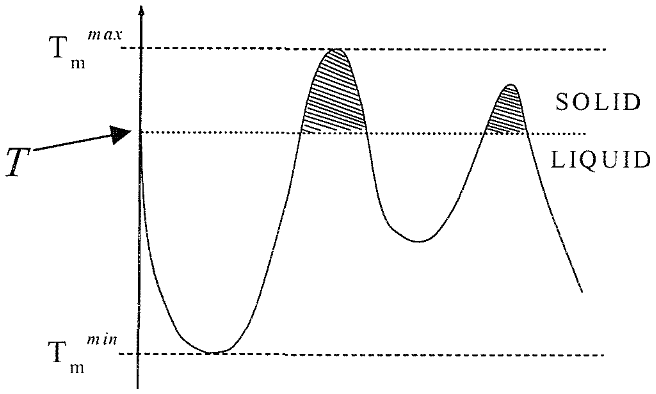

Fig. 6.17 *Schematic representation of how the local vortex liquid to solid melting temperature (T_m^{Loc}) might vary with position across the width of a sample.*

not significant. Here T is taken to represent the ambient temperature. Within those sections of the sample where the local melting temperature was higher than the ambient temperature, vortices would be expected to remain in a solid phase. In contrast, across the remainder of the sample the vortex system would already have melted by temperature T. This would lead to a situation whereby vortex liquid and solid regions coexisted within the sample at a unique temperature T. On variation of the ambient temperature, then the proportion of the system in liquid and solid phases would change accordingly. The upper and lower temperature limits of the transition region would, therefore, be defined by the maximum ($T_m^{\max}$) and minimum ($T_m^{\min}$) values respectively of the local melting temperature profile. Otherwise stated, between $T = T_m^{\min}$ and $T = T_m^{\max}$ the fraction of the system in the liquid phase would gradually increase from 0 to100%. From this idea of a melting temperature profile delimited coexistent phase region, it is possible to explain all of the observed features of the transition region.

6.6.3 Explanation of the Main Experimental Observations in the Context of the Coexistent Phase Model

6.6.3.1 Sharp Drop in the Ohmic Resistivity at Low Currents

The coexistent phase interpretation provides a natural explanation for why the ohmic resistivity should drop so sharply to zero on freezing, in comparison to the much broader linear a.c.-susceptibility or magnetisation transitions. In a system consisting of coexistent vortex liquid and solid regions, it is expected that the solid regions should be much more strongly pinned than the liquid. At low currents we would, therefore, expect voltage response to arise due to the motion of vortex liquid between static solid domains. As such, we would expect the low-current ohmic resistivity to be controlled by percolative processes. In a conductive percolative model [38, 39], where the system is simplistically described as consisting of two phases, one conductive the other non-conductive, then the conductivity falls to zero when the fraction in the non-conductive phase reaches a certain critical fraction of the system volume. This critical fraction depends on the dimensionality of the conducting system

[38], and can be understood as the point where it is no longer possible to trace a continuous path through the conductive phase. In the vortex system, a similar percolation process could apply to the dynamics of vortices in the case of coexistent vortex liquid and solid phases. In this case, the liquid and solid phases could be considered analogous to the conducting and non-conducting phases of the conductive percolative model. In this case the percolative limit would be marked by the point where the resistivity fell to zero, i.e. the point where there was no longer a continuous path for vortex liquid to flow between static solid domains. By comparing the width of the low-current ohmic kink with the broader linear region in the magnetisation, Fendrich *et al.* estimated the percolative limit in the case of the vortex system [31]. They found that this suggested a percolative limit for the dynamics of the vortex system where the fraction of the system in the vortex solid phase reached 20%. This corresponds closely to the width of the ohmic kink, as observed in our own measurements, with respect to the linear region in the $\chi'(T)$ dependences (see Fig. 6.9). The estimate of 20% for the percolative limit in the case of the vortex system compares to numerical-study predictions for conductive percolative systems [38], of between 10-30% for 3D and 40-50% for 2D systems.

6.6.3.2 Criterion Independent Transition region

The coexistent phase model can be used to explain the existence of a well-defined finite-width transition region in the vicinity of the melting transition. If the transition region were due to underlying variations of the local melting temperature, then the width of this region should be unaffected by the force with which the system is driven. This is consistent with the observation of a voltage criterion and a.c.-field independent transition region. Further to this, fluctuations of the local melting temperature are expected to become more pronounced with increasing magnetic field. This, therefore, potentially explains the field dependence of the transition width observed in our experiments. It should be noted, however, that this field dependence could also be explained within the framework of a glassy relaxation model [33]. Further to these indications, the sample dependence of the transition width seems to indicate that the transition region must in some way reflect sample specific local disorder.

6.6.3.3 S-shaped form of the V(I) Curves in the Transition Region

A model of coexistent liquid and solid phases can be used to explain the characteristic S-shaped form of the *V(I)* isothermals across the transition region (see section 6.4.2). A schematic representation of one such voltage versus current dependence is shown in Fig. 6.18.

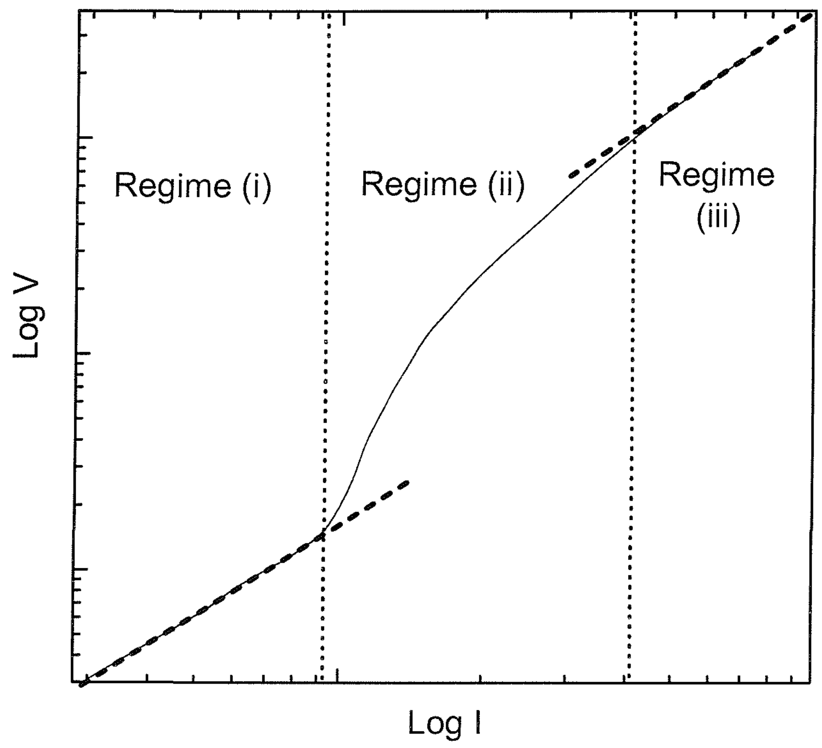

Fig. 6.18 Characteristic S-shaped form of the current–voltage dependences in the melting transition region. Dashed lines indicated the low and high current ohmic regimes.

We suggest that at the low current limit [Regime (i)], the ohmic response arises due to the flow of vortex liquid along channels between solid domains. At this limit, we might also expect an additional ohmic resistivity contribution due thermally assisted flux flow within the pinned vortex solid domains. If this were the case, a highly non-uniform current distribution would be expected. However, given that we have observed ohmic responses at the low current limit, this indicates that the motion of the strongly pinned vortex solid domains must only provide a small contribution to the overall dissipation.

Following the interpretation outlined above, the crossover between Regimes I and II must represent the point at which the vortex solid domains begin to move. Indeed, the sharpness of this transition supports the idea of this crossover being due to a depinning effect[§]. For current densities just in excess of the depinning threshold, the pinning and driving forces are expected to be comparable and as such, a highly non-uniform response is expected. This corresponds to non-ohmic behaviour within Regime (ii) on Fig. 6.18. Finally, in Regime (iii), when the driving force becomes sufficiently large, then it is expected that the response will once again become ohmic as the system enters an effectively free-flow regime (see Section 5.3.2). Thus, in summary the three different response regimes in the transition region can be described as follows:

Regime I	Solid domains pinned. Ohmic response arises due to liquid flowing in channels between static solid domains.
Regime II	Solid domains start to move but driving forces and pinning forces are still comparable, thus overall response highly non-ohmic.
Regime III	Driving force large in comparison to the pinning force, hence the driven vortex system experiences pinning as only a weak perturbation on the overall coherent motion.

6.6.3.4 Hysteresis and Switching Effects

In section 6.4 we described in detail a range of different hysteretic properties and switching effects associated with the melting transition. The results described in this section have been summarised in the list provided overleaf.

[§] If this feature reflected a transition between TAFF and flux creep regimes then a much smoother crossover would be expected.

(i) There are two distinct states of the system, which we will denote the **heated-state** and the **cooled-state**, and both are reproducible to within certain constraints.

(ii) States obtained on field-ramping and field-dropping are equivalent to the heated and cooled states respectively.

(iii) It is possible to switch from a heated-state to a cooled-state (or equivalently from a field-ramped state to a field-dropped state) by applying a current in excess of a certain threshold value.

(iv) It is ***not*** possible to switch from a cooled state to a heated state.

(v) The threshold current for switching between heated and cooled states (J_t) corresponds very closely to the crossover current (J_{cr}) between the low-current ohmic and intermediate current non-ohmic regimes.

These findings can now be fully explained within the framework of a model of coexistent vortex liquid and solid phases. We suggest that the differences observed between the properties of the heated and cooled states arise due to slightly different distributions of vortex liquid and solid phases. We account for these differences in terms of superheating effects (see also discussion of Section 6.4.3). On approaching the melting transition by warming from the vortex solid state, it is expected that there will be regions where the vortex solid will persist in superheated form [7, 9, 11]. Within a coexistent phase system, such regions would lie towards the peaks of the melting temperature profile. Thus, we would have a situation whereby the edge of domains, or even entire solid domains, would persist at ambient temperatures above their local melting temperature. On cooling down through the transition region, there would be no such superheated regions. As such, at any given temperature within the transition region, the proportion of the system in the solid phase would always be higher in the heated-state case. Stating this otherwise, the channels of liquid flow between the solid domains will be narrower in the case of a heated-state than for a cooled state. Since the hysteretic $\rho(T)$ dependences are measured using low current densities, the dynamic response is expected to be almost entirely due to the motion of vortex liquid between strongly pinned solid domains (see Section 6.6.3.3). Thus, it is clear why the response should be so much lower in the heated state, since the channels of liquid flow are expected to be much narrower in this case. Furthermore, it is apparent that there can be no history or time dependence in a regime where the dissipation is largely due to liquid flowing along channels between static solid domains. This explains both the reproducibility of the low-current $E(J)$ and $\rho(T)$ dependencies, as observed in our experiments, and the lack of time dependence observed in the $\rho(T)$ measurements of Jiang *et al.* [19]. These observations are in striking contrast to the expectations for a uniform "glassy" solid phase [33], for which time and history dependent relaxational behaviour is expected.

Recent numerical simulations by Dominguez *et al.* have suggested that sufficiently large currents, far in excess of the depinning threshold, should induce melting via the blowing out of thermally induced vortex loops [40, 41]. Our results demonstrate the existence of an additional mechanism for current induced melting, completely distinct from that proposed by Domiguez *et al.*. We suggest that when a current in excess of the depinning value is applied to a system containing vortex solid domains with superheated regions, then these domains will be displaced from the peaks of the local melting temperature profile. Thus the domains will move into regions where the local melting temperature is significantly lower, and partial or complete melting will occur as a result. Resolidification will take place at the peaks of the melting temperature profile, but not in those in the regions which were originally occupied by superheated solid. Thus the net result is a reduction in the size of the solid domains, this reduction being due to the removal of superheated regions of the solid.

From the explanation given above, it is clear how a sufficiently large current can switch the system from the heated state into the cooled state. Furthermore, it is obvious why this effect does not occur in reverse: A transport current can cause superheated regions of the vortex solid to melt but it cannot possibly induce solidification. Also, it is clear why both the cooled-state and the corresponding state obtained on switching should be stable. In the absence of superheated vortex solid regions, the coexistent phase system corresponds to the stable or equilibrium configuration for a particular temperature point. Thus it is not possible to destroy this configuration merely by applying a transport current. Only by changing the temperature can the distribution of vortex liquid and solid be changed within this equilibrium configuration.

6.7 Summary and Conclusions

In this chapter we presented a detailed description of the dynamic behaviour of the vortex system in $YBa_2Cu_3O_{7-\delta}$ single crystals, across the region of the vortex solid to liquid melting transition. In particular, we focussed on the region of the phase diagram, below the multicritical point, where this transition is first order. Results have been compared from a wide range of different experiments, acquired using both transport and a.c.-susceptibility techniques. In this way, we have built up of a picture of a clearly defined transition region near to the melting line, within which vortex liquid and solid phases coexist.

In common with other authors, we have observed hysteresis in the low-current ohmic $\rho(T)$ curves about the melting transition, and for the first time identified the signature of this hysteresis in the $E(J)$ dependences. From such observations, we have identified the existence of two distinct states at any particular temperature in the transition region, accessible via different thermomagnetic histories. The first of these states was a low resistivity state, reached on warming or field-ramping from a point within the vortex solid regime well below $B_m(T)$. The second state, which had a resistive response as much as an order of magnitude higher, was reached by cooling or dropping the field from a point well above $B_m(T)$. At the low current limit, both of these states were found to be stable and reproducible. However, we have found that on applying a current in excess of a particular threshold value is possible to switch the system from the low resistivity into the high resistivity state. Significantly, the threshold current for the switching effect was found to correspond very closely to a crossover current in the $V(I)$ dependences between a low-current ohmic and an intermediate current highly non-ohmic regime.

Contrary to theoretical predictions for ideal samples [22], we have identified a well-defined width associated with the melting transition. Signatures of this transition width were found in both transport and a.c.-susceptibility measurements, and the two types of measurement showed remarkable similarities. It was found that this transition region was as much as four times as broad as the drop in the low current ohmic resistivity at T_m. Importantly, it was found that the temperature width of the transition region was sample dependent: in the same field ($B = 2$ T) the width varied between samples over the approximate range 100-450 mK. This lead us to conclude that the transition region must arise due to slight sample specific variation in local oxygenation. The full explanation, for the behaviour observed in the transition region can now summarised as follows.

Within any real sample, there are expected to be slight variations in oxygenation, which should lead to concomitant variations in the local melting temperature. The resultant melting profile would allow for the coexistence of vortex liquid and solid phases. In such a coexistent phase regime, the low-current ohmic response should arise mainly due to the percolation of vortex liquid along channels between static solid domains. This explains the sharpness of low-current ohmic resistivity transition since the resistivity is expected to fall to zero on closing of the last continuous channel between solid domains. Given that the low current responses almost exclusively reflect the dynamics of the vortex liquid, we identify the crossover to the non-ohmic regimes as the point where the vortex solid domains start to move. Further to this, we have proposed that the hysteresis across the transition region reflects two distinct states, comprising different distributions of a vortex liquid and solid. Specifically, we suggest that the state reached on warming contains regions of superheated solid which are not present in the state obtained on cooling. Hence the vortex liquid channels are always narrower in the warmed-state case. The switching between states is thought to arise due to melting of the superheated regions following depinning of the vortex solid domains.

In summary, a model of coexistent vortex liquid and solid phases has been proposed which provides self-consistent explanation for a wide range of behaviour in the region of the vortex liquid to solid melting transition.

References

[1] G. Blatter, M.V. Feigel'man, V. B. Geshkenbein; A. I. Larkin and V. M. Vinokur, Rev. Mod. Phys. **66** (1994) 1125.
[2] E. H. Brandt, Rep. Prog. Mod. Phys. **58** (1995) 1465-1594.
[3] For a review see, L. F. Cohen and H. J. Jensen, Rep. Prog. Mod. Phys. **60** (1997) 1581.
[4] D. Bracanovic, University of Southampton Ph.D. Thesis.
[5] T. K. Worthington, F. H. Holtzberg and C. A. Field, Cryogenics **30** (1990) 417.
[6] D. S. Fisher, M. P. A. Fisher and D. A. Huse, Phys. Rev. B **43** (1991) 130.
[7] H. Safar, P. L Gammel, D. A. Huse, D. J. Bishop, J. P. Rice and D. M. Ginsberg, Phys. Rev. Lett. **69** (1992) 824.
[8] M. Charalambous, J. Chaussy and P. Lejay, Phys. Rev. B **45** (1992) 5091.
[9] W. K. Kwok, J. Fendrich, S. Fleschler, U. Welp, J. Downey and G. W. Crabtree, Phys. Rev. Lett. **72** (1994) 1092.
[10] W. K. Kwok, U. Welp, G. W. Crabtree, K. G. Vandervoort, R. Hulscher and J. Z. Liu, Phys. Rev. Lett. **64** (1990) 966
[11] W. K. Kwok, S. Fleschler, U. Welp, V. M. Vinokur, J. Downey and G. W. Crabtree, Phys. Rev. Lett. **69** (1992) 3370.
[12] S. Fleschler, W. K. Kwok, U. Welp, V. M. Vinokur, M. K. Smith, J. Downey and G. W. Crabtree, Phys. Rev. B **47** (1993) 14 448.
[13] R. M. Langan, S. N. Gordeev, P. A. J. de Groot, A. G. M. Jansen, R. Gagnon and L. Taillefer, Phys. Rev. B **58** (1998) 14548-14555.
[14] W. K. Kwok, U. Welp, G. W. Crabtree, K. G. Vandervoort, R. Hulsher and J. Z. Liu, Phys. Rev. Lett. **64** (1990) 966.
[15] Junod, M. Roulin, B. Revaz, A. Mirmelstein, J. -Y. Genoud, E. Walker and A. Erb, Physica C **282-287**, 1399 (1997).
[16] M. Roulin, A. Junod, E. Walker and A. Erb, Phys. Rev. Lett. **80**, 1722 (1998).
[17] V. M. Vinokur, B. Khaykovich, E. Zeldov, M. Konczykowski, R. A. Doyle and P. H. Kes, Physica C **295** (1998) 209.
[18] M. Charalambous, J. Chaussy, P. Lejay and V. M. Vinokur, Phys. Rev. Lett. **71** (1993) 436.
[19] W. Jiang, N. -C. Yeh, S. Reed, U. Kriplani and F. Holtzberg, Phys. Rev. Lett. **74** (1995) 1438.
[20] G. W. Crabtree, W. K. Kwok, U. Welp J. A. Fendrich and B. W. Veal, J. Low. Temp. Phys. **105** (1996) 1073.
[21] S. N. Gordeev, D. Bracanovic, A. P. Rassau, P. A. J. de Groot, R. Gagnon and L. Taillefer, Phys. Rev. B **57** (1998) 645-648.
[22] M Friesen and P Muzikar, *Physica C* **302** (1998) 67.
[23] W. DeSorbo, Rev. Mod. Phys. **36** (1964) 90.
[24] A. B. Pippard, Philos. Mag. **19** (1969) 217.
[25] A. I. Larkin and Yu N. Ovchinnikov, J. Low Temp. Phys. **34** (1979) 409.
[26] S. Bhattacharya and M. J. Higgins, Phys. Rev. Lett. **70** (1993) 2617.
[27] A. I. Larkin, M. C. Marchetti and V .M. Vinokur, Phys. Rev. Lett. **75** (1995) 2992.
[28] C. Tang, X. Ling, S. Bhattacharya and P. M. Chaikin, Europhys. Lett **35** (1996) 597.
[29] D. Bracanovic, S. N. Gordeev, S. Pinfold, R. Langan, M. Oussena, P. A. J. de Groot, R. Gagnon and L. Taillefer, Physica C **296** (1998) 1-6.

---

[30] S. N. Gordeev, A. P. Rassau, D. Bracanovic, P. A. J. de Groot, R. Gagnon and L. Taillefer, in Applied Superconductivity **1** (1997) 1113-1116.
[31] J. Fendrich, U. Welp, W. K. Kwok, A. E. Koshelev, G. W. Crabtree and B .W. Veal, Phys. Rev. Lett. **77** (1996) 2073.
[32] Y. Imry and M. Wortis, Phys. Rev. B **19** (1979) 3580.
[33] V. B. Geshkenbein, L. B. Ioffe and A. I. Larkin, Phys. Rev. B **48** (1993) 9917.
[34] J. W.M. Frenken and J. F. van der Veen, Phys. Rev. Lett. **54**, 134 (1985).
[35] R. W. Cahn, Nature **323** (1986) 668.
[36] J. R. La Graff and D. A. Payne, Physica C **212** (1993) 470.
[37] Y. Yan and W .Y. Liang, Phys. Rev. B **54** (1996) 16234.
[38] S. Kirkpatrick, Rev. Mod. Phys. **45** (1973) 574.
[39] G. Deutscher, in Percolation, *Localisation and Superconductivity*, Vol 9 of the NATO *Advanced Study Institutes: Series B* (Plenum, New York, 1984) p. 94.
[40] D. Dominguez, N. Grønbech-Jensen and A .R. Bishop, Phys. Rev. Lett. **75** (1995) 4670.
[41] D. Dominguez, N. Grønbech-Jensen and A .R. Bishop, Phys. Rev. Lett. **78** (1997) 2644.

CHAPTER 7. HISTORY DEPENDENCE AS A PROBE OF PINNING IN THE MELTING TRANSITION REGION

7.1 Introduction

History dependence is the name given to the phenomenon whereby the response of a system depends not only on the functions of state at the measurement point but also on the thermomagnetic and driving history prior to performing the measurement. An example of history dependence would be a difference arising between *V(J)* dependences for field cooled (**FC**) and zero field cooled (**ZFC**) states. History dependence is a feature of systems demonstrating a region of parameter space over which there two or more metastable energy-levels, as opposed to a unique equilibrium state. Such behaviour is well-known from spin glasses, in which the history dependence is known to reflect the accessibility of a wide range of metastable states [1]. In this context we understand a metastable state to be one which is stable to infinitesimal fluctuations but is not the equilibrium state of the system. By analogy with spin glasses, history dependences in the vortex system of low temperature superconductors such as Nb_3Ge has commonly been attributed to similar glassy behaviour [2]. In a glassy vortex system, responses are expected to be characterised by a broad distribution of relaxation times [3]. On observing a wide range of different superconducting systems, however, it has emerged that the vortex system manifests a number of other distinct classes of history dependent behaviour. In this introduction we review these different types of behaviour in order place our own observations in context.

In the case of $YBa_2Cu_3O_{7-\delta}$ history dependence has been observed in association with phase transitions in the vortex system. Hysteresis related to phase transitions is a familiar concept from the conventional melting/freezing transition. Generally speaking, such behaviour can be related to the metastability of phases outside their normal region of parameter space. This arises due to the energy cost associated with phase nucleation. With respect to conventional melting transitions, hysteresis reflects the existence of supercooled-liquid and/or superheated-solid phases [4]. In $YBa_2Cu_3O_{7-\delta}$ similar phase-transition related history dependence has been observed in the vicinity of both the vortex-melting (see Ref. 5 and references contained therein) and vortex-glass to Bragg-glass transitions [6]. Henceforth we will simply refer to the latter transition as the **VB-Glass transition**.

Hysteresis at the vortex-melting transition has been well characterised and was discussed in some detail in the previous chapter. It is worth noting that this type of hysteresis is so narrow that it falls below the resolution of all but the most careful measurements. History dependences observed in the vicinity of the melting transition have been interpreted within the framework of a model of coexistent vortex liquid and solid phases (see previous chapter). According to this interpretation, there is a region of parameter-space in the vicinity of the melting transition over which vortex liquid and solid phase coexist. As we demonstrated in the previous chapter, various features of the history dependences in this region can be explained in terms of the relative volumes and distribution of the vortex liquid and solid phases.

In respect of the VB-glass transition, history dependence have recently been observed in magnetisation measurements by Kokkaliaris *et al.* [6]. Minor loops showed deviation from the full magnetisation loop over a well-defined range of fields in the vicinity of the second magnetisation peak. In this case, the history dependence observations were explained in terms of differences in the dislocation population. Since the presence or absence of topological defects is expected to be the main qualitative difference between the vortex-glass and Bragg-glass phases respectively, it seems that this too is equivalent to persistence of the vortex glass phase below the VB-glass transition line.

In addition to glassy-relaxational behaviour and the hysteresis observed in the immediate vicinity of phase transitions there is, in addition a distinct class of hysteretic behaviour which manifests itself in terms of history dependences in the responses of the vortex system, ***throughout the solid regime.*** This type of history dependent behaviour has commonly been observed in conventional superconductors such as $NbSe_2$ and $CeRu_2$. In such cases, transport and magnetic responses measured at low temperatures are observed to be contingent on the manner in which the system is cooled across the peak effect regime. Clear differences are observed between *R(T)* curves obtained on warming, starting from the FC and ZFC states respectively[7, 8, 9]. Equivalent hysteresis between FC and ZFC states has also been observed in ac-susceptibility [10, 11, 12] and magnetisation [12] measurements.

Very recently Banerjee *et al.* [10] provided clear evidence that this type of history dependence arises solely as a consequence of pinning. On comparing FC and ZFC *R(T)* dependences for $NbSe_2$ samples with different levels of pinning, they found that in the purest samples the hysteresis between the ZFC and FC curves disappeared altogether. Thus, it seems that this hysteresis reflects two distinct states of the system: one effectively pinned (the FC state), the other much more weakly pinned (the ZFC state). It stands to reason, that if the distinction between these states is due to pinning, then such differences should disappear in the absence of pinning. Extending these ideas, Henderson and Andrei suggested that the strong and weakly pinned states could reflect **disordered and ordered** configurations of the vortex system respectively. This idea has been confirmed by the neutron diffraction studies of Huxley *et al.* [13], which demonstrated much shorter correlation lengths in the FC state than in the ZFC state.

An alternative method for probing the effectiveness of pinning in a particular vortex solid regime, is to contrast the *V(J)* dependences of the different states. In $CeRu_2$ it has been found that whereas the voltage response for the ZFC state (measured at low temperatures) develops smoothly from low currents [9], the FC state voltage shows a sharp onset at a well-defined threshold current. On increasing the current beyond this threshold, the response jumps to the same level as that for the ZFC state. Subsequent measurements of the *V(J)* dependence were then found to reproduce the same smooth curve. Similar behaviour has been observed in $NbSe_2$, but in this case depinning occurred via a series of steps rather than in a single jump [8]. Extending the earlier idea that the ZFC and FC states reflect effectively-pinned disordered and weakly-pinned ordered states respectively, it seems from these observations that the effect of a depinning current is to transform the system for a pinned disordered state to a depinned ordered state. The fact that the response for the depinned state is then reproducible, seems to hint towards the stability of the ordered state. Indeed, in relation to $NbSe_2$, Henderson *et al.* suggested that disordered state is only metastable below the peak effect regime and by applying a current in excess of the depinning threshold we effectively ***anneal the system*** into the equilibrium regime [8].

A very similar type of history dependence has also been observed by Fendrich *et al.* in transport measurements on $YBa_2Cu_3O_{7-\delta}$ [14]. In this case, all measurements were carried out on the FC state in the region below the first order melting transition. Hysteresis manifested itself in both *R(T)* and *V(I)* dependences as a clear difference between the initial (pinned state) curves and the curves subsequently measured following depinning. As in the case of conventional superconducting systems, depinning in $YBa_2Cu_3O_{7-\delta}$ sometimes occurred via a sharp kink and in other cases by way of a series of steps. Thereafter, *R(T)* and *V(J)* curves converged onto a smooth reproducible dependence. By analogy with conventional superconductors, it has been suggested that the hysteresis reflects two distinct configurations of the vortex solid with different degrees of relative disorder, i.e. a weakly-pinned relatively ordered solid state and a much more disordered and consequently more effectively pinned solid state. These observations seem to be in close correspondence to theory, which now predicts that the stable state of the vortex system below the first order freezing transition is a quasi-long-range ordered Bragg glass phase [15, 16] (see Section 4.4). This could explain the smooth reproducible dependences observed in the case of the depinned state. In this context, it appears that the disordered state obtained on FC across the melting transition is indeed only a metastable state of the system.

In spite of the progress in understanding this type of history dependence in the vortex solid regime, a number of important questions remain unanswered. In particular studies to date have not provided any indication as to how disordering develops within the vortex solid as the system is cooled across the freezing transition region. Further to these issues, questions remain with regard to the stability of the depinned regime. It was with such issues in mind, that we devised a novel method for controlling the exposure to pinning in the solidifying vortex system. The new technique is based upon the fact that a high amplitude **annealing**

current can be used to control the effectiveness of pinning within the vortex state. Indeed, by switching the annealing current on and off at different temperatures, we were able to control the way in which vortices interacted with the underlying disorder potential.

In Section 7.2 we provide a brief description of the practical details specific to the observation presented in this chapter. In Section 7.3 we review the concept of an annealing current in the context of the new technique. Sections 7.4 and 7.5 present observations of history dependences in the $R(T)$ and $V(I)$ dependences respectively. In sections 7.6 and 7.7 we consider the effect on the history dependence of increasing field, in the regions respectively below and above the multicritical point. Some of our most important observations are contained within section 7.8, in which we demonstrate that the observed history dependences have nothing to do with relaxation over experimental time-scales. Finally in section 7.9, we summarise the various findings, demonstrating their remarkable consistency with a model of coexistent vortex liquid and solid phases in the solidification transition region.

On reading this chapter it will become apparent that there are a number of procedural parameters associated with the new technique. These include, for example, the magnitude of the annealing current used to control the effectiveness of pinning within the solidifying system. For the most part the precise values of these parameters do not affect the main physics of our observations. For this reason, in the interest of clarity of presentation, we have deferred discussion of the procedural parameters to the Appendix of this chapter.

7.2 Specific Experimental Details

The measurements described in this chapter were carried out on one particular sparsely twinned crystal, Sample A (see Appendix A), inclined at an angle of 15^0 in order to eliminate the effect of twin-boundary pinning. Three key requirements for performing the experiments described in this chapter were:

(i) Temperature stability
(ii) Temperature reproducibility
(iii) Minimal temperature overshoot on approaching target points

The requirements for temperature stability and reproducibility have already been discussed in some detail in Chapter 3. As described in Section 3.4, we were able to achieve temperature stability and reproducibility of better than 5mK for both of the experimental systems used to carry out the measurements described in this chapter.* As a word of caution, it should be noted, however, that even with careful system design such figures for reproducibility only really apply to measurements carried out in a continuous series. There are a number of different reasons for this, notably slight changes in the applied magnetic induction when the magnetic field is dropped at some point between measurements. For this reason, in all cases where direct history comparisons are made, measurements were performed in a single continuous sequence.

With regard to the requirement for temperature stability, even with a fully optimised system, occasionally circumstances arise (such as those generated by an external noise spike)

---

* The majority of the measurements described in this chapter were performed using the Oxford Instruments 14 T cryostat working in combination with the Lakeshore temperature control unit (see Section 3.5.1) . A small number of measurements were performed using the purpose built SQUID picovoltmeter (see Section 3.5.3).

that cause the temperature to depart significantly from the desired level at a given point within the state preparation sequence. For this reason, at all stages in state preparation, a continuous record of the sample temperature was maintained using the GENDAT control program (see Appendix C). Thus, following a given measurement series, we were able to discard all data-points for which temperature had departed significantly from the desired thermal history.[*]

In the descriptions provided within this chapter we merely stated that the temperature was "fixed at a particular point". It should, however, be borne in mind that in all such cases a multi-stage procedure was adopted in order to minimise temperature overshoots. This procedure is described in detail in Section 3.4.2 of the Experimental Chapter.

7.3 Using an Annealing Current to Control Effectiveness of Pinning

In the preceding section, we reviewed the wide variety of history dependent behaviour manifested by the vortex system. The focus of this chapter, is on an entirely new type of history dependence technique for controlling the effectiveness of pinning within the solidified vortex system. This technique is based on an idea, introduced by Henderson *et al.* [8] and considered in the context of $YBa_2Cu_3O_{7-\delta}$ by Fendrich *et al.* [14] that a sufficiently large current can be used the **anneal** the vortex system from a metastable disordered configuration into a stable ordered configuration. Henceforth we will describe such currents as **annealing currents**.

Previous investigations on the effect of an annealing currents [8,14], were limited to studies on an already solidified system. In this chapter we extend this idea by considering the effect of applying annealing current during the cooling process itself and in particular across the solidification region. In later sections of this chapter we will consider the effect of

---

[*] The definition of significant departure depends to some extent on the point in the thermal history at which this occurs. For example a slight drop in temperature at low temperatures is expected to be much less significant than an equivalent increase in temperature close to the melting transition.

switching-off an annealing current at different temperature points during cooling. Here, in order to illustrate the basic principles, we consider the two simplest cases namely those of: applying an annealing current throughout cooling and zero current cooling. In the main frame of Fig. 7.1 we contrast three different *R(T)* curves (solid lines) obtained at the same sweep rate (0.2 K/min) with the same applied current ($I_0 = 10$ mA) and field (B = 4 T). History dependence is immediately evident, in that curve **C** differs markedly from curves **A** and **B**. Whereas curves **A** and **B** were obtained sequentially on cooling and warming respectively, with a 10 mA current applied throughout, curve C was obtained on warming having previously **zero current cooled (ZCC)** the system. Otherwise stated, the only difference

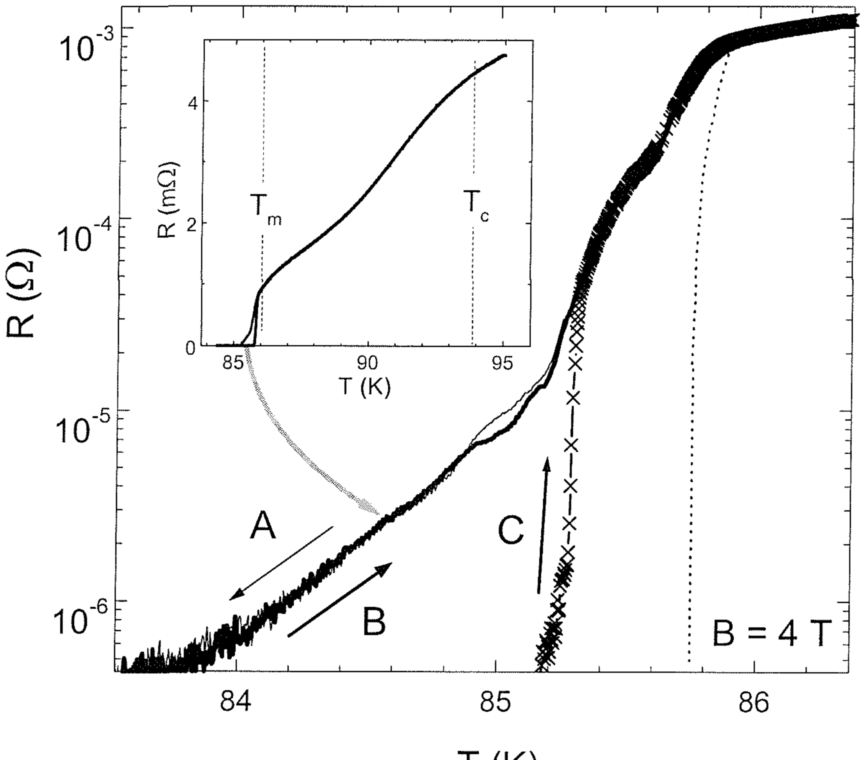

Fig. 7.1. *Effect of applying an "annealing current" during cooling. Curves A-C were obtained using an applied current of 10 mA. Curves A and B were measured sequentially on cooling and warming respectively, with an annealing current applied throughout. In contrast, curve C was obtained on warming having previously zero current cooled the system from a temperature above T_c. Notice in particular the striking difference between curves B and C. Dotted line indicates the position of the ohmic (I = 0.1 mA) resistivity transition.* ***Inset:*** *locates main frame in relation to melting temperature T_m.*

between curves **B** and **C** is whether or not an annealing current was applied on cooling the system down, prior to starting the measurement (in both cases measurements were commenced from a temperature $T = 82$ K).

From Fig. 7.1 it can be seen that whereas the ZCC system depins abruptly and at relatively high temperatures (curve C), the response for the **annealing current cooled (ACC)** system (curve B) develops gradually and from much lower temperatures. It is well known that the strength of elementary forces decreases with increasing temperature [17]. However, the fact that curves B and C differ markedly ***over the same temperature range*** implies that the overall strength of pinning depends not only on the elementary pinning forces but also on the effectiveness of interactions between vortices and pinning sites. On increasing temperature at constant applied current, the system is expected to depin where the elementary pinning strength has reduced to such an extent that the current becomes equal to the depinning current, I_d. The temperature point T_d, at which this occurs, will depend on the effectiveness of pinning of a particular vortex configuration. Hence, given that the ZCC system does not depin until relatively high temperatures, this implies a much more effectively pinned system than in the ACC case.

At this point is worth clarifying precisely what is meant by the term **effectiveness of pinning** as opposed to **strength of pinning**. Strength of pinning is the term used to describe forces arising due to the elementary pinning interactions inherent to a particular sample. The strength of pinning will depend on the nature of the dominant pinning sites (e.g. oxygen vacancies versus twin-boundaries), as well as the applied magnetic field and temperature. It should not, however, depend upon history. In contrast, effectiveness of pinning is the term we use to describe the actual net interaction of vortices with the underlying pinning sites. This measure of pinning is affected not only by the elementary pinning strength but also by the distribution of vortices within a sample.

Referring back to the ideas of Henderson *et al.* [8], we propose that the differing responses obtained in the ACC and ZCC cases reflect relatively ordered and disordered configurations of the vortex system respectively. We expect a disordered configuration to be more effectively pinned, since it reflects a system that has been able to relax towards local minima in the disorder potential. In contrast, for an ordered vortex configuration, in which intervortex interactions dominate, vortices will not generally reside over minima in the pinning potential. It seems, therefore, that the main effect of applying an annealing current during cooling is to suppress relaxation of vortices into the disorder potential. A possible explanation for this phenomenon was provided by the neutron diffraction studies of Yaron *et al.* [18]. In these experiments it was shown that at the high driving force limit, the driven vortex solid undergoes a transition into a relatively ordered dynamic regime manifesting Bragg peaks in its diffraction spectrum. If we assume that a 10 mA annealing current is sufficient to drive the solidifying system into such an ordered dynamic regime, then it is clear how we come to obtain a relatively ordered and weakly pinned system in the ACC case. This is also borne out by the various theoretical and numerical studies that have predicted a dynamic reordering transition at the high driving force limit (see Section 5.3.2).

In the preceding discussion we developed the concept of an annealing current, that is to say a current sufficiently large to screen the interaction between the solidifying vortex system and the underlying disorder potential. We suggested that by maintaining vortices in an ordered configuration, the annealing current has the effect of limiting the effectiveness with which a solidifying system becomes pinned. In the following sections we will explore the effect of switching on and off such an annealing current at different points during the cooling process. In this way we hope to develop an understanding of processes occurring across the solidification transition region.

7.4 History Dependences as a Probe of Changes in Pinning Across the Transition Region

In the previous section we saw that an annealing current can be used to suppress the interaction of the vortex system with the underlying disorder potential. Specifically, we considered the case where such as a current was applied throughout the cooling process. The question that we now pose, is whether the configuration of the vortex system at low temperatures can be controlled by switching on or off an annealing current at different

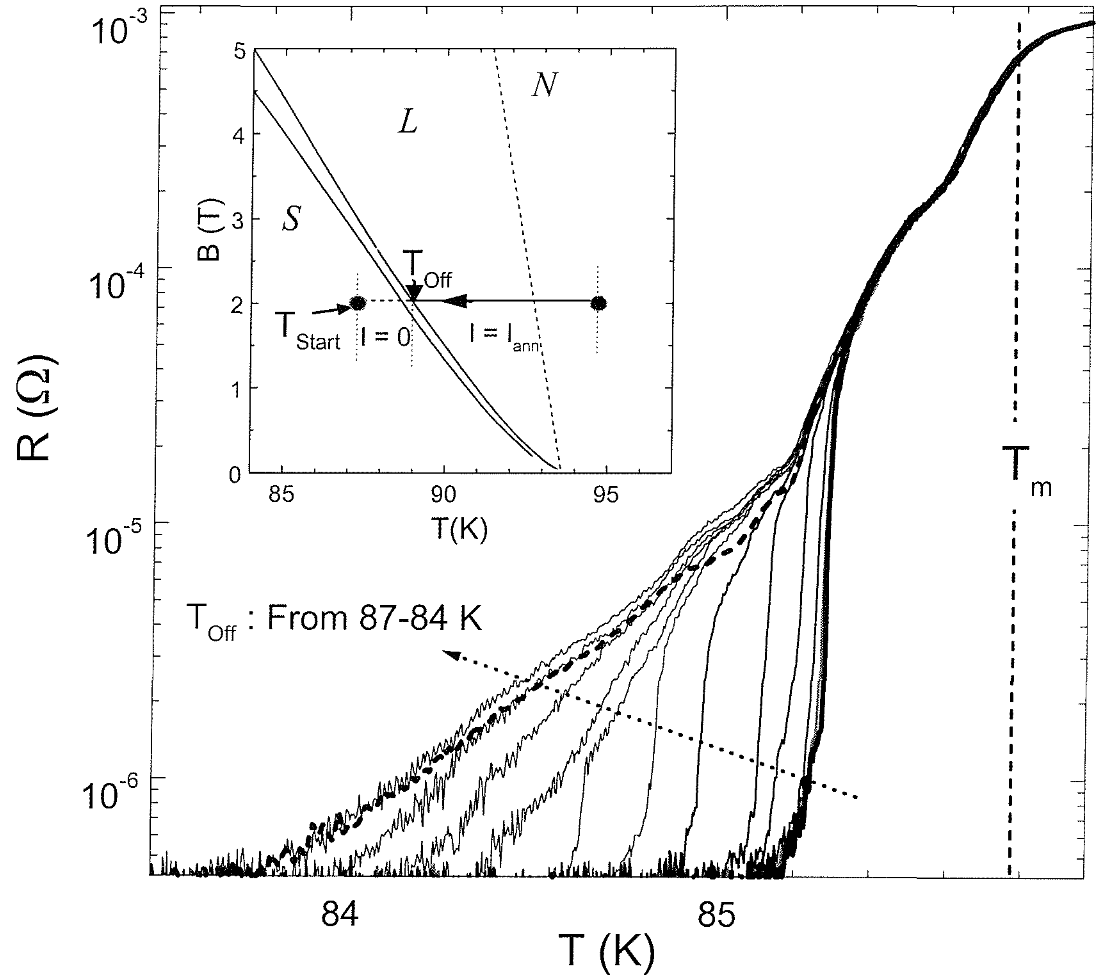

Fig. 7.2 ***Main frame*** *: Series of R(T) warming curves for $B = 4$ T and $I = 10$ mA, obtained following cooling procedures with successively lower T_{off} temperatures (see main text and discussion related to inset). Also shown for comparison (thick line and dashed thick line) are curves obtained following ZCC and ACC respectively.* ***Inset*** *:Schematic representation of cooling procedure used. All R(T) warming curves were commenced from temperature $T_{\mathrm{Bottom}} = 82$ K On cooling prior to performing the measurement, the annealing current was switched off at temperature T_{off}.*

points during cooling. The specific "state preparation method" chosen, was to cool the system with an annealing current applied from a temperature well above T_{m} down to the so-called **exposure temperature T_{off}**. At T_{off} the annealing current was then switched off before continuing cooling to a temperature T_{Bottom}, well below the lower limit of the melting transition region (see schematic inset to Fig 7.2). By repeating this state preparation technique for different values of T_{off} we hoped to observe variations in the effectiveness of pinning the system at low temperatures.

In the first instance we chose to probe the effectiveness of pinning within the solidified system by means of *R(T)* warming curves. In the preceding section, we saw how in the case of the fully ZCC and ACC states, the effectiveness of pinning manifested itself in terms of the temperature T_{depin} at which a measurable voltage response developed. While T_{depin} is not a direct measure of overall pinning strength, we can certainly say that where T_{depin} is higher the system must be more effectively pinned (see discussion in previous section). Here we propose to use the depinning temperature T_{depin} as an indication, albeit indirect, of overall pinning strength.

As demonstrated by the data of Fig. 7.2 (previous page), we have found that there is a clear and systematic effect of the temperature T_{off} on the subsequently measured warming curves. Shown in the figure are a series of *R(T)* warming curves (fine lines), all of which were obtained at a warming rate of +0.2 K/min with a 10 mA current applied. These curves differ only in terms of the temperature T_{off} at which the annealing current was switched off during prior cooling. From the figure it can be seen that just by varying T_{off}, it is possible to produce states with very different pinning properties. The interaction of the vortex system with the underlying pinning potential was at its strongest, as reflected by the high depinning temperatures, where the annealing current was not applied at any stage during cooling (thick line) or else was switched off above T_{m} (fine lines coincident with the thick line). For lower exposure temperatures, the system became progressively less effectively pinned, as evidenced by increasingly lower depinning temperatures. For sufficiently low T_{off}, well below T_{m}, the curves converged on a dependence indicative of a weakly-pinned state. The response obtained at this limit was very similar to that obtained following cooling with an annealing current applied throughout (thick dashed line). Previous observations have lead people to suggest the existence of just two distinct state of the pinned vortex solid immediately below the first order melting transition [8, 14]: a weakly pinned ordered solid phase (perhaps a Bragg glass), and much more disordered state attained on field cooling in the absence of an applied current. Our observations demonstrate that there are in fact a range of different states with a corresponding range of variation in the overall pinning strength.

As shown in Fig. 7.3, such trends can be made more obvious by plotting the depinning temperatures (T_d) for the curves of Fig. 7.2 as a function of the temperature T_{off} at which the annealing current was switched off during prior cooling. Here we define T_d according to a 0.5 μΩ criterion. Immediately obvious from this figure is the fact that the T_d versus T_{off} dependence bears a very close resemblance to the *R(T)* cooling curve (for $I = 10$ mA) across

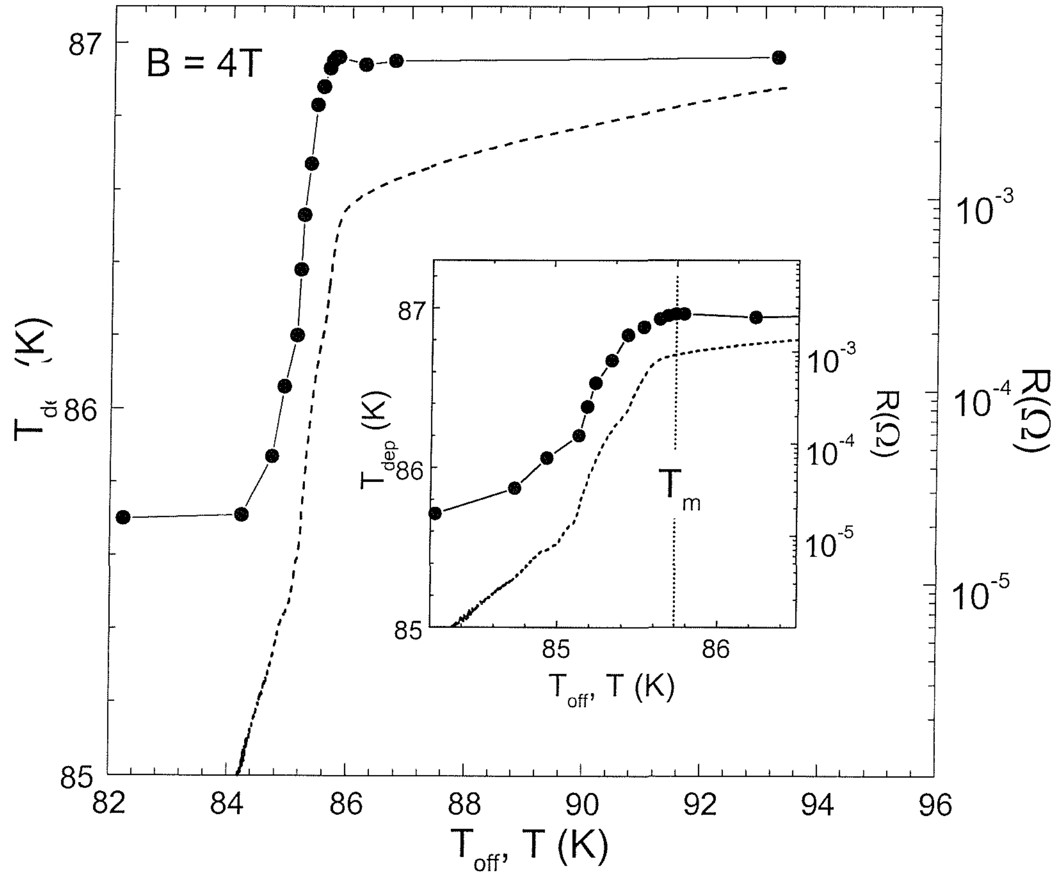

Fig. 7.3 *Circles : Depinning temperatures for the curves of Fig. 7.2 (obtained using a 0.5μΩ criterion) as a function of T_{off}, the temperature at which the current was switched off during prior cooling. Dashed lines : R(T) cooling curves for I = 10 mA. The dashed line indicates the melting temperature for this particular field.*

the same temperature range (dotted line). For T_{off} above T_{m} there is a plateau in the $T_{\text{d}}(T_{\text{off}})$ dependence. This seems to indicate that on ZCC from any point above the melting transition, that the vortex system solidifies into the same disordered and consequently effectively pinned state. Equally, there is a plateau at low temperatures, below the transition region. In this case this seems to indicate an ordered and therefore weakly pinned state. The question that then arises, is what is the nature of the states formed for values of T_{off} in the intermediate range between the two plateaux? We are not able to answer the question from the observations presented thus far but will return to this point in later sections.

Given the striking similarities between the $R(T)$ and $T_{\text{d}}(T_{\text{off}})$ dependencies an interesting question relates to how far they can be directly compared. In the case of the $R(T)$ cooling curve, the resistance reflects the dynamic response of the vortex system. It is not always clear to what extent this response can be attributed to the underlying thermal, inter-vortex and pinning interactions, as opposed to the nature of the drive itself (see Chapter 9). Indeed, this is one of the main problems associated with such dynamic techniques, making it difficult to interpret the results unambiguously. In contrast, the T_{d} versus T_{off} dependence, as depicted in Fig. 7.3, is not a direct measure of the dynamic response at temperature T_{off}. Rather, it reflects how the competition between the intervortex and pinning interactions at T_{off} and below affects the subsequent behaviour of the system. Thus by indirectly probing interactions within the system, history methods such as the one described above have the potential to avoid some of the ambiguities of more standard non-equilibrium techniques.

7.5 Using *V(I)* Depinning Curves to Measure the Pinning Strength of the Vortex Solid

The depinning temperature provides only an indirect measure of the effectiveness of pinning. On ramping temperature, we affect the various intrinsic parameters of the system including the strength of the underlying pinning interactions. An alternative method would be to use *V(I)* depinning curves as a method for probing the pinning interactions. Given that such curves are measured at fixed temperature and field, this ensures that the intrinsic parameters should be the same for each successive *V(I)* measurement and also remain constant over the course of a particular measurement. Hence the depinning currents deduced from *V(I)* dependences should provide a direct measure of effectiveness of pinning in different vortex solid states.

Fig 7.4 (overleaf) shows such a set of *V(I)* depinning curves, measured at a standardised temperature ($T_{\mathrm{meas}} = 85.3$ K) and field ($B = 4$ T), following different cooling histories. The thick line was measured after cooling from 95 K down to T_{meas}, in the absence of an applied current. In contrast the dashed line was obtained after applying an annealing current throughout cooling. The fine lines were obtained following a cooling procedure similar to that depicted in the inset to Fig. 7.2, but with a small waiting time ~ 1 minute at T_{off} before dropping to the measurement temperature T_{meas} (the significance of this waiting time will be considered later in Section 7.8). This procedure can be summarised as follows:

(i) Cool down from 95 K to and stabilise on temperature T_{off}
(ii) Switch off annealing current then wait for a time $t_{\mathrm{wait}} \sim 1$ minute with $I = 0$
(iii) With $I = 0$ drop to T_{meas} and stabilise* before measuring $V(I)$ curve.

---

[*] The reasons for choosing this particular value of T_{meas} will be considered in the Appendix to this chapter. Here, it is sufficient to comment that, had we used a different value of T_{meas} this would not have affected the essential physics of our observations.

The precise method used is schematically illustrated in the inset to Fig 7.4. This method implies that $T_{\rm off}$ should always be greater than $T_{\rm meas}$ but in some cases we desired to measure the effect of applying the annealing current down to lower temperatures. In such cases, the procedure differed slightly in that following the waiting period at $T_{\rm off}$, the system was the warmed up to $T_{\rm meas}$.

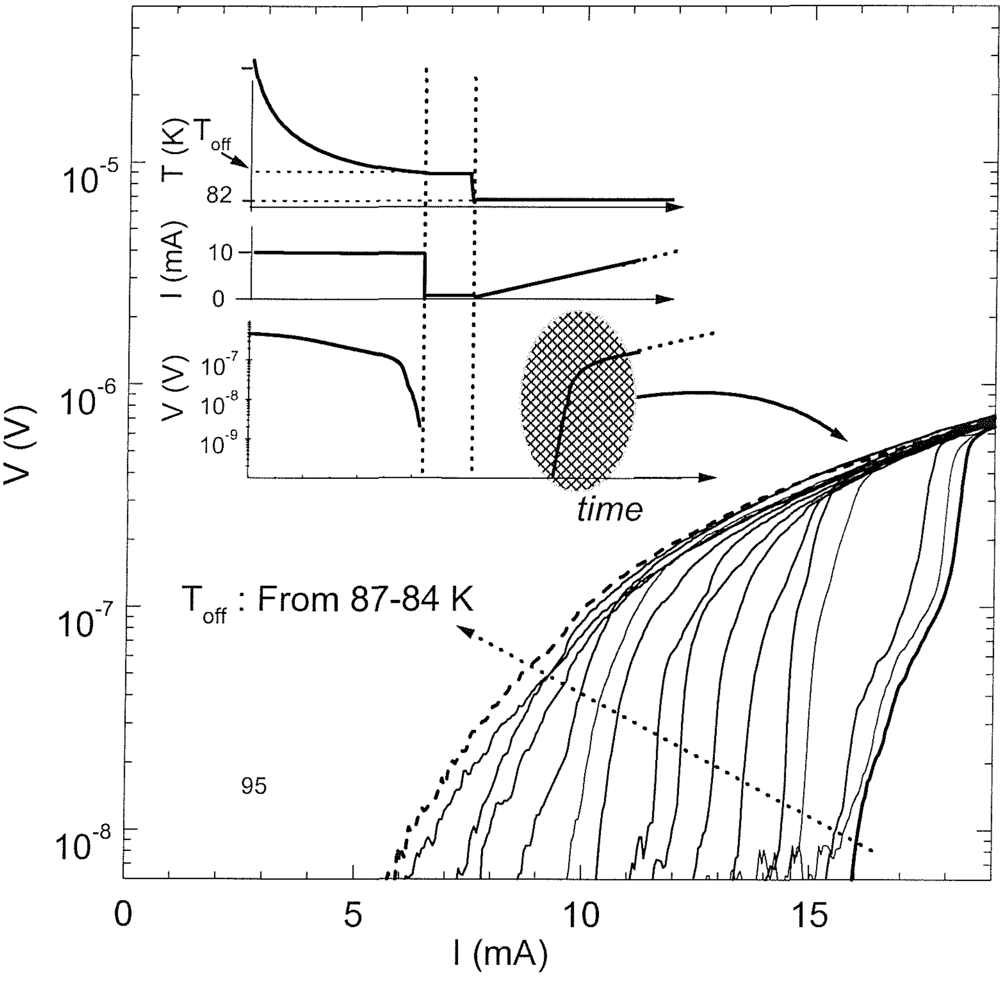

Fig. 7.4 *Thin lines : V(I) curves measured at a standardised temperature T=82 K and field B = 4 T. Note the semi-log scale. These curves differ only in the temperature T_{off} at which the annealing current was switched off during prior cooling. Thick line : curve measured after zero current cooling. Dashed line : curve measured after applying an annealing current throughout cooling.*

***Inset**: schematic representation of the state preparation method (see main text).*

From Fig. 7.4 it can be seen that there is a clear and systematic effect of the temperature $T_{\rm off}$ on the *V(I)* curves measured at temperature $T_{\rm meas}$. As in the case of the *R(T)* history dependences, the *V(I)* curves converge on the ZCC state dependence, as $T_{\rm off}$ is increased to progressively higher temperatures. At the limit of very low $T_{\rm off}$ the *V(I)* curves look similar to those for a state obtained on applying a current throughout cooling.

Once again, in order to reveal the form of the $T_{\rm off}$ dependence we have used a threshold criterion. In this case we have extracted values of the depinning current, $I_{\rm d}$, plotting them as a function of the exposure temperature $T_{\rm off}$. Shown in Fig. 7.5 is the $I_{\rm d}$ versus $T_{\rm off}$ dependence for the curves of Fig. 7.4 and other similar curves (for clarity of presentation we limited the number of curves displayed in Fig 7.4). Also shown for comparison in Fig. 7.5, is the *R(T)* cooling curve over the same temperature interval. As in the case of the $T_{\rm d}$ versus $T_{\rm off}$

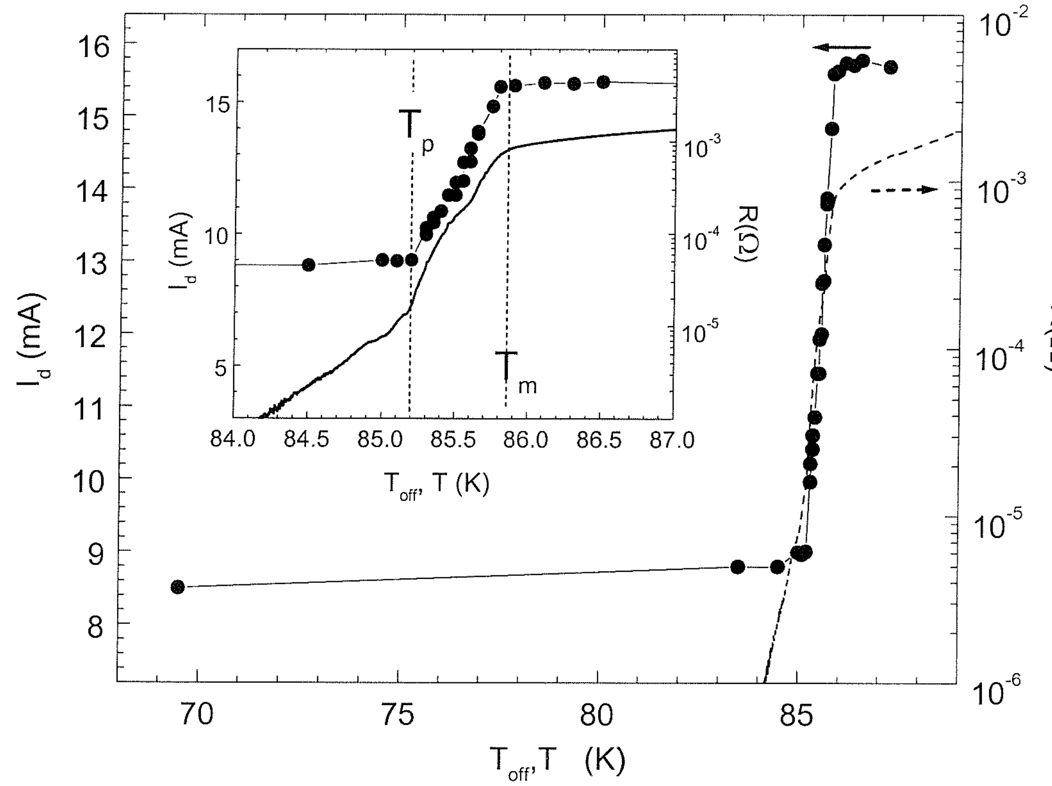

Fig. 7.5 *Circles : Depinning currents, deduced from curves such as those shown in Fig. 6 using a 10 nV criterion (B = 4 T). These have been plotted as a function of T_{off} (the temperature at which the annealing current was switched off during prior cooling). Dashed line: R(T) cooling curve for I =10 mA over the same temperature interval.*

dependence, three distinct regions are clearly identifiable in the $I_d(T_{off})$ dependence. However, in this case, the depinning current provides a direct measure of the effectiveness of pinning strength at the temperature T_{meas}.

The first clear feature of the data, is a plateau in the $I_d(T_{off})$ dependence at high temperatures the onset of which is almost exactly coincident with T_m. Following the arguments outlined above, we attribute points on the plateau to a particular effectively pinned and consequently disordered state of the system. Thus it follows that when an annealing current is switched off at any point above T_m, this is effectively the same as ZCC, and consequently the same disordered solid state is obtained. Furthermore, these observations demonstrate that the development of history dependence must be crucially related to the solidification process commencing at T_m. These observation are not altogether surprising, since intuitively we expect there to be no history dependence, either thermomagnetic or drive dependent, in the liquid regime.*

A second important feature of the data is the linear region of the $I_d(T_{off})$ dependence, starting at the melting temperature T_m. Remarkably the end-point of this region coincides very closely with the peak-effect temperature T_p.. In the previous chapter we described the interval between T_m and T_p as the melting **transition region**. Irrespective of the precise mechanism involved, these data provide extremely strong evidence that this is indeed the region across which solidification occurs. From the present observations alone, it is not possible to state with absolute confidence how this dependence of pinning strength on T_{off} reflects changes occurring across the transition region (we will discuss this in more detail below). However, in the framework of our present understanding, the data provide a clear indication that T_p indeed marks the point at which solidification is complete.

The final obvious feature of the $I_d(T_{off})$ dependence, is low-level plateau in I_d for values of T_{off} below T_p. This can be understood if it is realised that the effect of annealing current is to

---

* Except perhaps in the immediate vicinity of T_m.

ensure that the system solidifies into an ordered and hence weakly pinned solid state. If an annealing current is applied across the whole width of the solidification region, then the system should solidify into a uniformly ordered state. It is only when the annealing current is switched off prior to the completion of solidification that a less than completely ordered system is obtained. The plateau in the $I_d(T_{\rm off})$ dependence for $T_{\rm off} < T_p$, therefore reflects the fact that once the system has solidified into a uniformly ordered state, it is not possible to make it more ordered by the continued application of the annealing current. Equally, the exposure of such an ordered system to the disorder at lower temperatures well below T_m, by switching off the annealing current, seems to have no effect on the degree of ordering within the system. This implies that this weakly pinned ordered state is relatively stable, at least over temperature range and time-scales that we have investigated. This is consistent with theoretical predictions that the stable state of the vortex system in this region of the phase diagram should be a quasi-long-range ordered Bragg-glass phase [15, 16] (see also Section 5.3.2).

7.6 Effect of Magnetic Field on the Development of Pinning within the Field Cooled Vortex Solid

In the previous section we saw how our specially developed history dependence technique can be used to probe the development of pinning across the region of the vortex freezing transition. The previous measurements were for one particular applied field $B = 4$ T. We now compare data obtained using the same method but for three different applied fields, namely: 1.5 T, 3 T and 4 T.* In each case *V(I)* curves similar to those shown in Fig. 6 were measured for a range of different $T_{\rm off}$ values. Here, we recall that $T_{\rm off}$ represents the temperature at which the annealing current is switched off, as the system is cooled down towards to the measurement temperature $T_{\rm meas}$ (see insets to Figs. 7.2 and 7.4 together with

---

* All of these fields lie well below the multicritical field for the particular sample under investigation ($B_{\rm mc} \approx 6.5$ T).

related captions). Due to the field dependence of the melting temperature, for each given field a different T_{meas} was used (see Appendix of this chapter). For the fields of 1.5 T, 3 T and 4 T the selected measurement temperatures were respectively, 88.2 K, 86.4 K and 85.0 K.

Shown in Fig. 7.6 are $I_d(T_{\mathrm{off}})$ dependences for the three different fields, extracted from *V(I)* depinning curves similar to those shown in Fig. 7.4. Obvious from the figure is the essential similarity of form between the $I_d(T_{\mathrm{off}})$ dependences for the three different fields. In each case plateau in the depinning current for high and low values of T_{off}, are separated by transition regions. Recalling that I_d reflects the strength with which the system is pinned, then it seems that in all three cases the majority of pinning develops across this well-defined region. Significantly, the width of the transition region in the $I_d(T_{\mathrm{off}})$ dependences increases with increasing magnetic field.

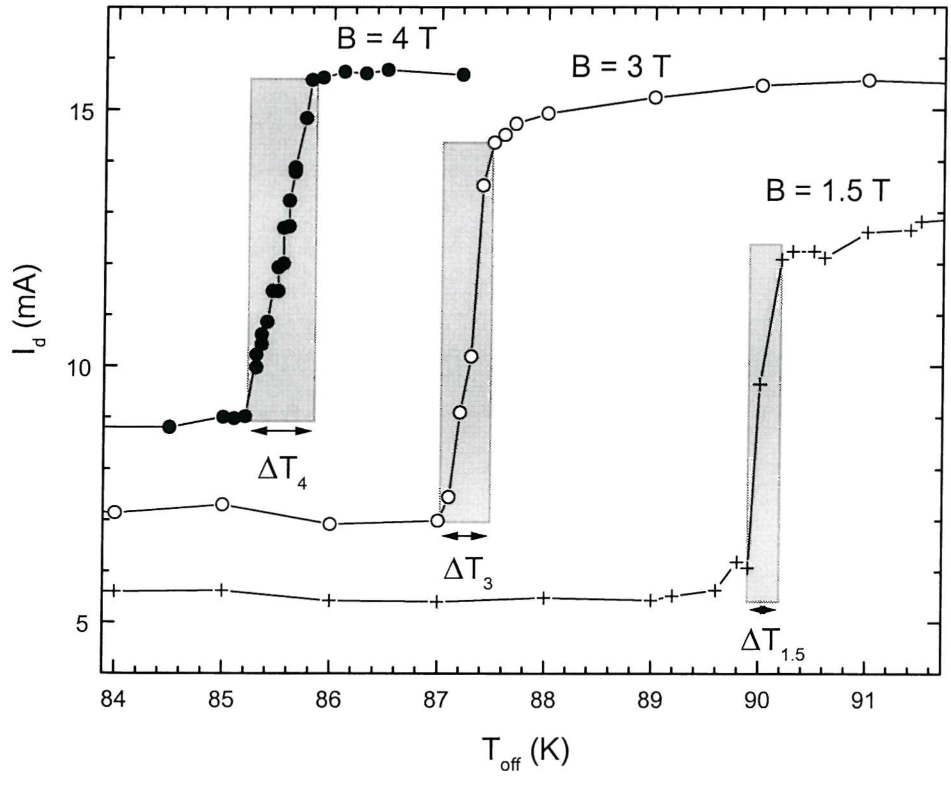

Fig. 7.6 *Depinning current versus T_{off} dependences for three different values of applied magnetic field. In each case the shaded boxes indicate the temperature regions over which the majority of pinning develops. Note that $\Delta T_{1.5} < \Delta T_3 < \Delta T_4$.*

7.7 Disappearance of History Dependence above the Multicritical Point

In the preceding section we saw how, for fields of up to 4 T, the width of the transition region increases with increasing field. A separate question relates to what happens as we further increase the magnetic field, above the so-called multicritical point. From standard transport measurements, we identify this as the point where the melting kink broadens strongly and hence it is supposed the transition becomes second order (see Section 5.2). By testing for history dependence above the multicritical point, we will be able to tell whether such behaviour is dependent on the first order nature of the melting transition.

We have chosen to perform this test by comparing history dependent $V(I)$ depinning curves for two fields, one below and one well above the multicritical point. In each case we contrast depinning curves for the extremes of the most strongly pinned and the most weakly pinned states. These are the states obtained respectively after : (1) Starting from well above T_m and applying an annealing current throughout the process of cooling down to the temperature point at which the $V(I)$ depinning curve is measured (the ACC state); and (2) Cooling down, again from high temperatures, however without applying a current at any stage during cooling (the ZCC state). The purpose of starting from above T_m is to ensure that any prior history dependence has been erased from the system. By contrasting isothermal $V(I)$ depinning curves for the ZCC and ACC states we essentially test for the presence or absence of history effects, rather than examining in detail the dependence on thermal history.

In Figure 7.7 (overleaf) we contrast two sets of isothermal ACC and ZCC state curves, for fields of 4 T (top frame) and 7 T (bottom frame).* As shown by the curves in the upper frame, at 4 T the distinction in terms of pinning properties between the ZCC and ACC states is very clear. For a wide range of measurement temperatures below the melting transition, the curves corresponding to ZCC state (dashed lines) depin at substantially higher currents than

---

* Standard $\rho(T)$ measurements place B_{mc} between 5 and 6 T (dependent on the chosen criterion).

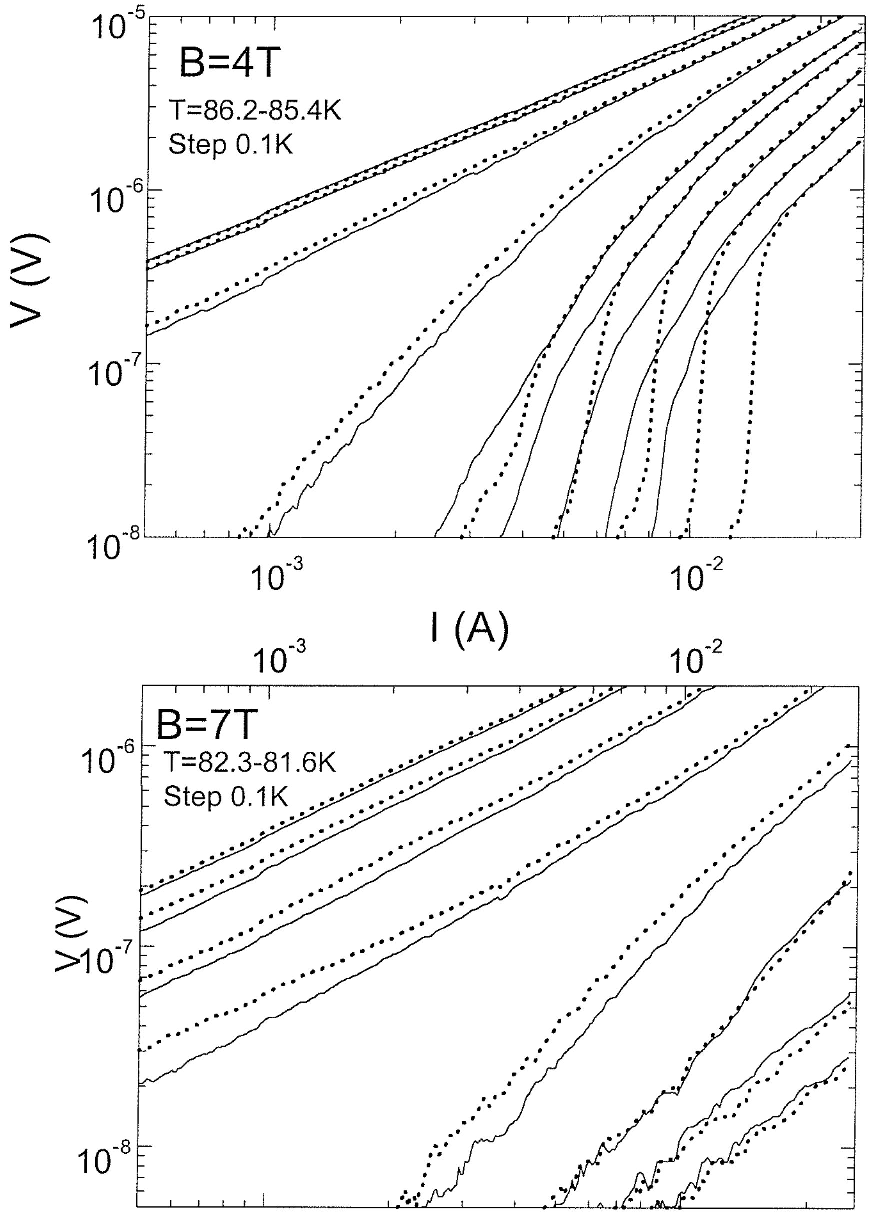

Fig. 7.7 *Comparison of V(I) depinning curves for two fields respectively below (top frame) and above (bottom frame) the multicritical point. Within each frame there are two sets of isothermals, each of which is over the same series of temperatures. The curves indicated by the continuous lines were obtained after applying an annealing current throughout cooling. In contrast the dotted lines were obtained following cooling in the absence of an applied current.*

their ACC state equivalents. Indeed, the curves presented in this frame are merely an alternative representation of the history dependence data presented in previous sections. In contrast, as illustrated by the curves in the lower frame, at B=7T the curves for ZCC and ACC states are very similar. This disappearance of history dependence above B_{mc} indicates that the observed effects must be in some way related to the first order nature of the melting transition.

7.8 Testing for Relaxation in the Transition Region

From the evidence presented thus far we have shown that the majority of pinning within the field-cooled state develops across a narrow transition region between T_{m} and T_{p}. Furthermore, we have demonstrated that the width of this region increases with increasing magnetic field and that above the multicritical point the sharp distinction in pinning properties between the vortex solid and the liquid states disappears altogether. We now return to a discussion of the processes occurring within the transition region itself.

Elementary pinning interactions smoothly decrease with decreasing temperature and hence they are not expected to change substantially across the melting transition region, which has a relatively narrow temperature width ~ 1 K. It follows that the linear drop off in pinning-effectiveness for T_{off} values between T_{m} and T_{p} must in some way reflect the ultimate distribution of vortices within the solidified vortex system. This stands to reason, given that we identify the low and high-temperature plateaux in the $I_{\text{d}}(T_{\text{off}})$ dependences with uniformly ordered and disordered states respectively. Our results thus far have indicated that any differences in the effectiveness of pinning at T_{meas} must arise as a result of processes occurring ***at or below*** T_{off}. This allows for two general ways in which states probed at T_{meas} could reflect processes occurring in the transition region.

(i) The pinning measured at T_{meas} could in some way reflect the state of the system at T_{off} itself. In other words, a signature of this state could be "frozen-in" when we switch off the annealing current. For this to be the case, the signature would have to persist down to the measurement temperature T_{meas}.

(ii) Alternatively the pinning which we measure at T_{meas} could reflect relaxation processes occurring between T_{off} and T_p (the lower limit of the solidification transition region). The observed linear increase of I_d with T_{off} could then be explained in terms of an increase in the relaxation rate within the softening solid system on approaching the melting temperature.

In order to distinguish between these two scenarios, it is necessary to test for relaxation effects within the melting transition region. Relaxation time-scales are expected to drop by several orders of magnitude from tens of minutes in the solid phase to less than seconds in the liquid phase [3, 19]. Although relaxation time-scales are very short within the liquid phase, our previous observations have indicated that this does not manifest itself in terms of history dependence. This is due to the fact that, with the possible exception of the immediate vicinity of the freezing transition, in spite of relaxation the vortex liquid phase remains effectively unpinned [20]. Equally, within the framework of a relaxation scenario, since relaxation rates are expected to fall off rapidly with decreasing temperature, we would expect the effects of relaxation to be most pronounced in the region of the "soft solid" immediately below T_m.

As part of the state preparation technique used in obtaining the *V(I)* depinning curves of Section 7.5, we allowed the system to remain at temperature T_{off} for a time t_{wait} before dropping to the measurement temperature. If there were significant relaxation effects over the time scale of our observations then we would expect the depinning current at T_{meas} to depend not only on T_{off} but also on t_{wait}. Overleaf we have schematically indicated how this would appear in terms of the $I_d(T_{\text{off}})$ dependences.

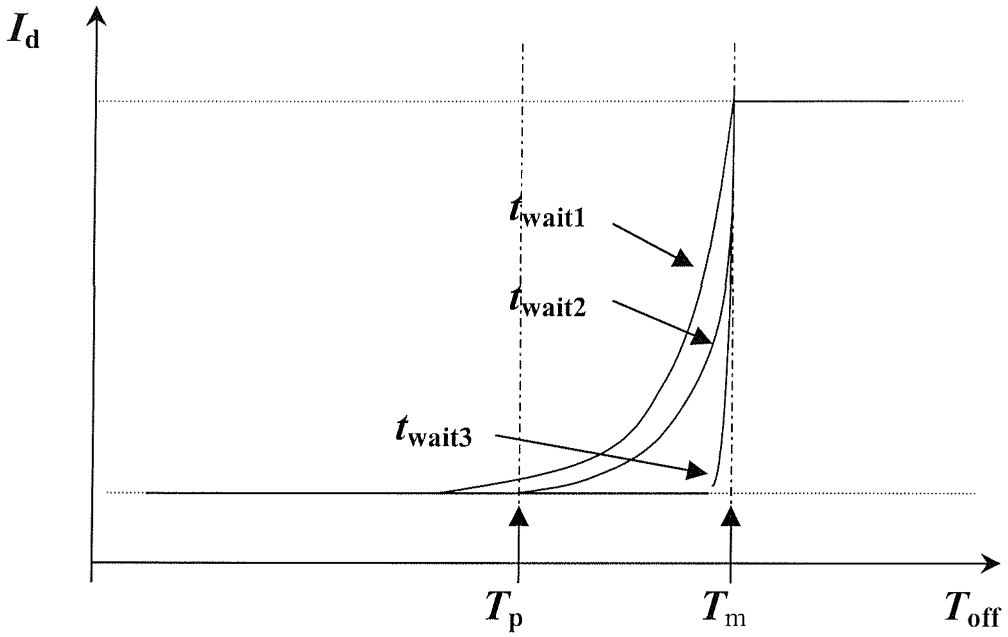

Fig. 7.8 *Schematic representation of the approximate form that would expect the depinning current versus exposure temperature (T_{off}) dependences to take, were there significant time dependent relaxation effects within the system. The figure contrasts $I_d(T_{off})$ dependences for three different waiting times at T_{off}, where $t_{wait3} < t_{wait2} < t_{wait1}$.*

The schematic representation of Fig. 7.8 illustrates the main feature that we would expect in terms of the relaxation behaviour, namely:

(i) For any particular exposure temperature T_{off} within the transition region, I_d would be expected to increase with increasing t_{wait}.

(ii) The effect of relaxation would be most pronounced immediately below T_m and decrease with decreasing exposure temperature. The curves for different waiting times should converge at low temperatures, where relaxation is expected to become negligible over observational time-scales.

(iii) As explained above, there should be no effect of relaxation within the vortex liquid phase. It follows therefore that curves for different t_{wait} should converge for T_{off} values above T_m.

If relaxation were significant over our observational time-scales it is very difficult to see how such time and temperature relaxation could lead to a linear dependence of I_d on T_{off} (as observed in our experiments). However, to decide definitively whether relaxation is the cause of the observed effects, it is necessary to test for a dependence of I_d on t_{wait} at different temperature points within the transition region. In Fig. 7.9 we present a series of *V(I)* curves (symbols) measured at temperature $T_{meas} = 85.0$ K and field $B = 4$ T, following different thermal histories. The dotted line and thick lines respectively represent the ZCC and

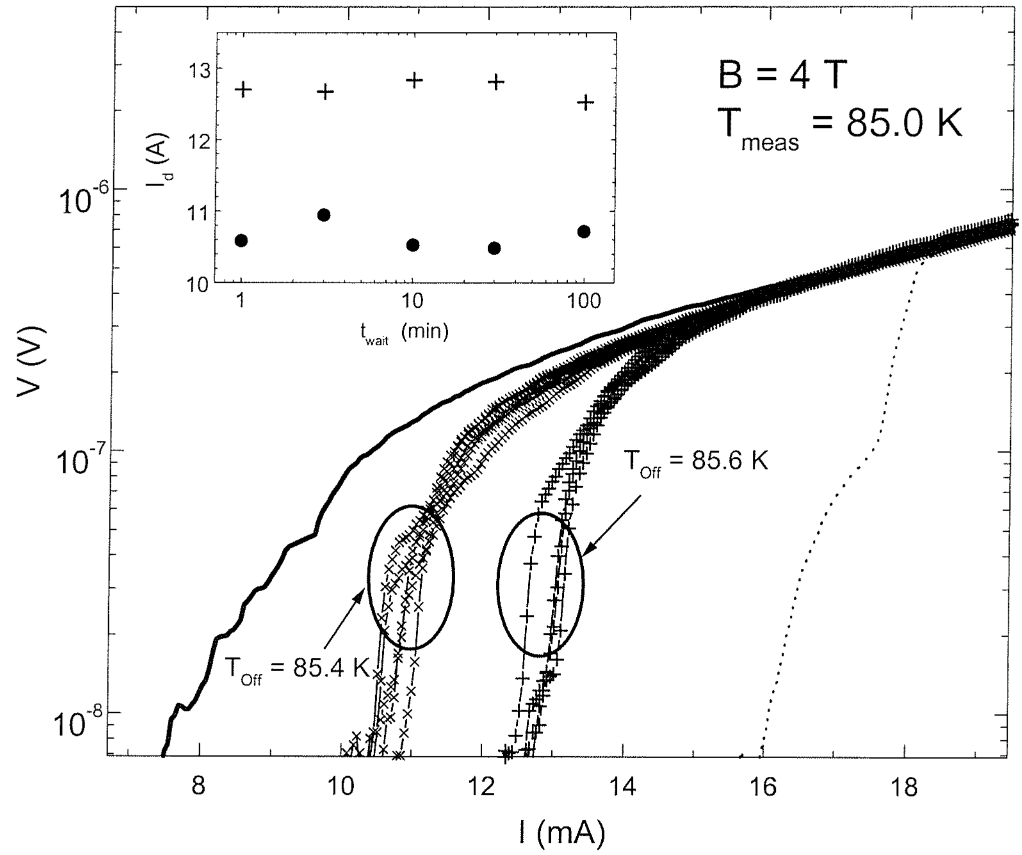

Fig. 7.9 *Solid lines : V(I) depinning curves obtained using the technique shown in the inset to Fig. 6, for a range of different waiting times at two different T_{off} temperatures: . Shown also for comparison are curves for the fully depinned (thick line) and most strongly pinned states (dotted line).* ***Inset**: depinning currents for the fine line in the main frame, extracted using a 10 nV criterion. Notice independence of the depinning current (lack of relaxation) on waiting time t_{wait} for both of the two T_{off} temperatures.*

depinned states, respectively. The fine lines were obtained following cooling histories equivalent to that described in section 7.5. However, whereas previously the waiting time t_{wait} at T_{off} was standardised as 60 s, in the case of the fine lines in Fig 7.9, a range of different waiting times t_{wait} were used. The curves in the figure are in two distinct sets, corresponding to the T_{off} temperatures 85.4 K (diagonal crosses) and 85.6 K (vertical crosses) respectively. Both of these T_{off} points lie within the solidification transition region for $B = 4$ T (see Fig. 7.6). There is some scatter between curves for a given T_{off} temperatures. However, from the inset to the figure it should be evident that there is no systematic relationship between the effective strength of pinning upon the waiting time.

These observations very clearly demonstrate that if time dependent relaxation effects do occur within the transition region, then they must take place over time-scales significantly longer (or indeed shorter) than our observational period (between 1 and 10 minutes). It follows, therefore, that the observed history dependent effects cannot be explained in terms of a gradual softening of the vortex solid on approaching the melting transition[*] Instead, we return to the idea that the dependence of pinning strength on T_{off} in some way reflects the state of the system at T_{off} itself. In the following section we present an interpretation of how this could arise in terms of a model of coexistent vortex liquid and solid phases.

---

[*] These results are also important from a practical point of view. If significant relaxation effects occurred, with a time-scale of the order of minutes, then the response measured at T_{meas} would depend not only on T_{off}, but also on the total length time taken to cool the system down to the measurement point. Since it is difficult to standardise this cooling time, it would be virtually impossible to directly contrast observations obtained following histories with different T_{off} and T_{meas} temperatures. The fact that we have observed no time dependent relaxation over observational time-scales is important in that it demonstrates that any delays in our state preparation process or differences in sweep rate should not affect our results.

7.9 Interpretation of the History Dependences in Terms of a Coexistent Phase Scenario

In Chapter 6 we considered a variety of observations, demonstrating the existence of a transition region in the vicinity of T_m. Based upon these observations and following on from ideas developed by ourselves [21] and other groups (see for example Ref. 22], we developed an explanation for the transition region in terms of a parameter window over which vortex liquid and solid phases coexist. Recent magneto-optical imaging experiments have provided a strong indication that phase coexistence does indeed occur within $Bi_2Sr_2CaCu_2O_8$ [23]. These observations cannot, however, be regarded as absolute proof of phase coexistence, since they were limited in their resolution to observing macroscopic variations in flux density, and not the distribution of individual vortices. We will now demonstrate a remarkable correspondence between the coexistent phase model and our history dependence observations.

Within the framework of a coexistent phase model, the relative proportions of the system in solid and liquid phases vary as the system is cooled across the transition region (for a more detailed discussion see Section 6.6 of the previous chapter). Within the transition region itself, the system is expected to comprise a well-defined spatial distribution of solid and liquid phases. The proportion of the system in the liquid phase should change continuously from 100% at the T_m to 0% at the lower limit of the transition region. In fact, as we will now see, this coexistent-phase model provides a clear explanation for the main features of our history dependence observations.

Central to our interpretation, is the idea that in the presence of an annealing current, solidification occurs into a stable ordered solid phase (see discussion in Section 7.3). If an annealing current were applied down to a point T_{off} within the solidification transition region then according to the coexistent phase model, a well-defined proportion of the system should have solidified. Thus, at T_{off} we would expect the system to comprise mixture of ordered-solid and liquid regions. If the annealing current was then switched off and cooling continued down to a temperature T_{meas}, below the lower limit of the transition region, then the remaining liquid regions should solidify. In the absence of an annealing current, the configuration of vortices within these solidifying regions would be solely determined by a competition between shear and thermal interactions. Hence, for a system with significant pinning, the vortices in these regions would be expected to freeze into a disordered solid [19]. In the absence of significant relaxation within experimental time-scales, as was indeed indicated by the results of Section 7.8, the clear distinction between the ordered and disordered regions of vortex solid should persist down to T_{meas}. It follows that the distribution of (ordered) solid and liquid at T_{off} should correspond exactly to that of ordered and disordered solid at T_{meas}.

Given that we expect vortices in the disordered regions to be significantly more effectively pinned than those in the relatively ordered regions, this implies that the overall strength of pinning at T_{meas} should depend on the proportion of the system in the disordered solid phase. Following the arguments outlined above, this will in turn depend on the proportion of the system which remained in the liquid phase at T_{off}. This interpretation therefore provides a clear explanation as to why the depinning current increases with increasing T_{off} for temperatures within the transition region. The higher the temperature at which we expose the system to the underlying pinning potential the larger the proportion of the system will solidify into a disordered and consequently strongly pinned solid phase.

The interpretation outlined above also explains why we observe plateaux in the I_{d} versus T_{off} dependence for T_{off} temperatures above and below the transition region. Considering initially the former scenario, if the annealing current is switched off at any point above T_{m} then on cooling across the transition region the system should solidify into a uniformly disordered solid phase. That is to say, if the annealing current is switched off when the system is liquid throughout, then the precise temperature point at which this occurs has no effect whatsoever on subsequent pinning properties. Following similar arguments, if the annealing current is switched off at any point past the lower end of the coexistent phase region, then the entire system should already solidified into an ordered solid phase. Given that this phase is stable over time, irrespective of the precise temperature point below T_{p} at which the annealing current is switched off, the same ordered configuration should be attained.

From the arguments outlined above it seems that the coexistent phase model provides a clear and consistent explanation for some of the overall structure of our observations. In addition the model accounts for the more detailed features of our results, namely:

The width the transition region increases with increasing field. As discussed at length in section 5.5.1 of the previous chapter, this can be easily be explained within the framework of a coexistent phase model. The main point made in this section was that phase coexistence could arise due to weak long wavelength inhomogeneities in sample oxygenation. This could result in a corresponding spatial variation in the local melting temperature across the sample. The effect of this inhomogeneity and hence the resultant melting temperature variations would be expected to accentuated with increasing magnetic field.

History dependence disappears above the multicriticai point. Sharp distinctions between the different phases allows for their coexistence over a particular region of parameter space. Above the multicritical point, at which the transition vortex freezing transition becomes second order, it is expected that the sharp distinction between solid and liquid phases should disappear. Hence, above this point it is no longer possible to speak in terms of distinct region of solid and liquid. It is clear, therefore why a distinct coexistent phase region should disappear above this point.

Absence of time dependent relaxation effects. In section 7.8 we presented observations which demonstrated the complete independence of the pinning strength at T_{meas}, on the length of time spent in zero current at temperature T_{off}. This is entirely contrary to expectations for a glassy relaxation scenario (see Section 7.8). In contrast, from the coexistent phase interpretation, the reasons for this lack of time dependence are clear. Within this interpretation, the strength of pinning at low temperatures is determined not by relaxation processes occurring at and below and below T_{off}, but by the state the system has ***already attained*** on reaching T_{off}. The distribution of ordered and disordered solid at T_{meas} is a direct reflection of the distribution of solid and liquid at T_{off}. This distribution is controlled by local thermodynamic conditions at T_{off} and should not therefore be subject to significant relaxation processes. Further to this, it is worth noting that the absence of relaxation within ordered regions of the solid phase is entirely consistent with the idea that the stable state of the system below the freezing transition is a quasi long-range ordered Bragg Glass phase (see Section 4.3.4).

It seems from the evidence collated in this section that there is compelling support for the coexistent phase model. Given that we accept this model to be correct, it should now be possible from our data to estimate the relative proportions of the system in the solid and liquid phases at any particular point in the transition region. At any temperature within the transition region the proportion of the system in the liquid phase can be expressed in terms of the equation:

$$P_{liq}(T) \approx \frac{I_d(T) - I_{d1}}{I_{d2} - I_{d1}}$$

Here $I_d(T)$ is the depinning current measured at $T = T_{meas}$ following a state preparation history with $T = T_{off}$. I_{d1} and I_{d2} represent the depinning currents for T_{off} values below and above the transition region respectively (see inset to Fig. 7.5). In Fig. 7.10 we illustrate the results of applying this calculation to the data of Fig. 7.9.

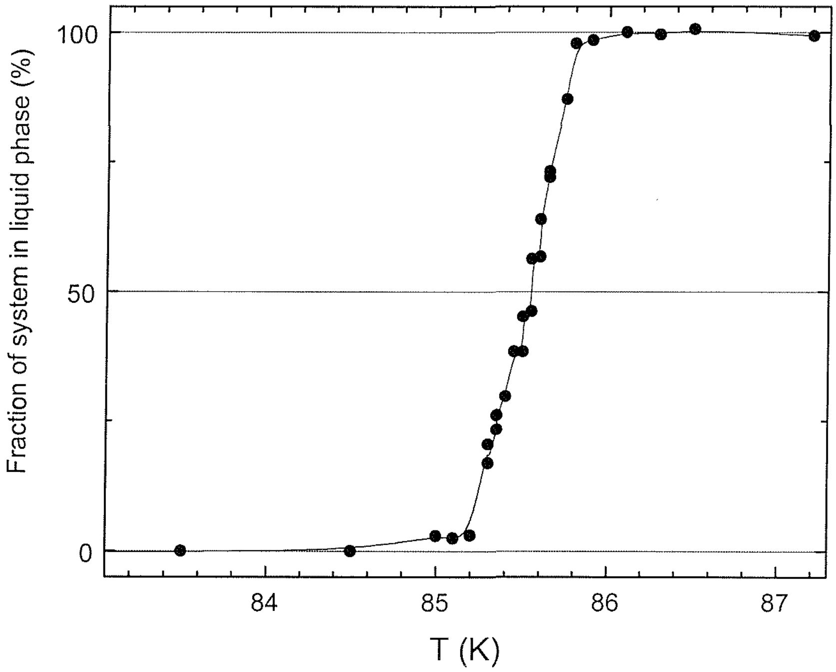

Fig. 7.10 *Estimation of the variation of the proportion of the vortex system in the liquid phase on traversing the transition region for B = 4 T. The figure is deduced from the data in the main frame of Fig. 7.5 recalculated on the basis of the equation given above.*

We justify the use of this model by noting that the *V(I)* curves for T_{off} values within the transition region, depin very abruptly (see Fig. 7.4). This implies that the effectively-pinned disordered regions are responsible for holding the whole vortex system. Thus, the vortex system depins when the sum of Lorentz forces applied to all vortices exceeds the sum of the pinning forces within the disordered regions.

7.10 Summary and Conclusions

In summary, in this chapter we have demonstrated that, at any unique thermodynamic point within the vortex solid regime, dependent only on prior history, states with a wide range of different pinning strengths can be obtained. We relate this variation of effectiveness of pinning to differences in the degree of disorder within the frozen vortex system. We have developed a novel method for controlling solidification of the vortex system, based upon the concept of a so-called annealing current, namely a current which is sufficiently large to wash out the effect of pinning disorder on the driven system. By using an annealing current to control the precise temperature point at which the solidifying vortex system is exposed to disorder, we have found that the changes occurring in the vortex system on solidification occur across a well defined transition region between the melting temperature T_{m} and the peak effect temperature T_{p}.

Building upon concepts proposed in the previous chapter we went on to examine the idea that the transition region defines a temperature interval over which vortex solid and liquid phases coexistent. A remarkable consistency has demonstrated between this interpretation and the essential features of our history dependence observations. Both the broadening of the transition region with increasing field as well as the complete disappearance of history dependence above the multicritical point are entirely consistent with this scenario. The strongest proof, however, stemmed from the failure to observe any relaxation over experimental time-scales at temperature points within the transition region. Were the transition region due to the temperature dependence of relaxation rates within a soft vortex solid, then we would expect significant time dependent relaxation effects to be observed within the system. The absence of such relaxation effects provides very strong support for the coexistent phase interpretation.

Our observations also provide strong support for the idea that the stable phase of the vortex system below the freezing transition is a quasi long-range ordered Bragg glass phase [15]. Firstly there is the absence of relaxation (over experimental time-scales) within the depinned state. Since this is an ordered solid state this indicates the inherent stability of an ordered solid phase. Thus, although there is the possibility for the system to become more strongly pinned in remains stable in relatively weakly pinned configuration. Secondly, whereas the properties of the pinned solid state are very dependent on history, the depinned-state properties are entirely history independent. Thus, our observations indicate that there is a stable, history independent, ordered phase of the system below the freezing transition line, entirely consistent with the predictions for a Bragg glass phase [15].

Chapter 7 Appendix: Dependence of Main Observations on Procedural Parameters and Precise Method Used in History Dependent Technique

In the main part of the chapter we presented the most important features of history dependence observations without regard to precise form of the state preparation technique used. In particular we did not consider the values chosen for the so-called **procedural parameters**, an example of which would be the annealing current. Within this Appendix we consider in more detail the affect of such procedural factors on our core observations.

Dependence on Annealing Current, I_{ann}

In all of our history measurements, an annealing current, $I_{\mathrm{ann}} = 10$ mA was used to control solidification within the system. We justified this parameter choice by stating that, provided the annealing current was sufficiently large, the results of experiments should be the same (see Section 7.3). We will now demonstrate that is indeed the case and discuss the reasons behind this.

As was explained in more detail in Section 7.3, the main effect of an annealing current is to drive the system into an ordered dynamic state. Thus an annealing current can be categorised as a drive in excess of the dynamic reordering threshold, as discussed in a number of theories and numerical simulations (see Section 5.3.2). Provided that the applied current exceeds the threshold current for this reordering transition, it should not matter how large it actually is: the fundamental effect on the structure of the dynamic system should be the same. Where the applied current exceeds the level for dynamic reordering, this ensures that solidification occurs into an ordered solid state. However, if a current less than the threshold were applied, then would be expected to have a very different effect on the driven system. Disorderly flow of vortices would be expected. Hence on cooling in the presence of a current below the reordering threshold, we might expect to obtain a more strongly pinned state. The fact that these assumptions are justified is borne out by the data of Fig. 7.11 (overleaf).

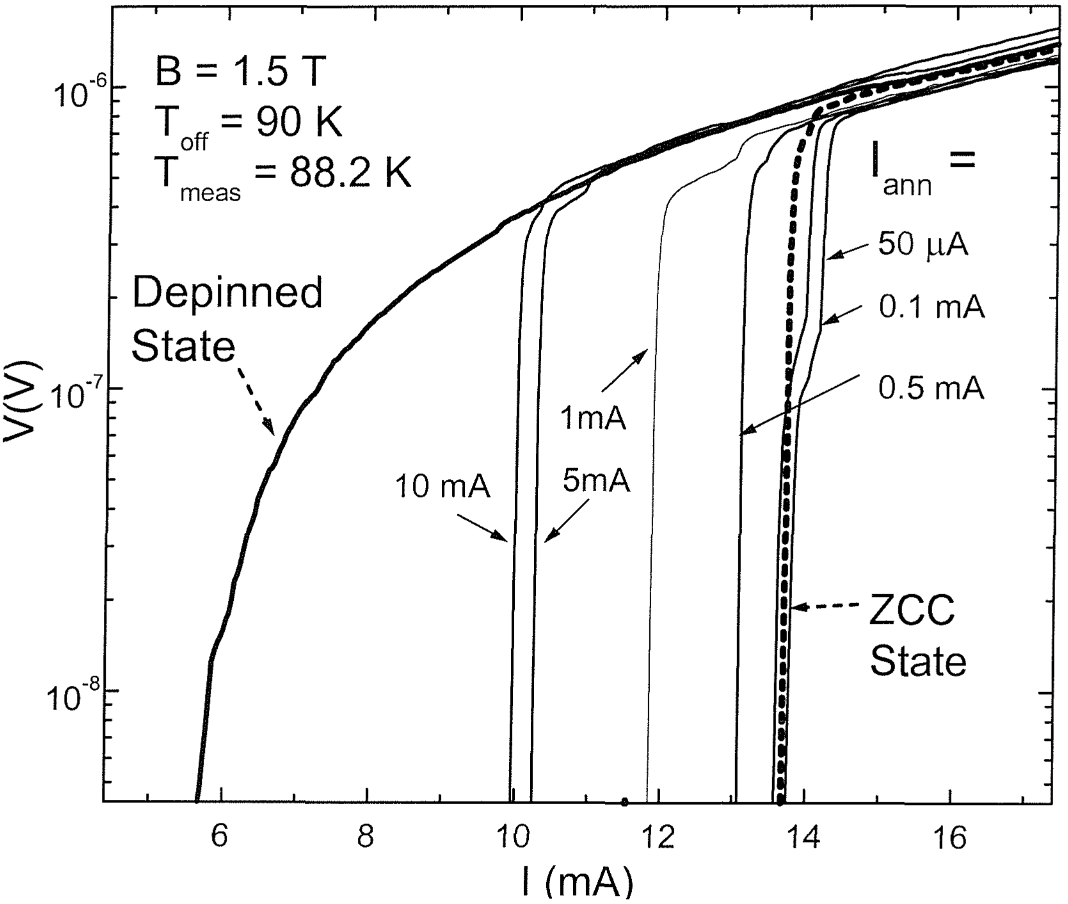

Fig. 7.11 *Fine lines : Current voltage curves measured following the standard cooling history method with* $T_{\mathrm{off}} = 90K$. *The curves differ in the magnitude of the "annealing current" applied during the first part of the cooling. Also shown are the curves for the fully depinned state (thick line) and ZCC state (dotted line) at the same temperature and field.*

Here we show a series of *V(I)* depinning curves (fine lines) measured at a temperature $T_{\mathrm{meas}} = 88.2$ K and field $B = 1.5$ T following the usual history technique (see Inset of Fig. 7.4). For all of these curves the annealing current was switched off at a temperature $T_{\mathrm{off}} = 90$ K, which lies roughly at the midpoint of the solidification transition region for B = 1.5 T (see Fig. 7.6). The curves differ only in terms of the magnitude of the current (I_{ann}) applied during the first part of cooling. From the figure, it can be seen that at the limit of low "annealing current" (the name is not strictly justified in this case) the curves converge on the ZCC state dependence. Thus a low "annealing current" can be considered virtually equivalent to no current at all, in terms of its affect on the solidification process. For higher annealing currents, ($I_{\text{ann}} > 0.5$ mA) the system is seen to depin at substantially lower currents. This reduction in the pinning strength could reflect an increased ordering of the driven system in the vicinity of the dynamic reordering transition. At the limit of high current ($I_{\text{ann}} \geq 5$ mA), there are only relatively small differences between these curves for different annealing currents. Thus, it seems that the magnitude of the current does not have a substantial effect on our observations at this limit. The implication is, that there is a threshold current (in this case ~ 5 mA) and provided that the current we apply is in excess of this threshold it does not matter exactly how large it is. In practise we chose to use a 10 mA current. This can clearly be classed as a "high-driving-force" current, and yet was sufficiently low to limit the risk of damage to the sample contacts.*

Dependence on Measurement Temperature, T_{meas}

The measurement temperature T_{meas} is the point at which we probe the system to identify how strongly pinned it has become following our specific cooling procedure. In Section 7.5 we showed that the pinning in the vortex solid state develops across a narrow range between T_{m} and T_{p}. Thus provided that $T_{\text{meas}} < T_{\text{p}}$, the basic features of our observations should be unaffected by the precise measurement point. For $T_{\text{meas}} > T_{\text{p}}$, however, it is not straightforward to decide in how far the response reflects the measurement point itself as opposed to the prior history. For this reason we restricted our studies to measurement points where $T_{\text{meas}} < T_{\text{p}}$. The fact that the essential features of our observations were the same for different T_{meas} points below the transition region is indicated by the data of Fig. 7.12.

---

* When a high amplitude ac current is to be applied for any length of time to is necessary to consider the possible risk of damage to the contacts. This is slightly different to the case which arises during a current-voltage sweep where the current is ramped up to a very high maximum value and then immediately dropped back down. Again there is a risk associated with such a procedure. However, it is clear that the risk is lower than if the current were applied continuously for long periods of time

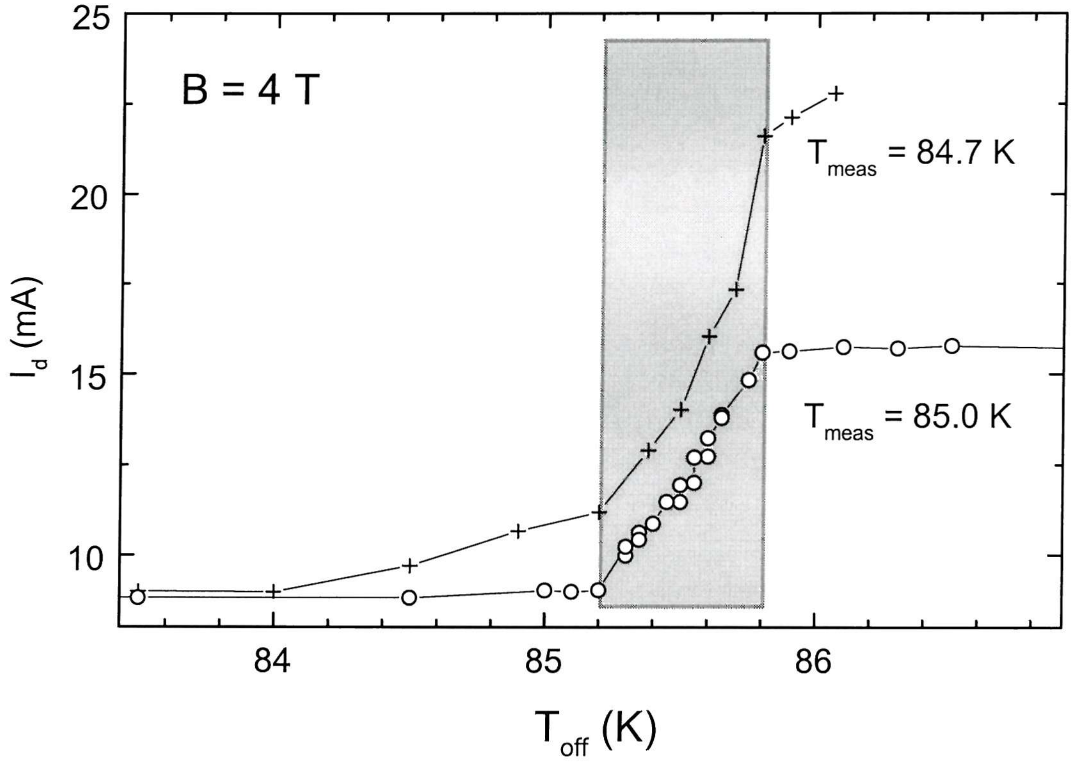

Fig. 7.12 *Depinning current versus T_{off} dependences in a field of 4 T, acquired at two different measurement points, both of which lie below the solidification transition region.*

The $I_d(T_{off})$ dependences for these two measurement points mark out the same transition region, as indicated by the shaded box in the figure. Thus the essential feature of our observations remain unchanged, namely a transition region in the vicinity of T_m, the width of which is determined by the magnetic field.

The observations of Fig. 7.12 also serve to highlight some of the main differences between the data obtained at different measurement points. It is immediately obvious from the figure that in the case of the lower measurement temperature the endpoints of the transition region are much less distinct. This reflects the fact that at lower temperatures the measured voltage response is correspondingly lower, and hence there is a much larger scatter in the measurement of the depinning current. For this reason it would seem preferable to choose a measurement point similar to that of the lower curve in Fig. 7.12 rather than that of the upper curve. In fact, there is a further additional factor, again evident from the data of Fig. 7.12, namely that of the range of the depinning current itself. As we increase the measurement temperature we decrease the range over which the depinning current varies. Thus in Fig. 7.12, for $T_{\mathrm{meas}} = 84.7$ K the depinning current varies over the approximate range 7.5-23 mA, whereas for the higher measurement point $T_{\mathrm{meas}} = 85$ K the depinning current varies over the much smaller range 7.5 mA – 15 mA. From this point of view it is preferable to take to measurement point to lower measurement temperatures where the range of variation in I_d range is larger. Clearly a compromise needs to be reached, the main factors affecting this compromise being:

(i) T_{meas} must lie below the melting transition region. If it lies within this region then it becomes very difficult to separate the effect of the measurement point itself from that of the prior history.

(ii) A measurement point should be selected for which there is a large difference between the depinning currents for the most strongly pinned (ZCC) and most weakly pinned (depinned) states. This effectively increases the resolution of the $I_d(T_{\mathrm{off}})$ dependence allowing for more effective identification of the upper and lower limits of the solidification transition region. This requirement pushes the measurement point to lower temperature.

(iii) The range of depinning currents must not be so large as to exceed the practical upper limit. In our experiments we imposed an upper limit of 25 mA on the applied current, in order to limit the risk of damage to our sample contacts. Thus for any measurement temperature at which the most strongly pinned (ZCC) state had a depinning current greater than 25 mA, the upper part of the $I_d(T_{\mathrm{off}})$ dependence would be inaccessible.

Due to these various conflicting practical constraints, the measurement temperature T_{meas} was the most difficult parameter to select in our experiments.

Effect of the precise cooling technique

The final factor which we consider, is the effect of the precise form of the thermal history on the results of our measurements. According to coexistent phase interpretation presented above, the temperature T_{off} (at which the annealing current is switched off during cooling) is the only physically significant point within the history dependence. In order to demonstrate that this is indeed the case, we have considered three distinct state preparation methods. These methods were as follows (see left-hand frame of Fig. 7.13):

Method 1.	Normal history method. Starting from a temperature well above T_m (thereby ensuring that any prior history dependence is erased) cool down to T_{off} with an annealing current applied. Switch off annealing current and cool down to T_{meas}.
Method 2.	Starting for temperature T_{meas} warm up with an annealing current applied as far as T_{off}. Switch off the annealing current and cool back down to T_{meas}.
Method 3.	Starting from a temperature above T_m cool down to T_{off} with an annealing current applied. Switch off the annealing current then cool down to temperature well below the normal measurement temperature T_{meas}. Leave the system at this low temperature for ~ 5 min then warm back up to T_{meas}.

As demonstrated by the *V(I)* depinning curves in the right hand frame of Fig. 7.13 (overleaf), in spite of the substantial differences between these state preparation methods, virtually identical states were obtained as a result of these different techniques. This impressive correspondence proves that the temperature T_{off} is indeed the significant controlling factor in determining the strength of pinning within the frozen vortex system. Further to this we can draw two ancillary conclusions. Firstly we can state that, in terms of erasing history dependence from the system, the application of a high amplitude current is equivalent to taking the system to high temperatures [cf. curves (a) and (b)]. Secondly we make the observation that time spent at low temperatures in the absence of an applied current [curve (c)] has no effect upon the strength of pinning within the vortex system. This is additional proof for the absence of relaxation effects within the system, even at low temperatures.

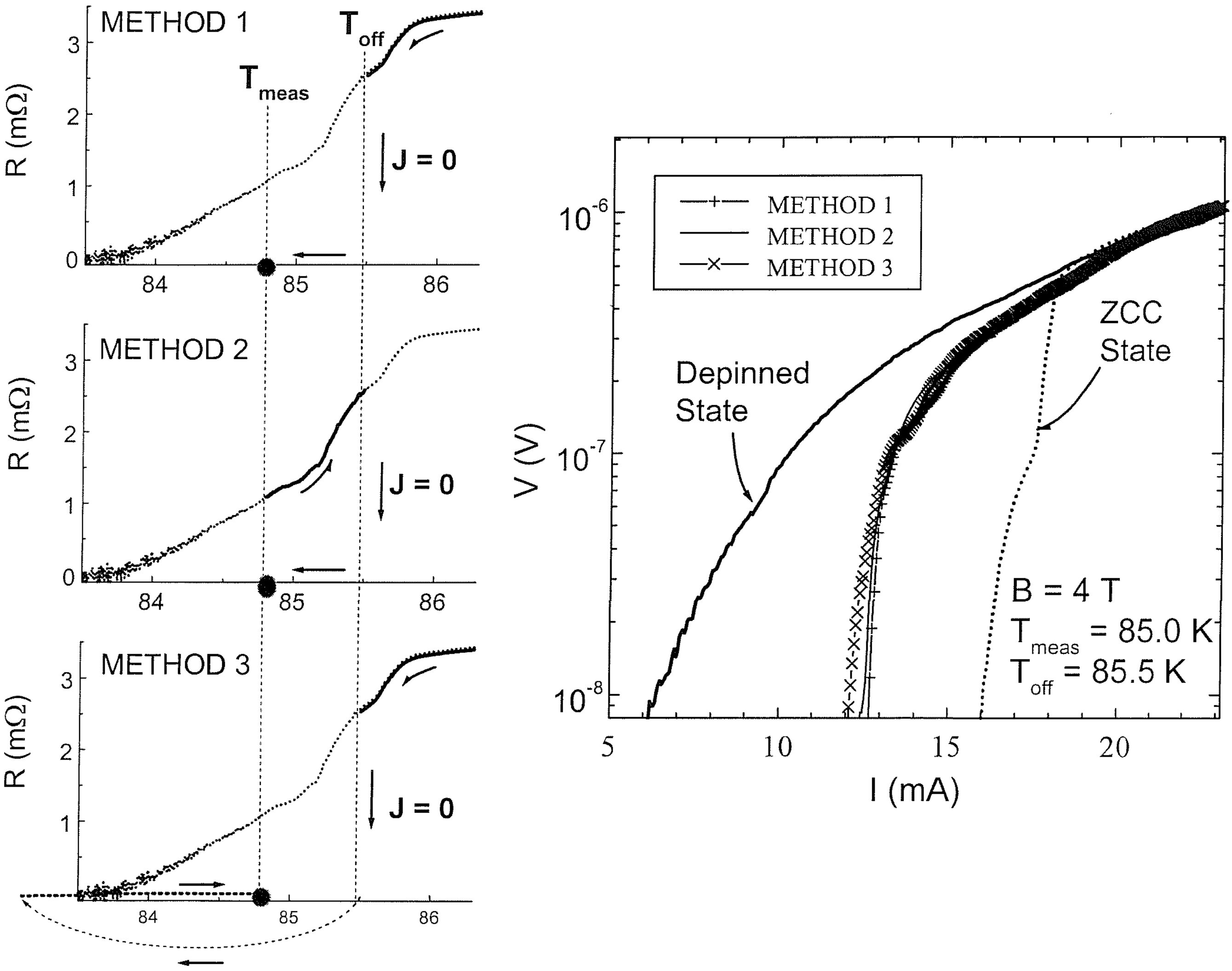

Fig. 7.13 ***Right-hand frame****, V(I) depinning curves for states obtained following three different histories, as illustrated schematically in the* ***left hand frame*** *and described in more detail in the text.*

References

[1] J. A. Mydosh : Spin Glasses, an Experimental Introduction (Taylor and Francis, London 1993).

[2] R. Wördenweber, P. H. Kes and C. C. Tsuei, Phys. Rev. B **33** (1986) 3172.

[3] V. B. Geshkenbein, Phys. Rev. B **48** (1993) 9917.

[4] E. M. Lifshitz and L. P. Pitaevskii, Landau and Lifshitz Course of Theoretical Physics, *Statistical Physics Part 2* (Butterworth-Heinemann, 1996).

[5] G. W. Crabtree, W. K. Kwok, U. Welp, J. A. Fendrich and B. W. Veal, J. Low. Temp. Phys. **105** (1996) 1073.

[6] S. Kokkaliaris, P. A. J. de Groot, S. N. Gordeev, A. A. Zhukov, R. Gagnon and L. Taillefer, Phys. Rev. Lett. **82** (1999) 5116.

[7] X. S. Ling, J. E. Berger and D. E. Prober, Phys. Rev. B **57** (1998) R3249.

[8] W. Henderson, E. Y. Andrei, M. J. Higgins and S. Bhattacharya, Phys. Rev. Lett. **77** (1996) 2077.

[9] N. R. Dilley, J. Herman, S. J. Han and M. B. Maple, Phys. Rev. B **56** (1997) 2379.

[10] S. S. Banerjee N. G. Patil, S. Ramakrishnan, A. K. Grover, S. Bhattacharya, P. K. Mishra, G. Ravikumar, T.V. Chandrasekhar Rao, V. C. Sahni, M. J. Higgins, C. V. Tomy, G. Balakrishnan and D. McK Paul, Phys. Rev. B **59** (1999) 6043.

[11] G. Ravikumar, V. C. Sahni, P. K. Mishra, T. V. Chandrasekhar Rao, S. S. Banerjee, A. K. Grover, S. Ramakrishnan, S. Bhatacharya, M. J. Higgins, E. Yamamoto, Y. Haga, M. Hedo, Y. Inada and Y. Onuki , Phys. Rev. B **57** (1998) R11,069.

[12] S. S. Banerjee, N. G. Patil, S. Saha, S. Ramakrishnan, A. K. Grover, S. Bhattacharya, G. Ravikumar, P. K Mishra, T. V. Chandrasekhar Rao, V. C. Sahni, M. J. Higgins, E. Yamamoto, Y. Haga, M. Hedo, Y. Inada and Y. Onuki., Phys. Rev. B **58** (1998) 995.

[13] A. D. Huxley, R. Cubbitt, D. McPaul, E. Forgan, M. Nutley, H. Mook, M. Yethiraj, P. Lejay, D. Caplan and J. M. Penisson, Physica B **223&224** (1996) 169.

[14] J. A. Fendrich, U. Welp, W. K. Kwok, A. E. Koshelev, G. W. Crabtree and B. W.Veal, Phys. Rev. Lett. **77** (1996) 2073.

[15] T. Giamarchi and P. Le Doussal, Phys. Rev. B **55** (1995) 1242.

[16] V. M. Vinokur, B. Khaykovich, E. Zeldov, M. Konczykowski, R. A. Doyle and P. H. Kes, Physica C **295** (1998) 209.

[17] R. Griessen *et al.*, Phys. Rev. Lett. **72** (1994) 1910.

[18] U. Yaron *et al.*, Nature (London) **376**, 753 (1995).

[19] G. Blatter, Rev. Mod. Phys. **66** (1994) 1125.

[20] S. N. Gordeev, A. P. Rassau, R. M. Langan, P. A. J. de Groot, V. B. Geshkenbein, R. Gagnon and L. Taillefer, Phys. Rev. B **60** (1999) 10477.

[21] A. P. Rassau, S. N. Gordeev, P. A. J de Groot, R. Gagnon and L. Taillefer, Physica B (in press).

[22] A. I. Rykov, S. Tajima, F. V. Kumartsev, E. M. Forgan and C. Simon, Phys. Rev. B **60**

[23] A. Soibel, E. Zeldov, M. Rappaport, Y. Myasoedov T. Tamegai, S. Ooi, M. Konczykowski and V. Geshkenbein, unpublished.

CHAPTER 8. DRIVE DEPENDENT DYNAMICS IN THE VORTEX SOLID REGIME

8.1 Introduction

As we have seen from preceding chapters, the driven vortex system of $YBa_2Cu_3O_{7-\delta}$ manifests a wide range of different dynamic responses, reflecting strong competition between pinning, thermal and inter-vortex interactions. This competition of interactions is expected to be most pronounced in the region of the vortex solid just below the freezing transition. At the low driving force limit, the dynamics of the system are dominated by pinning and the sharp resistivity-drop on freezing [1] simply reflects a transition from a mobile liquid to a static solid state. However, the strong competition between the various interactions across the freezing/melting transition region becomes apparent when larger driving forces are applied. On applying higher currents there is strong non-ohmic broadening of the transition [2], often occurring in conjunction with a pronounced minimum in the $\rho(T)$ dependence just below the melting transition (the peak effect [3]). For a more detailed discussion of these non-ohmic responses see Chapter 6. Further indicators of the complexity of the vortex solid dynamics have been provided by detailed analysis of noise responses and history dependences in the peak effect region of $NbSe_2$ single crystals [4]. In the case of $YBa_2Cu_3O_{7-\delta}$, a variety of hysteretic behaviour has been observed in the transport responses of the vortex solid [5], again indicative of the non-trivial relationship between static and dynamic vortex behaviour.

As was discussed in more detail in Chapter 5, theoretical and numerical studies have predicted a wide variety of dynamic regimes within the vortex solid state, dependent on driving force magnitude, pinning strength and pin-distribution as well as temperature and field. Although the specific details of the various dynamic regimes remain controversial, a broad division of regimes has emerged into: (a) thermally activated regime at low driving forces; (b) incoherent or plastic flow regime at intermediate driving forces[*]; and (c) coherent and relatively ordered dynamic regime at high driving forces. Here, we focus on the distinction between the latter two regimes, describing them generically as the **plastic and elastic dynamic regimes** respectively. It should be noted, however, that this clear distinction of naming is somewhat artificial, in that there is almost always some degree of local plasticity even in a nominally elastic regime (see Section 5.3.4).

While transport measurements cannot tell us about the detailed structure of a particular dynamic regime, many clues can be gleaned from the voltage response. Indeed, qualitative arguments lead us to identify a number of clearly recognisable signatures in transport measurements, distinguishing between the two broad classes of dynamic regime.

Plastic Dynamic Regime

The onset of a significant voltage response above the level of thermal activation is expected to occur gradually, as progressively more and more vortices participate in the motion. In general, above threshold relatively low-level non-ohmic voltage responses are expected, reflecting the importance of pinning. The precise nature of these responses is expected to depend on the strength and distribution of pinning centres within a particular sample. In cases where the pattern of vortex flow changes over the course of time, relatively high noise levels are also expected.

Elastic Dynamic Regime

In an elastic dynamic regime the response is expected to be ohmic and accompanied by relatively low levels of noise. This reflects the relatively weak interaction of the system within the underlying pinning potential.

Implicit in the predictions outlined above, is the idea that the level of ordering within a dynamic vortex system is reflected in its voltage response. This can be understood in terms of the fact that in a relatively ordered dynamic system inter-vortex interactions dominate, hence

---

[*] The width of the window for plastic flow dynamics contracts significantly with decreasing disorder.

it is not energetically favourable for vortices to move far from their "equilibrium" positions within the moving frame. As a result, the driven system experiences the underlying pinning potential as only a weak perturbation on the overall ordered motion. In contrast, for a disordered system, due to fragmentation over much shorter length scales, the driven system is readily able to adjust its motion to accommodate variations in the underlying disorder potential. Consequently, the influence of pinning is much stronger in this case and a much lower level non-ohmic response is expected.

In addition to the dependence of the vortex solid dynamics on the magnitude of the driving force, various studies published by ourselves [6, 7, 8] and other groups [9, 10], have indicated a clear dependence on the modulation form of the drive. In this chapter, we present a comprehensive review of our observations on the drive modulation dependence of the driven vortex solid. In outline, the structure of this chapter is as follows. A summary of the experimental details specific to the observations presented in this chapter is presented in Section 8.2. In section 8.3 we contrast the responses of the system to the three basic types of modulation form namely: single polarity (unidirectional); double polarity (bidirectional) and asymmetric (bidirectional). In particular, we draw attention to the highly anomalous response observed in the case of asymmetric drives, whereby the voltage underwent large amplitude low frequency oscillations with periods orders of magnitude lower than the drive frequency. In sections 8.4, 8.5 and 8.6 we present a detailed characterisation of the voltage amplitude oscillations and summarise the various results in Section 8.7. An interpretation of the oscillatory vortex dynamics is developed in Section 8.8, central to which is the idea that the asymmetrically driven vortex system comprises two distinct domains, one ordered the other disordered, the relative proportion of these domains changing periodically over the course of time. In Section 8.9 we present details of various history dependences and memory effects observed on switching between different drive modulation forms. The observations within this section provide strong support for the interpretation of the oscillatory vortex dynamics developed in Section 8.8. Furthermore, these results provide a strong indication of relative stability of ordered dynamic phase. Finally, in section 8.10 we present a summary of our main findings and conclusions.

8.2 Specific Experimental Details

The effects described in this chapter have been observed on a number of different $YBa_2Cu_3O_{7-\delta}$ single crystals, all of which were grown using a self-flux method in Y-stabilised ZrO_2 crucibles (see Chapter 2). In general, oscillatory voltage-amplitude responses, as described and characterised in section 8.5, were only observed in samples with sufficiently low defect densities. For clarity of presentation, all of the data presented in this chapter refer to one particular detwinned single crystal (Sample B in listing of Appendix A). Transport measurements were performed using the SQUID picovoltmeter arrangement (see Section 3.5.3). Of relevance to these particular measurements, was large frequency bandwidth of this system (> 1 kHz), which allowed for distortion free measurement of responses to drives with a range of different frequencies and modulation forms.

Unless otherwise indicated, all of the observations described in this chapter were performed in a field of 2 T ($H//c$) and temperature $T = 87$ K. This measurement point lies 2 K below the thermodynamic melting line hence the results presented in this chapter correspond to the dynamic behaviour of the vortex solid. To determine the influence of thermal effects on our data we measured $\rho(T)$ curves in the region of the melting transition for a range of different currents. It was found that the sharp onset of the resistivity kink (conventionally associated with the vortex solid to liquid melting transition) occurred at the same temperature for all currents of up to 20 mA. Thus, since the largest current that we used in our studies was 5 mA (corresponding to a current density of 22 A/cm^2), this implies that our observations cannot be due to thermal effects.

8.3 Response of the Vortex System to Different Drive Modulation Forms: Unidirectional, Bidirectional & Asymmetric

Fig. 8.1 illustrates the strikingly different voltage responses observed on applying transport currents with the same amplitude but different modulation forms ($T = 87$ K, $B = 2$ T and $I_0 = 3$ mA). Whereas the sections of the curve marked SPSW and DPSW were obtained using single-polarity and double-polarity square wave-drives, the **ASW** section was obtained in response to a more unconventional **asymmetric square wave** drive.

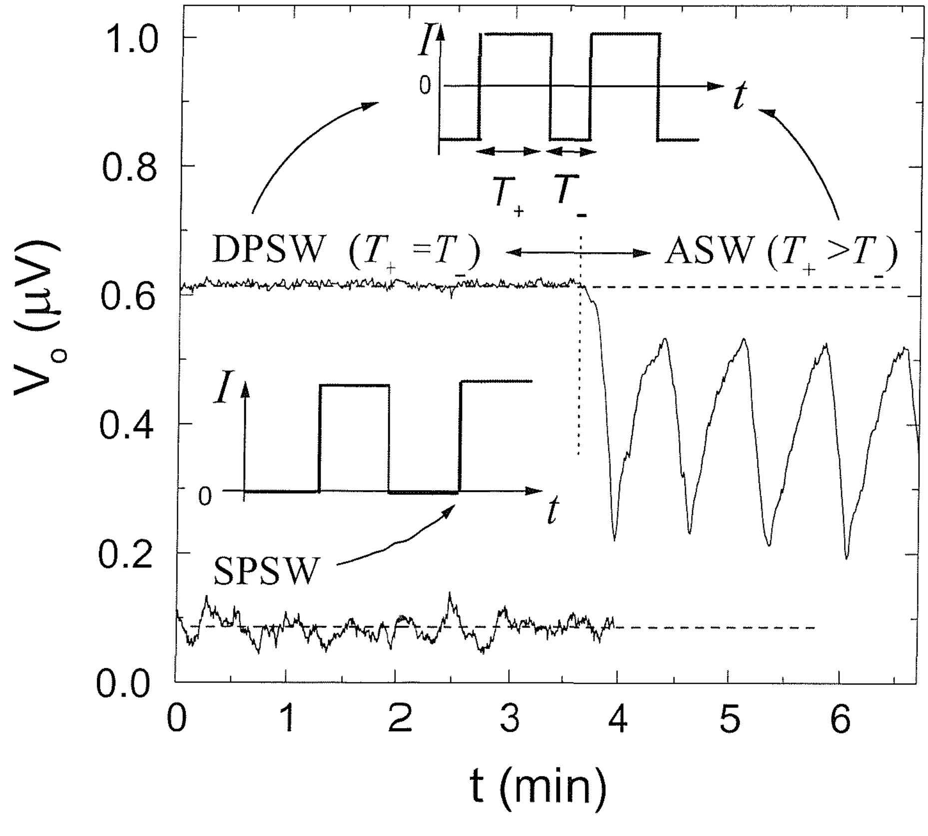

Fig. 8.1 *Time dependence of the voltage response amplitude (V_0) for different applied current modulation forms, namely: double polarity square wave (DPSW); single polarity square wave (SPSW) and asymmetric square wave (ASW). In all cases the applied current had an amplitude $I_0 = 3$ mA and was modulated with a frequency $f_m = 68$ Hz. Schematic insets illustrate the form of the driving currents used.*

In all three cases the drive current was modulated with a frequency $f_m = 68$ Hz. In the case of the ASW drive the asymmetry took the form of difference between the durations of the positive and negative going parts of the square wave period T_+ and T_- respectively (see inset). From this we define a temporal asymmetry:

$$\alpha_t = (T_+ - T_-)/(T_+ + T_-) \tag{8.1}$$

Note that for the ASW data shown in Fig. 8.1, $\alpha_t = 0.1$. It is evident from this figure that the system responds very differently to these three classes of drive. In the case of the SPSW (single polarity square wave) modulation the time averaged voltage response amplitude is low and associated with high levels of voltage noise. For the **DPSW** (double polarity square wave) current, V_0 is relatively high and noise levels are much lower than in the **SPSW** case. The most strikingly different response, however, is obtained in the case of the **ASW** (asymmetric square wave) drive. In contrast to the constant level responses obtained in the DPSW and SPSW cases, for the ASW drive the voltage response amplitude (V_0) demonstrated pronounced periodic variations with time, reflecting a modulation over time of the instantaneous voltage amplitude. In general, the shape of these **voltage amplitude oscillations** was asymmetric, such that the rising edge of each oscillation cycle had a shallower gradient than the falling edge. Whilst the falling edges were approximately linear, the rising edges tended to be less smooth, manifesting a fine structure that often repeated itself across oscillation cycles. Significantly, the frequency (f_{osc}) of these $V_0(t)$ oscillations (~ 0.01 Hz) was much lower than the modulation frequency f_m= 68 Hz of the driving current. Furthermore, as we will demonstrate in Section 8.5.3, f_{osc} was ***independent*** of the modulation frequency for $f_m > 40$ Hz.

Clarification of the term voltage amplitude oscillations is provided in Fig. 8.2. The upper frame shows response, similar to that depicted in Fig. 8.1, as measured using a lock-in detection technique. In the lower frame a schematic representation is provided of how such oscillations of in the voltage amplitude would appear if they were viewed in real time.

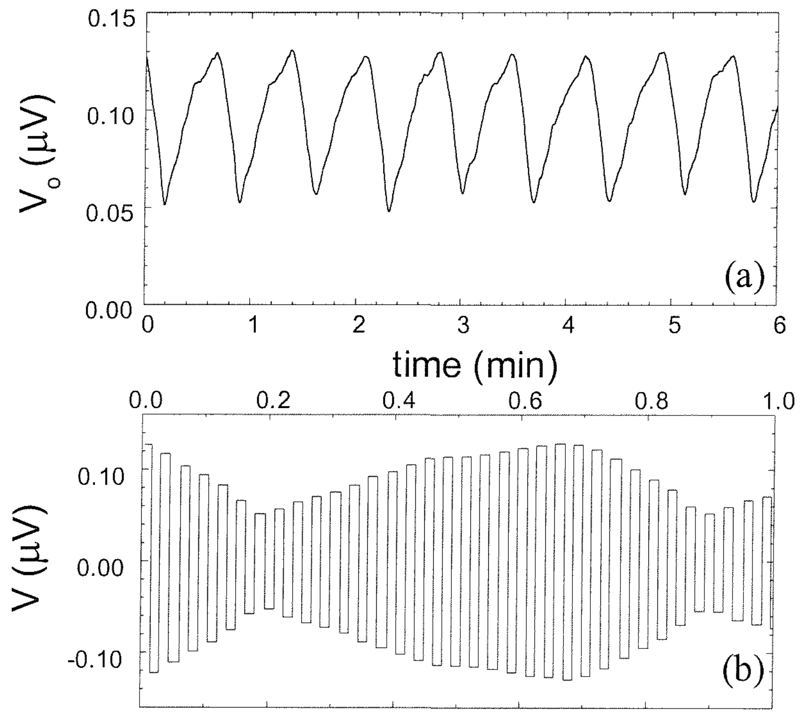

Fig. 8.2 ***(a)*** *Typical example of voltage amplitude (V_0) oscillations obtained on applying a driving current with an asymmetric square wave (ASW) modulation [frequency, f_m = 68 Hz; amplitude I_0 = 3 mA and temporal asymmetry α_t = 0.1 (as defined in the text)].* ***(b)*** *Schematic representation of the initial section of the curve in frame (a), as it would be observed in real time. Note that for clarity of presentation the square wave oscillations in this lower frame have been shown to have a frequency ~1 Hz. In reality the typical modulation frequencies were of the order of 100 Hz thus one oscillation period would consist of about 4000 voltage pulses.*

Returning to a discussion of Fig. 8.1, we note that the amplitude of the response to an ASW drive varies between upper and lower limits ($V_0^{\max}$ and $V_0^{\min}$) which lie between the responses levels for the SPSW and DPSW cases respectively (dashed lines in Fig. 8.1). In fact, we have found that the ratio $V_0^{\max}/V_0^{\min}$ is dependent upon the probing current amplitude (the maximum value that we observed was $V_0^{\max}/V_0^{\min} \approx 3$). For the case shown in Fig. 8.1, the ratio $V_0^{\max}/V_0^{\min} \approx 2$. Since the voltage amplitude undergoes such large oscillations it is clear that this must reflect substantial changes in the structure of the driven system. Moreover, we suggest that, since $V_0^{\max}$ and $V_0^{\min}$ lie between the response levels for the SPSW and DPSW driven system, that ASW driven system is in some way intermediate between the extremes of the SPSW and DPSW cases.[†] Indeed, an ASW drive can in a certain senses be considered to be intermediate between a symmetric double polarity drive and a an entirely unipolar single polarity drive. In Section 8.8 we will discuss this idea in more detail.

Thus far, we have considered oscillations arising in response to a square wave (ASW) drive with an asymmetry in the length of its positive and negative going periods. In fact, we have found that neither the square-wave form, nor the temporal asymmetry per se, were crucial in establishing oscillations. As depicted in Fig. 8.3, $V_o(t)$ oscillations similar to those shown in Fig. 8.1 and Fig. 8.2 can be obtained for a variety of different applied current asymmetries and modulation forms. Curve A of Fig. 8.3 is equivalent to that shown in Fig. 8.2(a) and corresponds to a square wave current with a "temporal" asymmetry $\alpha_t = 0.1$. Curve B was obtained in response to an asymmetric square wave, which in this case had an asymmetry in its amplitude. This type of asymmetry was produced by superimposing a small DC offset (I_{dc}) onto a DPSW current with amplitude I_o, thus we define the amplitude asymmetry parameter as $\alpha_a = I_{dc}/I_o$ ($\alpha_a = 0.025$ for the data represented by curve B). It can be seen from Fig. 8.3, that oscillations arising in response to a drive with an amplitude asymmetry, have practically the same shape as those obtained using a temporal asymmetry. In Section 8.5.2 we will demonstrate that the oscillations are more sensitive to the amplitude asymmetries than to temporal asymmetries.

[†] The intermediate nature of an asymmetric drive is most easily understood on consideration of the particular case of amplitude asymmetries. A square wave with amplitude asymmetry is obtained by superimposing a DC offset onto an initially symmetric DPSW drive. The larger the offset, the larger is the asymmetry and for a sufficiently large offsets the modulation becomes unidirectional and hence is equivalent to the SPSW case. Thus, whereas for an SPSW drive the system is driven in a single direction and for a DPSW drive it is alternately driven with equal force in opposite directions, for an ASW drive the system is driven in both directions but the drive is not equal in the two directions. For a drive with asymmetry in its amplitude this inequality takes the form of a difference in the driving force, whereas for a drive with period asymmetry it is reflected in the lengths of time for which the system is driven in the two opposite directions.

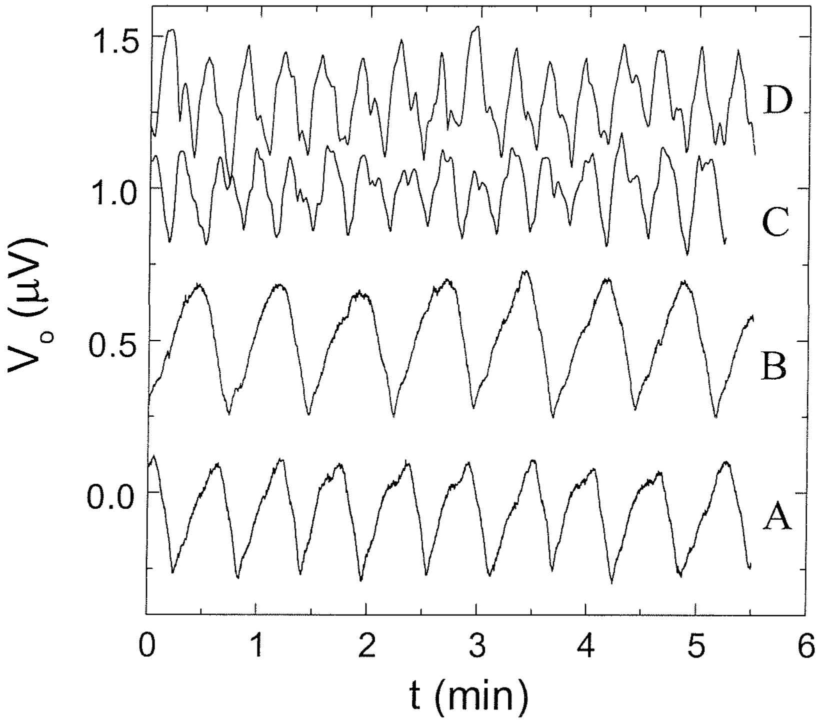

Fig. 8.3 *Voltage amplitude oscillations obtained using various types of (asymmetric) applied current modulation (for clarity the curves have been vertically shifted). Curves A and B were obtained using square waves which were asymmetric in terms of the their period ($\alpha_t = 0.1$) and their amplitude ($\alpha_a = I_{dc}/I_o = 0.025$) respectively. Curves C and D were obtained in response to, respectively, asymmetrically modulated sinusoidal and triangular driving currents. In the case of curves C and D, the asymmetry was achieved by superimposing a DC offset ($I_{dc} = 0.25$ mA) onto a pure oscillatory waveform of amplitude $I_o = 5$ mA. Note that the curves in this figure have been vertically shifted for clarity.*

Modulation by a square wave has one important disadvantage: the reaction of the vortex system and measurement electronics to the sharp fronts of the probing current can be quite complicated. In order to demonstrate that this "sharpness" of the drive does not play a direct role in establishing the $V_0(t)$ oscillations, we investigated the effect of applying asymmetric sinusoidal (curve C, Fig. 8.3) and triangular (curve D, Fig. 8.3) current modulations. In both cases the asymmetry was produced by superimposing a direct current ($I_{dc} = 0.25$ mA) onto a pure sinusoidal or triangular wave-form (amplitude $I_0 = 5$mA) thus giving an asymmetry parameter $\alpha_a = 0.05$ ($\alpha_a = I_{dc}/I_0$). It can be seen from the figure that voltage amplitude oscillations were observed in both of these cases, but they were not as regular as those obtained in response to an ASW drive. This difference can be attributed to the fact that, for triangular and sinusoidal modulations, the applied driving force and hence the interaction of the vortex system with the underlying pinning potential varies continuously over the course of a given modulation period. From this point of view, it is much easier to analyse the behaviour of vortices in the case of a square wave current with a "temporal" asymmetry. For this type of modulation form the Lorentz force is constant over a given current pulse hence the macroscopically averaged interaction of the vortices with the bulk pinning centres is not expected to vary.

The results presented in Fig. 8.3 clearly demonstrate that the precise shape of the alternating current is ***not*** a crucial factor in terms of establishing $V_0(t)$ oscillations. However, the fact that we did not observe oscillations in either the SPSW or DPSW cases would seem to indicate that there are two key requirements for establishing oscillations, namely:

(i) The backwards and forwards shaking action generated by an alternating drive
(ii) An asymmetry in the shaking action, either in terms of its magnitude or its time action.

Whilst the general shape of the oscillations was the same for the different types of alternating modulation form, the most perfect oscillations were obtained using ASW currents. For this reason, in the characterisation provided in the following sections, the discussion has for the most part been restricted to ASW currents with temporal asymmetries. Except where it is explicitly mentioned, the responses to other types of asymmetric modulation can be assumed to be the same.

8.4 *B(T)* Window for the Oscillatory Effects

Voltage amplitude oscillations were only observed over a limited window in parameter space close to the melting line. To establish the temperature width of this window we have compared $R(T)$ curves for different types of probing current modulation (see Fig. 8.4). In all

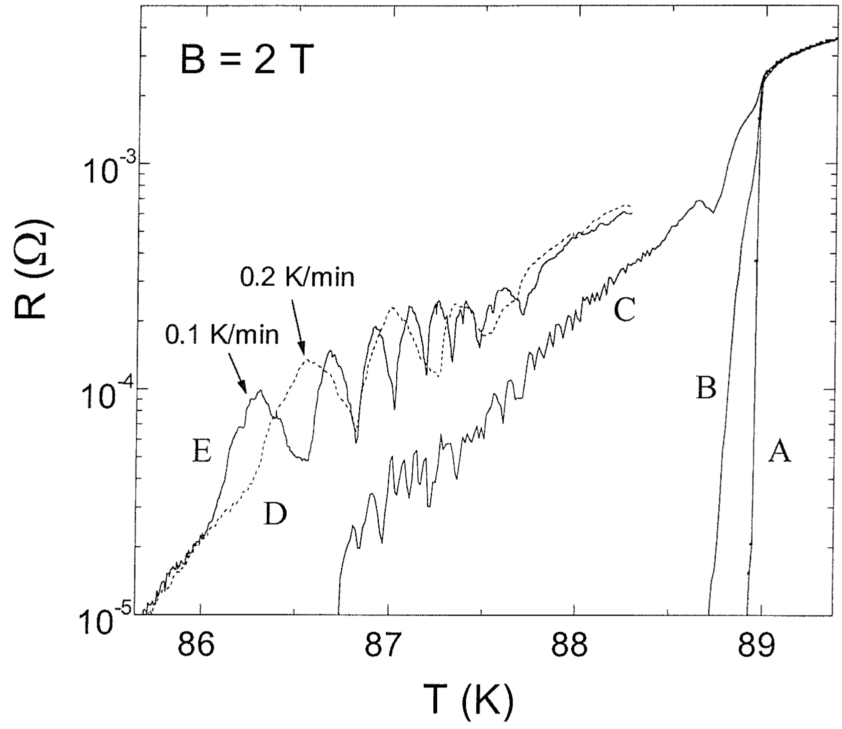

Fig. 8.4 *Resistance versus temperature curves obtained with different applied current modulation forms and amplitudes. Curves A-C were obtained using SPSW current modulations with applied current amplitudes $I_o = 0.1$, 1.0 and 3.0 mA respectively (in each case they were obtained by cooling at a rate of 0.2 K/min). Curves D and E were both obtained using an ASW current with amplitude $I_o = 3$ mA and asymmetry $\alpha_t = 0.03$ but with different cooling rates of 0.2 K/min and 0.1 K/min respectively. Notice in particular the difference between curve C and curves D and E, which were obtained with the same amplitude of applied current but with different modulation forms.*

cases, above the melting transition at T_m, the $R(T)$ curves can be seen to be independent of the applied current amplitude. Below T_m pronounced differences develop between the *R(T)* curves for different applied current modulation forms. Consistent with our observations of voltage as a function of time, nonmonotonic *R(T)* responses were only observed when asymmetric driving currents were applied (curves D and E). The *R(T)* curves for the SPSW case (curves A-C) displayed a form typical of clean detwinned $YBa_2Cu_3O_{7-\delta}$ crystals [11, 12], with a sharp drop in the low current ohmic resistance at $T_m = 89$ K broadening strongly on application of higher currents. At low temperatures, the SPSW voltage response for $I = 3$ mA (curve C) showed irreproducible fluctuations much larger than the base noise levels associated with the picovoltmeter arrangement. This seems to be indicative of a highly nonuniform regime of vortex flow.

Confirmation of the underlying time dependence of the nonmonotonic $R(T)$ dependences is revealed on comparing curves obtained with the same amplitude ($I_o = 3$ mA) and asymmetry ($\alpha_t = 0.03$) of drive, but with different cooling rates. Whereas Curve D was obtained on cooling at a rate dT/dt 0.2 K/min, in the case of Curve E the cooling rate was 0.1 K/min. Above a particular resistance level of ($\approx 3 \times 10^{-5}\,\Omega$) both of these curves are highly nonmonotonic, consisting of a series of unequally spaced maxima and minima. However, Curve E, obtained at the slower cooling rate, manifests approximately twice as many peaks as curve D. It follows that this nonmonotonicity in the $R(T)$ dependences is a manifestation of the same effect which gave rise to the oscillations in the $V_o(t)$ dependences (as shown in Figs. 8.1 and 8.2). We therefore deduce that the form of curves D and E arises due to the superposition of a ***time dependent*** oscillatory component onto a monotonic temperature dependent component. Curves D and E show the same monotonic trend, reflecting the temperature dependence of the resistance but the oscillatory components differ due to the different sweep rates.

An important distinction between the curves obtained using the different modulation forms is that, for the same applied current amplitude, the resistance (at a given temperature $T < T_p$) was always found to be higher in the ASW case that for the SPSW case. In addition, the $R(T)$ dependences obtained using an ASW drive were always much less noisy. These observations, are in agreement with the discussion presented in Section 8.3, the implication being that ASW modulation leads to a more ordered flux flow regime together with a higher overall vortex mobility than in the SPSW case.

In Fig. 8.5 we show *R(T)* dependences similar to curves D and E of Fig. 8.4 but obtained with three different amplitudes of applied ASW current (at a cooling rate of 0.2 K/min). From this figure it is clear that oscillations only appeared for higher I_0 values where the effect of the pinning wells was sufficiently suppressed by the applied current. For small ASW current amplitudes ($I_0 < 1.5$mA) the resistance was seen to drop monotonically to zero, the response in this case being indistinguishable from that obtained using SPSW or DPSW current modulation forms.

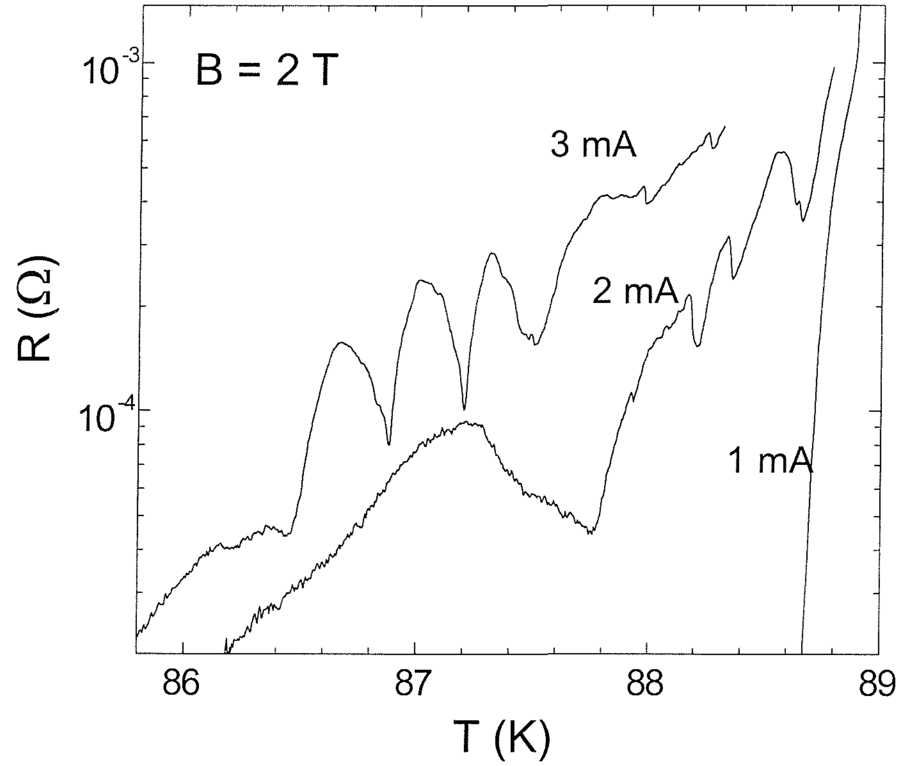

Fig. 8.5 *Resistance versus temperature curves obtained on cooling at a rate 0.2 K/min for three different amplitudes of applied ASW current. In each case the ASW modulation had asymmetry $\alpha_t = 0.03$.*

Shown in Fig. 6 are *R(T)* oscillations, obtained on driving the system with an ASW current (I_0 = 3 mA and α_t = 0.03) for different magnitudes of applied magnetic field. As the magnitude of the applied magnetic induction *B* is increased, the *R(T)* curves shift to lower temperatures, following the decrease in the melting temperature T_m. It can be seen from this figure that the temperature interval between successive minima decreases with increasing *R* and in general that the maxima and minima are more closely spaced for lower magnetic

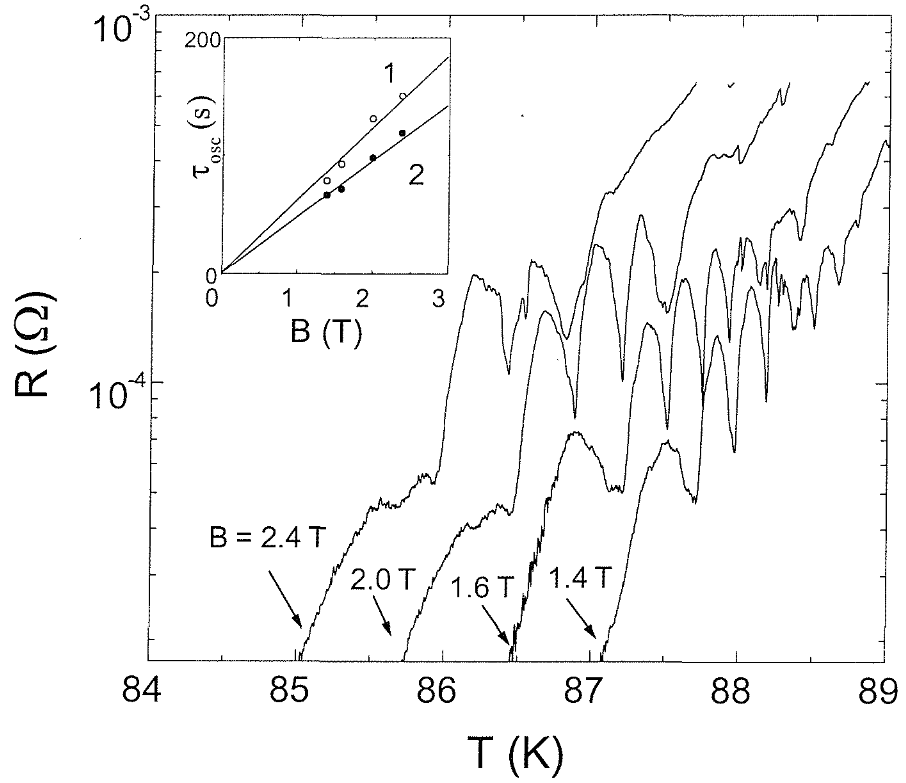

Fig. 8.6 *Resistance versus temperature curves (cooling rate 0.2 K/min) obtained for different values of applied magnetic field. Notice that for any given field, the temperature interval between successive minima along the curves decreases with increasing R. Since all of the curves were obtained at the same constant cooling rate, this spacing provides a measure of the period of the underlying* $V_o(t)$ *oscillations. Inset: Variation of the period of the underlying oscillations with applied magnetic field. The points represented by open circles were deduced from the spacing of the first two minima along the R(T) curves in the main frame of the figure, whereas those represented by closed circles were extracted from the spacing of the second and third minima.*

fields. Changes in the spacing of the minima reflect underlying changes in the period τ_{osc} of the associated $V_0(t)$ oscillations. Thus, since all of the curves were measured at the same (constant) cooling rate, we can use this spacing to estimate the period of the underlying $V_0(t)$ oscillations. The inset of Fig. 8.5 shows how τ_{osc}, as estimated from the spacing of minima along $R(T)$ curves, varied with applied magnetic field. The open circles were extracted from the spacing of the first and second minima at the low temperature end of the $R(T)$ curves whereas the closed circles were extracted from the second and third minima. In both cases the extracted $\tau_{\mathrm{osc}}(B)$ dependences can be seen to be linear.

8.5 Effect of Applied Current Parameters on the Oscillations

8.5.1 Applied Current Amplitude

Obtained using an ASW current (with temporal asymmetry $\alpha_t = 0.1$), the $V_0(I)$ dependence depicted in Fig. 8.7 was measured at constant field $B = 2$ T and temperature $T = 87$ K. The amplitude of the voltage response V_0 was measured whilst increasing the ASW current amplitude at a constant rate of 10^{-6} A/s. The curve obtained in this way represents the superposition of a slow monotonic increase in the mean voltage $<V>$ onto a $V_0(t)$ oscillation. Significantly, the oscillations were observed to appear abruptly at a particular threshold current $I_t = 2.45$ mA. Above this point, the period of the oscillations decreased as the current was ramped. Furthermore it can be seen that the oscillations became increasingly erratic at higher currents thus there exists a relatively narrow current window over which the conditions for establishing of the oscillations are optimal.

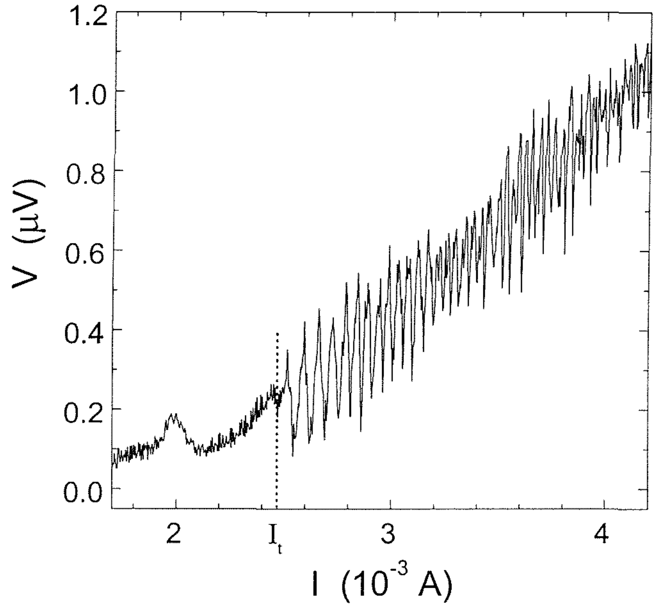

Fig. 8.7 *Voltage response variation obtained on increasing the amplitude of an asymmetrically modulated ($\alpha_t = 0.1$) drive current at a rate of 10^{-6} A/s. Notice in particular that the oscillations appear abruptly at a threshold current $I_t = 2.45$ mA.*

8.5.2 Magnitude of modulation asymmetry

Fig. 8.8 presents $V_0(t)$ oscillations obtained using an ASW current (amplitude $I_0 = 3$ mA) with different values of "temporal" asymmetry α_t. Where the modulation was symmetric ($\alpha_t = 0$) the amplitude of the voltage response was constant and practically the same response was observed for very small asymmetries. Voltage amplitude oscillations only appeared for asymmetries in excess of a critical value $\alpha_{cr} \approx 0.01$, and the oscillations were most regular for asymmetries in the range $0.03 < \alpha_t < 0.16$.

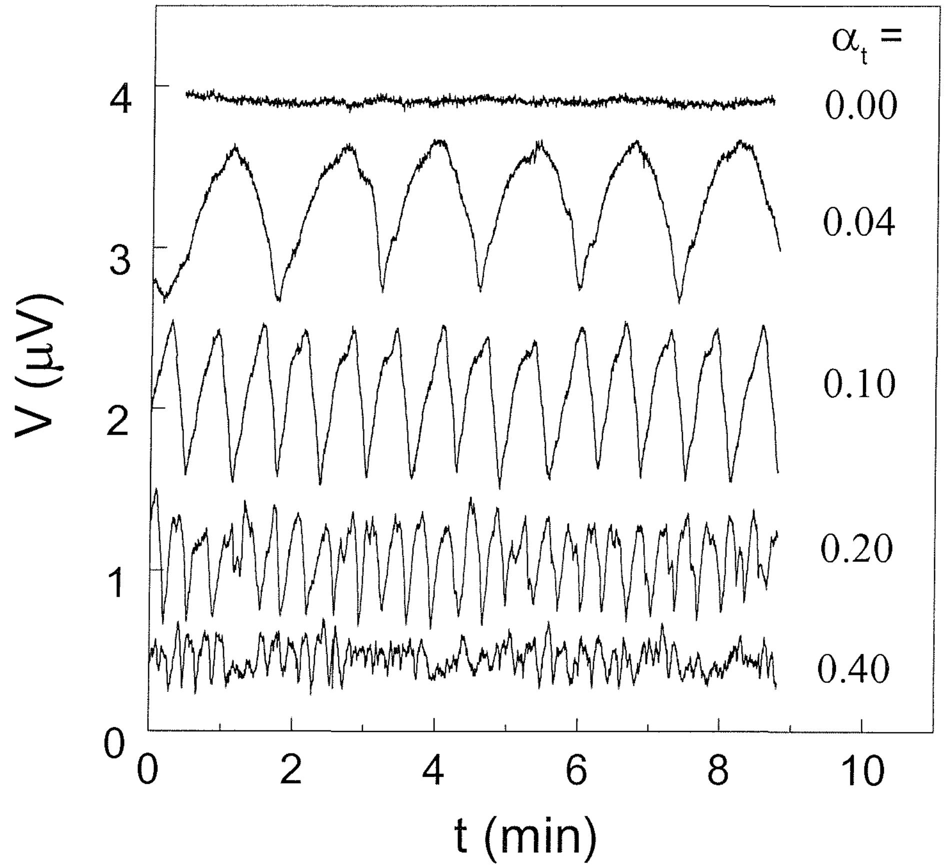

Fig. 8.8 *Voltage response oscillations obtained using asymmetrically modulated square wave currents with a range different temporal asymmetries α_t (for clarity the curves have been vertically shifted). In all cases amplitude $I_0 = 3$ mA. Note that $\alpha_t = 0$ corresponds to a symmetric double polarity square wave current.*

Shown in Fig. 8.9 are Fourier power spectra derived from the curves presented in Fig. 8.8 (the spectrum for $\alpha = 0$ has been omitted since there was clearly no oscillatory response in this case). These spectra show clear peaks at a fundamental frequency and several smaller peaks at the harmonics. The appearance of harmonics is simply a reflection of the non-sinusoidal nature of the $V_0(t)$ dependences. The data points represented by the open circles in Fig. 8.10 show how the fundamental frequency f_{ocs} of the oscillations (extracted from the Fourier spectra) varied as a function of α_t.

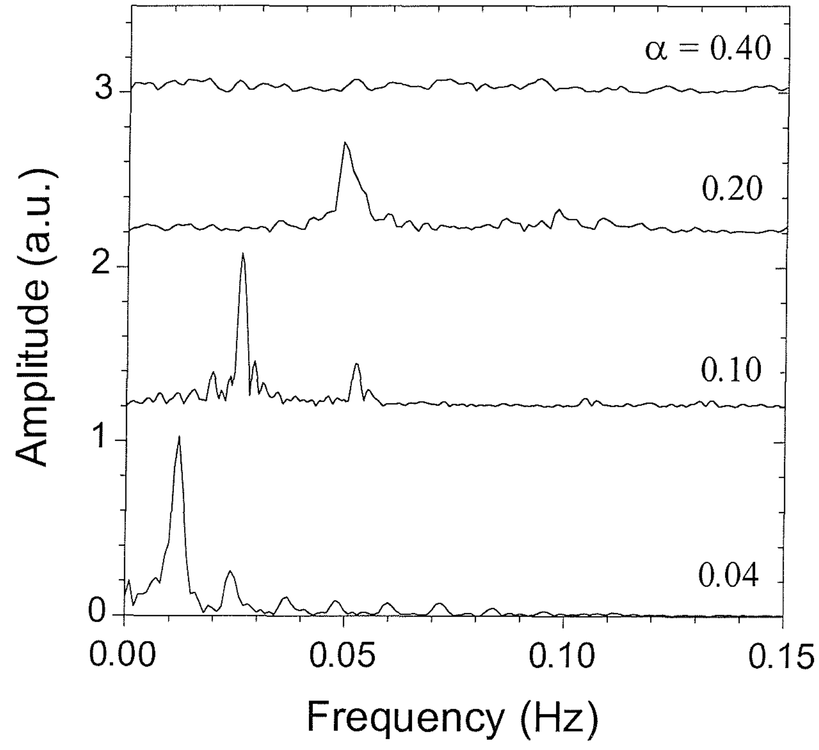

Fig. 8.9 *Fourier transform power spectra obtained from the curves shown in Fig. 8.8 (the spectrum obtained from the DPSW response has been omitted since there were clearly no periodic components in this case). Note that the shape and position of the fundamental peaks in these spectra changes as the applied current asymmetry is increased (for clarity of presentation the spectra have been vertically shifted and the curves for* $\alpha = 0.2$ *and* $\alpha = 0.4$ *have been scaled by factors of 2 and 20 respectively).*

It can be seen that f_{ocs} increased linearly with increasing α_t over the approximate range 0.04 - 0.16. For $\alpha_t > 0.16$ the $f_{\mathrm{ocs}}(\alpha_t)$ dependence starts to deviate from a linear form. This corresponds to the point at which the $V_0(t)$ curves become increasingly erratic and is seen as a decrease in the height of the peaks in the Fourier power spectra (Fig. 8.9). The more erratic the oscillations became, the larger was the deviation of $f_{\mathrm{osc}}(\alpha_t)$ from a linear dependence. For asymmetries above about 0.4, the $V_0(t)$ dependences became very irregular and the peaks in the Fourier spectra disappeared altogether.

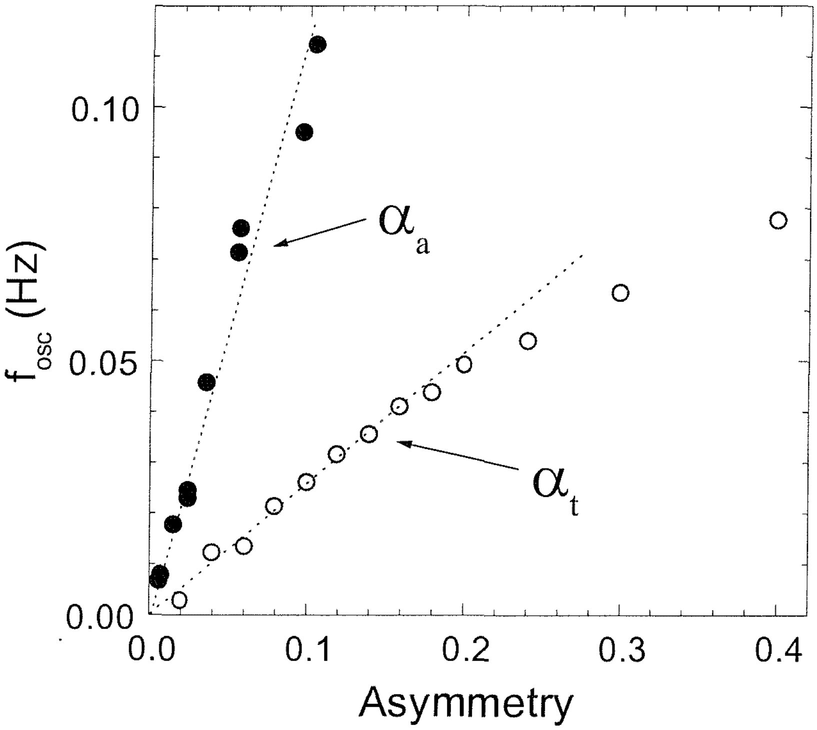

Fig. 8.10 *Shows how the period of the voltage response oscillations (extracted from the fundamental peaks of spectra like those shown in Fig. 8.9) varies as a function of applied modulation asymmetry. The open and closed circles represent oscillations obtained using temporal and amplitude asymmetries respectively.*

We have also studied how the oscillations evolved as the "amplitude asymmetry" parameter α_a was varied. As in the case of temporal asymmetries, the Fourier transforms of the $V_0(t)$ curves revealed that the fundamental frequency of the oscillations (f_{osc}) increased linearly with the magnitude of the asymmetry (closed circles in Fig. 8.10). However, the gradient of the two dependences differed by a factor of 4.5. This difference is due to the fact that f_{osc} depends only indirectly upon the asymmetry of the driving current. In the case of a temporal asymmetry, the asymmetry of the voltage response is identical to that of the driving current. However, for amplitude asymmetries, due to the non-linear *V(I)* dependence, the amplitude asymmetry parameter of the voltage response $\alpha_{\mathrm{a}}^{V} = V_{\mathrm{dc}} / V_{\mathrm{ac}}$ is larger than that of driving current $\alpha_{\mathrm{a}}^{I} = I_{\mathrm{dc}} / I_{\mathrm{ac}}$ (elsewhere we have written α_{a}^{I} more simply as α_{a}). In the case of a power law voltage-current characteristic ($V \propto I^{n}$) the relation between the asymmetries can be written as $\alpha_{\mathrm{a}}^{V} \approx n\alpha_{\mathrm{a}}^{I}$. For the data presented in Fig. 8.7, the *V*(*I*) dependence for currents in the region of 3 mA can be approximated to a power law dependence with $n \approx 4$. This value of n is in reasonable agreement with the ratio of the gradients of the $f_{\mathrm{osc}}(\alpha_{\mathrm{a}})$ and $f_{\mathrm{osc}}(\alpha_{\mathrm{t}})$ dependences (see Fig. 8.10). It should be noted, however, that the oscillatory component of the dependences makes it difficult to extract a precise value for the power index (n) from *V*(*I*) curves such as that shown in Fig. 8.7. Notwithstanding this limitation, we conclude that the fundamental frequency of $V_{\mathrm{o}}(t)$ oscillations is directly related to the net vortex velocity, of which voltage asymmetry parameter is a measure.

The effective amplification of the applied asymmetry due to the strongly non-linear *V*(*I*) dependences can lead to a situation whereby, over a certain range of fields and temperatures, a nominally symmetric current with a tiny parasitic amplitude asymmetry result in a relatively large response voltage asymmetry. Thus oscillations might be observed, even if the applied current was thought to be symmetric. This effect is particularly pronounced at low temperatures where the *V(I)* dependence power-law-index of $YBa_2Cu_3O_{7-\delta}$ single crystals can be as high as 20. For a sample at a temperature and field such that n is equal to 10, an oscillatory voltage response would be observed if the current source has parasitic offset of just 0.1%. This corresponds to a response voltage asymmetry of 0.01, the lower limit at which oscillations were observed.

8.5.3 Modulation frequency

We have seen that the amplitude of the voltage response, as well as the voltage noise are quite different in the cases of DC and ASW currents. It follows that the difference should disappear at the limit of low modulation frequency. Fig. 8.11 shows $V_0(t)$ dependences for three different frequencies of ASW current.

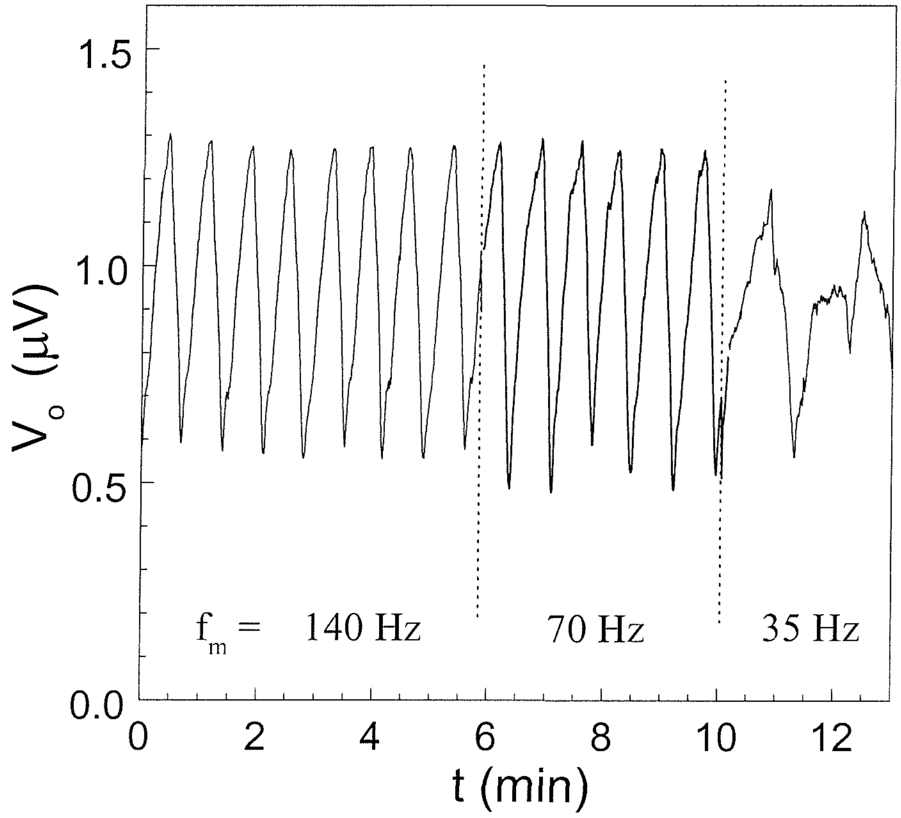

Fig. 8.11 *Demonstrates that above a certain limit, the period of the voltage response oscillations is unaffected by the frequency (f_m) of the driving current modulation. The oscillations shown were obtained using an ASW current with α_t = 0.1 and I_o = 3 mA.*

In general, it was found that for modulation frequencies in the range 40 Hz $< f_m <$ 200 Hz, the $V_0(t)$ dependence manifested oscillations whose period and shape were independent of f_m. At lower modulation frequencies, the $V_0(t)$ dependences became increasingly erratic and for $f_m < 4$ Hz the oscillations disappeared altogether, such that the voltage response was virtually indistinguishable from that obtained in the DC case.

8.6 Stability of the Structure ASW Generated Structure during a period of Absence of the Applied Drive

A very important feature of the oscillatory dynamics is the associated memory effects (see Fig. 8.12). As would be expected, the oscillations can be stopped at any point by switching off the applied current. What is surprising, however, is that when the ASW is reapplied after a period of zero applied current, oscillations resume with precisely the same frequency and phase as the point at which they left-off. It is as if the interruption had never occurred at all. This result seems indicative of some sort of superstructure, as generated in response to the ASW drive and "frozen-in" during the zero current interruption.

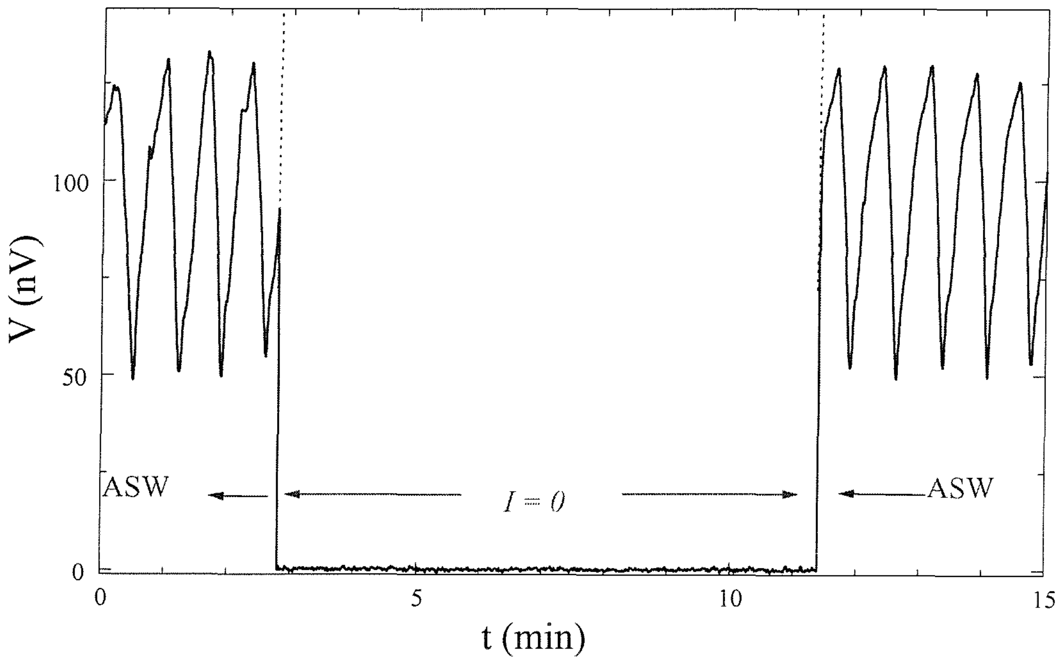

Fig. 8.12 *Demonstration of the stability over time of the ASW generated vortex structure. It appears that during a zero current interruption of the ASW drive, the spatial distribution of vortices generated in response to the ASW drive remains "frozen-in." This is reflected in the fact that on reapplying the ASW drive, oscillations resume with exactly the same frequency and phase as prior to the interruption.*

8.7 Summary of Main Experimental Results

The dynamic response of the driven vortex solid in clean untwinned $YBa_2Cu_3O_{7-\delta}$ single crystals, has been found to be dependent on the form of the applied current modulation. Whilst DC or single polarity square wave (SPSW) currents induced nonuniform flux flow, characterised by high levels of voltage noise, the shaking of a double polarity square wave (DPSW) current increased the overall voltage response while suppressing the voltage noise. This reduction in the noise-levels suggests that the motion of vortices becomes more uniform when they move backwards and forwards with zero net velocity (v_{net}).

In the case of asymmetric square wave (ASW) drive, highly unusual effects were observed. Over a short time scale ($t < 1/f_{\mathrm{m}}$ for $f_{\mathrm{m}} > 40$ Hz), the voltage response reproduced the time dependence of the applied current. However, over longer time scales (10^1 - 10^3 s) the amplitude of the voltage response showed a slow period variation with time. The frequency of these voltage response oscillations was found to increase with the time averaged voltage amplitude $<V_{\mathrm{o}}>$ [6, 7]; the asymmetry α of the response voltage; and the reciprocal of the applied field $1/B$. Therefore, since $v_{\mathrm{net}} \propto \alpha_{\mathrm{t}} < V_{\mathrm{o}} > /B$, we deduce that $f_{\mathrm{osc}} \propto v_{\mathrm{net}}$. Experiments with variable applied current asymmetries have shown that the $V_{\mathrm{o}}(t)$ oscillations only appear for a limited range of α_{t} values and equivalently over a certain window of v_{net} values. When v_{net} was low ($\alpha_{\mathrm{t}} < 0.01$) the vortex dynamics were the same as in the case of symmetric DPSW currents. For large v_{net} ($\alpha_{\mathrm{t}} > 0.4$) the system manifested the same behaviour as in the case of DC or SPSW currents. Oscillations were only observed for ASW currents with intermediate α_{t} values. We have also seen that the oscillations only appeared when sufficiently large probing currents were applied, which implies that the driving Lorentz force must exceed some threshold value in order for the effect to occur. One final point to note is that, as shown by the data presented in Fig. 8.5, there was a minimum resistance level ($R_{\mathrm{min}} \sim 5 \times 10^{-5}$) below which oscillations were not observed. This implies there exists a minimum velocity v_{cr} at which the vortices must be driven in order for voltage oscillation effects to occur.

8.8 Interpretation the Voltage Oscillation Effects

The voltage response of a superconductor in the mixed state can be related to the total number of vortices in the sample N and their average velocity $<v>=\sum_{i} v_i / N$ via the expression:

$$V = N < v > \phi_0 / w \tag{8.2}$$

where w is the width of the sample and ϕ_0 is the flux quantum. It follows from Eq. 8.2, that independent of the detailed mechanism involved, the oscillations that we have observed must be caused by variations in time of either the quantity of vortices in the sample (N) or of their average velocity ($<v>$). In our experiments we have found that the ratio of the maximum to the minimum voltage responses $V_0^{\max}/V_0^{\min}$ can be as large as three, thus in order to account for the oscillations either N or $<v>$ must vary by the same amount. In fact, we will now demonstrate that the maximum possible variation in N that could occur over the course of our experiments was some orders of magnitude smaller than this.

The internal magnetic field in the sample can differ from the external field by as much as the self-field B_{sf} generated by the combination of the shielding current I_{sh} and transport current I. This can be estimated using the formula $B_{\mathrm{sf}} \approx \mu_0 (I + I_{\mathrm{sh}})/w$ [13]. The highest probing current used in our experiments was $I = 5$ mA and the shielding current (as estimated from DC magnetisation data) did not exceed 5 mA. Using these upper current values we obtain a value for the self-field $B_{\mathrm{sf}} \sim 10^{-4}\,\mathrm{T}$. Since our measurements were performed in fields in excess of 1 T, this implies that N was effectively constant. It follows that the observed oscillations of the voltage response must be due to periodic variations in the average vortex velocity.

There are two obvious ways in which variations in the vortex velocity could lead to commensurate variations in the output voltage response. One possibility is that the oscillations could reflect changes in the number of vortices that were actually moving, which would imply a highly nonuniform flux flow regime. Alternatively the oscillation effects could be due to changes in the velocity of the vortex system as a whole, which would imply that the overall motion of the vortex system was coherent. In the latter case, the transit time for vortices, moving across a sample of width w, would be given by $\tau_{\mathrm{tr}} = w/v_{\mathrm{net}}$ where v_{net} is the net drift velocity of the vortices. For an ASW current with temporal asymmetry α_{t} this transit time can be expressed as:

$$\tau_{\mathrm{tr}} = Blw/(\alpha_{\mathrm{t}} < V_{\mathrm{o}} >), \tag{8.3}$$

where l is the distance between voltage contacts and $<V_{\mathrm{o}}>$ is the mean voltage response (evaluated by integration over one period of the voltage oscillations). Note that in arriving at this formula, we have assumed the voltage response has the same asymmetry α_{t} as the applied current modulation.

In Table I (overleaf) we present τ_{tr} values, calculated from experimental data (using Eqn. 8.3), for various different parameter (I, α_{t}, f_{m}, B, T) regimes in which clear oscillations (with period τ_{osc} and mean value $<V_{\mathrm{o}}>$) were observed. From the table it can be seen that both τ_{osc} and τ_{tr} varied substantially between the various regimes. However, in all cases the ratio $\tau_{\mathrm{osc}} / \tau_{\mathrm{tr}}$ was approximately equal to two. We believe that this constant value for the ratio cannot be fortuitous, especially given the range and diversity of parameters considered.

TABLE I. Values of the measured oscillation period (τ_{osc}), calculated transit time (τ_{tr}) and the ratio of the two (τ_{osc} / τ_{tr}), for a range of different parameter values.

I(mA)	α_τ	f_m (Hz)	B(T)	T(K)	$<V_o>$ (μV)	τ_{osc}(s)	τ_{tr}(s)	τ_{osc}/τ_{tr}
3	0.10	68	2	87.0	0.108	29.3	14.0	2.10
3	0.10	128	2	87.0	0.103	29.1	13.9	2.09
3	0.04	68	2	87.0	0.126	84.1	40.2	2.09
4	0.10	68	2	86.4	0.147	24.5	11.0	2.23
5	0.10	68	2	87.0	0.262	9.90	4.48	2.21
3	0.10	68	3	86.0	0.089	59.2	27.2	2.18

It is clear, therefore, that any attempt to interpret the oscillatory effects must also be able to explain the value of this ratio. In particular, as will be outlined below, this observation allows us to reject any interpretation based upon a model of nonuniform flux flow.

One example of how nonuniform flux flow could arise is provided by the channelling interpretation as proposed by D'Anna *et al.* [14], in order to account their observations relating to the response of the vortex system in the plastic flow regime. On measuring the voltage response of an untwinned $YBa_2Cu_3O_{7-\delta}$ crystal in the geometry $J\Pi ab$, $H\Pi ab$ ($J \perp H$) they observed sharp peaks in the voltage noise spectrum which they associated with the motion of vortices along channels between static solid domains. However, from Eq. 8.2, it is clear that if the number of vortices which were actually moving (N_m) was a small fraction of the total number of vortices in the sample (N), then in order to produce the same voltage response the vortices traversing the channels would have to move with higher velocities than in the case of coherent motion. Thus the time taken for any given vortex to traverse the length of a channel (τ_{ch}) would be much shorter than the oscillation periods (τ_{osc}) observed in our experiments. It should be apparent that in order to account for the oscillatory effects, it is necessary to identify a time scale comparable to the period of the oscillations. To arrive at an "effective" transit time of the same order as τ_{osc} in the framework of the channelling interpretation would be necessary to introduce an exotic mechanism involving the slow coherent opening and closing of channels. It is, however, difficult to imagine how such a model could account for the remarkable correspondence between τ_{osc} and τ_{tr}. In the discussion which follows we will assume that the vortex system moves as a coherent whole, such that its motion can be characterised by a single overall drift velocity. Our interpretation of the oscillatory effects is based upon the idea that the modulation of the voltage response reflects periodic variations in the relative disorder of this system and thus of its overall mobility. Using this interpretation we have been able to provide an explanation for the correspondence between τ_{tr} and τ_{osc}.

We have seen that in response to a pure oscillatory (DPSW) drive, the vortex system exhibits much lower noise levels than in the case of a unidirectional (SPSW) drive (see Fig. 8.2). This strongly suggests that these two cases represent distinct dynamic states, characterised by different degrees of relative disorder. Henceforth we shall refer to these regimes as the "ordered" and "disordered" states respectively. However, it is not immediately obvious how this distinction should arise: even in a defect free system, the flow of vortices across the surface of a sample is expected to be disordered [15] and surface imperfections (present on the surface of all real samples) can only be expected to increase the nonuniformity of this flow. We suggest that the essential distinction between the DPSW and SPSW driven states is the way in which the vortex system "heals" *after* its disorderly flow across the surface [16, 17]. In the case of a unidirectional drive the system is driven with a relatively high velocity and in a single direction. As such, the "disordered state" generated as vortices are "torn" across the surface will be given little or no opportunity to heal. For an oscillatory drive, however, the repeated backwards and forwards motion of the vortices about their equilibrium positions could allow a gradual "healing" of the vortex lattice into a relatively "ordered" state. Thus overall, the motion of the vortices in the DPSW case would be expected to be much more coherent. Another important distinction between these two dynamic states is their very different mobilities, as reflected by the disparity between the mean voltage responses (see Fig. 8.2). The relatively low time averaged voltage response obtained in the SPSW case indicates that the "disordered" dynamic state has much lower overall mobility. This can be readily understood when we consider that in this case, the system is better able to accommodate variations in the bulk pinning potential and thus interacts more strongly with the pinning centres.

An ASW drive can be regarded as lying somewhere between the extremes of DPSW and SPSW modulations. This seems to hint that the ASW driven state is in some way intermediate between the "ordered" and "disordered" states which arise in the case of pure oscillatory and direct drives respectively. As shown in Fig. 8.2, some support for this idea is provided by the fact that the voltage response for the ASW driven states oscillates between maximum and minimum levels which lie between the DPSW and SPSW responses for the same applied current amplitude. In order to account for the oscillations it terms of a "disorder model" it is necessary to explain how the state of the system could change periodically in such a way that it was always constrained between these two extremes.

There are two obvious ways in which the overall disorder of the system could change with time. One possibility is that the relative disorder of the system *as **a whole*** could evolve with time. It is, however, difficult to see how this could lead to the feedback mechanism necessary to explain the oscillations. Alternatively, a situation could arise whereby ordered and disordered states (which could be likened to those obtained in response to DPSW and SPSW drives respectively) coexisted within the sample in regions which were separated by well defined boundaries. In this case, the variation of the overall disorder of the system would be due to changes in the proportion of these two dynamic states, with the maxima and minima in the oscillations representing the points along the oscillation cycle at which the system was wholly in one or other of these two state. Both experimental [18, 19] and theoretical [20, 21] studies have provided evidence that the transition between ordered and disordered dynamic states is hysteretic. Where hysteresis arises, this is expected to lead to an inherent stability of states which allows for their coexistence over a particular region of parameter space thus a dual state dynamic regime is at least theoretically possible. In the interpretation that follows we will assume that under the influence of an ASW drive, the system consists of two distinct dynamic states separated by a well defined boundary. Since nucleation occurs along the surface of the sample which lies parallel to the applied current (*I*) it seems reasonable to suggest that this state boundary would also be parallel to *I*.

If the vortex system was divided into two well defined regions, as outlined above, then the periodicity of the voltage response could be due to the motion of the boundary between these regions. We suggest that under the influence of an ASW drive, this boundary drifts across the sample with a net velocity equal to the drift velocity of the individual vortices. One implication of this interpretation is that, in the disordered regions, dislocations of the vortex lattice must move across the sample with the same velocity as that of the vortex system itself. Numerical simulations have indicated that, at least under certain conditions, the dislocation superstructure may remain static [16]. However, a recent numerical simulation by Scheidl and Vinokur [22] demonstrated that the relative velocity of the vortices and the defect superstructure may decrease with increasing driving force and that there may even be transition at a critical driving velocity to a comoving regime in which dislocations move together with vortices. Since the instantaneous velocity is expected to be high for the relatively large current amplitudes used in our experiments, it seems reasonable that our measurements should correspond to the high velocity comoving regime as identified by Scheidl and Vinokur. Moreover, the fact that we have observed a threshold current magnitude, below which the oscillations were not observed, could reflect the crossover to a comoving regime.

Within the framework of the two state interpretation the transit time (calculated using Eqn. 8.3) can be associated with the time taken for the state boundary to move across the width of the sample. If we arbitrarily assume that a given oscillation cycle starts with the system in a completely ordered state, then we can conveniently divide the oscillation cycle into two parts.

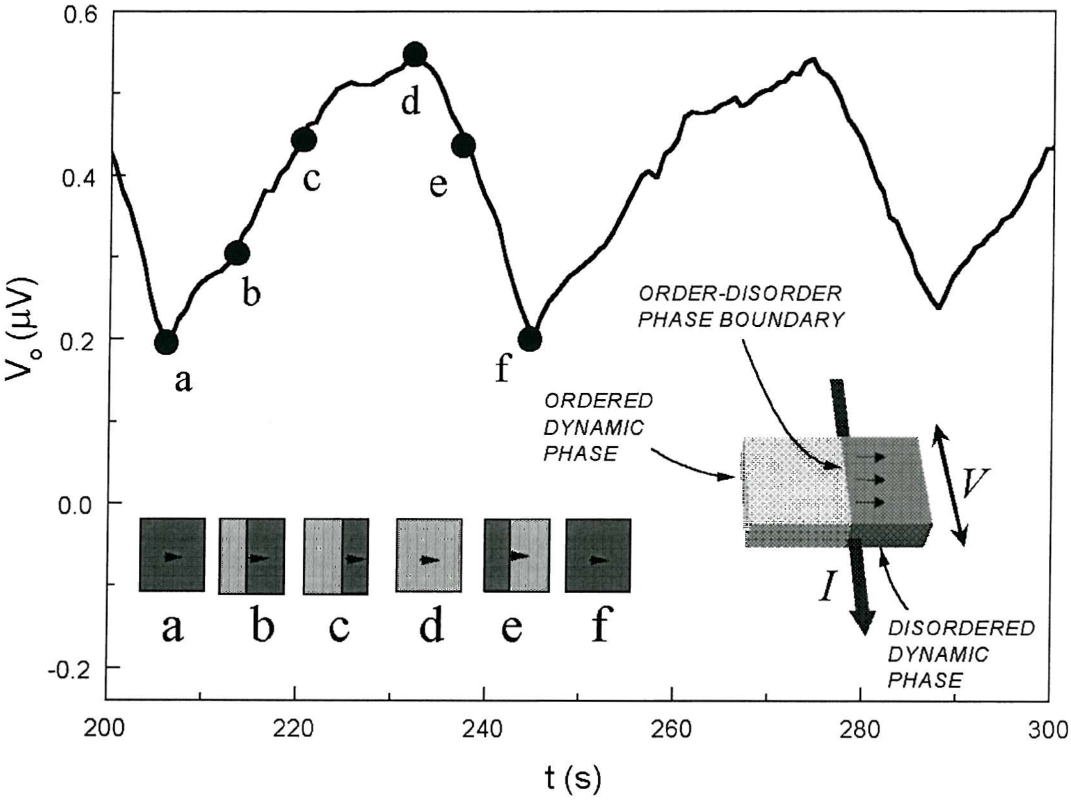

Fig. 8.13 *Typical form of the voltage amplitude oscillations arising in response to an ASW drive. Schematic frames (a-f) illustrate how the relative proportion of ordered and disordered dynamic phase regions is supposed to change over the course of an oscillation cycle. Schematic figure on right hand side indicates the direction of motion of the order-disorder phase-boundary, in relation to the applied current (I) and measured voltage (V).*

Over the first part of the cycle, the proportion of the system in the disordered state would gradually increase until it was wholly disordered. As the proportion of the two dynamics states changed the boundary separating them would move across the width of the sample. It should, therefore, be clear that over the course of any given oscillation cycle the boundary between dynamic states would move ***twice*** across the width of the sample. Furthermore, the amplitude of the instantaneous velocity of the vortices would be expected to vary continuously between maximum and minimum values as the relative proportion of the two dynamic states changed. This periodic velocity response would be expected to lead to concomitant variations in the output voltage amplitude, thereby accounting for the $V_0(t)$ oscillations (see Fig. 8.13).

The interpretation, as outlined above is suggestive, in that could explain many features of the $V_0(t)$ oscillations such as: the relationship between τ_{osc} and τ_{tr} ; the threshold values of α_t and I; and the fact that the oscillation period is independent of the modulation frequency. However, there are a number of important questions that remain to be answered, particularly in relation to the specific feedback mechanism involved. One implication of the state boundary interpretation is that the dynamic state developing across the incoming surface should always be different to that leaving the sample at the outgoing surface. That is to say that where the vortices leaving the sample were in a ordered dynamic state the state forming at the incoming surface would be disordered and vice versa. It is not clear how such a situation could develop but we tentatively suggest that it might have something to do with "tensions" arising between the different dynamic states. If we accept that there is a difference between the mobility of the two dynamic states, then we would expect a two-state system to have a mobility that differed from that of a system consisting entirely of vortices in one or other of these states. Thus, where there was a mobile ordered state at the outgoing surface this might be expected to "pull" the disordered state along with a higher velocity than its "free drift velocity." The resulting tension between dynamic states could perpetuate the formation of the disordered state at the incoming surface. In a similar fashion, the presence of a disordered phase at the outgoing surface could restrict the motion of the incoming vortices allowing them to form into a well ordered state. The qualitative arguments outlined above give some idea as to how might oscillations arise, however, more specific theoretical work will definitely be required if rigorous explanation of these intriguing oscillatory effects is to be obtained.

Further insight into the mechanism of the oscillations might also be provided by effects that occur in the quasi-1D linear chain compounds such as $NbSe_3$ or $K_{0.3}MoO_3$. At a critical temperature, known as the Peierl's temperature, these systems undergo a transition into a charge density wave state (CDW) which manifests collective mode dynamics [23]. There are a number of similarities between the dynamics of this collective mode and those of a driven FLL [24]. In the DC driven state of a CDW system, sharp peaks have been observed in the frequency spectrum of the voltage response at a fundamental frequency and subsequent harmonics [25]. These spectra are similar in appearance to the Fourier spectra extracted from our own data (see Fig. 8.9). Moreover, it has been shown that the frequency of the fundamental peak in the CDW spectra is proportional to the applied current [26]. Although not immediately apparent, a similar dependence is displayed by our own results. An amplitude asymmetry can be considered to be equivalent to a pure AC modulation superimposed onto a DC drive. By definition, amplitude asymmetry $\alpha_a = I_{dc}/I_{ac}$, thus this asymmetry is proportional to the DC bias. We have found that the fundamental frequency (f_{osc}) of the induced oscillations is proportional to the applied asymmetry and it follows that $f_{osc} \propto I_{dc}$. Thus, as for the CDW case the fundamental frequency of the oscillations is proportional to the "underlying" DC drive-current. In the case of CDWs the peaks in the Fourier spectra are associated with a periodic superstructure which has been directly observed in various diffraction experiments [27]. The similarities between the Fourier spectra presented in this paper and those observed in the CDW case provides further support for the idea that the $V_o(t)$ oscillation effects could also explained in terms of the in terms of the motion some sort of a periodic superstructure

8.9 History Dependence & Memory Effects on Switching Between Drives.

In this section we investigate the effect upon the dynamic vortex state generated by an asymmetric drive of changes in driving conditions. In this way, we have provide strong support for an interpretation of the oscillatory effects, in terms of two dynamic-phase domains within the sample, the boundary between domains drifting under the action of the asymmetric drive. Furthermore, from analysis of the history dependent responses, we demonstrate the stability of the ordered dynamic phase.

8.9.1 Switching from Asymmetric to Symmetric Drives

In Fig. 8.14 we illustrate the effect of switching the driving current between ASW and DPSW modulation forms. The time varying response seen at either end of each of these curves corresponds to the oscillatory state, of which we presented a detailed description and interpretation in the preceding section. Under the influence of a symmetric double polarity drive, it is expected that vortices should move backwards and forwards about their equilibrium positions without any net motion. Thus, it might be expected that on applying a DPSW drive to the ASW-generated structure, that the voltage response should always remain constant. However, as illustrated by curves A, B and C, rather than being stable the voltage response was frequently found to change markedly during the period of application of the DPSW drive. Specifically the voltage response amplitude increased significantly, before stabilising on a relatively high-level plateau. It seems, therefore, that a DPSW drive has the effect of "healing" an ASW-generated vortex structure into a uniformly ordered state. This is consistent with the observations of Section 8.3 (also supported by the work of Henderson *et al.* [10]) that the shaking action of a DPSW drive tends to order the driven system.

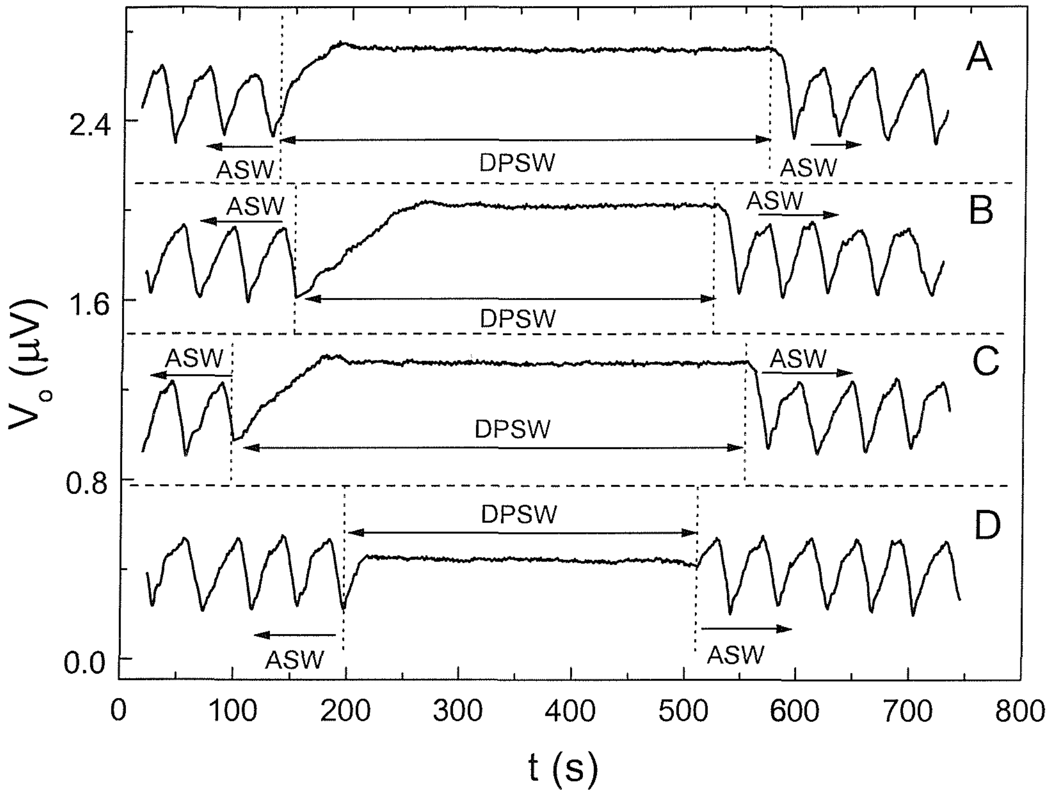

Fig. 8.14 *Demonstrates the effect of applying a DPSW current at different points along the ASW driven oscillation cycle. Note that for clarity, curves A-C have been vertically shifted by 1.2, 0.8 and 0.4 μV respectively.*

As illustrated by the curves of Fig. 8.14, on interrupting an ASW generated vortex structure at different points along its development cycle the system has a strong tendency to stabilise on the same ordered-state plateau (curves A ,B and C). Only in occasional cases (curve D), does the voltage response remain constant during the period of application of the DPSW current. The propensity of the response to stabilise on this particular voltage response level, independent of prior structural history, seems indicative of a stable state of the driven system. It is not clear, however, whether the evolution towards this relatively ordered state occurs via an *in situ* "healing" of the disordered regions or else by a gradual net motion of such regions out of the sample.

8.9.2 Applying a Single Polarity Drive to the ASW Superstructure

In Fig. 8.15, we consider the effect of applying two types of unidirectional drive (DC and SPSW) to the ASW generated vortex structure. In both cases, on reapplying the ASW modulation coherent oscillations do not immediately resume. Instead, oscillations gradually redevelop their coherence in a fashion suggestive of a number of periodic components of differing phase. It seems that these components becoming increasingly coupled over time, such that eventually the oscillations reacquire their original form. The decoupling effect could potentially arise due to channels opening up in the system during the period of application of the unidirectional drive. Such channels would separate the system into distinct regions, which on reapplying the ASW-drive would resume oscillations independently of each other and hence with different phases.

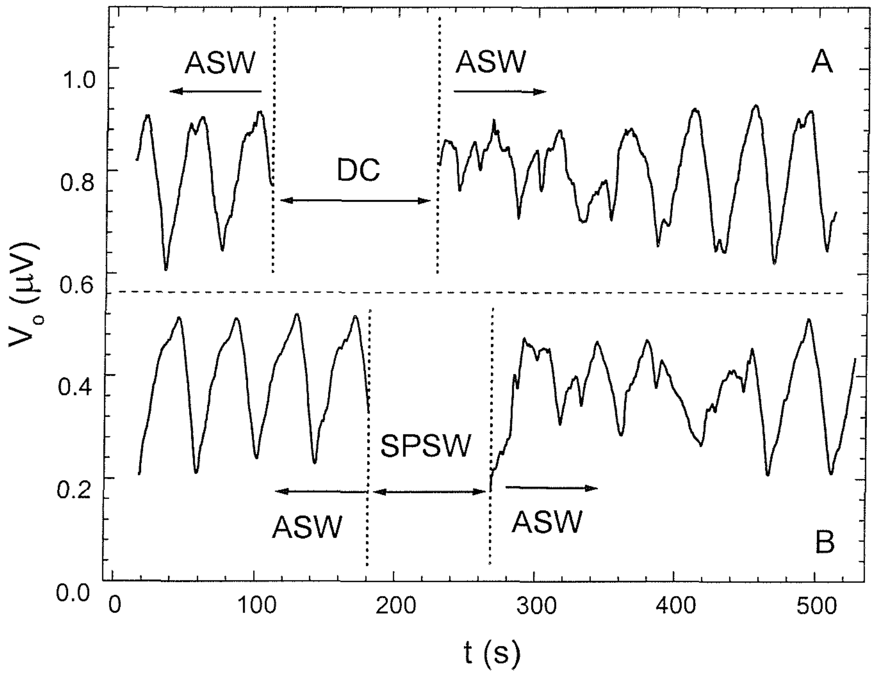

Fig. 8.15 *Effect of applying unidirectional drives to an ASW generated vortex structure: Curve A, DC interruption; Curve B, single polarity square wave (SPSW) interruption. For the purposes of presentation, curve A has been vertically shifted by 0.4 μV.*

As illustrated by the curves of Fig 8.16, we have found that in every case on switching to an SPSW drive, the voltage response passes through a transient period before stabilising on a low voltage plateau. Just as the system had the tendency to stabilise in a particular high mobility ordered phase under the action of the DPSW drive, it seems that this low-level plateau is also representative of a stable state of the driven system. In this case, the low mobility response seems indicative of a disordered dynamic regime.

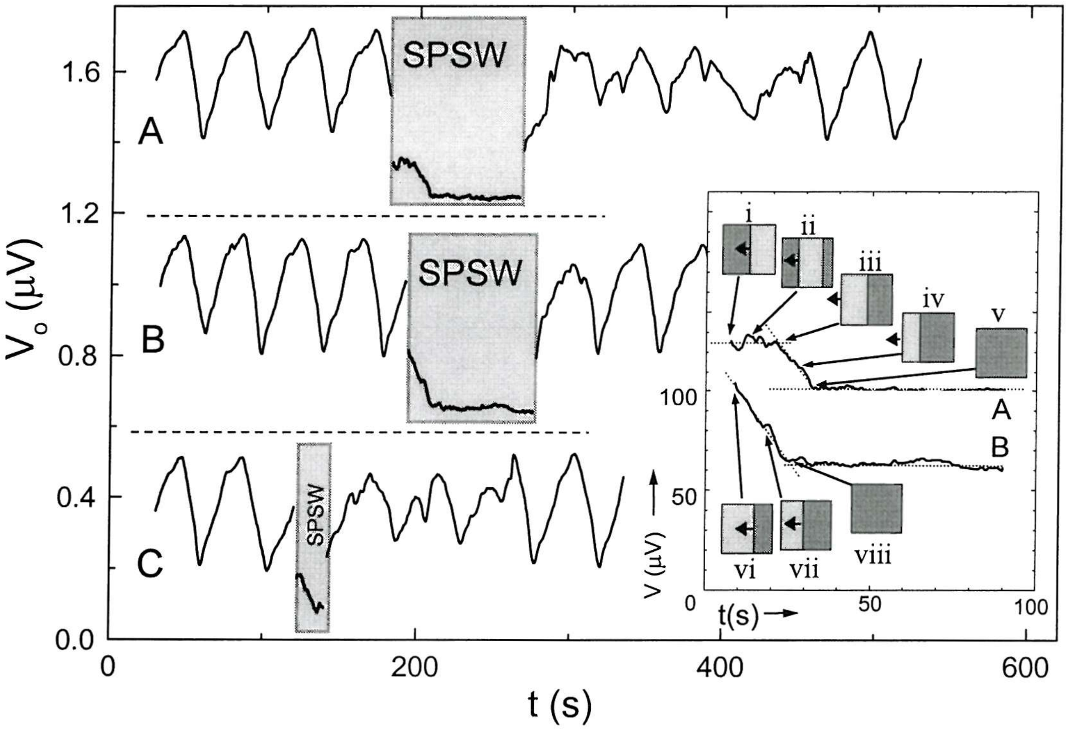

Fig. 8.16 *Main frame: Demonstrates the effect of applying an SPSW current at different point along the ASW driven oscillation cycle. Curves A and B have been vertically shifted by 0.8 and 0.4 μV respectively. Inset: expanded view of the transient SPSW responses following interruptions on ascending (curve A) and descending (curve B) branches of the ASW-driven oscillation cycle. These curves have been repositioned to facilitate direct comparison. Schematic frames (i-viii) illustrate the development of the dynamic phase distribution in these two cases.*

Significantly, the precise form taken by the SPSW transient response, prior to reaching the disordered state plateau, depended critically on the point along the ASW-driven oscillation cycle at which the switch-over to SPSW drive occurred. Transient responses obtained following switchovers at points where the voltage response level was approximately equal, but occurring on ascending and descending branches of the ASW-driven oscillation cycle, were ***not*** found to be equivalent (curves A and C).

In the cases where the switch-over to an SPSW drive occurred during the descending branch of ASW-driven oscillation cycle (curve A in inset and main frame), the response stabilised for some time at a relatively high-level before dropping to the disordered state plateau. Continuing from our earlier arguments, all else being equal, when the voltage amplitude is stable so too must be the overall degree of disorder within the driven system. Thus the point where the response starts to fall-off must mark the stage at which the overall relative-disorder of the system starts to increase. In the case of switch-overs occurring on the ascending branch of the ASW-driven oscillation cycle, this fall-off immediately follows the switch-over to the SPSW drive.

In fact, the two-phase interpretation of the voltage-amplitude oscillations provides a clear explanation for the distinction arising between the ascending and descending-branch cases. The essential idea is that the dynamic state of the vortices first to be forced out of the sample on switching to the SPSW drive will depend on which of the two phases is in increasing proportion at the point of interruption. Taking the example of curve B, since the switch-over occurred on an ascending branch of the oscillation cycle, this implies that the relatively ordered dynamic-phase regions were in increasing proportion at the point of interruption (see schematic insets to Fig. 8.13). Since the polarity of the applied SPSW was opposite to that of the ASW drive, this means that the ordered phase region that was previously at the incoming surface, would now be at the outgoing surface with respect to the SPSW drive. Thus, consistent with our observations, the relative ordering of the system should immediately begin to decrease as the ordered phase region is forced out of the sample [see curve B of the inset and associated schematic frames (vi)-(viii)]. In contrast, for a switch-over occurring on a descending branch of the oscillation cycle (as represented by the data in curve A), it would be the relatively disordered phase which would be first to be forced out of the outgoing surface of the sample. During this period, the structure of the system would change as the ordered phase region drifted across the sample [see insets (i)-(iii)]. However, since the relative proportion of ordered and disordered phase regions would remain constant, so too should the overall relative disorder and hence the voltage response. Only when the ordered phase region reached the outgoing surface would the voltage response begin to drop [schematic frames (iii)-(v)].

The observations presented in Fig. 8.16 are important for two reasons. Firstly, they provide clear support for the two-phase interpretation of the oscillation effects, in that the distinction between ascending and descending branch switchovers can be readily explained within the framework of this model. Furthermore, the data imply that rather than being broken apart by a unidirectional drive, ordered-phase domains move coherently out of the sample. Thus, the fracturing of the structure evident on restarting the ASW modulation must arise after the ordered domains have been driven out of the sample. This resilience to disordering implies a high degree of stability to the ordered dynamic phase.

8.10 Summary & Conclusions

Investigations have been carried out on the dynamics of the vortex system in $YBa_2Cu_3O_{7-\delta}$ single crystals at temperatures just below the thermodynamic melting temperature. We have found that the response of the system depends not only on the magnitude of the driving force but also on the form of the current modulation. Pure oscillatory (double polarity) driving currents were observed to result in much higher average voltage responses and lower levels of voltage noise than in the case of a unidirectional (single polarity or direct) drives. On the basis of the striking differences between these responses we identified them with two distinct dynamic states, characterised by differing degrees of relative disorder. We have proposed an explanation for how this distinction could arise, the essential idea being that, in the case of a unidirectional drive, the vortex system is given little or no opportunity to heal after its disorderly flow across the surface of the sample. In contrast, in the case of the double polarity drive the backwards and forwards motion leads to a gradual ordering into a coherently moving dynamic state.

In order to investigate the effect of varying the net velocity of the vortex system whilst keeping the driving force constant, we devised a technique based upon the use of asymmetrically modulated driving currents with relatively low period or amplitude asymmetries (~ 1 %). The response of the vortex system in these cases was found to be highly unusual, reflecting a dynamic state unlike any that has been identified to date. In response to an asymmetrically modulated square wave current (modulation frequency $f_m = 68$ Hz) the voltage response amplitude (V_0) executed slow periodic oscillations (typically $f_{osc} \sim 0.01$ Hz) over a large range of V_0 values (in some cases V_0^{max} / V_0^{min} was as large as 3). Moreover, the frequency of the oscillations was found to be entirely independent of the drive frequency except at the very low frequency limit where the oscillations broke down altogether. Similar oscillation effects were observed when a sinusoidal or triangular waveform with a superimposed DC offset was applied, thereby demonstrating that the square-wave-form of the modulation is not, in itself, crucial in establishing oscillations. We have found that the oscillatory effects were confined to a relatively limited window of parameter space with maximum and minimum currents, asymmetries and temperatures for which oscillations were observed. Over the parameter region for which oscillatory effects were observed, the oscillation period was found to approximately correspond to the time which it would take vortices to drift coherently twice across the width of the sample.

We have proposed an interpretation of the oscillatory effects based upon the idea of two distinct dynamic states, one more ordered than other, coexisting within the sample. These states can be likened to the "ordered" and "disordered" states, which we have associated respectively with pure oscillatory and unidirectional driving current modulations. In the framework of our interpretation the oscillations can be explained in terms of the slow drift of the boundary between the two dynamic states, with one period of the oscillations corresponding to the amount of time taken for this boundary to move twice across the width of the sample. In this way, we are able to account for the observed factor-of-two correspondence between the period of the oscillations and the transit-time for vortices drifting coherently across the width of the sample.

We have obtained additional support for this interpretation by observing the effect of applying different types of drive modulation to the structure generated by an asymmetric drive. In particular, on switching from an ASW drive to an SPSW drive and back again we observed a clear dependence on whether such a switchover occurred on the ascending or the descending branch of the ASW generated oscillation cycle. It is very difficult to see how such a difference could arise if the oscillations were due to uniform variations across the whole sample. Furthermore, these data implied that rather than being broken apart by a unidirectional drive, ordered-phase domains move coherently out of the sample. This resilience to disordering implies a high degree of stability to the ordered dynamic phase.

In conclusion, we have demonstrated that much of the dynamic behaviour of the vortex system of $YBa_2Cu_3O_{7-\delta}$ can be understood in terms of two dynamic states, one relatively ordered the other more disordered. Irrespective of prior structural changes, the driven dynamic system has a tendency to stabilise on two specific voltage-levels: a relatively high level indicative of the ordered dynamic state and a much lower disordered-state plateau. Oscillations of the voltage amplitude, observed on applying an asymmetric drive, were understood in terms of periodic changes over time in proportion of two distinct domains, one in the ordered phase, the other disordered. Clear support was provided for this interpretation, from the observation of transient responses on switching between asymmetric and unidirectional drives. Furthermore, from analysis of such transient responses we were able to demonstrate the stability of the ordered dynamic phase.

References

[1] W. K. Kwok, U. Welp, G. W. Crabtree, K. G. Vandervoort, R. Hulsher and J. Z. Liu, Phys. Rev. Lett. **64** (1990) 966; Phys. Rev. Lett. **69** (1992) 3370; H. Safar, P. L. Gammel, D. A. Huse, D. J. Bishop, J. P. Rice and D. M. Ginsberg, *ibid.* **69** (1992) 824.

[2] W. K. Kwok, J. Fendrich, S. Fleschler, U. Welp, J. Downey, G. W. Crabtree, Phys. Rev. Lett. **72** (1994) 1092.

[3] W. K. Kwok, J. A. Fendrich, C. J. van der Beek and G. W. Crabtree, Phys. Rev. Lett. **73** (1994) 2614 .

[4] S. Bhattacharya and M. J. Higgins, Phys Rev. Lett **70** (1993) 2617; Phys. Rev. B **49** (1994) 10004; A. C. Marley, M. J. Higgins and S. Bhattacharya, Phys. Rev. Lett **74** (1995) 3029; M. J. Higgins and S. Bhattacharya, Physica C **257** (1996) 232; W. Henderson, E. Y. Andrei, M. J. Higgins and S. Bhattacharya, Phys. Rev. Lett **77** (1996) 2077.

[5] J. A. Fendrich, U. Welp, W. K. Kwok, A. E. Koshelev, G. W. Crabtree and B. W. Veal, Phys Rev. Lett. **77** (1996) 2073.

[6] S. N. Gordeev, P. A. J. de Groot, M. Oussena, A. V. Volkozub, S. Pinfold, R. Langan, R. Gagnon and L. Taillefer, Nature (London) **385** (1997) 324.

[7] S. N. Gordeev, A. P. Rassau, P. A .J. de Groot, R. Gagnon and L. Taillefer, Phys. Rev. B **58** (1998) 527.

[8] A. P.Rassau, S. N. Gordeev, P. A. J. de Groot, R. Gagnon and L. Taillefer, Physica C **328** (1999) 14.

[9] W. Henderson, E. Y. Andrei and M. J. Higgins, Phys. Rev. Lett. **81**, 2352 (1998)

[10] Z. L. Xiao, E. Y. Andrei, M. J. Higgins, Phys. Rev. Lett. **83** (1999) 1664.

[11] H. Safar, P. L. Gammel, D. A. Huse, D. J. Bishop, J. P. Rice and D. M. Ginsberg, Phys. Rev. Lett. **69** (1992) 824.

[12] W. K. Kwok, S. Fleshler, U. Welp, V. M. Vinokur, J. Downey, G. W. Crabtree and M. M. Miller, Phys. Rev. Lett.. **69** (1992) 3370.

[13] E. Zeldov, J.R. Clem, M. McElfresh and M. Darwin, Phys. Rev. B **49** (1994) 9802; M. Däumling and D. C. Larbalestier, Phys. Rev. B **40**, (1989) 9350.

[14] G. D'Anna, P. L. Gammel, H. Safar, G. B. Alers, D. J. Bishop, J. Giapitzankis and D. M. Ginsberg, Phys. Rev. Lett. **75** (1995) 3521.

[15] I. Aranson and V. M. Vinokur, Phys. Rev. Lett. **77** (1996) 3208; I. Aranson and V. M. Vinokur, Phys. Rev. B **57** (1998) 3073.

[16] D. W. Braun, G. W. Crabtree, H. G. Kaper, A. E. Koshelev, G. K. Leaf, D. M. Levine and V. M. Vinokur, Phys. Rev. Lett. **76** (1996) 831.

[17] F. Pardo, F. de la Cruz, P. L. Gammel, C. S. Oglesby, E. Bucher, B. Batlogg and D. J. Bishop, Phys. Rev. Lett. **78** (1997) 4633.

[18] U. Yaron, P. L. Gammel, D. A. Huse, R. N. Kleiman, C. S. Oglesby, E. Bucher, B. Batlogg, D. J. Bishop, K. Mortensen and K. N. Clausen, Nature **376** (1995) 753.

[19] W. Henderson, E. Y. Andrei, M. J. Higgins and S. Bhattacharya, Phys. Rev. Lett. **77** (1996) 2077.

[20] V. M. Vinokur, T. Nattermann, Phys. Rev. Lett. **79** (1997) 3471.

[21] N. Grønbech-Jensen, A. R. Bishop and D. Dominguez, Phys. Rev. Lett. **76** (1996) 2985.

[22] S. Scheidl and V. M. Vinokur, Phys. Rev. B **56** (1997) 8522.

[23] G. Grüner and A. Zettl, Phys. Rep. **119** (1985) 117; G. Grüner, Rev. Mod. Phys **60** (1988) 1129.

[24] S. N. Coppersmith and A. J. Millis, Phys. Rev. B **44** (1991) 7799.

[25] R. M. Fleming and C. C. Grimes, Phys. Rev. Lett. **42** (1979) 1423.
[26] P. Monceau, J. Richard and M. Renard, Phys. Rev. B **25** (1982) 931; A. Zettl and G. Grüner, *ibid.* **29** (1984) 755; S. E. Brown and G. Grüner, *ibid.* **31** (1985) 8302.
[27] *Charge Density Waves in Solids* (Elsevier, Holland), 1989, edited by L. P. Gor'kov and G. Grüner.

CHAPTER 9. CONCLUSIONS

9.1 Overview of Main Findings

This thesis has been concerned with both the statics and the dynamics of vortices within the high temperature superconductor $YBa_2Cu_3O_{7-\delta}$. The vortex system of high temperature superconductors provides an interesting example of a widely applicable generic problem, namely that of an interacting system exposed to a background of random quenched disorder. It is clear, therefore, that some of the observations presented within this thesis could have implications for other physical systems.

The first clear conclusion from our study, is that there exists a **well-defined transition region in the vicinity of the melting line**, over which vortex **liquid and solid phases coexist**. The evidence for this transition region has come from a wide range of transport and a.c. susceptibility data, presented in Chapters 6 and 7 of this thesis. In particular, we have found that this clearly defined transition region only exists below the multicritical point, in the region of the phase diagram where the vortex liquid freezes via a first order phase transition. Within this region, the width of the transition region decreases with decreasing magnetic field. Furthermore, we have found that the width of the transition region shows a strong sample dependence. These observations are clearly explainable in terms of long-wavelength fluctuations of sample oxygenation, giving rise to concomitant variations of the local melting temperature. This would allow for the coexistence of vortex liquid and solid phases over a well-defined region of the parameter space, delimited by the upper and lower limits of the local melting temperature profile.

Crucially, we have found that **within the transition region there is a complete lack of relaxation over experimental time-scales**. This definitively precludes the possibility that the broadening of the melting transition could be due to continuous glassy-relaxation. In contrast, the absence of relaxation over experimental time-scales is entirely consistent with the coexistent phase model.

We have found that the within the transition region, **the distribution of solid and liquid domains has a controlling influence on the vortex dynamics.** Since the majority of dissipation is expected to arise due to vortex liquid flowing along channels between static solid domains, this leads to a **percolative mode of dynamics in the transition region.** The percolative limit corresponds to the point where ≈30% of the system is in the liquid phase.

Somewhat surprisingly, we have found that the **spatial distribution of vortex solid and domains at any given thermodynamic point depends not only on the sample specific melting temperature profile but also on the manner in which the measurement point is reached**. An order of magnitude difference between the voltage-response levels in the transition region for states obtained respectively following warming or cooling, was explained in terms of differences in the width of the liquid channels between the pinned solid domains. Current induced switching from the state obtained on warming to a state equivalent to that obtained on cooling was attributed to the melting of superheated sections of the solid domains thereby widening the channels for liquid flow.

Our second main group of conclusions relate to the fact that the **interaction between the vortex system and underlying pinning disorder can be controlled by means of an applied transport current**. We have related the effectiveness with which a particular dynamic regime is pinned, to the degree of relative disordering in the driven system. Specifically, we have concluded that whereas disordered dynamic states interact strongly with the underlying disorder potential, **relatively ordered dynamic states experience the pinning potential as only a relatively weak perturbation on their otherwise coherent motion**.

In Chapter 7 we deduced that a sufficiently large amplitude current, which we call an annealing current, can drive the vortex system into a relatively ordered dynamic phase. We were then able to show that the **effectiveness of pinning that develops within the solidifying vortex system can be systematically controlled by means of such an annealing current**. On switching off the annealing current at different points across the freezing transition region, we were able to generate states that manifested very different degrees of pinning effectiveness at lower temperatures. We concluded that a signature of the distribution of vortex solid and liquid phase domains at the point at which we turn off the annealing current is frozen-in to the system, such that a lower temperatures there is an equivalent distribution of ordered and disordered solid domains. Given that disordered solid regions are expected to be more strongly pinned, this explains the dependence of the effectiveness of pinning at low temperatures, on the temperature at which the annealing current is switched-off during cooling.

In Chapter 8, we were able to show that in addition to the dependence of the state of the driven system on the amplitude of the applied current, the **modulation form of the drive also has a controlling influence upon the dynamic regime**. For the same applied current amplitude, very different responses were obtained, dependent on the applied modulation form. Specifically we found that **whereas undirectional drives tend to force the system into a disordered dynamic regime, the backwards and forwards shaking action of an alternating drive has the effect of healing-out the disorder from the driven system.** We have suggested that this could be due to the fact that, in general, vortices nucleating across the surface of a sample tend to do so in a disorderly fashion. Whereas for a unidirectional drive, the system is then given no opportunity to heal, the backwards and forwards shaking action of an alternating drive could over time lead to a gradual ordering of the vortices within the bulk of the sample.

Some of our most interesting observations were obtained in response to an applied current modulation form intermediate between the extremes of unidirectional and pure alternating drives. In response to asymmetric alternating drives we found that the voltage response amplitude varied periodically with time between the levels obtained in the undirectional and pure oscillatory cases. Surprisingly, we found that the frequency of these oscillations was orders of magnitude lower than the applied drive frequency. These observations were strongly suggestive of a periodic evolution with time of the relative ordering of the driven system. Indeed, several features of the oscillations, including a 2:1 ratio between the oscillation period and the estimated vortex transit time, lead us to suggest that this behaviour was due to a defect superstructure, drifting across the sample with the same net velocity as that of individual vortices. Specifically we concluded that the **oscillatory behaviour arose due to the coexistence within the sample of ordered and disordered phase regions**. The periodicity can, therefore, be attributed to periodic changes over time in the proportion of these two dynamic phases, each of which has a different degree of interaction with the underlying disorder potential.

Finally, we have gathered a range of evidence in support of the theory that **the stable thermodynamic phase of the system in the region of phase space below the first order melting transition is a quasi long-range ordered Bragg glass phase** [1]. We have observed that there are actually two possible states of the system in this region of the phase diagram: a stable weakly pinned or depinned state and a metastable strongly pinned state. We have associated these weakly and strongly pinned states with ordered and disordered configurations of the vortex system respectively. Whereas the strongly pinned state manifests a range of history dependence and irreversibility, the weakly pinned state is elastic and entirely independent of history. Furthermore, we observed a complete absence of relaxation within the depinned state: in spite of the possibility for it to become more strongly pinned, the system remains stable within a weakly pinned configuration. This description of a weakly pinned, history independent, elastic state seems entirely consistent with the predictions for a quasi-long range ordered Bragg glass phase [1]. The absence of relaxation is, therefore, highly significant, in that it suggests that the Bragg glass phase is indeed a stable rather than metastable state of the system. Further evidence of the inherent stability of the Bragg glass phase was provided by observing of the effect of applying a unidirectional drive to an ordered state vortex domain. It was found that rather than tearing-apart the ordered-phase domain *in-situ*, the unidirectional drive had the tendency to force such a region out of the sample as single coherent unit. Once again this is suggestive of a phase with a high degree of stability.

9.2 Suggested Future Work

It would be interesting to investigate in more detail the sample dependence of the melting transition region. Specifically, we could attempt to control the sample oxygen distribution. Erb *et al.* have provided evidence that more homogeneous oxygen distributions can be achieved by annealing samples at higher pressures and temperatures [2]. This suggests a possible study, in which we could observe the effect on the transition region width of annealing a particular sample under different conditions.

In relation to the hysteretic switching effects in the vicinity of the melting transition, it would be interesting to probe in more detail the structural changes occurring during switching. If we were to employ a pulsed current technique it might be possible to induce a partial restructuring of the vortex solid domains. As described above, we interpreted the current-induced switching effects in terms of melting of superheated regions on the edges of the vortex solid domains. It seems therefore that by applying a sufficiently short current-pulse, it should be possible to displace the vortex solid domains sufficiently to induce only a partial melting of the superheated regions of the vortex solid. As such, a vortex domain configuration could be attained, in which the channels for vortex liquid flow had a width intermediate between that attained in the warmed state and cooled state cases. In the context of the transport response hysteresis, this would allow us to access a state with a response level in the centre of the hysteresis loop. This would be an important test of the current induced melting hypothesis and might provide insight into the nature of the structural rearrangement that arises in response to a switching current.

There is undoubtedly scope for exploring in more detail the drive dependent history effects which have been observed in the melting transition region. For example, we could measure more carefully the point at which the annealing current becomes sufficiently large for the history effects to be observed. We could then explore what happens within the solidifying system as this limit is approached. In this way, we would potentially obtain further insight into the way in which the applied driving current controls the interaction with the underlying disorder potential. Further to this, we could use the history dependence techniques developed within this thesis to test for relaxation in both the ordered and disordered states, over even longer time-scales.

In relation to the drive dependent dynamics many questions still remain to be answered. For example, we could investigate in more detail the transient responses on switching between different drive modulation forms. A systematic investigation could be performed to determine why the ASW generated superstructure is in some cases stable to a symmetric alternating drive but in other cases drifts up to a unique ordered-state level. In particular, we should investigate in more detail the effect of switching to different drives, at various different points along the oscillation cycle.

Studies of oscillatory dynamics in geometry *H//ab* might also provide value further insights into the mechanism behind the oscillations. In this geometry the role of the sample surface is accentuated, due to increase in the ratio of the flux-penetration surface to the volume. For this reason, all effects related to the surface should be observed more clearly. Relatedly, we might wish to consider the effect of sample geometry and in particular to check whether the 2:1 ratio between the oscillation period and transit time holds for samples with different widths.

Further to this, our observations of the anomalous oscillatory dynamics recommend a number of investigations using techniques other than standard transport measurements. Firstly, it would be very interesting to perform Hall probe studies on the oscillations, using a method similar to that recently employed by Paltiel *et al.* to study vortex dynamics in $NbSe_2$ [3]. Equally, magneto-optic techniques might be useful for testing the theory that the oscillations reflect the motion of coherent domains with differing degrees of relative disorder. In order to better develop our understanding of the mechanism for the oscillations it will also be necessary to perform detailed numerical simulations. Indeed, it has recently come to our attention that studies of this nature are currently being carried out by Zeldov *et al.* [4].

References

[1] T. Giamarchi and P. Le Doussal, Phys. Rev. Lett **72** (1994) 1530; T. Giamarchi and P. Le Doussal, Phys. Rev. B **52** (1995) 1242.
[2] A. Erb, J. Y. Genoud, F. Marti, M. Däumling, E. Walker and R. Flükiger, J. Low Temp. Phys. **105** (1996) 1023; A. Erb *et al.*, cond-mat/9805222 (unpublished).
[3] Y. Paltiel, E. Zeldov, Y. N. Myasoedov, H. Shtrikman, S. Bhattacharya, M. Higgins, Z. L. Xiao, E. Y. Andrei, P. L. Gammel and D. J. Bishop, Nature **403** (2000) 398.
[4] E. Zeldov, *Private Communication.*

Appendix A : Main Sample Listing

Sample	Doping	Twinning	Dimensions	Contact Spacing
A	Optimal	Sparse	2.10 mm x 0.75 mm x 85 μm	0.48 mm
B	"	Detwinned	1.10 mm x 0.35 mm x 65 μm	0.68 mm
C	"	"	1.69 mm x 1.08 mm x 91 μm	No contacts attached
D	Overdoped	Naturally untwinned	1.65 mm x 0.39 mm x 60 μm	0.925 mm
E[*]	Optimal	Densely twinned (polycrystalline)	3.01 mm x 1.64 mm x 230 μm	1.37 mm

---

[*] Unlike the other samples considered within this thesis, which were all high purity single crystalline samples, this particular sample was a polycrystalline melt-grown sample with strong pinning due to grain boundaries, twin boundaries, and impurities. This sample is only referred to once within this thesis, in Section 6.1 of Chapter 6. For full details of how this sample was grown, see: A. Crisan, S. N. Gordeev, S. Manton, A. P. Rassau, S. Popa, C. Beduz, P. A. J. de Groot, R. Gagnon and L. Taillefer, Physica C **309** (1999) 1.

Appendix B : Summary of Temperature Sensor Characteristics

SENSOR TYPE	Approximate Useful Temperature Range[†]	Magnetoresistance (MR): ΔT/T(%) At T=88 K for different magnetic fields.			Typical dimensionless sensitivity[‡] (S_d) at 77.4 K	*Comments on limitations and application to which it is put in our experimental arrangements*
		2.5 T	8 T	14 T		
Carbon-glass CGR-1-1000	1.4K-100K	0.05	0.45	1.32	-0.53	Standard for magnetic field measurements prior to introduction of LS Cernox series. Used for temperature control in conjunction with OI ITC4 temperature controller for 16T rig.
Cernox CX 1050	1.4K- 325K	<0.05	<0.07	<0.05	-1.0	Ideal for use in magnetic fields. Used as a sample temperature sensor in 16T rig and in measurements at GHMFL.
GaAlAs Diodes	1.4K –325K	<0.1	Not Quoted	Not Quoted	-0.07	Reasonable MR over a wide range of temperatures for B < 5 T. Used for both temperature measurement and control in the SQUID pV-meter.
Capacitance CS 501 GR	4.2-300K	<0.01	<0.01	<0.01	+0.46	Virtually zero MR but exhibit significant dielectric ageing effects on temperature cycling thus are unsuitable for measurements where high reproducibility is required.[§] Used for temperature control in measurements at GHMFL.

[†] Taking into account both measurement sensitivity and the magnetoresistance

[‡] For a resistive sensor sensisitivty $S_d = (T/R)*(dR/dT)$: Equivalent expressions can be written for other thermometric properties.

[§] L. G. Rubin and W. N. Lawless, Rev. Sci. Instrum. 42 (1971) 571-573.

Appendix C : Excerpts from Manual of the GENDAT© Generalised Data Acquisition Program

C1. Introduction

The generalised data acquisition program (GENDAT) has been designed to be used with a wide variety of experimental systems. It has the facility to easily add or remove devices from a particular system. Furthermore, it can be programmed to execute a complex series of instructions each of which may involve different control or measurement devices. The program achieves this in two main ways, each of which will be discussed in the following sections.

C2. Dynamic Association Between Physical & Program Variables

All data-acquisition programs must associate physical variables with program variables. Having made this association, the program representation of the physical parameter can be manipulated in a number of ways :

(i) The value can be directly displayed on the screen.

(ii) It can be saved to an output data file

(iii) If another parameter has been associated with a different physical variable then these two variables can be plotted against each other on a graph

Conventionally, data acquisition programs are designed around a static relationship between program variables and physical parameters. Thus, in for the example given above this could be represented as follows:

© Copyright Andreas Rassau, 1999.

X1 → *B1*, controlled by OI power supply

Y1 → *V1*, measured by K199

Static physical-variable to program-parameter association for a system with two physical parameters and two corresponding program parameters.

A conventional (static association) approach has the advantage of simplicity in that, for example, the X and Y variables of displayed graph always represent the field and voltage respectively. This makes it easier when deciding how to label these graphs, and also how to label columns in the output data. From a programming point of view this is by far the simplest approach. The static approach does, however, have two important disadvantages :

(i) If we wish to change the device associated with a particular variable then changes must be made on the level of the program code itself. An example of this would be if we were to change the device measuring ***V1*** from a K199 voltmeter for a K2000. Whilst the parameters measured would remain the same, the way in which the program reads the data would be different.

(ii) If we wish to measure a completely different parameter, then again changes would have to made to the source code. As above, the device data acquisition code will have to be rewritten but also changes will have to made to graph labelling routines etc. Often these changes will be substantial, amounting to an almost complete rewrite of the program.

In the case where a wide variety of different variables are measured and devices are frequently exchanged, a *dynamic parameter association* has considerable advantages over the static alternative. In the case of dynamic parameter association, program parameters are assigned to physical variables but only on a temporary basis. As for the static case, each physical variable has a device associated with it. Consider an example in which there are four such physical variables :

1. Magnetic field (***B1***): Controlled by an OI power supply.
2. Temperature (***T1***): Controlled by a Lakeshore 340 temperature controller.
3. Voltages (***V1 and V2***): Measured by a Keithley 199 voltmeter and Stanford SR830 lock-in amplifier respectively.

Taking our previous example, of a program with plots a graph of parameter **X1** versus parameter **Y1** then this allows for four different measurement combinations namely:*V1*(***B1***), *V2*(***B1***), *V1*(***T1***) and *V2*(***T2***).

In a static physical-parameter to program-variable architecture this would require the program to have four different implementations each with different routines to read the data into **X1** and **Y1** and to display/save it once it has been measured. In terms of an association diagram this could be represented as follows :

X1 → ***B1*, controlled by OI power supply** **Y1** → ***V1*, measured by K199**	**X1** → ***T1*, controlled by LS 340.** **Y1** → ***V1*, measured by K199**
X1 → ***B1*, controlled by OI power supply** **Y1** → ***V2*, measured by SR 830**	**X1** → ***T1*, controlled LS 340** **Y1** → ***V2*, measured by SR 830**

Static physical-variable to program-parameter associations for a system with four physical parameters but just two program parameters. Here the program requires four different implementations running in parallel

If it is well known in advance which parameter combinations will be measured, then sections of the program can be built up to support each of these combinations. However, as is often the case, if new variables or devices are added additional parallel sections will need to be added to the code in each case. The alternative approach is to develop architecture which allows for the associations between physical variables to be changed from within the program without needing to change the source code. This so-called *dynamic variable-association architecture* is the system on which GENDAT is based. In order for this approach to work a number of things are a required :

1. A library of IO routines (known as a **Device Library**) comprising data-exchange code for a wide variety of physical devices. If the device library is comprehensive then there should be no need to access the source code at all. In the case where new devices are acquired, then routines for these devices must be added to the device library. By maintaining the device library as a distinct entity, the changes required are restricted to this well-defined part of the program.
2. A user configurable framework for associating physical-parameters with program-variables (known as a **Linker**). For the system shown in the example above this should give the user the option from within the program to choose any of the following parameter combinations : ***V1*(*B1*)**, ***V2*(*B1*)**, ***V1*(*T1*)** and ***V2*(*T2*)**.
3. A means to deduce the names, units and other labels for the program parameters, based upon the user configured parameter associations (known as a **Referencer**). For example, if the variable if the program parameter **Y1** is associated with physical variable ***T1*** then the program should have some means of telling that **Y1** represents a temperature and has units of Kelvin.

In terms of an association diagram these different aspects of the dynamic configuration can be represented as follows:

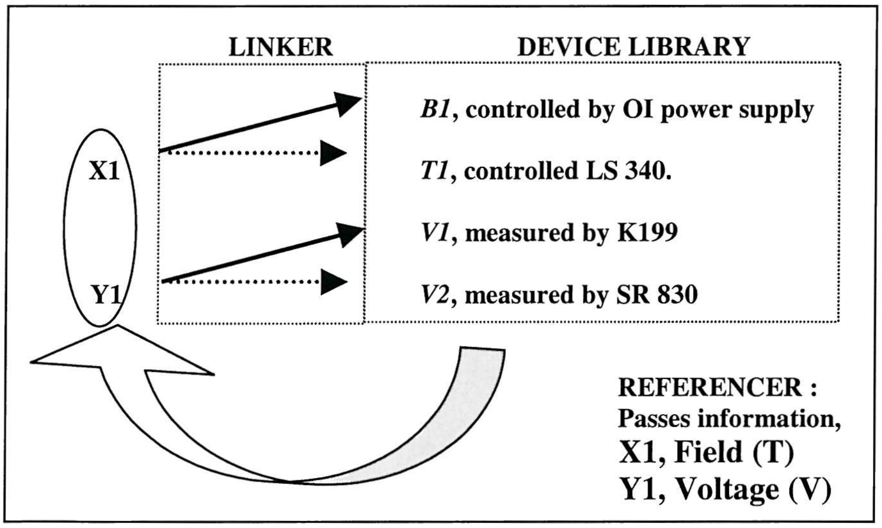

Dynamic physical-variable to program-parameter associations for a system with four physical parameters and two program parameters. As shown, X1 has been associated with B1 and Y1 with V1. Using the linker the user can change the associations from within the program. Display information for the program parameters (such as axis labelling) is passed within the program by the referencer.

C3. Script Instructions

Having associated program parameters with specific physical devices the next stage is to tell the program which of these parameters should be controlled/measured and how they should be displayed or output to files. In a static program-parameter to physical-parameter architecture this is normally achieved by prompting the user with a series of questions to ask them exactly what they want to measure. However, this has two important disadvantages:

(i) If an experimental system is constructed with a wide variety of different devices and device options it can become tedious to answer a long series of questions each time the program is run.

(ii) Normally, such an approach allows the execution of just one sweep before new instructions have to be entered.

Within a dynamic program-parameter to physical-parameter architecture it becomes possible to adopt a fundamentally different approach. In this alternative approach, instead of prompting the user for each new instruction, a series of instructions are passed to the program by way of a specially formatted text file known as a *Script File*. The script file contains a sequence of instructions, written with a special syntax, telling the program which program variables it should measure/fix. Without going into the specific details of the Script Language used by GENDAT, consider a series of natural language instruction that could be considered equivalent to a script file.

* Fix **B** = 1T

* Fix **I** =1mA
    * Sweep **T** from 50K to 100 K whilst measuring **V1**
    V1 should be plotted against **T**
    At the same time measure **V2**

A series of natural language instructions that could be represented by the specifically formatted text of a script file.

It should be noted that the variables listed within a script are program-parameters. They must first be linked to specific devices before the script can be executed. This has the advantage that, if we want to change the device that measures **V1** for example then we need only make a change in a separate configuration file. There is no need to change every instance of **V1** within the script itself.

Clearly before the script can be executed it must be converted into a format recognisable to the program. This task is performed by a part of the program known as the *Compiler.* On compilation the compiler checks the script to see the if the syntax is correct and that values provided have the correct numeric format. If an error is found in the script then the compiler will tell the user the nature and location of the problem. It is only after a script has been compiled that the program parameters within the script can be linked to specific physical devices. The linking is performed by a separate section of the program known as the *Linker.*

C4. Glossary

Physical variable:	Also known as a *Physical Parameter*, this is the value of an experimental parameter as measured or controlled by a specific physical device. An example of a physical variable is the voltage (***V***) measured by a Keithley 199 voltmeter.
Control Variable	Also known as an *Output Variable/Parameter*, this is a physical variable that is actively fixed by a particular control device. The magnetic field (***B***) set by a Oxford Instruments power supply is an example of a control variable.
Measured Variable:	Also known as an *Input Variable*, this is the value of physical parameter read by a particular measurement instrument. The voltage (***V***) measured by a Keithley 199 voltmeter is an example of a measured variable.
Null Variable	A physical variable which for some reason is not directly measured or fixed by the program. An example would be the resistance of a particular shunt resistor, which whilst known is not controlled or measured by the program. Null variables are used as information labels, their values being directly entered by the user.
Program variable:	Label within the program code associated with a particular physical parameter. For example, if the program plots a graph then the program

	variables associated with this graph could be called **X1** and **Y1**. Each of these program variables must be assigned to a different physical variable.
Variable Association:	In order for the program to acquire data each of the program variables must have a physical variable (or equivalently device) assigned to it. Thus for the examples given above, **X1** and **Y1** (the axes of the graph displayed on the computer screen) could be assigned to **B1** and **V1** the experimentally controlled/measured values for the field and the voltage respectively.
Linking	The process of associating physical variables and program parameters.
Linker	The part of a program responsible for linking.
Device Library	A library of I/O routines for use with a variety of different physical devices, allowing the physical variables associated with these devices to be measured or controlled.
Device Library	A library of I/O routines for use with a variety of different physical devices, allowing the physical variables associated with these devices to be measured or controlled.
Script	A series of instructions, within a specially formatted text file, providing information for the program on which parameters it should fix/measure and how they should be displayed. In its simplest form a script will consist of a single Fix-Instruction or Sweep-Instruction (see below). A more complicated script will consist of a sequence such instructions, which the user may choose to execute sequentially or else in any chosen order. **NB** the parameters listed appearing in the script are program parameters. Before measurements can be made these parameters must be associated with specific devices from within the Device Library using a Linker.
Script Language	The simplified language in which the script text must be written so that the program can understand it. The script language has predefined syntax rules.
Fix-Instruction	A script instruction specifying parameters to be fixed and providing the values that they should be fixed at.

Sweep-Instruction	A script instruction specifying a parameters to be swept and the range over which it should be swept. A sweep instruction must also specify at least one parameter to be tracked. For example, in the case of a program that plotted data on a graph, the tracked parameter would be plotted against the swept parameter.
Compiling	The process of converting the script from a text file to a format that will be recognised by the program. During compilation the syntax of the script is checked.
Compiler	The section of the program responsible for compiling the script